# Temporal Integrators for Langevin Equations with Applications to Fluctuating Hydrodynamics and Brownian Dynamics

by

Steven Delong

A dissertation submitted in partial fulfillment

of the requirements for the degree of

Doctor of Philosophy

Department of Mathematics

New York University

May, 2015

_____

Professor Aleksandar Donev

# Dedication

To my parents, Elizabeth and David, and to my fiancee, Lydia.

# Acknowledgments

# Abstract

Thermal fluctuations play a significant role in the dynamics of small scale hydrodynamics systems. These fluctuations can be modeled through the addition of stochastic forcing terms resulting in a system of Langevin equations which require specialized stochastic temporal integrators. We develop a general family of such schemes by adding random forcing to standard predictor corrector solvers in a way that gives second order weak accuracy for the commonly used linearized approximation to the original dynamics. We also construct predictor-corrector methods for integrating the overdamped limit of systems of equations with a fast and slow variable in the limit of infinite separation of the fast and slow timescales. The multiplicative noise in the overdamped equations gives rise to a thermal drift term which we handle using a random finite difference method in a computationaly efficient way. We further develop specialized temporal integrators for the equations of Brownian Dynamics, using a Stokes solver combined with immersed boundary techniques to compute hydrodynamic interactions. This approach is extended to describe the dynamics of immersed rigid bodies by employing normalized quaternions to represent orientation. We test our schemes by performing several numerical experiments and comparing to analytic or existing computational results.

# Contents

# List of Figures

# List of Tables

# Chapter 1

# Introduction and Background

Fluctuating Hydrodynamics (FHD) models the underlying discrete nature of fluids by including stochastic effects at macroscopic and mesoscopic scales of fluid motion. These effects stem from the microscopic structure of fluids, which are comprised of individual molecules interacting with each other. In principle, one could simulate the behavior of every individual particle to get an accurate description of the fluid's motion. However, it is impractical to handle the large number of degrees of freedom necessary to fully resolve the system, and furthermore, the timescales of the microscopic motion are much shorter than the timescales of the mesoscopic dynamics of interest. For computational feasibility, one must therefore resort to a statistical description of the system's coarse grained variables. The equations of FHD model the effects of the untracked microscopic degrees of freedom by including stochastic flux terms in the classical Navier-Stokes-Fourier equations of fluid dynamics and related conservation laws.

The equations of motion are constructed by adding stochastic fluxes to the system to balance the irreversible dissipative fluxes, resulting in Langevin systems of stochastic ordinary or partial differential equations. The temporal integration of these equations presents several difficulties and is the focus of this work. These systems take different forms depending on the problem being considered, and we describe a variety of integrators to handle these different cases. In particular, we propose second-order schemes for linearized equations, which have time-dependent additive noise, as well as first-order integrators for systems involving a fast and a slow variable, which have multiplicative noise and contain nontrivial stochastic drift terms.

There are several novel contributions to the temporal integration of fluctuating hydrodynamics and Brownian dynamics problems described in this manuscript. First, we develop a family of semi-implicit temporal integration schemes for fluctuating hydrodynamics which are second order weakly accurate for the linearized approximation to the FHD equations. This approximation is valid in the presence of weak noise (i.e., the regime where the central limit theorem applies), which is often the case in practical applications. These integrators are consistent with the multiplicative equations of motion, and can be applied to the nonlinear dynamics without committing *a priori* to the linearized equations. Furthermore, these schemes can treat the stiff diffusive terms implicitly, allowing for a larger time step size.

Second, we develop temporal integrators for two-variable systems which numerically perform adiabatic elimination. In the presence of a large separation of timescales between variables, these schemes accurately integrate the slow variable of interest without having to resolve the dynamics of the rapidly evolving fast variable. These overdamped integrators allow one to take much larger time steps than when using inertial integrators. This improvement in efficiency makes it feasible for the first time to simulate transient diffusive mixing in binary liquids in a microgravity environment. The schemes are applied to the original inertial system, removing the need to compute and write down the overdamped equations for the slow variable and allowing one to reuse existing software components.

Third, we introduce a Random Finite Difference (RFD) scheme for approximating stochastic drift terms arising from multiplicative noise in the dynamics of the slow variables in fast-slow systems. The most common method used for this purpose is Fixman's midpoint scheme, which requires calculating the action of the inverse of the mobility operator. This computation is expensive at best, and prohibitive in the case when the mobility matrix is not directly computed. This new RFD approach allows us to develop efficient numerical schemes for Langevin equations with kinetic noise, and it furthermore provides an efficient way of handling the stochastic drift term when the action of the mobility operator is obtained by using a computational fluid solver.

Fourth, we develop the Fluctuating Immersed Boundary(FIB) method. This method combines a fluctuating Stokes solver with the immersed boundary method to simulate the dynamics of colloidal spherical particles immersed

in a viscous solvent, in the overdamped regime. This approach handles a wide variety of boundary conditions computationally, avoiding the need to analytically compute a Green's function for each separate geometry. The thermal noise is incorporated directly in the fluid in an way that is efficient and agrees with physical intuition. The stochastic drift term is handled using a combination of an RFD term and a predictor-corrector step, requiring just one Stokes solve per time step, effectively doubling the computational efficiency over a direct implementation of the RFD approach. The final method scales linearly with the number of immersed particles even in the presence of boundaries, unlike existing methods used for Brownian Dynamics of colloidal and polymeric fluids.

Finally, we develop temporal integration schemes for rigid bodies of arbitrary shape immersed in a viscous solvent, including angular degrees of freedom. Simulating the time evolution of angular degrees of freedom requires parameterizing orientation, which we do in a numerically robust and efficient way by using normalized quaternions. We formulate, for the first time, an overdamped Langevin system of equations based on unit quaternions, and carefully account for the required stochastic drift terms. Our equations preserve the unit norm constraint on the quaternions and are time reversible with respect to the Gibbs-Boltzmann distribution. We develop temporal integrators for these equations which again employ our RFD method to efficiently handle the stochastic drift. This approach is agnostic to the choice of method used to apply the grand mobility, and can be used with a variety of analytic and computational techniques for modeling the hydrodynamics of suspensions of passive and active rigid particles.

This thesis is organized as follows. The rest of this chapter is dedicated to giving a brief overview of the manuscript and introducing concepts of accuracy in the stochastic setting which we use to analyze our schemes. Chapter 2 introduces several temporal integrators for Langevin equations that numerically linearize the equations around their deterministic mean and can be used for systems that exhibit a large separation of timescales. In Chapter 3 we discuss how to apply these integrators to solve systems of equations that arise in fluctuating hydrodynamics, paying attention to issues that arise when choosing spatial discretization. The material in Chapters 2 and 3 is based on references [1, 2]. Chapter 4 describes a novel fluctuating immersed boundary method for Brownian dynamics simulations, and develops a class of random finite difference temporal integrators; this work is based on reference [3]. In Chapter 5, we consider simulating the Brownian motion of rigid bodies immersed in a liquid, and develop the equations and integrators necessary for this task, which forms the basis for forthcoming publication [4]. Finally, chapter 6 gives concluding thoughts and remarks.

## 1.1 Temporal Integrators for Langevin Equations

After spatial discretization (truncation) of the stochastic partial differential equations (SPDEs) of FHD, one obtains a large-scale system of stochastic ordinary differential equations (SODEs) that has the familiar structure of Langevin equations common in statistical mechanics. In Chapter 2, we discuss a very general family of integrators for this system, which are useful for performing simulations of fluctuating hydrodynamics, but may also find use in other applications where Langevin systems arise. A rather general overdamped Langevin equation for a variable $\boldsymbol{x}(t)$ is

$$\frac{d\boldsymbol{x}}{dt} = -\boldsymbol{M}\partial_{\boldsymbol{x}}U(\boldsymbol{x}) + \sqrt{2k_BT}\boldsymbol{M}_{\frac{1}{2}} \diamond \boldsymbol{\mathcal{W}} \tag{1.1}$$

$$= -\boldsymbol{M}\partial_{\boldsymbol{x}}U(\boldsymbol{x}) + \sqrt{2k_BT}\boldsymbol{M}_{\frac{1}{2}}\boldsymbol{\mathcal{W}} + k_BT\,\partial_{\boldsymbol{x}}\cdot(\boldsymbol{M}) \tag{1.2}$$

where $\boldsymbol{M}\,(\boldsymbol{x})$ is a symmetric positive semidefinite mobility operator, $U(\boldsymbol{x})$ is the potential energy, $k_B$ is Boltzmann's constant, $T$ is temperature, and the "square root" of the mobility $\boldsymbol{M}_{\frac{1}{2}}$ satisfies the fluctuation dissipation relationship $\boldsymbol{M}_{\frac{1}{2}}\boldsymbol{M}_{\frac{1}{2}}^{\star} = \boldsymbol{M}$. The stochastic forcing $\boldsymbol{\mathcal{W}}\,(t)$ indicates a vector of independent white noise processes, with zero mean and covariance

$$\langle \mathcal{W}_i(t)\mathcal{W}_j(t')\rangle = \delta_{ij}\delta(t - t'),$$

where $\delta_{ij}$ is the Kronecker delta symbol, and $\delta(t - t')$ is the Dirac delta function. Here and in the rest of this thesis, we adopt the standard physics notation, formally identifying $\boldsymbol{\mathcal{W}} \equiv d\boldsymbol{\mathcal{B}}/dt$, where $\boldsymbol{\mathcal{B}}(t)$ is a collection of independent Wiener processes (standard Brownian motions). In the differential notation more common in the mathematics literature, eq. (1.1) takes the form

$$d\boldsymbol{x} = -\boldsymbol{M}\partial_{\boldsymbol{x}}U(\boldsymbol{x})dt + \sqrt{2k_BT}\boldsymbol{M}_{\frac{1}{2}} \diamond d\boldsymbol{\mathcal{B}}.$$

The interpretation of the noise (stochastic integral) is kinetic [5], denoted here by the symbol $\diamond$; the overdamped Langevin equation is re-written using an Ito interpretation in the second line of eq. (1.1), where in index notation

the divergence of the the mobility $\partial_{\boldsymbol{x}} \cdot (\boldsymbol{M})$ is

$$[\partial_{\boldsymbol{x}} \cdot (\boldsymbol{M}(\boldsymbol{x}))]_i = \frac{\partial}{\partial x_j} M_{ij}(\boldsymbol{x}).$$

The key property of the dynamics (1.1) is that it is time reversible with respect to the Gibbs-Boltzmann equilibrium distribution (invariant measure)

$$\rho_{eq}(\boldsymbol{x}) = Z^{-1} \exp\left(-U(\boldsymbol{x})/k_B T\right),$$

where $Z$ is a normalization constant.

The first difficulty that arises in integrating equation (1.1) is correctly handling multiplicative noise. The kinetic interpretation [5] of the noise term present in the generic Langevin equation (1.1) gives rise to the stochastic drift term $k_B T \, \partial_{\boldsymbol{x}} \cdot (\boldsymbol{M})$ in (1.2) which must be accurately reproduced by numerical temporal integrators. This requires approximating the divergence of the mobility operator. In some simulations, the mobility is never explicitly calculated, and one can only compute the action of the mobility algorithmically. The well known Fixman method can be used to generate the stochastic drift so long as the action of the inverse of mobility, or the "square root" of the inverse of the mobility, can be calculated. In the case when only the action of the $\boldsymbol{M}$ and $\boldsymbol{M}_{\frac{1}{2}}$ can be calculated, we introduce a novel Random Finite Difference (RFD) method to approximate the stochastic drift in expectation.

One can linearize equation (1.1) around its deterministic mean to formulate an approximation that is accurate when the magnitude of the noise in the SODEs is weak. We construct our integrators in such a way that they are second order weakly accurate for this linearized approximation. Additionally, we consider temporal integrators for systems with a fast and slow variable which treat the fast variable implicitly in order to numerically approximate the overdamped dynamics of the slow variable. This is useful for simulating the slow variable of interest without having to restrict the time step size based on the rapidly evolving fast variable. By using RFD terms, we make sure that these temporal integrators are also consistent in the fully nonlinear, multiplicative noise case.

## 1.2 Fluctuating Hydrodynamics

In chapter 3, we apply our temporal integrators to the equations of fluctuating hydrodynamics (FHD). These equations are obtained by adding a stochastic flux to balance each dissipative, irreversible flux [6]. Alternatively, one can derive the discrete equations of FHD directly by starting with the equations for the dynamics of a microscopic system and using the theory of coarse graining to eliminate all but the discrete variables of interest [7, 8]. At small length scales and time scales larger than sonic, we can describe the evolution of the fluctuating incompressible velocity field $\boldsymbol{v}$ with the fluctuating Stokes equations, $\boldsymbol{\nabla} \cdot \boldsymbol{v} = 0$ and

$$\rho \partial_t \boldsymbol{v} = -\boldsymbol{\nabla} \pi + \eta \boldsymbol{\nabla}^2 \boldsymbol{v} + \boldsymbol{\nabla} \cdot \left[ (2 k_B T \eta)^{\frac{1}{2}} \, \boldsymbol{\mathcal{W}} \right], \tag{1.3}$$

where $\rho$ is the constant density, $\eta = \rho \nu$ is the constant shear viscosity, $T$ is the constant temperature, and $k_B$ is Boltzmann's constant. Here $\pi$ represents the non-thermodynamic pressure, and the stochastic momentum fluxes are modeled via the spatio-temporal white noise random tensor field $\boldsymbol{\mathcal{W}}(\boldsymbol{r}, t)$ with covariance

$$\langle \mathcal{W}_{ij}(\boldsymbol{r}, t) \mathcal{W}_{kl}(\boldsymbol{r}', t') \rangle = (\delta_{ik} \delta_{jl}) \, \delta(t - t') \delta(\boldsymbol{r} - \boldsymbol{r}').$$

Note that this form of the noise is adequate in the incompressible, constant viscosity case; in the more general case, one should use the symmeterized noise $(k_B T)^{\frac{1}{2}} \left( \boldsymbol{\mathcal{W}} + \boldsymbol{\mathcal{W}}^T \right)$, where superscript $T$ indicates a transpose. Equation (1.3) is linear and can therefore be given rigorous meaning in the space of Gaussian distributions [9]. Furthermore, since the noise is additive (its magnitude does not depend on $\boldsymbol{v}$), there is no difference in the various interpretations of the stochastic integral here. At thermodynamic equilibrium (no forcing in bulk or the boundaries), equation (1.3) preserves the Gibbs-Boltzmann distribution with potential energy equal to the total kinetic energy of the fluid, subject to momentum conservation and restricted to the space of divergence-free vector fields,

$$P_{\text{eq}}(\boldsymbol{v}) = Z^{-1} \exp\left[ -\frac{\int d\boldsymbol{r} \, \rho v^2}{2 k_B T} \right] \boldsymbol{\delta} \left( \int d\boldsymbol{r} \, \rho \boldsymbol{v} \right) \delta\left( \boldsymbol{\nabla} \cdot \boldsymbol{v} \right).$$

Temporal integration of equation (1.3) presents several difficulties. First, the equations are discretized in space, and care must be taken to preserve the fluctuation-dissipation balance condition that holds for the continuum equations. This is further complicated in the presence of advection, which must be discretized as a skew adjoint,

3

divergence free operator applied to the gradient of the potential in order to conserve energy. Additionally, the diffusion term in equation (1.3) is stiff, and thus restricts the time step size for explicit integrators considerably. We employ the semi-implicit integrators described in Chapter 2 to handle this term implicitly, allowing for larger time step sizes. We catalog a few specific algorithms in Section 3.4 for both the inertial and overdamped equations. We test these methods on several numerical examples, and investigate giant concentration fluctuations in a binary liquid mixture in the presence of an imposed temperature gradient.

## 1.3 Fluctuating Immersed Boundary method

Complex fluids exhibit behaviors on a variety of length and time scales. In many interesting applications, such as polymer chains or colloidal suspensions, the dynamics of interest are the long time diffusive (Brownian) dynamics of immersed structures. In regimes where inertia dissipates much faster than mass (formally the limit of infinite Schmidt number), one obtains the overdamped Langevin system (1.1) for the positions of immersed particles. In Chapter 4, we describe the Fluctuating Immersed Boundary (FIB) method for simulating the Brownian Dynamics (BD) of spherical particles in bounded systems such as micro and nano channels.

One significant difficulty in BD is constructing the mobility operator $M(x)$, which takes forces on all of the particles and calculates their resulting velocities. This operator determines the effects of particle interaction as well as the effect of the boundary, and controls the hydrodynamic correlations among the diffusing particles. Many existing approaches perform analytic calculations of the mobility, but these are in general non-trivial and must be performed separately for each geometry considered[10, 11]. To allow for general boundary conditions, in this work we avoid analytic approximations of the mobility. Instead, we employ a numerical steady Stokes solver and immersed boundary techniques to calculate interactions between particles and the effects of domain boundaries.

Another challenge is correctly including the stochastic forcing term in a way that satisfies fluctuation-dissipation balance. Naively, this can be done by performing a Cholesky decomposition of the mobility matrix. However, this operation is not always possible without an explicit approximation to the mobility, and regardless, it is computationally expensive. We generate the stochastic term at the fluctuating hydrodynamics level, by incorporating stochastic forcing in the fluid equation (1.3). This is numerically efficient (especially in simulations with a large number of immersed particles), and reflects the physical intuition that fluctuations come from the thermal fluctuations in the fluid.

Finally, we must approximate the stochastic drift term that arises from the kinetic interpretation of the noise in the overdamped Langevin equation. The standard approach in the literature is to use Fixman's midpoint method [12, 13], which requires computing the action of the inverse of the mobility operator. Because we employ a numerical recipe for applying the mobility operator, this inverse is not directly computable, and we need to develop an alternative approach. In our method, the stochastic drift is split into pieces which are handled separately with a combination of random finite difference terms and a predictor-corrector step, and the result is an integrator that requires only one Stokes solve per time step.

We perform several numerical tests to validate our method, investigating the equilibrium distribution, as well as a few dynamic quantities. We compare to theory when available to illustrate the accuracy of our methods and the importance of carefully handling the stochastic drift term.

## 1.4 Brownian Dynamics of Rigid Bodies

The FIB method only considers spherical particles with no angular degrees of freedom. However, many interesting applications involve non-spherical particles, and their shapes significantly affect their motion and the hydrodynamic interactions with other particles and boundaries. We extend our methods in Chapter 5 to simulate the Brownian motion of rigid bodies with arbitrary shape immersed in a viscous solvent.

Simulating the motion of immersed non spherical structures requires choosing a way to represent orientation, and formulating the appropriate equations using this representation. Certain bodies possess symmetries which can simplify this problem (such as rods [14] or ellipsoids), but our goal is to parameterize the full orientation of general rigid bodies in three dimensions, allowing for arbitrary body shape. We use normalized quaternions to track the orientation of these bodies, which to our knowledge has not been done before for rigid structures in the overdamped regime. This representation is space efficient, numerically robust, and convenient to accumulate. Only quaternions of unit norm correspond to valid orientations, and we formulate a novel system of overdamped Langevin equations of motion that are time reversible with respect to the expected Gibbs-Boltzmann distribution restricted to the unit quaternion manifold.

The resulting equations of motion possess a stochastic drift term which is in general non-trivial to approximate. We develop two specialized temporal integration schemes for handling this term. The first is an application of the well known Fixman midpoint method [12, 13], which requires the calculation of the inverse of the mobility matrix. The second is a Random Finite Difference (RFD) scheme, which avoids this calculation and is therefore more computationally efficient. In both schemes, the orientation is updated through a multiplicative rotate procedure which preserves the unit norm constraint of the quaternion in a natural way while remaining consistent with the additive Langevin system.

We verify both schemes by simulating the motion of various rigid bodies near a single no slip wall. To perform these simulations we employ a "bead" model [15, 16, 17, 18, 19, 20] to approximate the grand mobility tensor of the body. However, the equations of motion and our temporal integration methods do not rely on this model, and they can in principle be used with any approach that can calculate the action of the mobility tensor. In particular, the equations and associated temporal integrators developed here can be used to extend the FIB method to suspensions of rigid bodies of complex shapes in bounded domains, based on a recent extension of the immersed boundary method to rigid bodies [21].

## 1.5   Addendum: Weak order conditions

The equations of fluctuating hydrodynamics are stochastic in nature, and when discussing temporal integrators for them we will need precise notions of accuracy in a probabilistic setting. There are two relevant concepts of finite-horizon accuracy that arise for temporal integration schemes for stochastic differential equations: the weak order of accuracy of a scheme, and the strong order of accuracy. A scheme that is weakly accurate to high order will give a good approximation of expectation values of sufficiently well-behaved functions of the underlying process, while strong order of accuracy gives guarantees about the convergence of paths of the simulated dynamics.

We first define the notion of weak accuracy. Suppose we have a continuous stochastic process $\boldsymbol{x}(t)$, which we approximate with a discrete trajectory $\boldsymbol{x}_{\Delta t}(n\Delta t)$ obtained using a numerical time stepping scheme with fixed time step size $\Delta t$. We say this scheme is *weakly $p$ order accurate* if given any finite time $T$, for any function of polynomial growth $f$ which is continuously differentiable $2(p+1)$ times, we have that for all $\Delta t < \Delta t_0$ for some $\Delta t_0 > 0$,

$$|\mathbb{E}\left(f\left(\boldsymbol{x}\left(T\right)\right)\right) - \mathbb{E}\left(f\left(\boldsymbol{x}_{\Delta t}\left(T\right)\right)\right)| \leq C\Delta t^p,$$

for a constant $C\left(T\right)$ independent of $\Delta t$ [22].

For the same stochastic process, we say that a scheme is *strongly $q$ order accurate* if for any time $T$, for all $\Delta t < \Delta t_0$ for some $\Delta t_0$,

$$\mathbb{E}\left(|\boldsymbol{x}\left(T\right) - \boldsymbol{x}_{\Delta t}\left(T\right)|\right) \leq C\Delta t^q,$$

where again $C(T)$ is a constant independent of $\Delta t$.

In this work we focus on weak order of accuracy of our schemes. This is in large part because we anticipate that these schemes will be used in Monte Carlo simulations to measure expectation values of physical observables, and would therefore benefit from higher weak, rather than strong, accuracy. Achieving a high order of strong accuracy is technically more challenging and expensive; in this work we are content with schemes that exhibit $q = 1/2$ strong order of accuracy. We obtain 1st order weak accuracy for all problems considered herein, and we achieve 2nd order weak accuracy in cases where the noise term is additive, as in linearized Langevin equations.

Let us consider second-order weakly accurate *one-step* temporal discretizations with a constant time step $\Delta t$ for the general Ito SDE

$$\frac{d\boldsymbol{x}}{dt} = \boldsymbol{a}\left(\boldsymbol{x}\right) + \boldsymbol{K}(\boldsymbol{x})\boldsymbol{\mathcal{W}}\left(t\right), \tag{1.4}$$

where the drift $\boldsymbol{a}\left(\boldsymbol{x}\right)$ is a vector-valued function, and the noise amplitude $\boldsymbol{K}(\boldsymbol{x})$ is a matrix-valued function. Let us denote the numerical approximation with $\boldsymbol{x}^n \approx \boldsymbol{x}\left(n\Delta t\right)$. The simplest temporal integrator for (1.4) is the weakly first-order accurate Euler-Maruyama scheme,

$$\boldsymbol{x}^{n+1} = \boldsymbol{x}^n + \Delta t\,\boldsymbol{a}^n + \Delta t^{\frac{1}{2}}\boldsymbol{K}^n\boldsymbol{W}^n, \tag{1.5}$$

where the superscript denotes where the term is evaluated, for example, $\boldsymbol{a}^n \equiv \boldsymbol{a}\left(\boldsymbol{x}^n\right)$. Here $\boldsymbol{W}^n$ is a vector of independent standard Gaussian variates (i.e., normally-distributed pseudorandom numbers with mean zero and unit variance), generated independently at each time step. The SDE (1.4) can, in fact, be defined through the limit $\Delta t \to 0$ of the scheme (1.5). The stochastic term

$$\Delta t^{\frac{1}{2}}\boldsymbol{W}^n = \Delta\boldsymbol{\mathcal{B}}^n$$

is equivalent in law to the (Wiener) increment of the Brownian motions $\boldsymbol{\mathcal{B}}(t)$ over the time step. Alternatively, one can view (1.5) as an application of the deterministic explicit Euler method to (1.4), with the "discrete white noise" $\Delta t^{-1/2}\boldsymbol{W}^n$ representing the rough forcing $\boldsymbol{\mathcal{W}}(t) = d\boldsymbol{\mathcal{B}}/dt$. This viewpoint is particularly useful when extending higher-order standard deterministic schemes to the stochastic context.

Let us consider one-step schemes for the general nonlinear additive-noise system of SDEs (1.4). The general theory of weak accuracy for stochastic integrators is well-established and reviewed, for example, in Section 2.2 of [22]. The key result is that for a scheme to have weak order $p$, the first $(2p+1)$ moments of the discrete (approximate) and continuum (true) increment must match to order $\Delta t^{p+1}$. The precise theorem can be stated as follows for the case of second order accuracy. First, we define a class of functions $F$ of polynomial growth. We say that a function $f$ on $\mathbb{R}^d$ is in $F$ if there exist constants $k, K \in \mathbb{R}_+$ such that

$$|f(\boldsymbol{x})| \leq K\left(1 + |\boldsymbol{x}|^k\right), \quad \forall \boldsymbol{x} \in \mathbb{R}^d.$$

Now consider the process defined by eq. (1.4), and suppose that $\boldsymbol{a}$ and the columns of $\boldsymbol{K}$ are both Lipschitz continuous, and suppose that they and their derivatives of up to order 6 exist and are in $F$. Let $\boldsymbol{x}^n_{\boldsymbol{y},t}$ be the value of the numerical approximation at time $n\Delta t$ if it is started at point $\boldsymbol{y}$ at time $t$. Likewise, denote a continuous trajectory started at point $\boldsymbol{y}$ at time $t$ evaluated at a later time $t'$ by $\boldsymbol{x}_{\boldsymbol{y},t}(t')$. We define the one step increments $\bar{\Delta}\boldsymbol{x}^n(\boldsymbol{x}_0) = \boldsymbol{x}^{n+1}_{\boldsymbol{x}_0,n\Delta t} - \boldsymbol{x}_0$ and $\Delta\boldsymbol{x}^n(\boldsymbol{x}_0) = \boldsymbol{x}_{\boldsymbol{x}_0,n\Delta t}(n\Delta t + \Delta t) - \boldsymbol{x}_0$. Suppose there exists $K_1, K_2 \in F$ such that for any choice of $\boldsymbol{x}_0$, and any choice of components $i(j) \in \{1, \ldots, d\}\ \forall j = 1, \ldots, 6$ where $d$ is the dimension of $\boldsymbol{x}$, we have

$$\left| E\left(\prod_{j=1}^{s} \Delta x^n_{i(j)}(\boldsymbol{x}_0) - \prod_{j=1}^{s} \bar{\Delta} x^n_{i(j)}(\boldsymbol{x}_0)\right)\right| \leq K_1(\boldsymbol{x}_0)\Delta t^3, \quad s = 1, \ldots, 5$$

$$E\left(\prod_{j=1}^{s} \left|\bar{\Delta} x^n_{i(j)}(\boldsymbol{x}_0)\right|\right) \leq K_2(\boldsymbol{x}_0)\Delta t^3, \quad s = 1, \ldots, 6.$$

Further suppose that for sufficiently large $m$, the expectation $E\left(|\boldsymbol{x}^n|^{2m}\right)$ exists and is uniformly bounded with respect to $N = T/\Delta t$ and $n = 0, 1, \ldots N$. Then the approximation $\boldsymbol{x}^n$ is second order weakly accurate, see [22] for the proof and a generalization to other orders of weak accuracy.

# Chapter 2

# Temporal Integrators for Langevin Equations

In this chapter, we are concerned with temporal integration of the Langevin systems that stem from fluctuating hydrodynamics and other mesoscopic models. In practical applications, several difficulties arise that require the development of temporal integration schemes. The first complication in FHD is the appearance of multiplicative noise. In the context of SPDEs, such multiplicative noise is often purely formal and cannot be interpreted mathematically in continuum formulations unless the nonlinear terms are regularized [23, 24], or suitable renormalization terms are added [25]. In most cases, a precise formulation of the multiplicative noise terms is not known and the importance of various stochastic drift terms arising due to the multiplicative nature of the noise have not been explored. A precise mathematical interpretation can, however, be given to the equations of *linearized* FHD (LFHD), which are in fact the most common model used in the literature [26]. The LFHD equations can in some cases be derived rigorously from the microscopic dynamics as a form of central limit theorem for the Gaussian fluctuations around the deterministic hydrodynamic equations, which are themselves a form of law of large numbers for the macroscopic observables [27, 28, 29, 30, 31]. One can, at least formally, obtain the LFHD equations from the nonlinear FHD equations by expanding to leading order in the magnitude of the stochastic forcing terms (more precisely, the inverse of the coarse-graining length scale).

Such linearization of nonlinear FHD equations leads to a system of two equations, the usual *nonlinear* deterministic equation, and a *linear* (additive-noise) stochastic differential equation (SDE) for the Gaussian fluctuations around the mean. A naive approach to temporal integration of the equations of LFHD might be to first solve the deterministic equation, itself a nontrivial problem except in the simplest of cases, and *then* solve a linear SDE with a time-dependent but additive noise of magnitude determined by the deterministic solution. Here we present predictor-corrector integrators that can accomplish these two steps together without ever explicitly writing the LFHD equations. Specifically, here we construct schemes that numerically linearize the equations around a numerically-determined deterministic solution. Our analysis shows how to achieve second-order weak accuracy for the LFHD equations by choosing where to evaluate the amplitude of the stochastic forcing terms. In certain cases, the resulting integrators will also be first-order weakly accurate for the (discrete or regularized) *nonlinear* FHD equations. For nonlinear Langevin equations with multiplicative noise, in general, it is difficult to construct integrators of weak order higher than one. Second-order weak Runge-Kutta (derivative-free) schemes have been constructed [32] for systems of SODEs, however, using these types of methods in the contexts of SPDEs is non trivial.

A second difficulty that often arises in FHD is the appearance of large separation of time scales between the different hydrodynamic variables. In incompressible FHD, velocity fluctuations are the most rapid, since flows at small scales are typically viscous-dominated and momentum diffuses much faster than does mass. As the dynamics of interest is usually the slow dynamics of the concentration field or discrete particles advected by the velocity fluctuations, specialized multiscale temporal integrators are required to avoid the need to use small time step sizes that resolve the fast dynamics. This can be accomplished by analytically performing adiabatic mode elimination and eliminating the fast variable from the description to obtain a limiting or *overdamped* equation for the slow variables, and then numerically integrating the limiting dynamics. In this work we develop predictor-corrector schemes that in essence numerically take the overdamped limit of a two-scale (fast-slow) system of SODEs in which the fast variable enters linearly. Our predictor-corrector schemes are applicable to a broad range of two-scale Langevin equations that frequently arise in practice in a variety of contexts. Their key feature is that they obtain all of the

stochastic drift terms numerically without requiring derivatives. This makes it relatively easy to take a code that integrates the original fast-slow *inertial* dynamics using a (semi-)implicit method, and to convert it into a code that integrates the overdamped dynamics. Furthermore, the schemes we construct here are second-order weakly accurate for the linearized overdamped equations. In order to facilitate the integration of our methods in existing codes our algorithms make use of the components already required to integrate the original fast-slow equations without making use of the large-separation of scales. The result is a new algorithm that reuses the base code but can take a time step several orders of magnitude larger.

In this work we demonstrate that simple predictor-corrector methods can address the difficulties discussed above with a minimal amount of effort on the part of the user. Specifically, we develop simple predictor-corrector schemes for temporal integration of Langevin SDEs that arise in fluctuating hydrodynamics and accomplish the following design goals:

1. They reuse the same computational components already available in standard computational fluid dynamics (CFD) solvers, such as linear solvers for viscosity or diffusion, advection schemes, etc.

2. In the deterministic context they are second-order accurate and relatively standard.

3. For nonlinear but additive noise SDEs they are second-order weakly accurate (see Section 1.5).

4. They numerically linearize the FHD equations and solve the LFHD equations weakly to second-order.

5. For LFHD, they give higher-order accurate static correlations (static structure factors) at steady state (see section 2.2.1).

6. They can be used to integrate two-scale fast-slow systems in the overdamped limit, preserving all of the above properties but now referring to the limiting dynamics.

7. In the general nonlinear multiplicative-noise case, they are weakly first-order accurate and do not require any derivative information.

Some of the temporal integrators described here have been used previously in more specialized works. In [23], an overdamped SPDE for the concentration of the immersed particles [24] is solved using the techniques detailed here. In [33], our methods are applied to the low Mach number equations of FHD. In chapter 4 we construct temporal integrators for the equations of Brownian Dynamics, which is a multiplicative-noise overdamped SDE. These overdamped Langevin equations result when one eliminates the fast velocity degrees of freedom from a system of equations for the motion of particles immersed in a fluctuating Stokes fluid. In this chapter we present the temporal integrators used in these specialized scenarios in greater generality, with the hope that they will be useful for other Langevin equations. We also explain the analysis required to study the order of weak accuracy of the schemes, making it easier for other researchers to further generalize these methods or to apply them in specific contexts.

## 2.1   Generic Langevin Equations

In this chapter, we will consider temporal integrators for a class of generic Langevin equations for the coarse-grained variables $\boldsymbol{x}(t)$ [34],

$$\frac{d\boldsymbol{x}}{dt} = -\boldsymbol{N}\left(\boldsymbol{x}\right)\frac{\partial U}{\partial \boldsymbol{x}} + \left(2k_B T\right)^{1/2}\boldsymbol{M}_{\frac{1}{2}}\left(\boldsymbol{x}\right)\boldsymbol{\mathcal{W}}(t) + \left(k_B T\right)\frac{\partial}{\partial \boldsymbol{x}}\cdot\boldsymbol{N}\left(\boldsymbol{x}\right), \tag{2.1}$$

where $\boldsymbol{\mathcal{W}}(t)$ denotes white noise, the formal time derivative of a collection of independent Brownian motions, and an Ito interpretation is assumed. Here $U\left(\boldsymbol{x}\right)$ is the thermodynamic driving potential, such as an externally-applied conservative potential or a *coarse-grained free energy.* In the following, the explicit dependence on $\boldsymbol{x}$ is suppressed, and the *mobility operator* is written as $\boldsymbol{N} \equiv \boldsymbol{N}\left(\boldsymbol{x}\right)$, and the noise operator $\boldsymbol{M}_{\frac{1}{2}}\left(\boldsymbol{x}\right)$ obeys the *fluctuation-dissipation balance* condition

$$\boldsymbol{M}_{\frac{1}{2}}\boldsymbol{M}_{\frac{1}{2}}^{\star} = \boldsymbol{M} = \frac{1}{2}\left(\boldsymbol{N} + \boldsymbol{N}^{\star}\right), \tag{2.2}$$

where star denotes an adjoint. This ensures that the dynamics (2.1) is (under suitable assumptions) ergodic with respect to the Gibbs-Boltzmann distribution

$$P_{\text{eq}}\left(\boldsymbol{x}\right) = Z^{-1}\exp\left[-\frac{U\left(\boldsymbol{x}\right)}{k_B T}\right], \tag{2.3}$$

where $Z$ is a normalization constant. In the notation we have chosen, in component form $(\partial_{\boldsymbol{x}} \cdot \boldsymbol{N})_i = \partial_j N_{ij}$, where repeated indices are implicitly summed throughout this paper. Please note that this is different from the less-standard notation used in [1], where the drift term is written as $(k_B T) \, \partial_{\boldsymbol{x}} \cdot \boldsymbol{N}^{\star}$.

The last term in (2.1) is an additional "stochastic" or "thermal" drift term, as can be seen from the fact that it is proportional to $k_B T$. This term contains information about the noise and therefore depends on the particular interpretation of the stochastic integral. The stochastic drift term, however, also contains information about the anti-symmetric part of the generator $\boldsymbol{N}$ that is unrelated to the stochastic noise term. If the skew-adjoint component $\boldsymbol{L} = \frac{1}{2} (\boldsymbol{N}^{\star} - \boldsymbol{N})$ is divergence-free, $\partial_{\boldsymbol{x}} \cdot \boldsymbol{L} = 0$, the associated dynamics is incompressible in phase space [35] and the stochastic drift term disappears if one uses the kinetic interpretation [5] of the stochastic integral, denoted with the stochastic product $\diamond$,

$$\partial_t \boldsymbol{x} = -\boldsymbol{N} \frac{\partial U}{\partial \boldsymbol{x}} + (2 k_B T)^{1/2} \, \boldsymbol{M}_{\frac{1}{2}} \diamond \boldsymbol{\mathcal{W}}. \tag{2.4}$$

In the case when $\boldsymbol{N} = \boldsymbol{M}$ is self-adjoint, $\boldsymbol{L} = 0$, the kinetic SDE (2.4) corresponds to a Fokker-Planck equation for the evolution of the probability distribution $P(\boldsymbol{x}, t)$ for observing the state $\boldsymbol{x}$ at time $t$,

$$\frac{\partial P}{\partial t} = \frac{\partial}{\partial \boldsymbol{x}} \cdot \left\{ \boldsymbol{M} \left[ \frac{\partial U}{\partial \boldsymbol{x}} P + (k_B T) \frac{\partial P}{\partial \boldsymbol{x}} \right] \right\}, \tag{2.5}$$

where we note that the term in square brackets vanishes when $P = P_{eq}$. The kinetic stochastic integral [5] is a combination of an Ito and Stratonovich interpretation, which can be denoted symbolically as

$$\begin{aligned} \partial_t \boldsymbol{x} &= -\boldsymbol{M} \frac{\partial U}{\partial \boldsymbol{x}} + (2 k_B T)^{1/2} \, \boldsymbol{M} \circ \boldsymbol{M}^{-1} \boldsymbol{M}_{\frac{1}{2}} \boldsymbol{\mathcal{W}} \tag{2.6} \\ &= -\boldsymbol{M} \frac{\partial U}{\partial \boldsymbol{x}} + (2 k_B T)^{1/2} \, \boldsymbol{M}_{\frac{1}{2}} \boldsymbol{\mathcal{W}} + (k_B T) \frac{\partial}{\partial \boldsymbol{x}} \cdot \boldsymbol{M}, \end{aligned}$$

indicating that the terms after $\circ$ are evaluated at the beginning of the time interval in the spirit of the Ito interpretation, while the terms before $\circ$ are evaluated at the midpoint of the time interval, in the spirit of the Stratonovich interpretation. Note that $\boldsymbol{M}^{-1} \boldsymbol{M}_{\frac{1}{2}}$ in the first line can be replaced with any matrix $\boldsymbol{M}_{-\frac{1}{2}}$ that preserves the covariance of the noise, $\boldsymbol{M}_{-\frac{1}{2}} \boldsymbol{M}_{-\frac{1}{2}}^{\star} = \boldsymbol{M}^{-1}$. A useful identity for converting between the kinetic form and the Ito form is, given two matrices $\boldsymbol{A}(\boldsymbol{x})$ and $\boldsymbol{B}(\boldsymbol{x})$,

$$\begin{aligned} \boldsymbol{A} \circ \boldsymbol{B} \boldsymbol{\mathcal{W}} &\equiv \frac{1}{2} (\partial_{\boldsymbol{x}} \boldsymbol{A}) : \left( \boldsymbol{B} \boldsymbol{B}^T \boldsymbol{A}^T \right) + \boldsymbol{A} \boldsymbol{B} \boldsymbol{\mathcal{W}} \tag{2.7} \\ &= \frac{1}{2} \left( \partial_{\boldsymbol{x}} \cdot \left( \boldsymbol{A} \boldsymbol{B} \boldsymbol{B}^T \boldsymbol{A}^T \right) - \boldsymbol{A} \, \partial_{\boldsymbol{x}} \cdot \left( \boldsymbol{B} \boldsymbol{B}^T \boldsymbol{A}^T \right) \right) + \boldsymbol{A} \boldsymbol{B} \boldsymbol{\mathcal{W}}, \end{aligned}$$

where $\left\{ (\partial_{\boldsymbol{x}} \boldsymbol{A}) : \left( \boldsymbol{B} \boldsymbol{B}^T \boldsymbol{A}^T \right) \right\}_i = (\partial_l A_{ij}) B_{jk} B_{mk} A_{lm}$ and we use the product rule to obtain the second line of (2.7). We can obtain the equivalence between the first and second lines of (2.6) by choosing $\boldsymbol{A} = \sqrt{2 k_B T} \boldsymbol{M}$ and $\boldsymbol{B} = \boldsymbol{M}^{-1} \boldsymbol{M}_{\frac{1}{2}}$.

### 2.1.1 Overdamped Langevin Equations

As a simple but illustrative example of a Langevin equation that our methods can be applied to we consider the Langevin equation with position-dependent friction tensor $\boldsymbol{\gamma}(\boldsymbol{x})$,

$$\begin{aligned} m \frac{d\boldsymbol{v}}{dt} &= \boldsymbol{F}(\boldsymbol{x}) - \boldsymbol{\gamma}(\boldsymbol{x}) \boldsymbol{v} + \sqrt{2 k_B T \boldsymbol{\gamma}(\boldsymbol{x})} \, \boldsymbol{\mathcal{W}}(t) \\ \frac{d\boldsymbol{x}}{dt} &= \boldsymbol{v}, \end{aligned} \tag{2.8}$$

where $\boldsymbol{x}(t)$ is the position of a particle diffusing under the influence of an external force $\boldsymbol{F}(\boldsymbol{x}) = -\partial_{\boldsymbol{x}} U(\boldsymbol{x})$, $\boldsymbol{v}(t)$ is the particle velocity, and $m$ is its mass. It is well-known that in the low-inertia limit $m \to 0$, the velocity can be eliminated as a fast degree of freedom to obtain the overdamped Langevin equation [36, 37]

$$\frac{d\boldsymbol{x}}{dt} = \boldsymbol{\gamma}^{-1}(\boldsymbol{x}) \boldsymbol{F}(\boldsymbol{x}) + \sqrt{2 k_B T} \, \boldsymbol{\gamma}^{-\frac{1}{2}}(\boldsymbol{x}) \boldsymbol{\mathcal{W}}(t) + (k_B T) \partial_{\boldsymbol{x}} \cdot \boldsymbol{\gamma}^{-1}(\boldsymbol{x}), \tag{2.9}$$

which is of the form (2.1) with a self-adjoint mobility $\boldsymbol{N} = \boldsymbol{M} \equiv \boldsymbol{\gamma}^{-1}$ and with $\boldsymbol{M}_{\frac{1}{2}} \equiv \boldsymbol{\gamma}^{-\frac{1}{2}} = \boldsymbol{M}^{\frac{1}{2}}$ being a matrix square root or a Cholesky factor of $\boldsymbol{\gamma}^{-1}$. Even though the overdamped equation strictly only applies in the limit of infinite separation of time scales, it will be a very good approximation so long as there still remains a large separation of time scales between the fast velocity and the slow position.

### 2.1.1.1 Fixman Scheme

In this work we construct predictor-corrector algorithms that integrate the overdamped equation (2.9) by instead directly discretizing the inertial equation (2.8) without the inertial term $\partial_t \boldsymbol{v}$. By carefully constructing the corrector stage we will obtain the correct stochastic or thermal drift term in (2.9). For the simple Langevin equation (2.8) a trapezoidal integrator goes from time step $n$ to time step $n+1$ via the two stages,

$$
\begin{aligned}
\boldsymbol{\gamma}^n \boldsymbol{v}^n &= \boldsymbol{F}^n + \sqrt{\frac{2k_B T}{\Delta t}} \, (\boldsymbol{\gamma}^n)^{\frac{1}{2}} \, \boldsymbol{W}^n \\
\boldsymbol{x}^{p,n+1} &= \boldsymbol{x}^n + \boldsymbol{v}^n \Delta t \quad \text{(predictor)}
\end{aligned} \tag{2.10}
$$

$$
\begin{aligned}
\boldsymbol{\gamma}^{p,n+1} \boldsymbol{v}^{p,n+1} &= \boldsymbol{F}^{p,n+1} + \sqrt{\frac{2k_B T}{\Delta t}} \, (\boldsymbol{\gamma}^n)^{\frac{1}{2}} \, \boldsymbol{W}^n \\
\boldsymbol{x}^{n+1} &= \boldsymbol{x}^n + \left( \frac{\boldsymbol{v}^n + \boldsymbol{v}^{p,n+1}}{2} \right) \Delta t \quad \text{(corrector)},
\end{aligned} \tag{2.11}
$$

where superscripts denote the point at which a given quantity is evaluated, for example, $\boldsymbol{\gamma}^{p,n+1} = \boldsymbol{\gamma}\left(\boldsymbol{x}^{p,n+1}\right)$, and $\boldsymbol{W}^n$ is a collection of independent and identically distributed (i.i.d.) standard normal random variables sampled independently at each time step. This predictor-corrector method is only first-order accurate for the multiplicative-noise case. When one is interested in linearized equations (e.g., a particle trapped by a harmonic potential to remain close to a stable minimum of the potential) the predictor-corrector schemes we construct in section 2.3 are second-order weakly accurate. It is not hard to show that the scheme (2.11) is equivalent to the well-known Fixman integrator for (2.9) [12].

Note that the final Fixman update can be written in the form

$$
\begin{aligned}
\boldsymbol{x}^{n+1} &= \boldsymbol{x}^n + \left( \frac{\boldsymbol{M}^n \boldsymbol{F}^n + \boldsymbol{M}^{p,n+1} \boldsymbol{F}^{p,n+1}}{2} \right) \Delta t + \sqrt{2k_B T \Delta t} \, (\boldsymbol{M}^n)^{\frac{1}{2}} \, \boldsymbol{W}^n, \\
&+ \Delta t \, (k_B T) \left( \boldsymbol{M}^{p,n+1} - \boldsymbol{M}^n \right) \left( 2k_B T \Delta t \, \boldsymbol{M}^n \right)^{-\frac{1}{2}} \boldsymbol{W}^n,
\end{aligned} \tag{2.12}
$$

where the mobility $\boldsymbol{M} = \boldsymbol{\gamma}^{-1}$. The first line is seen as an application of the (second-order) explicit trapezoidal rule for the deterministic drift terms and the Euler-Maryama method for the stochastic terms, while the second line gives the stochastic drift term $\Delta t \, (k_B T) \, \partial_{\boldsymbol{x}} \cdot \boldsymbol{M}(\boldsymbol{x})$ in expectation, as we explain next. Note that the Fixman scheme can be seen as a direct application of the Euler-Heun [1] predictor-corrector method [38] to the split Ito-Stratonovich form (2.6). Based on (2.6) a midpoint variant of the method, which we will use in subsequent chapters, takes the form

$$
\begin{aligned}
\boldsymbol{x}^{p,n+\frac{1}{2}} &= \boldsymbol{x}^n + \frac{\Delta t}{2} \boldsymbol{M}^n \boldsymbol{F}^n + \sqrt{\frac{\Delta t \, k_B T}{2}} (\boldsymbol{M}^n)^{\frac{1}{2}} \boldsymbol{W}^n \quad \text{(predictor)} \\
\boldsymbol{x}^{n+1} &= \boldsymbol{x}^n + \Delta t \, \boldsymbol{M}^{p,n+\frac{1}{2}} \boldsymbol{F}^{p,n+\frac{1}{2}} + \sqrt{2\Delta t \, k_B T} \boldsymbol{M}^{p,n+\frac{1}{2}} (\boldsymbol{M}^n)^{-\frac{1}{2}} \boldsymbol{W}^n \quad \text{(corrector)},
\end{aligned} \tag{2.13}
$$

as originally proposed by Fixman [12].

### 2.1.1.2 Random Finite Difference

A key feature of the Fixman method is that it requires access to the action of both $\boldsymbol{\gamma}^{-1}$ and $\boldsymbol{\gamma}^{\frac{1}{2}}$, or equivalently, $\boldsymbol{\gamma}$ and $\boldsymbol{\gamma}^{-\frac{1}{2}}$. This is a great disadvantage in cases when only the action of the mobility $\boldsymbol{M} = \boldsymbol{\gamma}^{-1}$ and its factor $\boldsymbol{M}^{\frac{1}{2}}$ are easily computable [3]. An alternative method to obtain the drift term $(k_B T) \, \partial_{\boldsymbol{x}} \cdot \boldsymbol{M}(\boldsymbol{x})$ in expectation is to use the general relation,

$$
\lim_{\delta \to 0} \frac{1}{\delta} \left\langle \left( \boldsymbol{M}\left(\boldsymbol{x} + \delta \Delta \boldsymbol{x}\right) - \boldsymbol{M}\left(\boldsymbol{x}\right) \right) \Delta \boldsymbol{p} \right\rangle = \partial_{\boldsymbol{x}} \cdot \boldsymbol{M}(\boldsymbol{x}), \tag{2.14}
$$

where $\Delta \boldsymbol{x}$ and $\Delta \boldsymbol{p}$ are Gaussian variates with mean zero and covariance $\left\langle \Delta \boldsymbol{x}_i \Delta \boldsymbol{p}_j \right\rangle = \delta_{ij}$. The second line in the Fixman method (2.12) can be seen as an application of (2.14) with $\delta = \sqrt{\Delta t}$ and $\Delta \boldsymbol{x} = (2k_B T \, \boldsymbol{M}^n)^{\frac{1}{2}} \boldsymbol{W}^n$ and $\Delta \boldsymbol{p} = (2k_B T \, \boldsymbol{M}^n)^{-\frac{1}{2}} \boldsymbol{W}^n$. The choice $\Delta \boldsymbol{x} = \Delta \boldsymbol{p}$ is, however, much simpler to use than the Fixman choice because it does not require the application of either $(\boldsymbol{M}^n)^{-1}$ or $(\boldsymbol{M}^n)^{-\frac{1}{2}}$. Here $\delta$ is a small discretization parameter that can be taken to be related to $\Delta t$ as in the Fixman method, but this is not necessary. One can more appropriately

---

[1] The Euler-Heun method is the natural generalization of the Euler-Maruyuama method to SDEs with Stratonovich noise [38].

think of (2.14) as a "random finite difference" (RFD) with $\delta$ representing the small spacing for the finite difference, to be taken as small as possible while avoiding numerical roundoff problems. The advantage of the "random" over a traditional finite difference is that only a small number of evaluations of the mobility per time step is required. Note that the subtraction of $\boldsymbol{M}(\boldsymbol{x})\Delta\boldsymbol{p}$ in (2.14) is necessary in order to control the variance of the RFD estimate.

For the simple Langevin equation (2.8) an RFD approach uses the same predictor (2.10) as in the Fixman algorithm, but now with corrector,

$$\boldsymbol{v}^{p,n+1} = \left(\boldsymbol{\gamma}^{p,n+1}\right)^{-1}\boldsymbol{F}^{p,n+1} + \sqrt{\frac{2k_BT}{\Delta t}}\,\left(\boldsymbol{\gamma}^n\right)^{-\frac{1}{2}}\boldsymbol{W}^n$$

$$\boldsymbol{x}^{n+1} = \boldsymbol{x}^n + \left(\frac{\boldsymbol{v}^n + \boldsymbol{v}^{p,n+1}}{2}\right)\Delta t$$
$$+ (k_BT)\frac{\Delta t}{\delta}\left[\boldsymbol{\gamma}^{-1}\left(\boldsymbol{x}^n + \delta\,\widetilde{\boldsymbol{W}}^n\right) - \boldsymbol{\gamma}^{-1}\left(\boldsymbol{x}^n\right)\right]\widetilde{\boldsymbol{W}}^n, \tag{2.15}$$

where $\widetilde{\boldsymbol{W}}^n$ is a collection of independent standard normal variates that are uncorrelated with $\boldsymbol{W}^n$. Because the corrector stage for the velocity evaluates the noise amplitude at the beginning of the time step there are no stochastic drift terms generated from the term $\left(\boldsymbol{v}^n + \boldsymbol{v}^{p,n+1}\right)\Delta t/2$, and the RFD in the last line of (2.15) is necessary to generate the missing drift in expectation.

It is not hard to see that (2.15) is a Markov chain that is consistent with the Ito overdamped equation (2.9). To demonstrate consistency we only need to show that to leading order, the first moment of the increment is equal to the deterministic drift in expectation,

$$\lim_{\Delta t \to 0}\frac{1}{\Delta t}E\left(\boldsymbol{x}^{n+1} - \boldsymbol{x}^n\right) = \boldsymbol{M}^n\boldsymbol{F}^n + (k_BT)\,\partial_{\boldsymbol{x}}\cdot\boldsymbol{M}(\boldsymbol{x}^n),$$

which follows directly from (2.14), and that in expectation the second moment of the increment matches the covariance of the noise,

$$\lim_{\Delta t \to 0}\frac{1}{\Delta t}E\left(\left(\boldsymbol{x}^{n+1} - \boldsymbol{x}^n\right)\left(\boldsymbol{x}^{n+1} - \boldsymbol{x}^n\right)^T\right) = 2k_BT\,\boldsymbol{M}^n,$$

which is trivially true because the random increment in both the predictor and corrector stages is $\sqrt{2k_BT\Delta t}\,\left(\boldsymbol{M}^n\right)^{\frac{1}{2}}\boldsymbol{W}^n$.

The two schemes (2.10,2.11) and (2.10,2.15) do not, of course, exhaust all possibilities. For example, in the corrector stage for velocity we could evaluate the noise amplitude at the predicted value,

$$\boldsymbol{v}^{p,n+1} = \left(\boldsymbol{\gamma}^{p,n+1}\right)^{-1}\boldsymbol{F}^{p,n+1} + \sqrt{\frac{2k_BT}{\Delta t}}\,\left(\boldsymbol{\gamma}^{p,n+1}\right)^{-\frac{1}{2}}\boldsymbol{W}^n.$$

It is not difficult to show, however, that with this choice the term $\left(\boldsymbol{v}^n + \boldsymbol{v}^{p,n+1}\right)\Delta t/2$ in the corrector stage for the position would generate an incorrect stochastic drift term for non-scalar problems. Therefore, additional RFD terms would be required to remove any spurious drift terms and add the correct ones. In this work we construct several schemes for integrating two-scale systems such as (2.9) that generate the correct drift terms using random finite differences, and, furthermore, also obtain second-order weak accuracy for the overdamped equations linearized around a stable deterministic trajectory. With additional effort, is also possible to obtain second-order weak accuracy for the nonlinear overdamped equation by using weak Runge-Kutta schemes of the kind developed in [32], which also rely on an RFD-like approach to avoid explicit evaluation of derivatives.

## 2.2   Temporal Integrators for Linearized Langevin Equations

In this section we consider a relatively general system of Langevin equations for the coarse-grained variable $\boldsymbol{x}(t)$,

$$\frac{d\boldsymbol{x}}{dt} = \boldsymbol{f}(\boldsymbol{x}) + \boldsymbol{K}(\boldsymbol{x})\diamond\boldsymbol{\mathcal{W}}(t) = \boldsymbol{H}(\boldsymbol{x})\boldsymbol{x} + \boldsymbol{h}(\boldsymbol{x}) + \boldsymbol{K}(\boldsymbol{x})\diamond\boldsymbol{\mathcal{W}}(t), \tag{2.16}$$

where $\boldsymbol{H}(\boldsymbol{x})\boldsymbol{x}$ is a term that we may choose to treat semi-implicitly in cases when it is stiff, and $\boldsymbol{h}(\boldsymbol{x})$ denotes the remaining terms which are difficult to treat implicitly. In cases when the noise is multiplicative one must choose a specific interpretation of the stochastic integral, here we have chosen the kinetic product $\diamond$ [5] in agreement with our motivating equation (2.4). The system (2.16) may arise from a spatial discretization of fluctuating hydrodynamics SPDEs, but similar equations arise in a variety of contexts.

Our focus will be on developing methods for integrating the system of equations obtained after linearizing (2.16) around the solution $\bar{\boldsymbol{x}}(t)$ of the deterministic system of equations (obtained by simply dropping the noise term),

$$d\bar{\boldsymbol{x}}/dt = \boldsymbol{H}(\bar{\boldsymbol{x}})\bar{\boldsymbol{x}} + \boldsymbol{h}(\bar{\boldsymbol{x}}) \qquad (2.17)$$

$$d(\delta\boldsymbol{x})/dt = \boldsymbol{M}(\bar{\boldsymbol{x}})\delta\boldsymbol{x} + \boldsymbol{K}(\bar{\boldsymbol{x}})\boldsymbol{\mathcal{W}}(t), \qquad (2.18)$$

where $\delta\boldsymbol{x} = \boldsymbol{x} - \bar{\boldsymbol{x}}$ is the (presumably small) fluctuation around the deterministic dynamics. Here the Jacobian of $\boldsymbol{f}(\boldsymbol{x})$ is denoted with

$$\boldsymbol{M}(\bar{\boldsymbol{x}}) = \partial_{\boldsymbol{x}}\boldsymbol{f}(\bar{\boldsymbol{x}}) = \boldsymbol{H}(\bar{\boldsymbol{x}}) + (\partial_{\boldsymbol{x}}\boldsymbol{H}(\bar{\boldsymbol{x}}))\bar{\boldsymbol{x}} + \partial_{\boldsymbol{x}}\boldsymbol{h}(\bar{\boldsymbol{x}}),$$

more specifically, in index notation

$$M_{ij} = H_{ij}(\bar{\boldsymbol{x}}) + (\partial_j H_{ik}(\bar{\boldsymbol{x}}))\bar{x}_k + \partial_j h_i(\bar{\boldsymbol{x}}).$$

Note that the noise in (2.18) is time-dependent but still additive, and different interpretations of the stochastic integral are equivalent.

One can more precisely justify the system (2.18) by assuming that the noise is very weak. In particular, the deterministic equation (2.17) can be seen as a law of large numbers describing the most probable trajectory in the weak-noise limit, with the Ornstein-Uhlenbeck equation (2.18) as a central-limit theorem for the small nearly Gaussian fluctuations around the average. It is important to note that one must assume here that the deterministic dynamics is stable, that is, small perturbations do not lead to large deviations of the averages, which is a good assumption far from phase transitions or bifurcation points. Note, however, that the linearized equations cannot be used to describe rare events (large deviations) or events that occur on exponentially-long timescales.

The essential difficulty in integrating (2.18) directly is that the linearization needs to be performed around a time-dependent state $\bar{\boldsymbol{x}}(t)$ that is not known *a priori* but is rather itself the solution of a nonlinear system of equations. Furthermore, one must calculate the Jacobian $\boldsymbol{M}$ explicitly, and this is often quite tedious since many more terms appear in the linearization than do in the original nonlinear equations (this is especially true for fluctuating hydrodynamics). Instead, we will construct methods that directly work with the original nonlinear equation (2.16) but with a noise term that is deliberately made very weak, as some of us first proposed and applied in [39] to a case of a *steady* deterministic state. In fact, if the assumption of weak noise used to justify the linearization is actually correct, the noise does not have to be artificially reduced in magnitude at all and using the actual (physical) value of the noise amplitude will give indistinguishable results. While it is of course always better to simply integrate the original nonlinear dynamics in cases where it is known, it is important to emphasize that nonlinear fluctuating hydrodynamics is very poorly understood and in most cases the nonlinear equations are ill-posed; a notable exception are (3.2,3.3) and (3.7) because the nonlinear advective term there was carefully regularized in a physically-relevant manner [23]. By contrast, the linearized equations are well-defined because there are no nonlinear terms and a precise meaning can be given in the space of (Gaussian) distributions [9]. Another important reason for focusing on the linearized equations is that while integrating the nonlinear equations to second-order (weakly) is rather nontrivial in the case of multiplicative noise [32], it is not hard to construct simple second-order integrators for the linearized equations, as we demonstrate here.

Before we describe methods for solving (2.17,2.18), we describe how to construct temporal integrators for just (2.18), assuming that $\bar{\boldsymbol{x}}(t)$ is known and given to us, and therefore the noise amplitude $\boldsymbol{K}(\bar{\boldsymbol{x}}(t)) \equiv \boldsymbol{K}(t)$ is only a function of time.

### 2.2.1 Equilibrium Fluctuation Spectrum

An important property of Langevin-type equations, including those of fluctuating hydrodynamics, is the existence of a non-trivial stationary distribution (invariant measure). It is important for numerical schemes to have an equilibrium distribution that is in, some appropriate sense, close to that of the continuum equations. A recently proposed-approach [40] is to add a Metropolis-Hastings acceptance-rejection rule to a classical deterministic scheme such as the Euler-Maruyama scheme. This "Metropolization" ensures that the equilibrium distribution of the numerical approximation is controlled, however, at the cost of reducing the temporal accuracy because of rejections. It is therefore important to ensure that the non-Metropolized numerical scheme produces a good approximation to the equilibrium distribution, so that rejections are infrequent.

Mattingly *et al.* [41] show that in some appropriate metric the invariant measure (which is assumed to exist) of the numerical scheme has the same order of accuracy as the weak order of accuracy over finite time intervals. This only provides an asymptotic error bound, however, and does not provide an estimate of the actual error. By focusing on the linearized equations of fluctuating hydrodynamics one can easily obtain explicit estimates for

the invariant measure of a given numerical scheme and thus understand the nature of discretization errors in the long-time dynamics. This approach was used in [42] to analyze and improve explicit Runge-Kutta schemes for compressible fluctuating hydrodynamics. Here we briefly review the main results and discuss some generalizations.

We consider the linear system of additive-noise SDEs

$$\frac{d\boldsymbol{x}}{dt} = \boldsymbol{L}\boldsymbol{x} + \boldsymbol{K}\boldsymbol{W}(t). \tag{2.19}$$

A general linear one-step temporal scheme for this equation has the form

$$\boldsymbol{x}^{n+1} = \boldsymbol{Q}\boldsymbol{x}^n + \Delta t^{\frac{1}{2}}\boldsymbol{R}\boldsymbol{W}^n,$$

where $\boldsymbol{Q}$ and $\boldsymbol{R}$ are some iteration matrices. Since this is a linear equation forced with by a Gaussian process, the solution is a Gaussian process and the equation can be explicitly solved to obtain the exact exponential integrator

$$\boldsymbol{x}^{n+1} = \exp(\boldsymbol{L}\Delta t)\boldsymbol{x}^n + \Delta t^{\frac{1}{2}}\boldsymbol{R}\boldsymbol{W}^n = \boldsymbol{Q}\boldsymbol{x}^n + \Delta t^{\frac{1}{2}}\boldsymbol{R}\boldsymbol{W}^n, \tag{2.20}$$

for which $\boldsymbol{Q} = \exp(\boldsymbol{L}\Delta t)$ and $\boldsymbol{R}$ will be obtained shortly. The equilibrium or steady-state covariance $\boldsymbol{C}_{\Delta t} = \langle \boldsymbol{x}^n (\boldsymbol{x}^n)^\star \rangle$ of this linear iteration is the solution of the linear system (see, for example, the derivation in [42])

$$\boldsymbol{Q}\boldsymbol{C}_{\Delta t}\boldsymbol{Q}^\star - \boldsymbol{C}_{\Delta t} = -\Delta t\, \boldsymbol{R}\boldsymbol{R}^\star. \tag{2.21}$$

In the limit $\Delta t \to 0$ any consistent and stable numerical scheme should give the correct equilibrium covariance $\boldsymbol{C} = \langle \boldsymbol{x}(t)\boldsymbol{x}^\star(t) \rangle$, which is the solution to [43, 44, 42]

$$\boldsymbol{L}\boldsymbol{C} + \boldsymbol{C}\boldsymbol{L}^\star = -\boldsymbol{K}\boldsymbol{K}^\star. \tag{2.22}$$

For the exponential integrator (2.20) we have that $\boldsymbol{Q} = \exp(\boldsymbol{L}\Delta t)$ and therefore this scheme will give the correct equilibrium covariance for any time step if

$$\boldsymbol{R}\boldsymbol{R}^\star = \Delta t^{-1}[\boldsymbol{C} - \boldsymbol{Q}\boldsymbol{C}\boldsymbol{Q}^\star] = \Delta t^{-1}[\boldsymbol{C} - \exp(\boldsymbol{L}\Delta t)\,\boldsymbol{C}\exp(\boldsymbol{L}^\star\Delta t)]. \tag{2.23}$$

In general, one cannot write an explicit solution to this equation unless one can explicitly diagonalize $\boldsymbol{L}$ and $\boldsymbol{C}$ in some basis.

### 2.2.1.1 Implicit Midpoint Rule

Runge-Kutta schemes approximate the matrix exponential in (2.20) with a polynomial (for fully explicit schemes) or a rational (for semi-implicit schemes) approximation. An important example is provided by the implicit midpoint (equivalently, trapezoidal) method (Crank-Nicolson scheme) applied to the linear problem (2.19),

$$\boldsymbol{x}^{n+1} = \boldsymbol{x}^n + \frac{\Delta t}{2}\boldsymbol{L}(\boldsymbol{x}^n + \boldsymbol{x}^{n+1}) + \Delta t^{\frac{1}{2}}\boldsymbol{K}\boldsymbol{W}^n. \tag{2.24}$$

In this scheme the iteration matrix $\boldsymbol{Q}$ is a $1-1$ Pade approximation of the matrix exponential,

$$\boldsymbol{Q} = \left(\boldsymbol{I} - \frac{\boldsymbol{L}\Delta t}{2}\right)^{-1}\left(\boldsymbol{I} + \frac{\boldsymbol{L}\Delta t}{2}\right) = \exp(\boldsymbol{L}\Delta t) + O(\Delta t^3), \tag{2.25}$$

and $\boldsymbol{R} = (\boldsymbol{I} - \boldsymbol{L}\Delta t/2)^{-1}\boldsymbol{K}$. It is not hard to show that the implicit midpoint scheme leads to the correct equilibrium covariance $\boldsymbol{C}$ for *any* time step since

$$\boldsymbol{R}\boldsymbol{R}^\star = \Delta t^{-1}[\boldsymbol{C} - \boldsymbol{Q}\boldsymbol{C}\boldsymbol{Q}^\star],$$

as seen from a straightforward explicit calculation,

$$\begin{aligned}
&\Delta t^{-1}[\boldsymbol{C} - \boldsymbol{Q}\boldsymbol{C}\boldsymbol{Q}^\star] \\
=\ &\Delta t^{-1}\left(\boldsymbol{I} - \frac{\boldsymbol{L}\Delta t}{2}\right)^{-1} \times \\
&\left[\left(\boldsymbol{I} - \frac{\boldsymbol{L}\Delta t}{2}\right)\boldsymbol{C}\left(\boldsymbol{I} - \frac{\boldsymbol{L}^\star\Delta t}{2}\right) - \left(\boldsymbol{I} + \frac{\boldsymbol{L}\Delta t}{2}\right)\boldsymbol{C}\left(\boldsymbol{I} + \frac{\boldsymbol{L}^\star\Delta t}{2}\right)\right]\left(\boldsymbol{I} - \frac{\boldsymbol{L}^\star\Delta t}{2}\right)^{-1} \\
=\ &\left(\boldsymbol{I} - \frac{\boldsymbol{L}\Delta t}{2}\right)^{-1}(-\boldsymbol{L}\boldsymbol{C} - \boldsymbol{C}\boldsymbol{L}^\star)\left(\boldsymbol{I} - \frac{\boldsymbol{L}^\star\Delta t}{2}\right)^{-1} \\
=\ &\left(\boldsymbol{I} - \frac{\boldsymbol{L}\Delta t}{2}\right)^{-1}\boldsymbol{K}\boldsymbol{K}^\star\left(\boldsymbol{I} - \frac{\boldsymbol{L}^\star\Delta t}{2}\right)^{-1} = \boldsymbol{R}\boldsymbol{R}^\star.
\end{aligned}$$

An alternative derivation of the fact that (2.24) gives the correct steady-state covariance for any time step $\Delta t$ can be found in the Appendix of Ref. [39]. That derivation is based on showing that the iteration (2.24) is a Metropolis-Hastings Monte Carlo algorithm to sample the invariant distribution of (2.19).

The implicit midpoint rule can easily be generalized to the nonlinear system (1.4),

$$\boldsymbol{x}^{n+1} = \boldsymbol{x}^n + \frac{\Delta t}{2}(\boldsymbol{a}^{n+1} + \boldsymbol{a}^n) + \Delta t^{\frac{1}{2}}\boldsymbol{K}\boldsymbol{W}^n,$$

and can easily be shown to be weakly second-order accurate. This scheme is a particularly good candidate for solving Langevin-type equations because it is a time-reversible and quasi-symplectic integrator that exactly conserves all quadratic invariants (e.g., a quadratic Hamiltonian). However, it requires the solution of a nonlinear system of equations at every time step, which is too expensive for large-scale hydrodynamic calculations and also makes the numerical method prone to failures. In the special case of the stochastic Burgers or Navier-Stokes equations, the only nonlinearity in $\boldsymbol{a}(\boldsymbol{x})$ comes from the advective term, which has the special form (to within irrelevant constants) $[\boldsymbol{S}(\boldsymbol{x})]\,\boldsymbol{x}$ and can be linearized as $\left[\boldsymbol{S}\left(\boldsymbol{x}^{n+\frac{1}{2}}\right)\right]\boldsymbol{x}$, where $\boldsymbol{x}^{n+\frac{1}{2}}$ is a mid-point estimate that has to be obtained via a predictor-stage. Such an approach gives a scheme that only requires solving a linear system at each time step, while still preserving quadratic invariants (e.g., total kinetic energy). It is, however, not a time-reversible scheme. Furthermore, solving the non-symmetric systems that arise when advection is discretized in a semi-implicit manner poses a significant linear algebra challenge, especially when constraints such as incompressibility are included. For this reason, in the next sections we consider implicit-explicit Runge-Kutta schemes in which only diffusive terms are, potentially, discretized implicitly.

### 2.2.2 Time-dependent noise

At first, it will not be necessary to assume that the equation for the fluctuations is linear, and we will therefore consider a more general SDE with time dependent additive noise,

$$\frac{d\boldsymbol{x}}{dt} = \boldsymbol{L}(\boldsymbol{x})\boldsymbol{x} + \boldsymbol{g}(\boldsymbol{x}) + \boldsymbol{K}(t)\boldsymbol{\mathcal{W}}(t), \tag{2.26}$$

which is a slight generalization of the constant additive noise equation. Such an equation may arise, for example, by considering a time-dependent temperature in the fluctuating Navier-Stokes equation (3.2). Here $\boldsymbol{\mathcal{W}}(t)$ denotes a collection of independent white-noise processes, formally identified with the time derivative of a collection of independent Brownian motions (Wiener processes) $\boldsymbol{\mathcal{B}}(t)$, $\boldsymbol{\mathcal{W}} \equiv d\boldsymbol{\mathcal{B}}/ds$, $\boldsymbol{g}(\boldsymbol{x})$ denotes all of the terms handled explicitly (e.g., advection or external forcing), and the term $\boldsymbol{L}(\boldsymbol{x})\boldsymbol{x}$ denotes terms that will be handled semi-implicitly (e.g., diffusion) for stiff systems (large spread in the eigenvalues of $\boldsymbol{L}$). In general, $\boldsymbol{L}(\boldsymbol{x})$ may depend on $\boldsymbol{x}$ since the transport coefficients (e.g., viscosity) may depend on certain state variables (e.g., concentration). Note that the equation (2.26) also includes the case where $\boldsymbol{L}(\boldsymbol{x}, t)$ and $\boldsymbol{g}(\boldsymbol{x}, t)$ depend explicitly on time, as can be seen by considering an expanded system of equations for $\boldsymbol{x} \to (\boldsymbol{x}, t)$.

Here we focus on weak integrators that are (at most) second-order accurate. The following is a relatively general mixed explicit-implicit predictor-corrector scheme for solving (2.26). The first stage in our schemes is a predictor step to estimate $\tilde{\boldsymbol{x}} \approx \boldsymbol{x}(n\Delta t + w_2\Delta t)$, where $w_2$ is some chosen weight (e.g., $w_2 = 1/2$ for a midpoint predictor or $w_2 = 1$ for a full-step predictor), while the corrector stage completes the step by estimating $\boldsymbol{x}^{n+1}$ at time $(n+1)\Delta t$,

$$\boldsymbol{x}^{(p)} = \boldsymbol{x}^n + \left((w_2 - w_1)\boldsymbol{L}^n\boldsymbol{x}^n + w_1\boldsymbol{L}^n\boldsymbol{x}^{(p)}\right)\Delta t + w_2\boldsymbol{g}^n\Delta t + \sqrt{w_2\Delta t}\,\boldsymbol{K}^n\boldsymbol{W}^{n,1}$$

$$\boldsymbol{x}^{n+1} = \boldsymbol{x}^n + \left((1 - w_3 - w_4 - w_5)\boldsymbol{L}^n\boldsymbol{x}^n + w_3\boldsymbol{L}^{(p)}\boldsymbol{x}^{(p)} + w_4\boldsymbol{L}^{(p)}\boldsymbol{x}^{n+1} + w_5\boldsymbol{L}^n\boldsymbol{x}^{n+1}\right)\Delta t$$

$$+ \Delta t \begin{cases} \left((1 - w_6)\boldsymbol{g}^n + w_6\boldsymbol{g}^{(p)}\right), & \text{or} \\ \boldsymbol{g}\left((1 - w_6)\boldsymbol{x}^n + w_6\boldsymbol{x}^{(p)}\right) \end{cases}$$

$$+ \left((1 - w_7)\boldsymbol{K}^n + w_7\boldsymbol{K}^{(p)}\right)\left(\sqrt{w_2\Delta t}\,\boldsymbol{W}^{n,1} + \sqrt{(1 - w_2)\Delta t}\,\boldsymbol{W}^{n,2}\right), \tag{2.27}$$

where we have denoted $\boldsymbol{K}^{(p)} = \boldsymbol{K}(t_n + w_2\Delta t)$ and superscripts and decorations denote the point at which a given quantity is evaluated, for example, $\boldsymbol{L}^{(p)} = \boldsymbol{L}(\boldsymbol{x}^{(p)})$. Note that this class of semi-implicit schemes requires solving only *linear* systems involving the matrix $\boldsymbol{L}(\boldsymbol{x})$ evaluated at a specific point and kept fixed. In the above discretization, the standard normal variates $\boldsymbol{W}_1^n$ correspond to the increment of the underlying Wiener processes $\boldsymbol{\mathcal{B}}(t)$ over the time interval $w_2\Delta t$, $\boldsymbol{\mathcal{B}}(n\Delta t + w_2\Delta t) - \boldsymbol{\mathcal{B}}(n\Delta t) = (w_2\Delta t)^{\frac{1}{2}}\boldsymbol{W}_1^n$ in law, while the normal variates $\boldsymbol{W}_2^n$

correspond to the independent increment over the remainder of the time step, $\boldsymbol{\mathcal{B}}\left((n+1)\Delta t\right) - \boldsymbol{\mathcal{B}}\left(n\Delta t + w_2\Delta t\right) = \left((1-w_2)\Delta t\right)^{\frac{1}{2}}\boldsymbol{W}_2^n$ in law. We give two alternative ways to handle the explicit terms in the corrector stage, which give the same order of accuracy, and, are, in fact, identical if $\boldsymbol{g}$ is linear. Which of the two ways of handling the explicit terms is better should be tested empirically for strongly nonlinear Langevin equations, as we do in section 3.5.1 using the stochastic Burgers equation as a model problem.

Different specific values for the $w$ coefficients determine different schemes. The accuracy of these schemes is analyzed in Addendum 2.6 and accounts for the time dependence of $\boldsymbol{K}$. We show that the scheme (2.27) is weakly second order accurate if the weights satisfy

$$
\begin{aligned}
w_3 w_2 + w_4 w_2 &= \frac{1}{2} \\
w_3 w_2 + w_4 + w_5 &= \frac{1}{2} \\
w_2 w_6 &= \frac{1}{2} \\
w_2 w_7 &= \frac{1}{2}.
\end{aligned}
\tag{2.28}
$$

We present three simple schemes that satisfy these properties next, the first fully explicit, and the other two semi-implicit. While these by no means exhaust all possibilities, they are representative and have several notable advantages for the case of time-independent noise as well.

### 2.2.2.1 Explicit Midpoint Scheme

A fully explicit midpoint predictor-corrector scheme is obtained for $w_1 = 0$, $w_2 = 1/2$, $w_3 = 1$, $w_4 = w_5 = 0$, $w_6 = 1, w_7 = 1$:

$$
\begin{aligned}
\boldsymbol{x}^{p,n+\frac{1}{2}} &= \boldsymbol{x}^n + \frac{\Delta t}{2}\left(\boldsymbol{L}^n \boldsymbol{x}^n + \boldsymbol{g}^n\right) + \sqrt{\frac{\Delta t}{2}}\boldsymbol{K}^n \boldsymbol{W}_1^n \\
\boldsymbol{x}^{n+1} &= \boldsymbol{x}^n + \Delta t\left(\boldsymbol{L}^{p,n+\frac{1}{2}}\boldsymbol{x}^{p,n+\frac{1}{2}} + \boldsymbol{g}^{p,n+\frac{1}{2}}\right) + \sqrt{\frac{\Delta t}{2}}\boldsymbol{K}^{p,n+\frac{1}{2}}\left(\boldsymbol{W}_1^n + \boldsymbol{W}_2^n\right).
\end{aligned}
\tag{2.29}
$$

This midpoint scheme has several notable strengths for fluctuating hydrodynamics:

1. It is fully explicit and thus quite efficient (but also subject to restrictive stability limits on the time step size for stiff systems).

2. It is a weakly second-order accurate integrator for (2.26).

3. It is third-order accurate for static structure factors (static correlations) for time-independent additive noise in the linearized setting 2.2.1, that is, for the equation

$$
\frac{d\boldsymbol{x}}{dt} = \boldsymbol{L}\boldsymbol{x} + \boldsymbol{K}\boldsymbol{\mathcal{W}}(t),
\tag{2.30}
$$

with constant $\boldsymbol{L}$ and $\boldsymbol{K}$.

It is also possible to construct an explicit trapezoidal scheme that only uses a single random increment per time step, $w_1 = 0$, $w_2 = 1$, $w_3 = 1/2$, $w_4 = w_5 = 0, w_6 = 1/2$, $w_7 = 1/2$, but for fluctuating hydrodynamics the explicit midpoint integrator is preferred because it gives third-order accurate static correlations.

### 2.2.2.2 Implicit Trapezoidal Integrator

We obtain a semi-implicit trapezoidal predictor-corrector scheme for $w_1 = 1/2$, $w_2 = 1$, $w_3 = w_5 = 0$, $w_4 = 1/2$, $w_6 = 1/2$, $w_7 = 1/2$:

$$
\begin{aligned}
\boldsymbol{x}^{p,n+1} &= \boldsymbol{x}^n + \frac{\Delta t}{2}\boldsymbol{L}^n\left(\boldsymbol{x}^n + \boldsymbol{x}^{p,n+1}\right) + \Delta t\,\boldsymbol{g}^n + \sqrt{\Delta t}\,\boldsymbol{K}^n \boldsymbol{W}^n \\
\boldsymbol{x}^{n+1} &= \boldsymbol{x}^n + \frac{\Delta t}{2}\left(\boldsymbol{L}^n \boldsymbol{x}^n + \boldsymbol{L}^{p,n+1}\boldsymbol{x}^{n+1}\right) + \frac{\Delta t}{2}(\boldsymbol{g}^n + \boldsymbol{g}^{p,n+1}) \\
&\quad + \frac{\sqrt{\Delta t}}{2}\left(\boldsymbol{K}^n + \boldsymbol{K}^{p,n+1}\right)\boldsymbol{W}^n.
\end{aligned}
\tag{2.31}
$$

This scheme has the following advantages:

15

1. It only requires solving two linear systems with the coefficient matrix $\boldsymbol{I} - (\Delta t/2)\,\boldsymbol{L}$, which is quite standard in computational fluid dynamics and can be done efficiently using multigrid techniques.

2. It is a weakly second-order accurate integrator for (2.26).

3. It is stable and gives the *exact static* correlations for (2.30) for *any* time step size $\Delta t$ 2.2.1.

The alternative handling of the explicit term leads to the corrector stage,

$$\boldsymbol{x}^{n+1} = \boldsymbol{x}^n + \frac{\Delta t}{2}\left(\boldsymbol{L}^n\boldsymbol{x}^n + \boldsymbol{L}^{p,n+1}\boldsymbol{x}^{n+1}\right) + \Delta t\,\boldsymbol{g}\left(\frac{\boldsymbol{x}^n + \boldsymbol{x}^{p,n+1}}{2}\right) + \frac{\sqrt{\Delta t}}{2}\left(\boldsymbol{K}^n + \boldsymbol{K}^{p,n+1}\right)\boldsymbol{W}^n, \qquad (2.32)$$

which has the same advantages as (2.31), but may behave differently for strongly nonlinear equations.

### 2.2.2.3 Implicit Midpoint Integrator

When $\boldsymbol{L}$ is constant, the first condition in (2.28), $w_2w_3 + w_2w_4 = 0$, is no longer necessary. One can make use of this by splitting equation (2.26) as follows at the beginning of each time step,

$$\frac{d\boldsymbol{x}}{dt} = \boldsymbol{L}(\boldsymbol{x})\boldsymbol{x} + \boldsymbol{g}(\boldsymbol{x}) + \boldsymbol{K}(t)\boldsymbol{\mathcal{W}}(t) = \boldsymbol{L}\left(\boldsymbol{x}^n\right)\boldsymbol{x} + (\boldsymbol{L}(\boldsymbol{x}) - \boldsymbol{L}\left(\boldsymbol{x}^n\right))\boldsymbol{x} + \boldsymbol{g}(\boldsymbol{x}) + \boldsymbol{K}(t)\boldsymbol{\mathcal{W}}(t)\,,$$

and treating $(\boldsymbol{L}(\boldsymbol{x}) - \boldsymbol{L}\left(\boldsymbol{x}^n\right))\boldsymbol{x} + \boldsymbol{g}(\boldsymbol{x})$ explicitly. Considering the problem this way gives rise to an implicit midpoint scheme that requires only linear solves of $\boldsymbol{L}^n$ at each timestep, $w_2 = 1/2$, $w_3 = 0$, $w_4 = 0$, $w_5 = 1/2$, $w_6 = 1$, $w_7 = 1$ :

$$
\begin{aligned}
\boldsymbol{x}^{p,n+\frac{1}{2}} &= \boldsymbol{x}^n + \left(\frac{1}{2} - w_1\right)\boldsymbol{L}^n\boldsymbol{x}^n\Delta t + w_1\boldsymbol{L}^n\boldsymbol{x}^{p,n+\frac{1}{2}} + \frac{\Delta t}{2}\boldsymbol{g}^n + \left(\frac{\Delta t}{2}\right)^{\frac{1}{2}}\boldsymbol{K}^n\boldsymbol{W}_1^n \\
\boldsymbol{x}^{n+1} &= \boldsymbol{x}^n + \frac{\Delta t}{2}\boldsymbol{L}^n\left(\boldsymbol{x}^n + \boldsymbol{x}^{n+1}\right) + \Delta t(\boldsymbol{L}^{p,n+\frac{1}{2}} - \boldsymbol{L}^n)\boldsymbol{x}^{p,n+\frac{1}{2}} + \Delta t\,\boldsymbol{g}^{p,n+\frac{1}{2}} \qquad (2.33) \\
&\quad + \left(\frac{\Delta t}{2}\right)^{\frac{1}{2}}\boldsymbol{K}^{p,n+\frac{1}{2}}\left(\boldsymbol{W}_1^n + \boldsymbol{W}_2^n\right).
\end{aligned}
$$

We are left with a choice for $w_1$ in the predictor stage. One obvious choice is $w_1 = 1/2$, which for linear equations makes the predictor stage a backward Euler step with time step size $\Delta t/2$. An alternative is to use $w_1 = 1/4$, which for linear equations makes the predictor stage an implicit midpoint step with time step size $\Delta t/2$. These two variations of the implicit midpoint scheme are compared experimentally in section 3.5. This scheme has the same advantages as those above:

1. Like (2.31), it only requires solving two linear systems with the coefficient matrix $\boldsymbol{I} - (\Delta t/2)\,\boldsymbol{L}$ and $\boldsymbol{I} - w_1\Delta t\,\boldsymbol{L}$.

2. It is a weakly second-order accurate integrator for (2.26) for any choice of the weight $w_1$.

3. It is stable and gives the *exact static* correlations for (2.30) for *any* time step size $\Delta t$ 2.2.1 and any choice of weight $w_1$.

### 2.2.2.4 Multiplicative noise

The scheme (2.27) with the conditions (2.28) is a second-order weak integrator for the additive-noise equation (2.26). With a simple addition of a random finite difference (RFD) term in the corrector, see Section 2.1.1.2, the scheme (2.27) can be turned into a first-order weak integrator for the nonlinear kinetic SDE

$$\frac{d\boldsymbol{x}}{dt} = \boldsymbol{L}(\boldsymbol{x})\boldsymbol{x} + \boldsymbol{g}(\boldsymbol{x}) + \boldsymbol{K}(\boldsymbol{x}, t) \diamond \boldsymbol{\mathcal{W}}(t)\,. \qquad (2.34)$$

Namely, if we interpret $\boldsymbol{K}^{(p)} = \boldsymbol{K}(\boldsymbol{x}^{(p)}, t_n + w_2\Delta t)$ as the noise amplitude evaluated at the predictor, the integrator (2.27) is consistent with a Stratonovich interpretation of the noise. If we want the integrator to be consistent with the kinetic interpretation, we need to add a missing piece of the stochastic drift term,

$$\frac{1}{2}\partial_{\boldsymbol{x}} \cdot (\boldsymbol{K}\boldsymbol{K}^\star) = \frac{1}{2}\left(\partial_{\boldsymbol{x}}\boldsymbol{K}\right) : \boldsymbol{K}^\star + \frac{1}{2}\boldsymbol{K}\left(\partial_{\boldsymbol{x}} \cdot \boldsymbol{K}^\star\right).$$

The first term on the right hand side in index notation reads $(\partial_j K_{ik}) K_{jk}$ and is the only drift term that appears if a Stratonovich interpretation of the noise is adopted. To obtain the second term, we need to add to the corrected $\boldsymbol{x}^{n+1}$ the following RFD increment,

$$\Delta \boldsymbol{x}^{n+1} = \frac{\Delta t}{2\delta} \boldsymbol{K} \left( \boldsymbol{K}^\star \left( \boldsymbol{x}^n + \delta \widetilde{\boldsymbol{W}}^n \right) - \boldsymbol{K}^\star \left( \boldsymbol{x}^n \right) \right) \widetilde{\boldsymbol{W}}^n, \tag{2.35}$$

where $\widetilde{\boldsymbol{W}}^n$ is a collection of i.i.d. standard normal increments generated independently of $\boldsymbol{W}^n$.

### 2.2.3 Linearization around complex deterministic flows

We now turn our attention to temporal integrators for the linearized system (2.17,2.18). The key difference with (2.26) is that we do not assume that $\bar{\boldsymbol{x}}(t)$ is known, rather, it is also obtained by the numerical method. Our approach will be to pretend we are integrating the nonlinear equation (2.16) but using very weak noise, so that we will effectively be integrating the linearized equation. Our goal will be to construct schemes that are second-order weakly accurate for the linearized system (2.17,2.18). For steady states, that is, when the deterministic or background state $\bar{\boldsymbol{x}}$ is independent of time, the linearized equation (2.18) is of the form (2.26) with the identification $\boldsymbol{x} \equiv \delta\boldsymbol{x}$ and $\boldsymbol{K}(t) \equiv \boldsymbol{K}(\bar{\boldsymbol{x}}, t)$, along with

$$\boldsymbol{L} \equiv \boldsymbol{H}(\bar{\boldsymbol{x}}) = \text{const.} \quad \text{and} \quad \boldsymbol{g}(\boldsymbol{x}) \equiv [(\partial_{\boldsymbol{x}} \boldsymbol{H}(\bar{\boldsymbol{x}})) \bar{\boldsymbol{x}} + \partial_{\boldsymbol{x}} \boldsymbol{h}(\bar{\boldsymbol{x}})] \boldsymbol{x} \tag{2.36}$$

as the part of the linear operator treated implicitly and explicitly, respectively. We would like to construct one fully explicit integrator that for steady states becomes equivalent to the explicit midpoint scheme (2.29), and one semi-implicit integrator that for steady states becomes equivalent to the implicit trapezoidal scheme (2.31). In this way, we obtain simple schemes that inherit all of the important strengths of the explicit midpoint and implicit trapezoidal schemes in describing fluctuations around a steady state, while also performing numerical linearization and maintaining second-order weak accuracy for time-dependent problems.

#### 2.2.3.1 Explicit schemes

Let us first consider fully explicit schemes, for which the analysis is considerably easier. A simple predictor-corrector update for the nonlinear equation (2.16) reads

$$\boldsymbol{x}^{(p)} = \boldsymbol{x}^n + w_2 \Delta t \, \boldsymbol{f}^n + \sqrt{w_2 \Delta t} \, \boldsymbol{K}^n \boldsymbol{W}_1^n \quad \text{(predictor)} \tag{2.37}$$

$$\boldsymbol{x}^{n+1} = \boldsymbol{x}^n + \left( (1 - w_3) \boldsymbol{f}^n + w_3 \boldsymbol{f}^{(p)} \right) \Delta t$$

$$+ \left( (1 - w_7) \boldsymbol{K}^n + w_7 \boldsymbol{K}^{(p)} \right) \left( \sqrt{w_2 \Delta t} \, \boldsymbol{W}_1^n + \sqrt{(1 - w_2) \Delta t} \, \boldsymbol{W}_2^n \right) \quad \text{(corrector)}.$$

If we now split the variables into deterministic and fluctuating components,

$$\begin{aligned} \boldsymbol{x}^{(p)} &= \bar{\boldsymbol{x}}^{(p)} + \delta\boldsymbol{x}^{(p)} \\ \boldsymbol{x}^{n+1} &= \bar{\boldsymbol{x}}^{n+1} + \delta\boldsymbol{x}^{n+1} \end{aligned} \tag{2.38}$$

and expand the predictor and corrector stages to first order in the fluctuations (i.e., linearize both stages in $\delta\boldsymbol{x}^{(p)}$ and $\delta\boldsymbol{x}^{n+1}$), we obtain that for weak fluctuations (2.37) is effectively applying the same explicit scheme to the linearized system (2.17,2.18). The analysis summarized in Addendum 2.7 shows that the scheme (2.37) is a second-order weakly accurate integrator for (2.17,2.18) if $w_2 w_3 = 1/2$ and $w_2 w_7 = 1/2$. Examples of second-order fully explicit schemes include the explicit midpoint scheme, obtained for $w_2 = 1/2$, $w_3 = 1$, $w_7 = 1$, and the explicit trapezoidal scheme, obtained for $w_2 = 1$, $w_3 = 1/2$, $w_7 = 1/2$. Note that at steady state the explicit midpoint scheme becomes equivalent to applying (2.29) directly to (2.18).

17

#### 2.2.3.2 Semi-implicit schemes

We now consider applying the relatively general predictor-corrector scheme (2.27) to (2.16), with the identification $\boldsymbol{L}(\boldsymbol{x}) \equiv \boldsymbol{H}(\boldsymbol{x})$ and $\boldsymbol{g}(\boldsymbol{x}) \equiv \boldsymbol{h}(\boldsymbol{x})$, which gives the semi-implicit scheme

$$
\begin{aligned}
\boldsymbol{x}^{(p)} =& \boldsymbol{x}^n + \left( (w_2 - w_1) \boldsymbol{H}^n \boldsymbol{x}^n + w_1 \boldsymbol{H}^n \boldsymbol{x}^{(p)} \right) \Delta t + w_2 \boldsymbol{h}^n \Delta t + \sqrt{w_2 \Delta t}\, \boldsymbol{K}^n \boldsymbol{W}_1^n \\
\boldsymbol{x}^{n+1} =& \boldsymbol{x}^n + \left( (1 - w_3 - w_4 - w_5) \boldsymbol{H}^n \boldsymbol{x}^n + w_3 \boldsymbol{H}^{(p)} \boldsymbol{x}^{(p)} + w_4 \boldsymbol{H}^{(p)} \boldsymbol{x}^{n+1} + w_5 \boldsymbol{H}^n \boldsymbol{x}^{n+1} \right) \Delta t \\
& + \begin{cases} \left( (1 - w_6) \boldsymbol{h}^n + w_6 \boldsymbol{h}^{(p)} \right) \Delta t, \quad \text{or} \\ \boldsymbol{h} \left( (1 - w_6) \boldsymbol{x}^n + w_6 \boldsymbol{x}^{(p)} \right) \Delta t \end{cases} \\
& + \left( (1 - w_7) \boldsymbol{K}^n + w_7 \boldsymbol{K}^{(p)} \right) \left( \sqrt{w_2 \Delta t}\, \boldsymbol{W}_1^n + \sqrt{(1 - w_2) \Delta t}\, \boldsymbol{W}_2^n \right).
\end{aligned}
\tag{2.39}
$$

If we substitute (2.38) in (2.39) and linearize both stages, we obtain that for weak noise the same scheme (but without the noise terms) is applied to the deterministic component,

$$
\begin{aligned}
\bar{\boldsymbol{x}}^{(p)} =& \bar{\boldsymbol{x}}^n + \left( (w_2 - w_1) \bar{\boldsymbol{H}}^n \bar{\boldsymbol{x}}^n + w_1 \bar{\boldsymbol{H}}^n \bar{\boldsymbol{x}}^{(p)} \right) \Delta t + w_2 \bar{\boldsymbol{h}}^n \Delta t \\
\bar{\boldsymbol{x}}^{n+1} =& \bar{\boldsymbol{x}}^n + \left( (1 - w_3 - w_4 - w_5) \bar{\boldsymbol{H}}^n \bar{\boldsymbol{x}}^n + w_3 - \bar{\boldsymbol{H}}^{(p)} \bar{\boldsymbol{x}}^{(p)} + w_4 \bar{\boldsymbol{H}}^{(p)} \bar{\boldsymbol{x}}^{n+1} + w_5 \bar{\boldsymbol{H}}^n \bar{\boldsymbol{x}}^{n+1} \right) \Delta t \\
& + \left( (1 - w_6) \bar{\boldsymbol{h}}^n + w_6 \bar{\boldsymbol{h}}^{(p)} \right) \Delta t \text{ or } \boldsymbol{h} \left( (1 - w_6) \bar{\boldsymbol{x}}^n + w_6 \bar{\boldsymbol{x}}^{(p)} \right) \Delta t.
\end{aligned}
\tag{2.40}
$$

while for the fluctuating component, in index notation,

$$
\begin{aligned}
\delta x_i^{(p)} =& \delta x_i^n + (w_2 - w_1) \left( \bar{H}_{ij}^n + \left( \partial_j \bar{H}_{ik}^n \right) \bar{x}_k^n \right) \delta x_j^n \Delta t \\
& + \left( w_1 \left( \partial_k \bar{H}_{ij}^n \right) \bar{x}_j^{(p)} \delta x_k^{(n)} + w_1 \bar{H}_{ij} \delta x_j^{(p)} \right) \Delta t \\
& + w_2 \left( \partial_j \bar{h}_i \right) \delta x_j^n \Delta t + \sqrt{w_2 \Delta t}\, K_{ij}^n W_j^{1,n} \\
\delta x_i^{n+1} =& \delta x_i^n + \left[ (1 - w_3 - w_4 - w_5) \left( \bar{H}_{ij}^n + \left( \partial_j \bar{H}_{ik}^n \right) \bar{x}_k^n \right) + w_5 \left( \partial_j \bar{H}_{ik}^n \right) \bar{x}_k^{n+1} \right] \delta x_j^n \Delta t \\
& + \left[ w_3 \left( \bar{H}_{ij}^{(p)} + \left( \partial_j \bar{H}_{ik}^{(p)} \right) \bar{x}_k^{(p)} \right) + w_4 \left( \partial_j \bar{H}_{ik}^{(p)} \right) \bar{x}_k^{n+1} \right] \delta x_j^{(p)} \Delta t \\
& + \left( w_4 \bar{H}_{ij}^{(p)} + w_5 \bar{H}_{ij}^n \right) \delta x_j^{n+1} \Delta t \\
& + \begin{cases} \left( (1 - w_6)(\partial_k \bar{h}_i^n) \delta x_k^n + w_6 (\partial_k \bar{h}_i^{(p)}) \delta x_k^{(p)} \right) \Delta t, \quad \text{or} \\ \partial_k \bar{h}_i^{(w)} \left( (1 - w_6) \delta x_k^n + w_6 \delta x_k^{(p)} \right) \Delta t \end{cases} \\
& + \left( (1 - w_7) \bar{K}_{ij}^n + w_7 \bar{K}_{ij}^{(p)} \right) \left( \sqrt{w_2 \Delta t}\, W_j^{1,n} + \sqrt{(1 - w_2) \Delta t}\, W_j^{2,n} \right),
\end{aligned}
\tag{2.41} \tag{2.42}
$$

where decorations and superscripts indicate where the derivatives are evaluated, for example, $\partial_k \bar{h}_i^{(p)} = \partial_k h_i \left( \bar{\boldsymbol{x}}^{(p)} \right)$, and $\partial_k \bar{h}_i^{(w)}$ is evaluated at $(1 - w_6) \bar{\boldsymbol{x}}^n + w_6 \bar{\boldsymbol{x}}^{(p)}$. The analysis summarized in Addendum 2.7 shows that this scheme is a second-order weakly accurate integrator for (2.17,2.18) if the conditions (2.28) hold.

This analysis leads us to the important conclusion that the same schemes can be used not only to integrate time-dependent Langevin equations (2.26) but also to numerically linearize (2.16), and integrate the equations (2.17,2.18) to second order weakly. In particular, for fully explicit schemes we recommend the midpoint scheme (2.29), and for implicit schemes we recommend the implicit trapezoidal scheme (2.31), with the identification $\boldsymbol{L}(\boldsymbol{x}) \equiv \boldsymbol{H}(\boldsymbol{x})$ and $\boldsymbol{g}(\boldsymbol{x}) \equiv \boldsymbol{h}(\boldsymbol{x})$. Depending on the interpretation of the noise, the same integrators may also be first-order weak integrators for the nonlinear equation (2.16), in particular, this is the case for Stratonovich noise. For kinetic noise, the RFD term (2.35) can be added to the corrector to obtain the required stochastic drift terms.

## 2.3 Fast-Slow Systems

In this section we consider a generic finite-dimensional Langevin equation of the form (2.1) in the case when there are two variables, $\boldsymbol{x} \leftarrow (\boldsymbol{x}, \boldsymbol{y})$, where $\boldsymbol{x} \in \mathcal{R}^N$ is the slow (relevant) variable and $\boldsymbol{y} \in \mathcal{R}^M$ is a fast variable. We

focus on a rather general form of such a fast-slow Langevin system,

$$\begin{bmatrix} \partial_t \boldsymbol{x} \\ \partial_t \boldsymbol{y} \end{bmatrix} = - \begin{bmatrix} \boldsymbol{A} & \epsilon^{-1}\boldsymbol{B} \\ -\epsilon^{-1}\boldsymbol{B}^\star & \epsilon^{-2}\boldsymbol{C} \end{bmatrix} \begin{bmatrix} \partial_{\boldsymbol{x}} U \\ \partial_{\boldsymbol{y}} U \end{bmatrix} + \sqrt{2k_B T} \begin{bmatrix} \boldsymbol{A}_{\frac{1}{2}} & \boldsymbol{0} \\ \boldsymbol{0} & \epsilon^{-1}\boldsymbol{C}_{\frac{1}{2}} \end{bmatrix} \begin{bmatrix} \boldsymbol{\mathcal{W}}_{\boldsymbol{x}}(t) \\ \boldsymbol{\mathcal{W}}_{\boldsymbol{y}}(t) \end{bmatrix}$$

$$+ (k_B T) \begin{bmatrix} \partial_{\boldsymbol{x}} \cdot \boldsymbol{A} \\ -\epsilon^{-1}\partial_{\boldsymbol{x}} \cdot \boldsymbol{B}^\star \end{bmatrix}$$

$$= - \boldsymbol{N}(\boldsymbol{x}) \begin{bmatrix} \partial_{\boldsymbol{x}} U \\ \partial_{\boldsymbol{y}} U \end{bmatrix} + (2k_B T)^{\frac{1}{2}} \boldsymbol{M}_{\frac{1}{2}}(\boldsymbol{x}) \boldsymbol{\mathcal{W}}(t) + (k_B T) \partial_{\boldsymbol{x}} \cdot \boldsymbol{N}(\boldsymbol{x}), \tag{2.43}$$

where $\epsilon$ is a parameter that controls the separation of time scales between the slow and fast variables, $\epsilon = 1$ in the original (inertial) dynamics. Here the linear operators $\boldsymbol{A}(\boldsymbol{x}) \succeq 0$, $\boldsymbol{B}(\boldsymbol{x})$ and $\boldsymbol{C}(\boldsymbol{x}) \succeq 0$ depend *only* on the slow variable $\boldsymbol{x}$, and $\boldsymbol{A}_{\frac{1}{2}}(\boldsymbol{x})$ and $\boldsymbol{C}_{\frac{1}{2}}(\boldsymbol{x})$ satisfy the fluctuation-dissipation balance condition (2.2), $\boldsymbol{A}_{\frac{1}{2}}\boldsymbol{A}_{\frac{1}{2}}^\star = \boldsymbol{A}$ and $\boldsymbol{C}_{\frac{1}{2}}\boldsymbol{C}_{\frac{1}{2}}^\star = \boldsymbol{C}$. The Langevin equation with position-dependent friction (2.8) is an example of this kind of system with the identification $\boldsymbol{y} \equiv \sqrt{m}\boldsymbol{v}$, $U(\boldsymbol{x},\boldsymbol{y}) = U(\boldsymbol{x}) + y^2/2$, $\epsilon \equiv \sqrt{m}$, $\boldsymbol{A} = 0$, $\boldsymbol{B} = -\boldsymbol{I}$, $\boldsymbol{C} = \boldsymbol{\gamma}$.

We will assume that the coarse-grained free energy $U(\boldsymbol{x},\boldsymbol{y})$ is *separable* and *quadratic* in the fast variable,

$$U(\boldsymbol{x},\boldsymbol{y}) = U_x(\boldsymbol{x}) + U_y(\boldsymbol{y}) = U_x(\boldsymbol{x}) + \frac{1}{2}(\boldsymbol{y} - \bar{\boldsymbol{y}}(\boldsymbol{x}))^T \boldsymbol{\Psi}(\boldsymbol{x})(\boldsymbol{y} - \bar{\boldsymbol{y}}(\boldsymbol{x})), \tag{2.44}$$

so that the equilibrium distribution (invariant measure) of $\boldsymbol{y}$ for *fixed* $\boldsymbol{x}$ is Gaussian with mean $\bar{\boldsymbol{y}}(\boldsymbol{x})$ and covariance $\boldsymbol{\Psi}(\boldsymbol{x})^{-1}$ that may depend on the slow variable. In particular, in the model equation (2.43) the fast variable enters only linearly (but the slow variable enters nonlinearly); this greatly simplifies the limiting dynamics [45] as $\epsilon \to 0$. In the more general case one cannot write a single SDE for the slow variable $\boldsymbol{x}$ that describes all aspects of the dynamics. Instead, depending on the type of observable and the time scale one is interested in, different equations arise in the limit.

As $\epsilon \to 0$ there is an infinite separation of time scales between $\boldsymbol{x}$ and $\boldsymbol{y}$, and we can perform adiabatic elimination of the fast variable [45]. The resulting overdamped dynamics is expected to be a good approximation to the original dynamics, $\epsilon = 1$. In the limit $\epsilon \to 0$, it can be shown [46, 47, 36] (for a review see also the book [37]) that the *limiting* or *overdamped* dynamics for $\boldsymbol{x}$ is

$$\partial_t \boldsymbol{x} = -\left(\boldsymbol{A} + \boldsymbol{B}\boldsymbol{C}^{-1}\boldsymbol{B}^\star\right)\partial_{\boldsymbol{x}} F + \sqrt{2k_B T}\left(\boldsymbol{A}_{\frac{1}{2}} \diamond \boldsymbol{\mathcal{W}}_{\boldsymbol{x}} + \boldsymbol{B}\boldsymbol{C}^{-1}\boldsymbol{C}_{\frac{1}{2}} \diamond \boldsymbol{\mathcal{W}}_{\boldsymbol{y}}\right) \tag{2.45}$$

$$= -\left(\boldsymbol{A} + \boldsymbol{B}\boldsymbol{C}^{-1}\boldsymbol{B}^\star\right)\partial_{\boldsymbol{x}} F + \sqrt{2k_B T}\left(\boldsymbol{A}_{\frac{1}{2}}\boldsymbol{\mathcal{W}}_{\boldsymbol{x}} + \boldsymbol{B}\boldsymbol{C}^{-1}\boldsymbol{C}_{\frac{1}{2}}\boldsymbol{\mathcal{W}}_{\boldsymbol{y}}\right)$$

$$+ (k_B T)\partial_{\boldsymbol{x}} \cdot \left(\boldsymbol{A} + \boldsymbol{B}\boldsymbol{C}^{-1}\boldsymbol{B}^\star\right),$$

and is time-reversible with respect to the equilibrium distribution $\sim \exp\left(-F(\boldsymbol{x})/k_B T\right)$. Here the symbol $\diamond$ denotes the kinetic stochastic interpretation [5]. For future reference, we note that the last stochastic drift in (2.45) can be expanded using the chain rule,

$$\partial_{\boldsymbol{x}} \cdot \left(\boldsymbol{B}\boldsymbol{C}^{-1}\boldsymbol{B}^\star\right) = \partial_{\boldsymbol{x}}\left(\boldsymbol{B}\boldsymbol{C}^{-1}\right) : \boldsymbol{B}^\star + \boldsymbol{B}\boldsymbol{C}^{-1}\left(\partial_{\boldsymbol{x}} \cdot \boldsymbol{B}^\star\right), \tag{2.46}$$

and similarly,

$$\partial_{\boldsymbol{x}} \cdot \boldsymbol{A} = \partial_{\boldsymbol{x}} \cdot \left(\boldsymbol{A}_{\frac{1}{2}}\boldsymbol{A}_{\frac{1}{2}}^\star\right) = \partial_{\boldsymbol{x}}\left(\boldsymbol{A}_{\frac{1}{2}}\right) : \boldsymbol{A}^\star + \boldsymbol{A}_{\frac{1}{2}}\left(\partial_{\boldsymbol{x}} \cdot \boldsymbol{A}_{\frac{1}{2}}^\star\right),$$

where the first term on the right hand side in index notation reads $\left(\partial_j A_{ik}^{\frac{1}{2}}\right) A_{jk}^{\frac{1}{2}}$, and is the only drift term that would have appeared if the overdamped dynamics used a Stratonovich interpretation.

Here $F(\boldsymbol{x})$ is the free energy in the slow variables, and can be obtained from the marginal distribution

$$\exp\left(-\frac{F(\boldsymbol{x})}{k_B T}\right) \sim \exp\left(-\frac{U_x(\boldsymbol{x})}{k_B T}\right) \int \exp\left(-\frac{U_y(\boldsymbol{x})}{k_B T}\right) d\boldsymbol{y} \sim |\boldsymbol{\Psi}(\boldsymbol{x})|^{-\frac{1}{2}}\exp\left(-\frac{U_x(\boldsymbol{x})}{k_B T}\right),$$

giving the relationship

$$F(\boldsymbol{x}) = U_x(\boldsymbol{x}) + \frac{k_B T}{2}\ln|\boldsymbol{\Psi}(\boldsymbol{x})|.$$

Note that one can evaluate the derivative of the determinant using Jacobi's formula,

$$\partial_{\boldsymbol{x}} F = \partial_{\boldsymbol{x}} U_x + \frac{k_B T}{2}\left(\boldsymbol{\Psi}^{-1} : \partial_{\boldsymbol{x}}\boldsymbol{\Psi}(\boldsymbol{x})\right), \tag{2.47}$$

19

where colon denotes a double contraction, $\left(\boldsymbol{\Psi}^{-1} : \partial_{\boldsymbol{x}}\boldsymbol{\Psi}\right)_k = \Psi_{ij}^{-1}\partial_k\Psi_{ij}$. One can construct a random finite difference approach (see Section 2.1.1.2) to evaluate this term in expectation, using the identity

$$\boldsymbol{\Psi}^{-1}\left(\boldsymbol{x}\right) : \left(\partial_{\boldsymbol{x}}\boldsymbol{\Psi}\left(\boldsymbol{x}\right)\right) = \lim_{\delta \to 0} \frac{1}{\delta} \left\langle \left[\boldsymbol{\Psi}^{-1}\left(\boldsymbol{x}\right) : \left(\boldsymbol{\Psi}\left(\boldsymbol{x} + \delta\boldsymbol{W}\right) - \boldsymbol{\Psi}\left(\boldsymbol{x}\right)\right)\right]\boldsymbol{W}\right\rangle, \tag{2.48}$$

where $\boldsymbol{W}$ is a collection of i.i.d. standard normal variables. This only requires a routine for evaluating the trace $\boldsymbol{\Psi}^{-1} : \boldsymbol{\Psi}$ once per time step, which is likely nontrivial in practice. However, the RFD (2.48) avoids computing derivatives and is certainly more efficient than computing $\boldsymbol{\Psi}^{-1} : \partial_{\boldsymbol{x}}\boldsymbol{\Psi}$ using finite differences to evaluate the gradient $\partial_{\boldsymbol{x}}\boldsymbol{\Psi}$, since this requires evaluating a trace for *each* slow variable. In this work we do not study models where $\boldsymbol{\Psi}\left(\boldsymbol{x}\right)$ depends on the slow variable further, and henceforth $F\left(\boldsymbol{x}\right) \equiv U_x\left(\boldsymbol{x}\right)$.

We now present two temporal integrators for solving (2.45). The first scheme can be seen as an application of the explicit midpoint scheme (2.29) to the overdamped equation (2.45), and, aside from some of the stochastic drift terms, consists of applying the explicit midpoint scheme to the original system (2.43) setting $\partial_t\boldsymbol{y} = 0$. Similarly, we also present an implicit trapezoidal scheme (2.31) applied to the overdamped equation (2.45). In the explicit midpoint scheme we use a random finite difference (RFD) approach to handle several of the stochastic drift terms, as in (2.15), and in the implicit trapezoidal scheme we show how one can use a Fixman-like approach for one of the drift terms, as in (2.11).

In the general nonlinear setting, the schemes presented in this section are only first-order weakly accurate. They are deterministically second-order accurate. With care, the schemes *can* be second-order weak integrators for the *linearized* limiting dynamics, as we explained in Section 2.2. Note that the stochastic drift terms play no role in the linearized overdamped dynamics because they are proportional to the small noise variance, and only terms of order one half in the noise variance are kept in the linearization. In order to achieve second-order accuracy the schemes below require solving three linear systems involving $\boldsymbol{C}$ per time step. In cases when first-order accuracy is sufficient, one can avoid the linear solve in the RFD term; this can save significant computer time in cases when computing the action of $\boldsymbol{C}^{-1}$ is the dominant cost. Furthermore, in the case of constant $\boldsymbol{C}$, one can re-use the predictor's deterministic increment in the corrector for a first order scheme requiring only one linear solve. In this case, the role of the corrector stage is simply to obtain all of the required stochastic drift terms [3].

Of course, the trapezoidal and the midpoint schemes we presented here do not exhaust all possibilities; they are representative of a broad class of schemes that uses the original dynamics to approximate the overdamped dynamics. By combining the techniques we described here one can construct various schemes tailored to particular problems. In each specific application, various terms may vanish, and a different approach may be more efficient, more stable, or simpler to implement, as we illustrate in Section 3.4 on several applications in fluctuating hydrodynamics.

### 2.3.1 Explicit Midpoint Scheme

In the explicit midpoint scheme, the predictor is an Euler-Maruyama step to the midpoint of the time step,

$$\begin{bmatrix} \left(\boldsymbol{x}^{p,n+\frac{1}{2}} - \boldsymbol{x}^n\right)/\left(\Delta t/2\right) \\ \boldsymbol{0} \end{bmatrix} = -\begin{bmatrix} \boldsymbol{A} & \boldsymbol{B} \\ -\boldsymbol{B}^\star & \boldsymbol{C} \end{bmatrix}^n \begin{bmatrix} \partial_{\boldsymbol{x}}F \\ \boldsymbol{\Psi}\left(\boldsymbol{x}\right)\left(\boldsymbol{y} - \bar{\boldsymbol{y}}\left(\boldsymbol{x}\right)\right) \end{bmatrix}^n \tag{2.49}$$

$$+ \sqrt{\frac{2k_BT}{\left(\Delta t/2\right)}} \begin{bmatrix} \boldsymbol{A}_{\frac{1}{2}} & \boldsymbol{0} \\ \boldsymbol{0} & \boldsymbol{C}_{\frac{1}{2}} \end{bmatrix}^n \begin{bmatrix} \boldsymbol{W}_{\boldsymbol{x}}^{n,1} \\ \boldsymbol{W}_{\boldsymbol{y}}^{n,1} \end{bmatrix},$$

In terms of just $\boldsymbol{x}$, the predictor step above is equivalent to an Euler-Maruyama half-step for the limiting equation, without the stochastic drift terms,

$$\boldsymbol{x}^{p,n+\frac{1}{2}} = \boldsymbol{x}^n - \frac{\Delta t}{2}\left(\boldsymbol{A} + \boldsymbol{B}\boldsymbol{C}^{-1}\boldsymbol{B}^\star\right)^n \left(\partial_{\boldsymbol{x}}F\right)^n + \sqrt{\frac{k_BT\Delta t}{2}}\boldsymbol{A}_{\frac{1}{2}}^n\boldsymbol{W}_{\boldsymbol{x}}^n + \sqrt{\frac{k_BT\Delta t}{2}}\left(\boldsymbol{B}\boldsymbol{C}^{-1}\boldsymbol{C}_{\frac{1}{2}}\right)^n\boldsymbol{W}_{\boldsymbol{y}}^n. \tag{2.50}$$

In practical implementation, however, we first solve a linear system for $\boldsymbol{y}$ and then take an Euler-Maryama step for $\boldsymbol{x}$ using the obtained solution for $\boldsymbol{y}$. This makes it very easy to convert a semi-implicit code for simulating the original dynamics (2.43) to simulate the overdamped dynamics, using a much larger time step size than possible for the original inertial dynamics. Note, however, that a solver for linear systems involving $\boldsymbol{C}$ must be implemented and applied each time step; this will in general significantly increase the cost of an overdamped step compared to a fully *explicit* scheme for the original dynamics. In practice, however, the extreme stiffness in the original dynamics will force us to use a semi-implicit scheme even for the original dynamics (for example, most fluid dynamics codes treat viscosity, or, more generally, diffusion, semi-implicitly), and the required linear solvers will already be available.

#### 2.3.1.1 First Order Method

If first-order weak accuracy is sufficient, we can reuse the same noise amplitude in the corrector stage as in the predictor stage, and include RFD terms to capture the stochastic drift terms,

$$
\begin{aligned}
\left[\begin{array}{c} \left(\boldsymbol{x}^{n+1} - \boldsymbol{x}^n\right)/\Delta t \\ \mathbf{0} \end{array}\right] = {} & -\left[\begin{array}{cc} \boldsymbol{A} & \boldsymbol{B} \\ -\boldsymbol{B}^\star & \boldsymbol{C} \end{array}\right]^{p,n+\frac{1}{2}} \left[\begin{array}{c} \partial_{\boldsymbol{x}} F \\ \boldsymbol{\Psi}\left(\boldsymbol{x}\right)\left(\boldsymbol{y} - \bar{\boldsymbol{y}}\left(\boldsymbol{x}\right)\right) \end{array}\right]^{p,n+\frac{1}{2}} \\
& + \sqrt{\frac{k_B T}{\Delta t}} \left[\begin{array}{cc} \boldsymbol{A}_{\frac{1}{2}} & \mathbf{0} \\ \mathbf{0} & \boldsymbol{C}_{\frac{1}{2}} \end{array}\right]^n \left[\begin{array}{c} \boldsymbol{W}_{\boldsymbol{x}}^{n,1} + \boldsymbol{W}_{\boldsymbol{x}}^{n,2} \\ \boldsymbol{W}_{\boldsymbol{y}}^{n,1} + \boldsymbol{W}_{\boldsymbol{y}}^{n,2} \end{array}\right] \\
& + \frac{k_B T}{\delta} \left[\begin{array}{c} \boldsymbol{A}\left(\boldsymbol{x}^n + \delta \widetilde{\boldsymbol{W}}^n\right) - \boldsymbol{A}\left(\boldsymbol{x}^n\right) \\ \boldsymbol{B}^\star\left(\boldsymbol{x}^n\right) - \boldsymbol{B}^\star\left(\boldsymbol{x}^n + \delta \widetilde{\boldsymbol{W}}^n\right) \end{array}\right] \widetilde{\boldsymbol{W}}^n .
\end{aligned}
\tag{2.51}
$$

Note that here we can re-use the same random numbers $\widetilde{\boldsymbol{W}}^n$ for both stochastic drift terms, but this is not necessary.

The corrector step includes random finite differences to capture the stochastic drift terms $(k_B T)\,\partial_{\boldsymbol{x}} \cdot \boldsymbol{A}$ and $(k_B T)\,\boldsymbol{B}\boldsymbol{C}^{-1}\left(\partial_{\boldsymbol{x}} \cdot \boldsymbol{B}^\star\right)$, as we did in (2.15). The remaining drift term

$$
(k_B T)\,\partial_{\boldsymbol{x}}\left(\boldsymbol{B}\boldsymbol{C}^{-1}\right) : \boldsymbol{B}^\star
$$

is obtained from the predictor step in the spirit of Runge-Kutta schemes, as can be confirmed by a Taylor series analysis (see Addendum 2.8 for further details). To see this, note that the stochastic increment in $\boldsymbol{x}^{p,n+1}$ involving $\boldsymbol{W}_{\boldsymbol{y}}^n$ is

$$
\Delta \boldsymbol{x}^p = \sqrt{2\Delta t k_B T}\left(\boldsymbol{B}\boldsymbol{C}^{-1}\boldsymbol{C}_{\frac{1}{2}}\right)^n \boldsymbol{W}_{\boldsymbol{y}}^n .
$$

In the corrector, we have the stochastic increment

$$
\Delta \boldsymbol{x}^c = \frac{1}{2}\left(\left(\boldsymbol{B}\boldsymbol{C}^{-1}\right)^n + \left(\boldsymbol{B}\boldsymbol{C}^{-1}\right)^{p,n+1}\right)\left(\sqrt{2\Delta t k_B T}\,\boldsymbol{C}_{\frac{1}{2}}^n \boldsymbol{W}_{\boldsymbol{y}}^n\right) .
$$

If we expand $\left(\boldsymbol{B}\boldsymbol{C}^{-1}\right)^{p,n+1}$ to first-order around $\boldsymbol{x}^n$, we see that $\Delta \boldsymbol{x}^c$ contains a term $\sim \partial_{\boldsymbol{x}}\left(\boldsymbol{B}\boldsymbol{C}^{-1}\right)^n \Delta \boldsymbol{x}^p \left(\boldsymbol{C}_{\frac{1}{2}}^n \boldsymbol{W}_{\boldsymbol{y}}^n\right)$, more precisely, in index notation, the $i$th component of the additional term is

$$
\sqrt{\frac{\Delta t k_B T}{2}}\,\partial_l \left(\boldsymbol{B}\boldsymbol{C}^{-1}\right)_{ij} \Delta x_l^p C_{jk}^{\frac{1}{2}} W_k^y = (k_B T)\,\Delta t\,\partial_l \left(\boldsymbol{B}\boldsymbol{C}^{-1}\right)_{ij}\, B_{lm} C_{mn}^{-1} C_{np}^{\frac{1}{2}} C_{jk}^{\frac{1}{2}}\, W_k^y W_p^y ,
$$

evaluated at time step $n$, where $\partial_k \equiv \partial/\partial x_k$. Upon taking expectation values, $\left\langle W_k^y W_p^y \right\rangle = \delta_{k,p}$, we obtain the required drift term $\partial_{\boldsymbol{x}}\left(\boldsymbol{B}\boldsymbol{C}^{-1}\right) : \boldsymbol{B}^\star$ in (2.46), since

$$
\partial_l \left(\boldsymbol{B}\boldsymbol{C}^{-1}\right)_{ij}\, B_{lm}\, C_{mn}^{-1} C_{nk}^{\frac{1}{2}}\left(C^{\frac{1}{2}}\right)_{jk}^\star = \partial_l \left(\boldsymbol{B}\boldsymbol{C}^{-1}\right)_{ij}\, B_{lm}\, \delta_{jm} = \partial_k \left(\boldsymbol{B}\boldsymbol{C}^{-1}\right)_{ij}\, B_{kj} .
\tag{2.52}
$$

#### 2.3.1.2 Second Order Method

If we want to obtain second-order weak accuracy for the *linearized* overdamped dynamics, we should evaluate the noise in the corrector at the predicted midpoint value, as in the explicit midpoint algorithm (2.29). This is however only consistent with a Stratonovich interpretation of the noise in the overdamped dynamics and is not consistent with the kinetic interpretation we seek. In order to be consistent with a kinetic interpretation, we need to add RFD terms to capture the correct stochastic drift terms (see Addendum 2.8),

$$
\begin{aligned}
\left[\begin{array}{c} \left(\boldsymbol{x}^{n+1} - \boldsymbol{x}^n\right)/\Delta t \\ \mathbf{0} \end{array}\right] = {} & -\left[\begin{array}{cc} \boldsymbol{A} & \boldsymbol{B} \\ -\boldsymbol{B}^\star & \boldsymbol{C} \end{array}\right]^{p,n+\frac{1}{2}} \left[\begin{array}{c} \partial_{\boldsymbol{x}} F \\ \boldsymbol{\Psi}\left(\boldsymbol{x}\right)\left(\boldsymbol{y} - \bar{\boldsymbol{y}}\left(\boldsymbol{x}\right)\right) \end{array}\right]^{p,n+\frac{1}{2}} \\
& + \sqrt{\frac{k_B T}{\Delta t}} \left[\begin{array}{cc} \boldsymbol{A}_{\frac{1}{2}}^{p,n+\frac{1}{2}} & \mathbf{0} \\ \mathbf{0} & \boldsymbol{C}_{\frac{1}{2}}^{p,n+\frac{1}{2}} \end{array}\right] \left[\begin{array}{c} \boldsymbol{W}_{\boldsymbol{x}}^{n,1} + \boldsymbol{W}_{\boldsymbol{x}}^{n,2} \\ \boldsymbol{W}_{\boldsymbol{y}}^{n,1} + \boldsymbol{W}_{\boldsymbol{y}}^{n,2} \end{array}\right] \\
& + \frac{k_B T}{\delta} \left[\begin{array}{c} \boldsymbol{A}_{\frac{1}{2}}^n\left(\boldsymbol{A}_{\frac{1}{2}}^\star\left(\boldsymbol{x}^n + \delta \widetilde{\boldsymbol{W}}_A^n\right) - \boldsymbol{A}_{\frac{1}{2}}^\star\left(\boldsymbol{x}^n\right)\right) \\ \boldsymbol{B}^\star\left(\boldsymbol{x}^n + \delta \widetilde{\boldsymbol{W}}_A^n\right) - \boldsymbol{B}^\star\left(\boldsymbol{x}^n\right) \end{array}\right] \widetilde{\boldsymbol{W}}_A^n \\
& - \frac{k_B T}{\delta} \left[\begin{array}{c} \mathbf{0} \\ \boldsymbol{C}_{\frac{1}{2}}\left(\boldsymbol{x}^n + \delta \left(\boldsymbol{B}\boldsymbol{C}^{-1}\boldsymbol{C}_{\frac{1}{2}}\right)^n \widetilde{\boldsymbol{W}}_C^n\right) - \boldsymbol{C}_{\frac{1}{2}}\left(\boldsymbol{x}^n\right) \end{array}\right] \widetilde{\boldsymbol{W}}_C^n ,
\end{aligned}
\tag{2.53}
$$

where $\widetilde{\boldsymbol{W}}_A^n$ and $\widetilde{\boldsymbol{W}}_C^n$ are independently-generated random vectors. As we show in Addendum 2.8, the scheme (2.53) is weakly first-order accurate in general, while also achieving second order weak accuracy for the linearized overdamped dynamics. In [3] we successfully used the scheme (2.49,2.53) to integrate the equations of Brownian Dynamics, which result when one eliminates the fast velocity degrees of freedom from a system of equations for the motion of particles immersed in a fluctuating Stokes fluid.

The midpoint scheme is (2.49,2.53) a *second-order* weak integrator for the *linearized* overdamped equations. This is because it can be seen as an application of the explicit midpoint scheme (2.29) to the limiting dynamics (2.45), which we concluded in Section 2.2.3 to be a second-order integrator for linearized Langevin equations. This shows the importance of carefully selecting where to evaluate the noise amplitude in the corrector stage in the nonlinear setting, and balancing this with RFD terms to ensure consistency with the nonlinear equations. In the case of constant $\boldsymbol{C}$, one can omit the last line in (2.53), similarly, if $\boldsymbol{A}$ is constant one can omit the corresponding RFD term. Fluctuating Hydrodynamics

### 2.3.2 Implicit Trapezoidal Scheme

In this section we explain how the implicit trapezoidal scheme (2.31) can be used to simulate the overdamped dynamics (2.45). We will assume that

$$\boldsymbol{A}\left(\boldsymbol{x}\right)\,\partial_{\boldsymbol{x}}F\left(\boldsymbol{x}\right)\equiv\boldsymbol{L}\left(\boldsymbol{x}\right)\boldsymbol{x}$$

and treat this term semi-implicitly. All remaining terms, including the stochastic drift term $\left(\boldsymbol{BC}^{-1}\boldsymbol{B}^{\star}\right)\partial_{\boldsymbol{x}}F$, which arises due to the elimination of the fast variable, will be handled explicitly.

The predictor step consists of taking an overdamped step for $\boldsymbol{y}$, which simply amounts to deleting the term $\partial_t\boldsymbol{y}$ in (2.43), followed by an implicit trapezoidal step for $\boldsymbol{x}$. Symbolically,

$$\begin{bmatrix} \left(\boldsymbol{x}^{p,n+1} - \boldsymbol{x}^n\right)/\Delta t \\ \boldsymbol{0} \end{bmatrix} = -\begin{bmatrix} \frac{1}{2}\boldsymbol{L}^n\left(\boldsymbol{x}^n + \boldsymbol{x}^{p,n+1}\right) + \left(\boldsymbol{B}\boldsymbol{\Psi}\right)^n\left(\boldsymbol{y}^n - \bar{\boldsymbol{y}}^n\right) \\ -\left(\boldsymbol{B}^{\star}\partial_{\boldsymbol{x}}F\right)^n + \left(\boldsymbol{C}\boldsymbol{\Psi}\right)^n\left(\boldsymbol{y}^n - \bar{\boldsymbol{y}}^n\right) \end{bmatrix} \\ + \sqrt{\frac{2k_BT}{\Delta t}}\begin{bmatrix} \boldsymbol{A}_{\frac{1}{2}} & \boldsymbol{0} \\ \boldsymbol{0} & \boldsymbol{C}_{\frac{1}{2}} \end{bmatrix}^n\begin{bmatrix} \boldsymbol{W}_{\boldsymbol{x}}^n \\ \boldsymbol{W}_{\boldsymbol{y}}^n \end{bmatrix}. \tag{2.54}$$

Note that here we have omitted all stochastic drift terms; we will rely on the corrector to obtain those. The corrector step consists of solving the following linear system for $\boldsymbol{x}^{n+1}$ and $\boldsymbol{y}^{p,n+1}$,

$$\begin{bmatrix} \left(\boldsymbol{x}^{n+1} - \boldsymbol{x}^n\right)/\Delta t \\ \boldsymbol{0} \end{bmatrix} = \begin{bmatrix} \Delta\boldsymbol{x}/\Delta t \\ \Delta\boldsymbol{y}/\Delta t \end{bmatrix} \tag{2.55}$$
$$- \begin{bmatrix} \frac{1}{2}\left(\boldsymbol{L}^n\boldsymbol{x}^n + \boldsymbol{L}^{p,n+1}\boldsymbol{x}^{n+1}\right) + \frac{1}{2}\left(\boldsymbol{B}\boldsymbol{\Psi}\right)^{p,n+1}\left(\boldsymbol{y}^{p,n+1} - \bar{\boldsymbol{y}}^{p,n+1}\right) \\ -\left(\boldsymbol{B}^{\star}\partial_{\boldsymbol{x}}F\right)^{p,n+1} \end{bmatrix}$$
$$+ \begin{bmatrix} \frac{1}{2}\left(\boldsymbol{B}\boldsymbol{\Psi}\right)^n\left(\boldsymbol{y}^n - \bar{\boldsymbol{y}}^n\right) \\ \left(\boldsymbol{C}\boldsymbol{\Psi}\right)^{p,n+1}\left(\boldsymbol{y}^{p,n+1} - \bar{\boldsymbol{y}}^{p,n+1}\right) \end{bmatrix}.$$

where the stochastic increments $\Delta\boldsymbol{x}$ and $\Delta\boldsymbol{y}$ are given in (2.56).

The stochastic increments $\Delta\boldsymbol{x}$ and $\Delta\boldsymbol{y}$ need to be carefully constructed in order to obtain the correct drift terms, and can be approximated in one of two ways. For the case when $\boldsymbol{A}$ is invertible, we can use a Fixman like approach to obtain the drift term $\left(k_BT\right)\partial_{\boldsymbol{x}}\cdot\boldsymbol{A}$ in the corrector step, just as we illustrated for the simple Langevin equation in (2.11),

$$\begin{bmatrix} \Delta\boldsymbol{x}/\Delta t \\ \Delta\boldsymbol{y}/\Delta t \end{bmatrix} = \sqrt{\frac{2k_BT}{\Delta t}}\begin{bmatrix} \frac{1}{2}\left(\boldsymbol{A}^n + \boldsymbol{A}^{p,n+1}\right)\left(\boldsymbol{A}^{-1}\boldsymbol{A}_{\frac{1}{2}}\right)^n & \boldsymbol{0} \\ \boldsymbol{0} & \boldsymbol{C}_{\frac{1}{2}}^n \end{bmatrix}\begin{bmatrix} \boldsymbol{W}_{\boldsymbol{x}}^n \\ \boldsymbol{W}_{\boldsymbol{y}}^n \end{bmatrix} \tag{2.56}$$
$$+ 2\frac{k_BT}{\delta}\begin{bmatrix} \boldsymbol{0} \\ \boldsymbol{B}^{\star}\left(\boldsymbol{x}^n\right) - \boldsymbol{B}^{\star}\left(\boldsymbol{x}^n + \delta\widetilde{\boldsymbol{W}}^n\right) \end{bmatrix}\widetilde{\boldsymbol{W}}^n.$$

The scheme (2.55,2.56) is only first-order weakly accurate even for the linearized overdamped dynamics.

If we want to obtain second-order weak accuracy for the *linearized* overdamped dynamics, we should evaluate the noise in the corrector at the predicted value, as in the implicit trapezoidal algorithm (2.31). In this case we

need to capture the remaining terms with an RFD approach, as we did in (2.53),

$$\begin{bmatrix} \Delta\boldsymbol{x}/\Delta t \\ \Delta\boldsymbol{y}/\Delta t \end{bmatrix} = \sqrt{\frac{2k_BT}{\Delta t}} \begin{bmatrix} \frac{1}{2}\left(\boldsymbol{A}_{\frac{1}{2}}^n + \boldsymbol{A}_{\frac{1}{2}}^{p,n+1}\right) & \boldsymbol{0} \\ \boldsymbol{0} & \boldsymbol{C}_{\frac{1}{2}}^{p,n+1} \end{bmatrix} \begin{bmatrix} \boldsymbol{W}_{\boldsymbol{x}}^n \\ \boldsymbol{W}_{\boldsymbol{y}}^n \end{bmatrix} \tag{2.57}$$

$$+ \frac{k_BT}{\delta} \begin{bmatrix} \boldsymbol{A}_{\frac{1}{2}}^n \left( \boldsymbol{A}_{\frac{1}{2}}^{\star}\left(\boldsymbol{x}^n + \delta\widetilde{\boldsymbol{W}}_A^n\right) - \boldsymbol{A}_{\frac{1}{2}}^{\star}\left(\boldsymbol{x}^n\right) \right) \\ 2\left(\boldsymbol{B}^{\star}\left(\boldsymbol{x}^n + \delta\widetilde{\boldsymbol{W}}_A^n\right) - \boldsymbol{B}^{\star}\left(\boldsymbol{x}^n\right)\right) \end{bmatrix} \widetilde{\boldsymbol{W}}_A^n$$

$$- \frac{k_BT}{\delta} \begin{bmatrix} \boldsymbol{0} \\ \left(2\boldsymbol{C}_{\frac{1}{2}}\left(\boldsymbol{x}^n + \delta\left(\boldsymbol{B}\boldsymbol{C}^{-1}\boldsymbol{C}_{\frac{1}{2}}\right)^n \widetilde{\boldsymbol{W}}_C^n\right) - \boldsymbol{C}_{\frac{1}{2}}\left(\boldsymbol{x}^n\right)\right) \end{bmatrix} \widetilde{\boldsymbol{W}}_C^n.$$

Note that the computation of $\left(\boldsymbol{B}\boldsymbol{C}^{-1}\boldsymbol{C}_{\frac{1}{2}}\right)^n \widetilde{\boldsymbol{W}}_C^n$ involves solving a linear system involving $\boldsymbol{C}$ and will thus, generally, significantly increase the computational effort per time step. In the case of constant $\boldsymbol{A}$ or $\boldsymbol{C}$, one can omit the corresponding RFD terms to simplify the scheme. For a Stratonovich interpretation of the limiting dynamics, one simply omits the last two lines of (2.57).

## 2.4 Conclusion

In this chapter, we constructed a general class of mixed explicit-implicit predictor-corrector schemes for integrating Langevin equations, and recommended two specific schemes. The first is a fully explicit midpoint rule, and the second is a semi-implicit scheme in which some of the terms are treated using an implicit trapezoidal rule and the rest are treated using an explicit trapezoidal rule. Here we showed how to add stochastic forcing terms to these schemes that ensure the following key properties: the schemes are second-order weakly accurate for linearized Langevin equations, and they are weakly first-order accurate for multiplicative kinetic noise. In particular, we discussed how to obtain all of the required stochastic drift terms without evaluating derivatives, by using random finite differences that give the required stochastic drift in expectation.

## 2.5 Addendum: $L$-Stable Scheme

In typical fluctuating hydrodynamics applications, for explicit schemes the time step is severely limited not by advection but by momentum or heat diffusion, notably, by viscous dissipation. For purely dissipative linear equations, implicit handling of momentum diffusion can yield $A$-stable schemes such as the implicit midpoint scheme (2.24). This allows the use of much larger time step size $\Delta t$, at least in principle. If one is interested in steady-state fluctuations, the implicit midpoint scheme (2.24) gives the correct spectrum of fluctuations for any $\Delta t$ (see the Appendix in Ref. [39] for a discussion of how to choose a suitable $\Delta t$).

However, for time dependent linear problems, only an exponential integrator can reproduce the correct dynamics for all modes (wave numbers) for all time step sizes. The implicit midpoint rule provides a notably bad approximation to the exponential decay of correlations for large $\Delta t$, since the Pade (1,1) rational approximation to the exponential (2.25), $\exp(-x) \approx (1 - x/2)/(1 + x/2)$ tends to -1 for $x \gg 1$ instead of decaying to zero. This leads to oscillatory dynamics for the modes that are under-resolved by the large time step size, i.e., for the thermal fluctuations at large wave numbers. A much better approximation to $\exp(-x)$ is provided by rational approximations that decay to zero as $x \to \infty$. In numerical analysis jargon this means handling the diffusive fluxes using an $L$-stable numerical method.

Let us consider the choice of weights in the general scheme (2.27) that yield a scheme that is weakly second-order accurate and $L$-stable in the implicit part of the dynamics. From the conditions for second-order accuracy (2.28) we obtain

$$w_3 = \frac{\frac{1}{2} - w_4 - w_5}{w_2},$$

and from the condition of $L$ stability we obtain

$$w_1 = \frac{\frac{1}{2} - w_4 - w_5}{1 - w_4 - w_5},$$

which gives the following rational approximation to the exponential decay of the dynamics,

$$\exp\left(-x\right) \approx \frac{\left(1 - 2\left(w_4 + w_5\right) + 2\left(w_4 + w_5\right)^2\right)x - 2\left(1 - w_4 - w_5\right)}{\left(\left(w_4 + w_5\right)x + 1\right)\left[\left(2\left(w_4 + w_5\right) - 1\right)x - 2\left(1 - \left(w_4 + w_5\right)\right)\right]}. \tag{2.58}$$
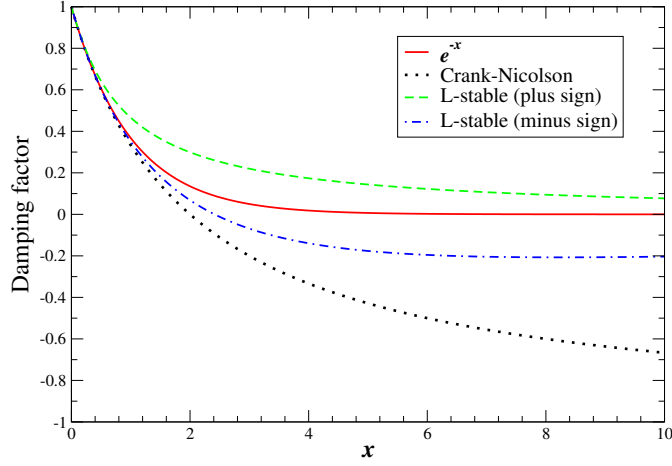
Figure 2.1: (Color online) Comparison of $\exp(-x)$ with three rational approximations. The approximation in the Crank-Nicolson scheme (2.25) does not decay to zero for large $x$. The approximation (2.58) decays to zero for $w_4 + w_5 = 1 \pm \sqrt{2}/2$, however, only the positive sign gives a strictly positive approximation.

A reasonable choice of $w_4$ can be taken to be the one that minimizes the mismatch between the coefficient in front of $x^3$ in the Taylor series expansion of the left and right hand sides [48], giving $w_4 + w_5 = 1 \pm \sqrt{2}/2$. In Fig. 2.1 we compare the two rational approximations by choosing the plus or minus sign. In the deterministic literature the choice of the minus sign has been favored [48, 49], however, we recommend the plus sign,

$$w_4 + w_5 = 1 + \frac{\sqrt{2}}{2},$$

because this gives a strictly positive approximation to the exponential decay of correlations instead of oscillatory behavior for the under-resolved modes (large $x$).

We are still left with the choice of $w_2$, where the two common choices for $w_2$ would be a mid-point, $w_2 = 1/2$, or an end-point, $w_2 = 1$, predictor stage. When all terms are handled explicitly ($\boldsymbol{L} = \boldsymbol{0}$), the choice $w_2 = 1/2$ gives third-order accuracy for the static covariance for linear problems (see Section 2.2.1). It can also be shown that this choice leads to third-order accuracy of the static covariances in the linearized setting if all terms are discretized implicitly ($\boldsymbol{g}(\boldsymbol{x}) = \boldsymbol{0}$). This suggests that a better, even if not unique, choice, is to take $w_2 = 1/2$, giving our preferred choice of weights for an $L$-stable predictor-corrector scheme,

$$w_1 = w_4 = 0, \ w_2 = \frac{1}{2}, \ w_3 = -(1 + \sqrt{2}), \ w_5 = 1 + \frac{\sqrt{2}}{2}, \ w_6 = 1, \ w_7 = 1. \tag{2.59}$$

In the linearized setting, this $L$-stable scheme gives second-order accurate covariances for small time step sizes; however, it does not produce the correct spectrum for the fluctuations for *large* time step sizes, unlike the implicit midpoint scheme (2.24). In particular, for large $\Delta t$ the $L$-stable scheme strongly damps the magnitude of the fluctuations of the fast (small wavelength or large wave number) modes. Therefore, if static covariances are the quantity of interest, the implicit midpoint rule should be used instead.

## 2.6   Addendum: Accuracy for Time-Dependent Noise

In this section, we show that the scheme (2.27) successfully captures the time dependence of $\boldsymbol{K}$ in the equation (2.26) to second order. The general theory of weak accuracy for stochastic integrators is well-established and reviewed, for example, in Section 2.2 of [22]. The key result is that, under certain assumptions, second-order weak accuracy is achieved if the first 5 moments of the one step numerical increment $\Delta \boldsymbol{x}^n = \boldsymbol{x}^{n+1} - \boldsymbol{x}^n$ match the moments of the true increment $\boldsymbol{x}\left(n\Delta t + \Delta t\right) - \boldsymbol{x}\left(n\Delta t\right)$ where $\boldsymbol{x}(n\Delta t) = \boldsymbol{x}^n$ with error no greater than $O\left(\Delta t^3\right)$ (See Addendum 1.5). The time dependence of the noise amplitude only adds one additional term (beyond constant noise) that a

second-order integrator must account for, which we find from the expansion

$$\int_{t_n}^{t_{n+1}} \boldsymbol{K}(s)\, d\boldsymbol{\mathcal{B}}(s) = \boldsymbol{K}(t_n) \int_{t_n}^{t_{n+1}} d\boldsymbol{\mathcal{B}}(s) + \boldsymbol{\partial K}(t_n) \int_{t_n}^{t_{n+1}} (s - t_n)\, d\boldsymbol{\mathcal{B}}(s) \tag{2.60}$$

$$+ \boldsymbol{\partial^2 K}(t_n) \int_{t_n}^{t_{n+1}} \frac{(s - t_n)^2}{2}\, d\boldsymbol{\mathcal{B}}(s) + O\left(\Delta t^{7/2}\right).$$

Here $\boldsymbol{\partial K}$ indicates a time derivative of $\boldsymbol{K}$, and likewise $\boldsymbol{\partial^2 K}$ indicates a second derivative in time. The first term in the second line is order $\Delta t^{5/2}$ and mean zero, so it will not affect second order weak accuracy. Likewise, terms which arise from the time dependence of $\boldsymbol{K}$ in the Taylor expansion of the deterministic part of (2.26) are all order greater than two and a half and mean zero. Therefore, the only additional expression which must be accounted for in the temporal integrator is the second term on the first line of equation (2.60). When matching increments for second order weak accuracy, this term appears only in the second moment of the increment, and only in the cross term with $\boldsymbol{K}(t_n) \int_{t_n}^{t_{n+1}} d\boldsymbol{\mathcal{B}}(s)$,

$$E\left[\left(\boldsymbol{x}(t_{n+1}) - \boldsymbol{x}(t_n)\right)\left(\boldsymbol{x}(t_{n+1}) - \boldsymbol{x}(t_n)\right)^\star\right] = \ldots + \left((\boldsymbol{\partial K})\boldsymbol{K}^\star + \boldsymbol{K}(\boldsymbol{\partial K})^\star\right) \frac{\Delta t^2}{2} + O(\Delta t^3) \tag{2.61}$$

where the terms that are present in the constant-noise case are denoted with ellipses.

In order to maintain second order weak accuracy, the additional term involving $\boldsymbol{\partial K}$ in (2.61) is matched in the temporal integrator by the way in which the noise is evaluated in the corrector step of (2.27),

$$\boldsymbol{x}^{n+1} - \boldsymbol{x}^n = \ldots + \left((1 - w_7)\boldsymbol{K}^n + w_7 \boldsymbol{K}^{(p)}\right)\left(\sqrt{w_2 \Delta t}\, \boldsymbol{W}^{n,1} + \sqrt{(1 - w_2)\Delta t}\, \boldsymbol{W}^{n,2}\right), \tag{2.62}$$

where deterministic terms are denoted by ellipses. Taylor expanding $\boldsymbol{K}^{(p)}$ in (2.62) gives the following two terms,

$$\boldsymbol{x}^{n+1} - \boldsymbol{x}^n = \ldots + \Delta t^{1/2}\, \boldsymbol{K}^n \left(\sqrt{w_2}\, \boldsymbol{W}^{n,1} + \sqrt{1 - w_2}\, \boldsymbol{W}^{n,2}\right)$$

$$+ \Delta t^{3/2} w_2 w_7 \boldsymbol{\partial K} \left(\sqrt{w_2}\, \boldsymbol{W}^{n,1} + \sqrt{1 - w_2}\, \boldsymbol{W}^{n,2}\right) + O(\Delta t^{5/2}). \tag{2.63}$$

The terms on the right hand side create the correct cross term in the second moment of the increment as long as $w_2 w_7 = 1/2$. Therefore, scheme (2.27) is second order weakly accurate even for time-dependent additive noise.

## 2.7 Addendum: Second-order weak integrators for linearized fluctuating hydrodynamics

Here we show that the scheme (2.39) is second order accurate for the linearized equations (2.17,2.18). For the scheme to be weakly second order accurate, we need the difference between the first five moments of the discrete and continuous increments for the composite variable $(\bar{\boldsymbol{x}}(t), \delta\boldsymbol{x}(t))$ to be $O\left(\Delta t^3\right)$ (see Section 1.5 and[22]). The scheme (2.40) for the mean is deterministic and standard Taylor series analysis shows that it is second-order accurate. Furthermore, because $\bar{\boldsymbol{x}}$ is deterministic, there are no cross-correlations between increments of $\bar{\boldsymbol{x}}$ and $\delta\boldsymbol{x}$, and therefore moments that involve both variables are guaranteed to match to the same order as the increments in $\delta\boldsymbol{x}$.

In order to examine the moments of the increment in $\delta\boldsymbol{x}$, let us re-write equation (2.18) in differential and index notation,

$$d(\delta x_i) = M_{ij}\left(\bar{x}(t)\right) \delta x_j\, dt + K_{ij}\left(\bar{x}(t)\right) d\mathcal{B}_j(t), \tag{2.64}$$

where as before $M_{ij} = H_{ij} + \partial_j(H_{ik})\bar{x}_k + \partial_j(h_i)$, giving

$$\partial_k(M_{ij}) = \partial_k(H_{ij}) + \partial_{kj}(H_{il})\bar{x}_l + \partial_j(H_{ik}) + \partial_{jk}(h_i).$$

Using the deterministic equation

$$d\bar{x}_k/dt = H_{kl}\bar{x}_l + h_k,$$

it can be shown that over a time interval $\Delta t = t^{n+1} - t^n$, the random variable $\delta x_i$ has the following continuous increment,

$$\Delta \left( \delta x_i \right) = \delta x_i(t') - \delta x_i \left( t \right) = \Delta t \, M_{ij} \delta x_j + K_{ij} \int_{t^n}^{t^{n+1}} d\mathcal{B}_j(s) \tag{2.65}$$

$$+ \frac{\Delta t^2}{2} \partial_k \left( M_{ij} \right) \delta x_j \left( \frac{d\bar{x}_k}{dt} \right) + \frac{\Delta t^2}{2} M_{ij} M_{jk} \delta x_k$$

$$+ \partial_k \left( K_{ij} \right) \left( \frac{d\bar{x}_k}{dt} \right) \int_{t^n}^{t^{n+1}} (s - t) \, d\mathcal{B}_j(s)$$

$$+ M_{ij} K_{jk} \int_{t^n}^{t^{n+1}} \int_t^s d\mathcal{B}_k(r) \, ds + O(\Delta t^{5/2}) \tag{2.66}$$

where in this equation and in the following, $d\bar{x}_k/dt$, as well as $\boldsymbol{M}$, $\boldsymbol{H}$, $\boldsymbol{K}$, and $\boldsymbol{h}$ and their derivatives, are all evaluated at the beginning of the time step.

In order to compare this to the discrete increment, we need to perform a Taylor expansion of every term in equation (2.42) that is not already evaluated at $\bar{\boldsymbol{x}}^n$. These expansions never need to include terms of higher order than $\Delta t^{3/2}$, considering that all terms in (2.42) are already at least order $\Delta t^{1/2}$ (any term that is $O(\Delta t^{5/2})$ is mean zero and thus irrelevant). Additionally, the only term to be expanded which is order $\Delta t^{1/2}$ before expansion is the stochastic term $w_7 K_{ij}^p \left( \sqrt{w_2 \Delta t} \, W_j^{1,n} + \sqrt{(1 - w_2) \Delta t} \, W_j^{2,n} \right)$, which depends only on the deterministic variable $\bar{\boldsymbol{x}}$. Thus an expansion of $K_{ij}^p$ to order $\Delta t^{3/2}$ only includes first order terms. All other terms in (2.42) to be expanded are of order $\Delta t$ or greater before expansion, so in fact we only need to consider first order expansions for all quantities evaluated at $\bar{\boldsymbol{x}}^p$ or $\bar{\boldsymbol{x}}^{n+1}$ in the discrete increment.

For $\delta \boldsymbol{x}$, we expand the update (2.41,2.42) to first order, substitute the result in the corrector update (2.42), and Taylor expand terms involving $\boldsymbol{M}$, $\boldsymbol{H}$, $\boldsymbol{K}$, and $\boldsymbol{h}$ evaluated at a point other than $\bar{\boldsymbol{x}}^n$ to first order. Note that both options for the handling of the explicit term in (2.39) yield the same increment to second order. After performing these expansions and collecting some terms, we get the final discrete increment to second order,

$$\Delta \left( \delta x_i \right) = \delta x_i^{n+1} - \delta x_i^n = \Delta t \, M_{ij} \delta x_j + \Delta t^{1/2} K_{ij} \left( \sqrt{w_2} W_j^1 + \sqrt{(1 - w_2)} W_j^2 \right) \tag{2.67}$$

$$+ \Delta t^2 \delta x_j \left( H_{km} \bar{x}_m + h_k \right) \left( (w_2 w_3 + w_2 w_4) \left( \partial_k (H_{ij}) + \partial_{kj} (H_{il}) \bar{x}_l \right) \right)$$

$$+ \Delta t^2 \delta x_j \left( H_{km} \bar{x}_m + h_k \right) \left( w_2 w_6 \partial_{kj} (h_i) + (w_2 w_3 + w_4 + w_5) \partial_j (H_{ik}) \right)$$

$$+ \Delta t^2 \left( (w_2 w_3 + w_4 + w_5) H_{ij} + (w_2 w_3 + w_2 w_4) \partial_j (H_{il}) \bar{x}_l \right) M_{jk} \delta x_k$$

$$+ \Delta t^2 w_2 w_6 \partial_j (h_i) M_{jk} \delta x_k$$

$$+ \Delta t^{3/2} w_2 w_7 \partial_k (K_{ij}) \left( H_{kl} \bar{x}_l + h_k \right) \left( \sqrt{w_2} \, W_j^1 + \sqrt{1 - w_2} \, W_j^2 \right)$$

$$+ \Delta t^{3/2} \left( (w_3 + w_4 + w_5) \sqrt{w_2} \, W_k^1 + (w_4 + w_5) \sqrt{1 - w_2} \, W_k^2 \right) H_{ij} K_{jk}$$

$$+ \Delta t^{3/2} (w_3 + w_4) \sqrt{w_2} \, \partial_k (H_{ij}) \bar{x}_k K_{jl} W_l^1$$

$$+ \Delta t^{3/2} w_6 \sqrt{w_2} \partial_k (h_i) K_{kl} W_l^1 + O(\Delta t^{5/2}),$$

where we have omitted bars since all quantities and derivatives are evaluated at $\bar{\boldsymbol{x}}^n$.

The first moment includes only the deterministic terms, and making use of the relations (2.28) confirms that they match the continuous increment with error $O(\Delta t^3)$. The second moment is more complicated due to the cross correlations that arise from the stochastic terms, but after some algebra and again making use of (2.28), we see that the increments match to the correct order. The third moment only contains the second order products of the first two terms in the right hand side of (2.67). The fourth moment contains only the fourth moment of the lowest order stochastic term, $K_{ij} \left( \sqrt{w_2 \Delta t} W_j^1 + \sqrt{(1 - w_2) \Delta t} W_j^2 \right)$. The fifth moment is zero for both increments. All of these moments match with error no greater than order $\Delta t^3$, and hence the scheme (2.42) is second order accurate.

## 2.8   Addendum: Kinetic noise in fast-slow system

In this section, we show that the schemes (2.49, 2.53) and (2.54, 2.55, 2.57) from section 2.3 produce the correct stochastic drift arising from the kinetic interpretation of the overdamped limit (2.45). It is useful to consider the

drift split into the following pieces,

$$\left[\partial_{\boldsymbol{x}} \cdot \left(\boldsymbol{A} + \boldsymbol{B}\boldsymbol{C}^{-1}\boldsymbol{B}^{\star}\right)\right]_i = \partial_j \left(A_{ij} + B_{ik}C_{kl}^{-1}B_{jl}\right) \tag{2.68}$$
$$= \partial_j \left(A_{ik}^{\frac{1}{2}}A_{jk}^{\frac{1}{2}}\right) + \partial_j \left(B_{ik}C_{kl}^{-1}\right)B_{jl} + B_{ik}C_{kl}^{-1}\partial_j\left(B_{jl}\right),$$

where we have rewritten $\boldsymbol{A}^{\frac{1}{2}} \equiv \boldsymbol{A}_{\frac{1}{2}}$ and $\boldsymbol{C}^{\frac{1}{2}} \equiv \boldsymbol{C}_{\frac{1}{2}}$ in order to simplify the notation. The first term on the right hand side of equation (2.68) can be split into

$$\partial_j \left(A_{ik}^{\frac{1}{2}}A_{jk}^{\frac{1}{2}}\right) = \partial_j \left(A_{ik}^{\frac{1}{2}}\right)A_{jk}^{\frac{1}{2}} + A_{ik}^{\frac{1}{2}}\partial_j\left(A_{jk}^{\frac{1}{2}}\right), \tag{2.69}$$

and the second term on the right hand side of equation (2.68) can be rewritten as

$$\partial_j \left(B_{ik}C_{kl}^{-1}\right)B_{jl} = \partial_j \left(B_{ik}C_{kl}^{-1}\right)B_{jn}\delta_{nl} = \partial_j\left(B_{ik}C_{kl}^{-1}\right)B_{jn}\left(C_{np}^{-1}C_{pm}^{\frac{1}{2}}C_{lm}^{\frac{1}{2}}\right) \tag{2.70}$$
$$= \partial_j \left(B_{ik}C_{kl}^{-1}C_{lm}^{\frac{1}{2}}\right)B_{jn}C_{np}^{-1}C_{pm}^{\frac{1}{2}} - B_{ik}C_{kl}^{-1}\partial_j\left(C_{lm}^{\frac{1}{2}}\right)B_{jn}C_{np}^{-1}C_{pm}^{\frac{1}{2}}.$$

Making use of relations (2.69, 2.70) gives the following form of the entire drift

$$\partial_j \left(A_{ij} + B_{ik}C_{kl}^{-1}B_{jl}\right) = \left(\partial_j\left(A_{ik}^{\frac{1}{2}}\right)A_{jk}^{\frac{1}{2}} + \partial_j\left(B_{ik}C_{kl}^{-1}C_{lm}^{\frac{1}{2}}\right)B_{jn}C_{np}^{-1}C_{pm}^{\frac{1}{2}}\right) \tag{2.71}$$
$$+ \left(A_{ik}^{\frac{1}{2}}\partial_j\left(A_{jk}^{\frac{1}{2}}\right) + B_{ik}C_{kl}^{-1}\partial_j\left(B_{jl}\right) - B_{ik}C_{kl}^{-1}\partial_j\left(C_{lm}^{\frac{1}{2}}\right)B_{jn}C_{np}^{-1}C_{pm}^{\frac{1}{2}}\right),$$

The first line of equation (2.71) is generated by the evaluation of the noise in the corrector step, and the second line will be approximated using RFD terms.

Both the implicit trapezoidal and explicit midpoint schemes have the following noise term in the corrector step,

$$x_i^{n+1} - x_i^n = \ldots + \sqrt{k_B T \Delta t}\left((1-w_7)A_{ik}^{\frac{1}{2},n} + w_7 A_{ik}^{\frac{1}{2},p}\right)\left(\sqrt{w_2}W_k^{n,1,x} + \sqrt{1-w_2}W_k^{n,2,x}\right)$$
$$+ \sqrt{k_B T \Delta t}\left((1-w_7)\left(B_{ik}C_{kl}^{-1}C_{lm}^{\frac{1}{2}}\right)^n + w_7\left(B_{ik}C_{kl}^{-1}C_{lm}^{\frac{1}{2}}\right)^p\right) \times \tag{2.72}$$
$$\left(\sqrt{w_2}W_m^{n,1,y} + \sqrt{1-w_2}W_m^{n,2,y}\right),$$

which after Taylor expanding operators evaluated at the predictor to $O\left(\sqrt{\Delta t}\right)$ and taking expectation with respect to $\boldsymbol{W}^x$ and $\boldsymbol{W}^y$, becomes

$$\langle x_i^{n+1} - x_i^n \rangle = \ldots + (2w_2 w_7)\,\Delta t\, k_B T\left(\partial_j\left(A_{ik}^{\frac{1}{2}}\right)A_{jk}^{\frac{1}{2}} + \partial_j\left(B_{ik}C_{kl}^{-1}C_{lm}^{\frac{1}{2}}\right)B_{jn}C_{np}^{-1}C_{pq}^{\frac{1}{2}}\right) + O\left(\Delta t^2\right). \tag{2.73}$$

The term on the right-hand side of (2.73) thus gives the first line of the drift (2.71) when $w_2 w_7 = 1/2$.

The RFD terms from both schemes give the following additional increment in $\boldsymbol{x}$,

$$x_i^{n+1} - x_i^n = \ldots + \frac{\Delta t\, k_B T}{\delta}A_{ik}^{\frac{1}{2}}\left(\boldsymbol{A}_{jk}^{\frac{1}{2}}(\boldsymbol{x}^n + \delta\widetilde{\boldsymbol{W}}) - A_{jk}^{\frac{1}{2}}(\boldsymbol{x}^n)\right)\widetilde{W}_j^A$$
$$+ \frac{\Delta t\, k_B T}{\delta}\left(B_{ik}C_{kl}^{-1}\right)^p\left(B_{kl}(\boldsymbol{x}^n + \delta\widetilde{\boldsymbol{W}}) - B_{kl}(\boldsymbol{x}^n)\right)\widetilde{W}_m^A, \tag{2.74}$$
$$- \frac{\Delta t\, k_B T}{\delta}\left(B_{ik}C_{kl}^{-1}\right)^p\left(C_{lm}^{\frac{1}{2}}\left(\boldsymbol{x}^n + \delta\boldsymbol{B}\boldsymbol{C}^{-1}\boldsymbol{C}^{\frac{1}{2}}\widetilde{\boldsymbol{W}}^C\right) - C_{lm}^{\frac{1}{2}}(\boldsymbol{x}^n)\right)\widetilde{W}_m^C \tag{2.75}$$

where all terms except for the RFD term have been omitted for this analysis. Expanding terms not evaluated at $\boldsymbol{x}^n$ to $O(\delta^2)$ in (2.74), and taking expectation with respect to $\widetilde{\boldsymbol{W}}^A$ and $\widetilde{\boldsymbol{W}}^C$ gives

$$\langle x_i^{n+1} - x_i^n \rangle = \ldots + \Delta t\,(k_B T)\left(A_{ik}^{\frac{1}{2}}\partial_j\left(A_{jk}^{\frac{1}{2}}\right) + B_{ik}C_{kl}^{-1}\partial_j\left(B_{jl}\right) - B_{ik}C_{kl}^{-1}\partial_j\left(C_{lm}^{\frac{1}{2}}\right)B_{jn}C_{np}^{-1}C_{pm}^{\frac{1}{2}}\right),$$

which corresponds to the drift term in the second line of equation (2.71). Together, the RFD terms in (2.74) and the noise terms in (2.72) create the entire stochastic drift from (2.45), demonstrating that our schemes are first order accurate for the fully nonlinear kinetic equations.

# Chapter 3

# Fluctuating Hydrodynamics

Fluctuating Hydrodynamics (FHD) accounts for stochastic effects arising at mesoscopic and macroscopic scales because of the discrete nature of fluids at microscopic scales [6, 50, 26]. In FHD, spatially-extended Langevin equations are constructed by including stochastic flux terms in the classical Navier-Stokes-Fourier equations of fluid dynamics and related conservation laws. It is widely appreciated that thermal fluctuations are important in flows at micro and nano scales; even more importantly, hydrodynamic fluctuations span the whole range of scales from the microscopic to the macroscopic and need to be consistently included in *all* levels of description [51, 52, 53, 23]. While the original formulation of fluctuating hydrodynamics was for compressible single-component fluids [6], the methodology can be extended to other systems such as fluid mixtures [26, 54, 33, 55], chemically reactive systems [56, 57, 58], magnetic materials [59], and others [27]. The structure of the equations of fluctuating hydrodynamics can be, to some extent, justified on the basis of the Mori-Zwanzig formalism [60, 8]. The basic idea is to add a *stochastic flux* corresponding to each dissipative (irreversible, diffusive) flux, leading to a continuum Langevin model that ensures detailed balance with respect to a suitable Einstein or Gibbs-Boltzmann equilibrium distribution [61].

After spatial discretization (truncation) of the stochastic partial differential equations (SPDEs) of FHD, one obtains a large-scale system of stochastic ordinary differential equations (SODEs) that has the familiar structure of Langevin equations common in statistical mechanics. The spatial discretization must be performed with specific attention to preserving fluctuation-dissipation balance (see Sections 3.2.2 and 3.3.2); alternatively, one can directly construct discrete Langevin equations with the proper structure from the underlying microscopic dynamics by using the theory of coarse-graining [7, 8].

This chapter is organized as follows. In section 3.1, we introduce the equations of fluctuating hydrodynamics and formulate a motivating example to which these schemes can be applied. section 3.2 discusses the fluctuating Burgers equation, which allows us to illustrate our methods without the complications introduced by the full fluctuating Navier-Stokes equation which we later consider in section 3.3. Both of these sections introduce the spatial discretizations used to formulate a system of SODEs from the continuum equations. Section 3.4 outlines specific versions of our schemes applied to a system of passive tracers advected by a fluctuating fluid, and in section 3.5, we numerically study the behavior of these temporal integration schemes applied to the fluctuating burgers equation and to diffusive mixing in a binary fluid. Finally, Section 3.6 gives some brief concluding remarks.

## 3.1  Equations of Fluctuating Hydrodynamics

The prototype stochastic partial differential equation (SPDE) of fluctuating hydrodynamics is the fluctuating Navier-Stokes equation. This equation approximates the dynamics of the velocity field $\boldsymbol{v}(\boldsymbol{r}, t)$ of a simple Newtonian fluid in the isothermal and incompressible approximation, $\boldsymbol{\nabla} \cdot \boldsymbol{v} = 0$,

$$\rho \left( \partial_t \boldsymbol{v} + \boldsymbol{v} \cdot \boldsymbol{\nabla} \boldsymbol{v} \right) = -\boldsymbol{\nabla} \pi + \eta \boldsymbol{\nabla}^2 \boldsymbol{v} + \boldsymbol{\nabla} \cdot \left[ \left( 2 k_B T \eta \right)^{1/2} \boldsymbol{\mathcal{W}} \right] + \boldsymbol{f} \tag{3.1}$$

where $\pi$ is the non-thermodynamic pressure, $\rho$ is the (constant) density, $\eta = \rho \nu$ is the (constant) shear viscosity and $\nu$ is the kinematic viscosity, and $\boldsymbol{f}(\boldsymbol{r}, t)$ is an additional force density such as gravity [26]. Note that here we use the standard physics notation instead of the differential notation more common in the mathematics literature, since the noise is additive and there is no difference between the different interpretation of stochastic integrals (e.g., Ito vs. Stratonovich). In the momentum conservation law (3.1), the stochastic momentum flux is modeled using a white-noise random Gaussian tensor field $\boldsymbol{\mathcal{W}}(\boldsymbol{r}, t)$, that is, a tensor field whose components are independent

(space-time) white noise processes,

$$\langle \mathcal{W}_{ij}(\boldsymbol{r}, t) \mathcal{W}_{kl}(\boldsymbol{r}', t')\rangle = (\delta_{ik}\delta_{jl})\,\delta(t - t')\delta(\boldsymbol{r} - \boldsymbol{r}').$$

Note that in principle the stochastic momentum flux should have the symmetrized form

$$(k_B T \eta)^{1/2}\left(\boldsymbol{\mathcal{W}} + \boldsymbol{\mathcal{W}}^T\right),$$

however, for incompressible flow with constant viscosity this is not necessary [39].

The fluctuating Navier-Stokes equation, like other augmented Langevin equations of interest [35], obeys a fluctuation-dissipation principle, as we discussed in Section 2.1. Specifically, (3.1) is constructed so that, at thermodynamic equilibrium, the invariant measure or equilibrium distribution for the fluctuating velocities with periodic boundaries is the Gibbs-Boltzmann distribution with a coarse-grained free energy or Hamiltonian given by the kinetic energy of the fluid, formally

$$P_{\text{eq}}\left(\boldsymbol{v}\right) = Z^{-1}\exp\left[-\frac{\int d\boldsymbol{r}\,\rho v^2}{2k_B T}\right]\boldsymbol{\delta}\left(\int d\boldsymbol{r}\,\rho\boldsymbol{v}\right)\delta\left(\boldsymbol{\nabla}\cdot\boldsymbol{v}\right).$$

This is ensured by constructing the stochastic forcing term so that its covariance is proportional to the viscous dissipation operator $\eta\boldsymbol{\nabla}^2$. The advective operator $(\boldsymbol{v}\cdot\boldsymbol{\nabla})$, is, at least formally, Hamiltonian [62] in nature, which means that it preserves the equilibrium distribution dictated by the competition between the dissipative and the stochastic forcing terms. These well-known observations about the structure of the continuum equations should guide the construction of spatio-temporal discretizations [63].

We have formally written equation (3.1) as an infinite dimensional stochastic differential equation. However, the interpretation of the nonlinear term $\boldsymbol{v}\cdot\boldsymbol{\nabla}\boldsymbol{v}$ requires giving a precise meaning to products of distributions, which cannot be defined in general and requires introducing some sort of regularization. An alternative is to define a discrete hydrodynamic field directly via some form of averaging of the molecular configuration of the fluid, and to obtain directly a finite-dimensional system of stochastic *ordinary* differential equations (SODEs) for the discrete variables through the Mori-Zwanzig formalism [8, 7, 64]. While such an approach has certain advantages from a coarse-graining perspective, the notion of a continuum equation and the applicability of traditional methods for computational fluid dynamics is lost or at least obscured.

Here we adopt a middle ground between the "continuum" and the "discrete" approach to fluctuating hydrodynamics. Specifically, we first spatially discretize the SPDE to obtain a system of SODEs, in the spirit of the "method of lines". Our focus here is on the temporal integrators for the resulting system of SODEs. We do *not* consider the convergence of the numerical method as the spatial discretization is refined, as one would in deterministic fluid dynamics. Rather, we fix the spatial discretization and assume that the hydrodynamic cells are sufficiently large, specifically, that they contain, on average, sufficiently many fluid molecules $N_p \gg 1$. This ensures that the equilibrium fluctuations will be on the order of $O(N_p^{-1/2})$ relative to macroscopic fields. We also assume that the transport coefficients have been *renormalized* to account for the finite number of fluid particles (molecules) used to define the hydrodynamic fields [65, 66]. There is strong numerical evidence that under these conditions spatio-temporal discretizations can correctly capture the leading-order (measurable) effects of fluctuations at large scales, such as fluctuation-driven transport in non-equilibrium systems [66], large-scale inhomogeneities arising during free fluid mixing [39], and diffusive effects on the very long-time dynamics such as drifts in propagating fronts [67] and shocks .

### 3.1.1 Diffusion of particles suspended in a fluctuating fluid

As a motivating example of a fluctuating hydrodynamic system of equations to which our methods will be applied, we study a model of diffusion of tagged (labeled) molecules in a liquid or of colloidal particles suspended in a fluid. A detailed mesoscopic model for diffusion in liquids has been described by some of us in previous work [23, 24]; here we only summarize some key points to give a specific setting for the discussion to follow. The hydrodynamic fluctuations of the fluid velocity $\boldsymbol{v}(\boldsymbol{r}, t)$ will be modeled via the incompressible fluctuating Navier-Stokes equation, $\boldsymbol{\nabla}\cdot\boldsymbol{v} = 0$, and

$$\rho\left(\partial_t \boldsymbol{v} + \boldsymbol{v}\cdot\boldsymbol{\nabla}\boldsymbol{v}\right) + \boldsymbol{\nabla}\pi = \eta\boldsymbol{\nabla}^2\boldsymbol{v} + \boldsymbol{\nabla}\cdot\left(\sqrt{2\eta k_B T}\,\boldsymbol{\mathcal{W}}\right) - \beta\rho c\,\boldsymbol{g}, \tag{3.2}$$

and appropriate boundary conditions. The last term in this equation models the effects of gravity using a Boussinesq constant density approximation, with $\boldsymbol{g}$ being the gravitational acceleration, and $\beta$ the solutal expansion coefficient. The concentration of diffusing particles is given by the mass fraction $c\left(\boldsymbol{r}, t\right) = (m/\rho)\,n\left(\boldsymbol{r}, t\right)$, where $n$ is the number

density and $m$ is the mass of the tracer particles. Note that because the noise is additive in (3.2) there is no difference between an Ito and a Stratonovich interpretation of the stochastic term. For technical reasons, in this work we will drop the nonlinear advective term $\boldsymbol{v} \cdot \boldsymbol{\nabla} \boldsymbol{v}$ and consider the time-dependent fluctuating Stokes equation; this is a good approximation since this term only plays an important role at very large scales.

For our purposes, we will model the evolution of the concentration $c\left(\boldsymbol{r}, t\right)$ via a fluctuating advection-diffusion Ito equation [68, 24],

$$\partial_t c + \boldsymbol{u} \cdot \boldsymbol{\nabla} c = \chi_0 \boldsymbol{\nabla}^2 c + \boldsymbol{\nabla} \cdot \left( \sqrt{2\chi_0 \rho^{-1} mc} \, \boldsymbol{\mathcal{W}}_c \right), \tag{3.3}$$

where $\boldsymbol{\mathcal{W}}_c\left(\boldsymbol{r}, t\right)$ denotes a white-noise vector field. Here $\chi_0$ is a *bare* or *molecular* diffusion coefficient, and the concentration is advected by the random field

$$\boldsymbol{u}\left(\boldsymbol{r}, t\right) = \int \boldsymbol{\sigma}\left(\boldsymbol{r}, \boldsymbol{r}'\right) \boldsymbol{v}\left(\boldsymbol{r}', t\right) d\boldsymbol{r}' \equiv \boldsymbol{\sigma} \star \boldsymbol{v}, \tag{3.4}$$

where $\boldsymbol{\sigma}$ is a smoothing kernel that filters out features at scales below a microscopic (molecular) scale $\sigma$, and $\star$ denotes convolution. It is important here that $\boldsymbol{u}$ is also divergence-free, $\boldsymbol{\nabla} \cdot \boldsymbol{u} = 0$. Formally, one often writes the advective term in (3.3) as $\boldsymbol{v} \cdot \boldsymbol{\nabla} c$ (this corresponds to $\boldsymbol{\sigma}\left(\boldsymbol{r}, \boldsymbol{r}'\right) = \delta\left(\boldsymbol{r} - \boldsymbol{r}'\right)$) but this only makes sense if one truncates the velocity equation (3.2) at some ultraviolet cutoff wave number $k_{\max} \sim \sigma^{-1}$; this kind of implicit smoothing kernel is applied by the finite-volume spatial discretization we employ (see Section 3.3.2), with the grid spacing playing the role of $\sigma$. Additional filtering may also be implemented in the finite-volume schemes, as described in Appendix B in [54]. The system of equations (3.2,3.3) is a useful model, for example, for the study of giant concentration fluctuations in low-density polymer [53, 69] or nanocolloidal suspensions [70], or in binary fluid mixtures in the presence of a modest temperature gradient [71, 72].

It can be shown that the coupled velocity-concentration system (3.2,3.3) can formally be written as an infinite-dimensional system of the form (2.1) with a physically-sensible coarse-grained energy *functional*

$$U\left[\boldsymbol{v}\left(\cdot\right), c\left(\cdot\right)\right] = \frac{\rho}{2} \int v^2\left(\boldsymbol{r}\right) d\boldsymbol{r} + \beta\rho \int c\left(\boldsymbol{r}\right)\left(\boldsymbol{r} \cdot \boldsymbol{g}\right) d\boldsymbol{r} + \left(k_B T\right) \int n\left(\boldsymbol{r}\right)\left(\ln\left(\Lambda^3 n\left(\boldsymbol{r}\right)\right) - 1\right) d\boldsymbol{r}, \tag{3.5}$$

where $n = \rho c / m$ is the number density of the diffusing particles, and $\Lambda$ is a fixed length-scale (e.g., the thermal de Broglie wavelength). A specific form of the mobility *operator* can also be written (see Section 3.3.2) for the advective terms and Ref. [24] for the diffusive and stochastic terms. Numerical methods for integrating systems such as (3.2,3.3) have been discussed in Refs. [39, 54]. In particular, after spatial discretization of the system of SPDEs (3.2,3.3) one obtains a system of SODEs of the generic Langevin form (2.1). We note that the last term in (3.5), which contains the free energy density of an ideal gas with number density $c\left(\boldsymbol{r}\right)$, is quite formal and poses notable mathematical (and numerical) difficulties [24]. In this work we will make a Gaussian approximation and use instead the Gaussian free energy $k_B T / \left(2\vartheta_0\right) \int c^2 d\boldsymbol{r}$, where $\vartheta_0 = \rho^{-1} mc_0$ and $c_0$ is the average concentration; this change simplifies the mobility to a constant matrix and the noise term in (3.3) becomes additive, $\boldsymbol{\nabla} \cdot \left(\sqrt{2\chi_0 \vartheta_0} \, \boldsymbol{\mathcal{W}}_c\right)$, see Sections 3.4 and **3.3**.

In practice, the physical properties of the fluid, notably, the viscosity and the diffusion coefficient, depend on the concentration. This is crucial, for example, to model experiments on the development of giant concentration fluctuations during the diffusive mixing of water and glycerol [73], since the viscosity and diffusion coefficient (by virtue of the Stokes-Einstein relation) depend very strongly on the concentration. Assuming that the density changes only weakly with concentration we can use a Boussinesq approximation. This approximation essentially amounts to assuming that the two fluid components have very similar density so that the fluid density $\rho$ can be considered constant; for a generalization that accounts for the fact that density depends on concentration see the low Mach number formulation in [54]. The fluctuating hydrodynamic equations in the case of variable transport coefficients can formally be written as

$$\begin{aligned}
\rho\left(\partial_t \boldsymbol{v} + \boldsymbol{v} \cdot \boldsymbol{\nabla} \boldsymbol{v}\right) + \boldsymbol{\nabla}\pi &= \boldsymbol{\nabla} \cdot \left(\eta\left(c\right) \bar{\boldsymbol{\nabla}} \boldsymbol{v} + \sqrt{2\eta\left(c\right) k_B T} \, \boldsymbol{\mathcal{W}}\right) - \beta\rho c \, \boldsymbol{g} \\
\partial_t c + \boldsymbol{v} \cdot \boldsymbol{\nabla} c &= \boldsymbol{\nabla} \cdot \left(\chi\left(c\right) \boldsymbol{\nabla} c + \sqrt{2k_B T \rho^{-1} \chi\left(c\right) \mu_c^{-1}\left(c\right)} \, \boldsymbol{\mathcal{W}}_c\right),
\end{aligned} \tag{3.6}$$

where in general the specified temperature $T\left(\boldsymbol{r}, t\right)$ may depend on position and time. Here $\bar{\boldsymbol{\nabla}} = \boldsymbol{\nabla} + \boldsymbol{\nabla}^T$ and $\mu_c = \partial\mu / \partial c$ is the derivative of the chemical potential of the binary mixture [54]. We have omitted stochastic or thermal drift terms since these are poorly understood (in fact, mathematically they are ill-defined) and not important in the linearized dynamics. Note that in the linearized equation there is no distinction between the bare and the effective diffusion coefficient, so $\chi(c)$ denotes the macroscopic diffusion coefficient of the ensemble-averaged

concentration [23, 24]. Similarly, in the linearized equations the nonlinear advective terms become a sum of linear terms, and therefore in (3.6) we can write $\boldsymbol{v} \cdot \boldsymbol{\nabla} c$ instead of $\boldsymbol{u} \cdot \boldsymbol{\nabla} c$ and still give a precise meaning to the linearized equations.

### 3.1.1.1 Overdamped Limit

One of the key difficulties in directly integrating the system (3.2,3.3) is the fact that in liquids momentum diffuses much more rapidly than does mass, i.e., the dynamics of the velocity is much faster than that of concentration. We used this fact in [23] to eliminate the fast velocity adiabatically (see Appendix A in [23] for technical details) and obtained a limiting or overdamped equation for the concentration that takes the form of a Stratonovich SPDE,

$$\partial_t c = -\boldsymbol{w} \odot \boldsymbol{\nabla} c + \beta \rho \eta^{-1} \left( \boldsymbol{G}_\sigma \star c \boldsymbol{g} \right) \cdot \boldsymbol{\nabla} c + \chi_0 \boldsymbol{\nabla}^2 c + \boldsymbol{\nabla} \cdot \left( \sqrt{2\chi_0 \rho^{-1} m\, c}\, \boldsymbol{\mathcal{W}}_c \right), \tag{3.7}$$

where $\odot$ denotes a Stratonovich dot product, and the advection velocity $\boldsymbol{w}\left(\boldsymbol{r}, t\right)$ is white in time, with covariance proportional to a Green-Kubo integral of the velocity auto-correlation function,

$$\langle \boldsymbol{w}\left(\boldsymbol{r}, t\right) \otimes \boldsymbol{w}\left(\boldsymbol{r}', t'\right) \rangle = 2\delta\left(t - t'\right) \int_0^\infty \langle \boldsymbol{u}\left(\boldsymbol{r}, t\right) \otimes \boldsymbol{u}\left(\boldsymbol{r}', t + t''\right) \rangle\, dt'' = \tag{3.8}$$

$$= \frac{2k_B T}{\eta} \delta\left(t - t'\right) \int \boldsymbol{\sigma}\left(\boldsymbol{r}, \boldsymbol{r}''\right) \boldsymbol{G}\left(\boldsymbol{r}'', \boldsymbol{r}'''\right) \boldsymbol{\sigma}^T\left(\boldsymbol{r}', \boldsymbol{r}'''\right) d\boldsymbol{r}'' d\boldsymbol{r}'''. \tag{3.9}$$

Here $\boldsymbol{G}$ denotes the Green's function for Stokes flow, and $\boldsymbol{G}_\sigma$ denotes $\boldsymbol{G}$ regularized by the smoothing kernel $\boldsymbol{\sigma}$; more explicitly, $\boldsymbol{G}_\sigma \star \boldsymbol{f}$ is a shorthand notation for the smoothed solution of the Stokes equation with unit viscosity: $\boldsymbol{w}_\sigma = \boldsymbol{G}_\sigma \star \boldsymbol{f}$ if $\boldsymbol{w}_\sigma = \boldsymbol{\sigma} \star \boldsymbol{w}$ and $\boldsymbol{w} = \boldsymbol{G} \star \boldsymbol{f}$ solves

$$\boldsymbol{\nabla} \pi = \boldsymbol{\nabla}^2 \boldsymbol{w} + \boldsymbol{f}, \qquad \boldsymbol{\nabla} \cdot \boldsymbol{w} = 0, \tag{3.10}$$

along with appropriate boundary conditions.

In this chapter we will describe an algorithm that can be used to integrate the overdamped limit (3.7) with a time step size several orders of magnitude larger than the time step size required to integrate the original inertial dynamics (3.2,3.3). The spatial discretization will be the same as for the original system and only the temporal integrator will change. We first described such a temporal integrator that *automatically* performs adiabatic mode elimination *without* directly discretizing or even writing the limiting dynamics in Appendix B of [23]. Here we generalize this to a broad class of systems of Langevin SDEs that contain a fast and a slow variable.

### 3.1.1.2 Linearized Fluctuating Hydrodynamics

At microscopic scales, the nonlinearity and Stratonovich nature of the advective term $\boldsymbol{w} \odot \boldsymbol{\nabla} c$ in (3.7) is crucial. This advection by the rapidly fluctuating random velocity field contributes to the effective diffusion, similar to eddy diffusivity in turbulent flows. In particular, the ensemble averaged concentration $\bar{c}\left(\boldsymbol{r}, t\right) = \langle c\left(\boldsymbol{r}, t\right) \rangle$ is described by Fick's macroscopic law with a renormalized diffusion coefficient

$$\partial_t \bar{c} = \boldsymbol{\nabla} \cdot \left[\left(\chi_0 + \boldsymbol{\chi}\right) \boldsymbol{\nabla} \bar{c}\right] = \boldsymbol{\nabla} \cdot \left(\boldsymbol{\chi}_{\text{eff}} \boldsymbol{\nabla} \bar{c}\right), \tag{3.11}$$

where the fluctuation-induced diffusion tensor $\boldsymbol{\chi}\left(\boldsymbol{r}\right)$ is given by a Green-Kubo formula and follows a Stokes-Einstein relation [23]. This enhancement of the diffusion coefficient is mathematically a stochastic drift term that comes from the divergence of the mobility operator (last term in (2.1)) when one writes (3.7) in the Ito formulation [23]. Our temporal integrators will capture this term using a predictor-corrector algorithm, without explicitly evaluating derivatives.

At mesoscopic length-scales $\delta \gg \sigma$ much larger than the molecular, in three dimensions, one expects that the fluctuations in $c_\delta = \bar{c} + \delta c$, where $\bar{c} = \langle c \rangle$ is the solution of the *deterministic* Fick's law (3.11), are small and approximately Gaussian (this is a form of a law of large numbers and a central limit theorem for the fluctuations). In particular, a widely-used model for the fluctuations in the concentration at such scales is *linearized fluctuating hydrodynamics* [26] (LFH). In LFH, one first solves the macroscopic *deterministic* hydrodynamic equations first, and then linearizes the formal nonlinear fluctuating hydrodynamic equations to leading order in the fluctuations. If we assume that there is no macroscopic convective motion of the fluid, so that the solution of the deterministic

Navier-Stokes equation $\bar{\boldsymbol{v}} = 0$ and $\delta\boldsymbol{v} \equiv \boldsymbol{v}$, the LFH equations become

$$\partial_t \bar{c} = \chi_{\text{eff}}\boldsymbol{\nabla}^2 \bar{c}$$

$$\partial_t (\delta c) = -\boldsymbol{v} \cdot \boldsymbol{\nabla}\bar{c} + \chi_{\text{eff}}\boldsymbol{\nabla}^2 (\delta c) + \boldsymbol{\nabla} \cdot \left( \sqrt{2\chi_{\text{eff}}\rho^{-1}m\,\bar{c}}\,\boldsymbol{\mathcal{W}}_c \right) \quad (3.12)$$

$$\rho\partial_t \boldsymbol{v} + \boldsymbol{\nabla}\pi = \eta\boldsymbol{\nabla}^2\boldsymbol{v} + \boldsymbol{\nabla} \cdot \left( \sqrt{2\eta k_B T}\,\boldsymbol{\mathcal{W}} \right) - \beta\rho (\delta c)\,\boldsymbol{g}.$$

In chapter 3, we describe how to numerically solve these types of linearized Langevin equations *without* solving the deterministic equations first and then explicitly linearizing around them. Specifically, we will construct temporal integrators that perform the linearization *numerically.*

Note that in cases when there is a large separation of time scales between the velocity and the concentration one may perform adiabatic elimination of the velocity; in the linearized setting this simply amounts to dropping the inertial term $\rho\partial_t \boldsymbol{v}$ and switching to the time-independent Stokes equation for the velocity. Formally, the linearized limiting or overdamped equation is

$$\begin{aligned} \partial_t \bar{c} &= \chi_{\text{eff}}\boldsymbol{\nabla}^2 \bar{c} \quad &(3.13) \\ \partial_t (\delta c) &= \beta\rho\eta^{-1} (\boldsymbol{G} \star (\delta c)\,\boldsymbol{g}) \cdot \boldsymbol{\nabla}\bar{c} + \left( \boldsymbol{G}_{\frac{1}{2}}\sqrt{2\eta^{-1}k_B T}\,\boldsymbol{\mathcal{W}} \right) \cdot \boldsymbol{\nabla}\bar{c} \\ &+ \chi_{\text{eff}}\boldsymbol{\nabla}^2 (\delta c) + \boldsymbol{\nabla} \cdot \left( \sqrt{2\chi_{\text{eff}}\rho^{-1}m\,\bar{c}}\,\boldsymbol{\mathcal{W}}_c \right), \end{aligned}$$

where $\boldsymbol{G}$ is the Green's function for steady Stokes flow and $\boldsymbol{G}_{\frac{1}{2}}$ symbolically denotes that the covariance of the additive-noise term $\boldsymbol{G}_{\frac{1}{2}}\boldsymbol{\mathcal{W}}$ is $\boldsymbol{G}$.

In this chapter we will describe several semi-implicit predictor-corrector temporal integrators that allow one to numerically linearize and then integrate, with second-order weak accuracy, the linearization (3.12) around the *time-dependent* solution of the *nonlinear* deterministic equations. We will also construct a *single* unified numerical method that can be used to integrate either the nonlinear (3.7) (microscopic scales, large noise) or the linearized (3.13) (mesoscopic scales, weak noise) overdamped equations. Which equation is appropriate depends sensitively on the spatial scale of interest, specifically, on the range of wavenumbers whose dynamics needs to be captured accurately.

In this work we will develop temporal integrators suitable also for the more general variable-coefficient equations (3.6). Since our temporal integrators will work with the original equations but in the end simulate the correct overdamped or linearized dynamics, we will never need to explicitly write down the (more complex) overdamped limit or the linearized system. We simply let the numerical method do that for us.

## 3.2 Fluctuating Burgers Equation

The analysis and numerical solution of the incompressible Navier-Stokes equation is complicated by the presence of the incompressibility constraint. We begin our discussion by constructing a spatial discretization of the simpler unconstrained *fluctuating Burgers equation* for the random field $u(x,t)$,

$$\partial_t u + c u\,\partial_x u = \nu\,\partial_{xx}^2 u + (2\nu)^{\frac{1}{2}}\,\partial_x \mathcal{Z}, \quad (3.14)$$

where $\nu$ is a diffusion coefficient and $c$ sets the scale for the advection speed. This equation mimics some of the properties of the fluctuating Navier-Stokes equation (3.1), in particular, it obeys a fluctuation-dissipation balance principle with respect to the Gibbs-Boltzmann distribution with a Hamiltonian $H = \int dx\,u^2/2$. The fluctuating Burgers equation can also be written in conservative form

$$\partial_t u = -\partial_x \left[ c\frac{u^2}{2} - \nu\partial_x u - (2\nu)^{\frac{1}{2}}\,\mathcal{Z} \right],$$

showing that the total momentum $\int u\,dx$ is conserved with periodic boundary conditions. Note that here the stochastic forcing term is linear and involves the spatial derivative of white noise [74], rather than white noise itself as in the stochastic Burgers equation studied, for example, in Ref. [75]. Equations of this type arise as coarse-grained models of the behavior of one dimensional lattice gases, such as the asymmetric excluded random walk model [74].

In this section we show how the fluctuating Burgers equation can be spatially discretized in a manner that leads to a generic Langevin equation of the form (2.1). This construction will be extended to the Navier-Stokes equations

with a passively-advected scalar in Section 3.3. Our approach to the spatial discretization follows standard practice in deterministic fluid dynamics. Specifically, we construct the spatially-discrete system by combining locally-accurate spatial discretizations of the differential operators (e.g., gradient, divergence and Laplacian) that appear in the the SPDE. However, in addition to focusing on accuracy and stability when choosing the spatial discretization, we pay particular attention to preserving *fluctuation-dissipation balance*. This means that we want to obtain a system of SODEs whose structure is given in (2.1) and whose invariant distribution (equilibrium distribution) is a natural discretization of the Gibbs distribution dictated by equilibrium statistical mechanics.

### 3.2.1 Continuum Fluctuating Burgers Equation

One can, at least formally, consider a generic Langevin equation for an infinite dimensional field [61]. The fluctuating Burgers equation (3.14) is a prototype of such an equation. In this formalism the coarse-grained Hamiltonian is a functional of the field and the partial derivatives should be interpreted as functional derivatives, and contractions by a field imply integrations over the spatial domain. For equation (3.14), the (formal) free energy functional is

$$H\left[u\left(x,t\right)\right] = \int \frac{u^2}{2} dx, \tag{3.15}$$

so that

$$\frac{\partial H}{\partial u} \equiv \frac{\delta H\left[u\left(x,t\right)\right]}{\delta u} = u.$$

The dissipative and fluctuating dynamics in (3.14) are generated by the constant operators,

$$\boldsymbol{M} = -\nu\partial_{xx}^2 \text{ and } \boldsymbol{B} = \nu^{\frac{1}{2}}\partial_x,$$

which in higher dimensions become multiples of the Laplacian and divergence operators, respectively. The conservative dynamics for the Burgers equation is Hamiltonian and generated by the skew-adjoint linear operator $\boldsymbol{S}\left(u\right)$ defined through its action on a field $w\left(x,t\right)$ [62],

$$\boldsymbol{S}\left(u\right)w = -\frac{c}{3}\left[u\partial_x w + \partial_x\left(uw\right)\right]. \tag{3.16}$$

The $\boldsymbol{v}\cdot\boldsymbol{\nabla}\boldsymbol{v}$ term in the higher-dimensional fluctuating Navier-Stokes equation (3.1) can similarly be written in terms of a skew-adjoint operator, although there are some complications in handling the divergence-free constraint [76].

A detailed description of the meaning and importance of the Hamiltonian nature of the nonlinear deterministic dynamics and the Poisson bracket associated with $\boldsymbol{S}$ is given in Refs. [62, 61]. For our purposes, the most important property of Hamiltonian dynamics is that it is incompressible in phase space,

$$\frac{\partial}{\partial u} \cdot \boldsymbol{S}\left(u\right) = \frac{\partial}{\partial u} \cdot \boldsymbol{N}^{\star}\left(u\right) = \boldsymbol{0}. \tag{3.17}$$

This implies that the dynamics of the inviscid Burgers equation preserves not just functions (such as the Hamiltonian itself) but also phase-space measures (such as the Gibbs distribution), and thus any probability density that is a function of $H$ only is a candidate equilibrium distribution. The inviscid Burgers equation may also be written in Hamiltonian form using the Hamiltonian $H = \int \left(u^3/6\right)dx$ with $\boldsymbol{S} = -\partial_x$ [62, 77]. However, in fluctuating hydrodynamics the choice of the coarse-grained Hamiltonian is dictated by statistical mechanics and the equilibrium Gibbs distribution is maintained via the fluctuation-dissipation balance between the viscous and stochastic terms.

### 3.2.2 Discrete Fluctuating Burgers Equation

The preceding discussion of how the fluctuating Burgers equation can be written in the form of a generic Langevin equation (2.1) is formal and merely informs our choice of spatial discretization. The discretized $\boldsymbol{u} = \{u_1, \ldots, u_N\}$ can be thought of as a finite-volume representation of the field $u(x,t)$ on a regular grid with spacing $\Delta x$, specifically, $u_j$ can be thought of as representing the average value of $u(x,t)$ over the interval (cell) $[j\Delta x, (j+1)\Delta x]$. As we already discussed, this is merely a formal association and the actual physical object is the discrete (coarse-grained) $\boldsymbol{u}\left(t\right)$ and not the hypothetical $u(x,t)$. Similarly, the spatially-discretized collection of white noise processes $(\Delta x)^{-1/2}\,\boldsymbol{\mathcal{W}}$ can formally be associated with the space-time white noise $\boldsymbol{\mathcal{Z}}$.

We take the coarse-grained Hamiltonian function to be the natural (local equilibrium [7]) discretization of (3.15),

$$H\left(\boldsymbol{u}\right) = \sum_{j=1}^{N} \frac{\Delta x}{2} u_j^2, \tag{3.18}$$

We will construct a spatial discretization that leads to a finite-dimensional generic Langevin equation of the form (2.1)

$$\partial_t \boldsymbol{u} = \boldsymbol{S}\frac{\partial H}{\partial \boldsymbol{u}} + \frac{\nu}{\Delta x}\boldsymbol{D}_2\frac{\partial H}{\partial \boldsymbol{u}} + \left(\frac{2\nu}{\Delta x}\right)^{1/2}\boldsymbol{D}_1\boldsymbol{\mathcal{W}}(t). \tag{3.19}$$

Here $\boldsymbol{\mathcal{W}}$ is a vector of $N_w$ independent white-noise processes (formally, time derivatives of independent Wiener processes), $\boldsymbol{D}_1$ is a matrix representing the spatial discretization of the divergence operator, such that $\boldsymbol{D}_2 = -\boldsymbol{D}_1\boldsymbol{D}_1^\star$ is a symmetric negative-semidefinite discretization of the Laplacian operator. This system of SODEs has as an invariant distribution the Gibbs distribution (2.3) if $\boldsymbol{S}$ is an antisymmetric matrix discretizing (3.16) that satisfies

$$\left[\frac{\partial}{\partial \boldsymbol{u}}\cdot\boldsymbol{S}\left(\boldsymbol{u}\right)\right]_k = \sum_j \frac{\partial S_{j,k}}{\partial u_j} = 0 \text{ for all } k. \tag{3.20}$$

We now construct specific finite-difference operators for $\boldsymbol{D}_1$ and $\boldsymbol{S}$.

A particularly simple choice that also generalizes to higher dimensions [42] is to associate fluxes with the half-grid points (faces of the grid in higher dimensions), and to define

$$(\boldsymbol{D}_1\boldsymbol{\mathcal{W}})_j = \frac{\mathcal{W}_{j+\frac{1}{2}} - \mathcal{W}_{j-\frac{1}{2}}}{\Delta x}, \text{ giving } (\boldsymbol{D}_1^\star\boldsymbol{u})_{j+\frac{1}{2}} = -\frac{u_{j+1} - u_j}{\Delta x}.$$

This construction gives the familiar three-point discrete Laplacian ($2d+1$ points in dimension $d$),

$$(\boldsymbol{D}_2\boldsymbol{u})_j = \frac{u_{j-1} - 2u_j + u_{j+1}}{\Delta x^2}, \tag{3.21}$$

and is therefore an attractive choice that satisfies the discrete fluctuation-dissipation principle [42]. If periodic boundary conditions are imposed, we set $u_0 = u_N$ and $u_{N+1} = u_1$ and $\mathcal{W}_{\frac{1}{2}} = \mathcal{W}_{N+\frac{1}{2}}$ (i.e., $N_w = N$). For Dirichlet boundary conditions we fix $u_0$ and $u_{N+1}$ at specified values and do not need to impose any boundary conditions on $\mathcal{W}$ (i.e., $N_w = N+1$).

A natural choice for $\boldsymbol{S}$ is formed by choosing a skew-adjoint discretization $\widetilde{\boldsymbol{D}}_1 = -\widetilde{\boldsymbol{D}}_1^\star$ of $\partial_x$, in general different from $\boldsymbol{D}_1$, and discretizing (3.16) directly as

$$(\boldsymbol{Su})_j = -\frac{c}{3}\left[u_j\left(\widetilde{\boldsymbol{D}}_1 u\right)_j - \left(\widetilde{\boldsymbol{D}}_1^\star u^2\right)_j\right] = -\frac{c}{3}\left[u_j\left(\widetilde{\boldsymbol{D}}_1 u\right)_j + \left(\widetilde{\boldsymbol{D}}_1 u^2\right)_j\right],$$

where $u^2 = \{u_1^2, \ldots, u_N^2\}$. We choose $\widetilde{\boldsymbol{D}}_1$ to be the second-order centered difference operator

$$\left(\widetilde{\boldsymbol{D}}_1 u\right)_j = \frac{u_{j+1} - u_{j-1}}{2\Delta x},$$

leading to an explicit expression that makes it clear that $\boldsymbol{Su}$ is a discretization of $-cuu_x$,

$$(\boldsymbol{Su})_j = -\frac{c}{3}\left[u_j\left(\frac{u_{j+1} - u_{j-1}}{2\Delta x}\right) + \frac{u_{j+1}^2 - u_{j-1}^2}{2\Delta x}\right] = -c\left(\frac{u_{j-1} + u_j + u_{j+1}}{3}\right)\left(\frac{u_{j+1} - u_{j-1}}{2\Delta x}\right).$$

The above discretization of the advective term has been considered frequently in the literature, as discussed in detail in Ref. [77]. It can be seen as a weighted combination of the "convective" and the "conservative" forms of advection [78] with weights $1/3$ and $2/3$, which is the unique choice of weights that gives a conservative and skew-adjoint discretization of advection. It is important to note that one can write the nonlinear term in conservative form,

$$(\boldsymbol{Su})_j = -\frac{c}{2}\left(\frac{u_{j+\frac{1}{2}}^2 - u_{j-\frac{1}{2}}^2}{\Delta x}\right), \text{ where } u_{j+\frac{1}{2}}^2 = \frac{u_j^2 + u_j u_{j+1} + u_{j+1}^2}{3}. \tag{3.22}$$

Due to the skew-symmetry, in the absence of viscosity the total "energy" (3.18) is conserved for periodic systems. It can also easily be shown that that the condition (3.17) is satisfied and therefore this particular discretization of the advective term preserves the Hamiltonian structure of the equations [77].

Putting the pieces together we can write the semi-discrete fluctuating Burgers equation as a system of SODEs, $j = 1, \ldots, N$,

$$\begin{aligned}\frac{du_j}{dt} &= -\frac{c}{6\Delta x}\left(u_{j-1} + u_j + u_{j+1}\right)\left(u_{j+1} - u_{j-1}\right) \\ &\quad + \frac{\nu}{\Delta x^2}\left(u_{j-1} - 2u_j + u_{j+1}\right) + \frac{(2\nu)^{1/2}}{\Delta x^{3/2}}\left(\mathcal{W}_{j+\frac{1}{2}}(t) - \mathcal{W}_{j-\frac{1}{2}}(t)\right).\end{aligned} \tag{3.23}$$

34

With periodic boundary conditions, this stochastic method of lines [79] discretization strictly conserves the total energy (3.18) and the total momentum

$$m(\boldsymbol{u}) = \sum_{j=1}^{N} \Delta x \, u_j.$$

The equilibrium distribution is the discrete Gibbs-Boltzmann distribution

$$P_{\text{eq}}(\boldsymbol{u}) = Z^{-1} \exp\left[ -\frac{\Delta x}{2} \sum_{j=1}^{N} u_j^2 \right] \delta\left( \Delta x \sum_{j=1}^{N} u_j - m_0 \right),$$

where $m_0$ is the initial value for the total momentum. In the next section, we construct efficient temporal discretizations of (3.23) that preserve these properties as well as possible.

## 3.3 Fluctuating Navier-Stokes Equation

The implicit-explicit schemes discussed in Section 2.2 are general schemes suitable for unconstrained SDEs and cannot directly be applied to the fluctuating Navier-Stokes equation (3.1). Some care is required in handling the incompressibility constraint in a computationally-efficient manner without compromising the stochastic accuracy. The spatio-temporal discretization we analyze here was proposed and applied in Ref. [39]; here we provide additional analysis and a discussion of alternative approaches. The equations in this section are primarily of academic interest, allowing us to test the behavior of our numerical schemes on the nonlinear equations in the presence of large magnitude additive noise. In practice, the noise is weak at the length scales of observation, and we are better served by considering the linearized approximation to the equations. This will be addressed further in Section 3.4.

### 3.3.1 Continuum Equations

In principle, the incompressibility constraint can be most easily handled by using a projection operator formalism to eliminate pressure from (3.1) and write the fluctuating Navier-Stokes equation in the form

$$\partial_t \boldsymbol{v} = \boldsymbol{\mathcal{P}} \left[ -\boldsymbol{v} \cdot \boldsymbol{\nabla} \boldsymbol{v} + \nu \boldsymbol{\nabla}^2 \boldsymbol{v} + \left( 2\nu \rho^{-1} k_B T \right)^{\frac{1}{2}} \boldsymbol{\nabla} \cdot \boldsymbol{\mathcal{Z}}_{\boldsymbol{v}} \right]. \tag{3.24}$$

Here $\boldsymbol{\mathcal{P}}$ is the orthogonal projection onto the space of divergence-free velocity fields, $\boldsymbol{\mathcal{P}} = \boldsymbol{I} - \boldsymbol{\mathcal{G}} \left( \boldsymbol{\mathcal{D}} \boldsymbol{\mathcal{G}} \right)^{-1} \boldsymbol{\mathcal{D}}$ in real space, where $\boldsymbol{\mathcal{D}} \equiv \boldsymbol{\nabla}\cdot$ denotes the divergence operator and $\boldsymbol{\mathcal{G}} \equiv \boldsymbol{\nabla}$ the gradient operator with the appropriate boundary conditions taken into account. We only consider periodic, no-slip and free-slip boundaries. With periodic boundaries we can express all operators in Fourier space and $\widehat{\boldsymbol{\mathcal{P}}} = \boldsymbol{I} - k^{-2}(\boldsymbol{k}\boldsymbol{k}^{\star})$, where $\boldsymbol{k}$ is the wave number. The application of the projection to the right hand side ensures that $\boldsymbol{\nabla} \cdot \boldsymbol{v} = 0$ at all times if the initial condition is divergence free. The divergence-free constraint is a constant linear constraint and the projection restricts the velocity dynamics to the constant linear subspace of divergence-free vector fields. The projection operator can be applied in more general settings, notably, in cases where the constraints are nonlinear and the noise is multiplicative; however, the resulting expressions are rather complex especially in the stochastic setting [80, 81].

In practice, the fluctuating velocities modeled by (3.24) advect other quantities, and it is this coupling between the velocity and other equations that is of most interest. Perhaps the simplest example is provided by a stochastic advection-diffusion for the concentration or density $c(\boldsymbol{r}, t)$ of a large collection of non-interacting *passive tracers*. For example, $c(\boldsymbol{r}, t)$ might corresponds to the light intensity pattern of fluorescently-labeled molecules suspended in the fluid in a Fluorescence Recovery After Photobleaching (FRAP) experiment. This example is not entirely realistic, as in practice the particles will interact with the surrounding fluid and have an effect on the velocity equations (see Section 3.4). In general, the equation for the concentration has multiplicative noise [39]. This arises because the coarse-grained free energy functional $H[\boldsymbol{x}(\boldsymbol{r}, t)] = H(\boldsymbol{v}, c)$ includes a contribution from the entropy of the passive tracer which is, in general, a non-quadratic even if local functional of $c$. For illustration purposes we can take a separable quadratic Hamiltonian (i.e., independent Gaussian fluctuations in velocity and concentration),

$$H(\boldsymbol{v}, c) = H_{\boldsymbol{v}}(\boldsymbol{v}) + H_c(c) = \frac{\rho}{2} \int v^2 \, d\boldsymbol{r} + \frac{k_B T}{2\epsilon} \int c^2 \, d\boldsymbol{r},$$

and write the the model additive-noise tracer equation

$$\partial_t c = -\boldsymbol{v} \cdot \boldsymbol{\nabla} c + \chi \boldsymbol{\nabla}^2 c + \boldsymbol{\nabla} \cdot \left[ (2\epsilon\chi)^{\frac{1}{2}} \boldsymbol{\mathcal{Z}}_c \right]. \tag{3.25}$$

The multiplicative noise case is not considered herein. Physically, $\epsilon$ measures the degree of coarse graining, $\epsilon \sim N_p^{-1}$, where $N_p$ is the number of tracer particles per coarse degree of freedom. Note that (3.25) is a conservation law because $\boldsymbol{v} \cdot \boldsymbol{\nabla} c = \boldsymbol{\nabla} \cdot (c\boldsymbol{v})$ due to incompressibility. Note that in practice it is often the case that fluctuations are small perturbations of the deterministic dynamics, and the advective term is negligible as it is second order in the magnitude of these fluctuations (second order in the coarse graining length scale). In this case, the equations of linearized fluctuating hydrodynamics are relevant, and for practical simulations the nonlinear terms can often be neglected (see Section 3.4). However, we include nonlinear advection here and discuss its discretization to emphasize that our schemes can treat advection correctly and are numerically robust in the presence of larger magnitude fluctuations.

The coupled velocity-concentration system (3.24,3.25) can formally be written in the form (2.1). The chemical potential $\mu(c) = \partial H / \partial c \sim c$. The mobility operator can be written as a sum of a skew-adjoint and a self-adjoint part,

$$\boldsymbol{N} = \boldsymbol{M} - \boldsymbol{S} = -\begin{bmatrix} \rho^{-1}\nu\left(\boldsymbol{\mathcal{P}}\boldsymbol{\nabla}^2\boldsymbol{\mathcal{P}}\right) & \mathbf{0} \\ \mathbf{0} & \epsilon\left(k_B T\right)^{-1}\left(\chi\boldsymbol{\nabla}^2\right) \end{bmatrix} - \rho^{-1}\begin{bmatrix} \left(\boldsymbol{\mathcal{P}}\boldsymbol{\omega}\boldsymbol{\mathcal{P}}\right) & \boldsymbol{\mathcal{P}}\boldsymbol{\nabla}c \\ -\left(\boldsymbol{\nabla}c\right)^T\boldsymbol{\mathcal{P}} & 0 \end{bmatrix}, \tag{3.26}$$

where $\boldsymbol{\omega}$ is the antisymmetric vorticity tensor, $\boldsymbol{\omega}_{jk} = \partial v_k/\partial r_j - \partial v_j/\partial r_k$, and we used the vector identity

$$\boldsymbol{\omega}\boldsymbol{v} = -\left(\boldsymbol{\nabla} \times \boldsymbol{v}\right) \times \boldsymbol{v} = -\boldsymbol{v} \cdot \boldsymbol{\nabla}\boldsymbol{v} + \boldsymbol{\nabla}\left(\frac{v^2}{2}\right).$$

Even though by skew symmetry the top right sub-block of $\boldsymbol{S}$ is nonzero, there is no coupling of concentration back in the velocity equation because

$$\left(\frac{\partial H}{\partial c}\right)\boldsymbol{\nabla}c = \left(\frac{dH_c}{dc}\right)\boldsymbol{\nabla}c = \boldsymbol{\nabla}H_c$$

is a gradient of a scalar and is eliminated by the projection. The velocity equation therefore remains of the form (3.24).

### 3.3.2 Spatial Discretization

For a detailed description of the spatial discretization of (3.24,3.25) that we employ we refer the reader to Ref. [39]. The discretization of the velocity equation is based on a staggered or MAC grid [82] in which the component of velocity along a given dimension is discretized on a uniform grid that is shifted by half a grid spacing along that dimension. Following the stochastic methods of lines that we used for the Burgers equation in Section 3.2.2, the spatial discretization of (3.1) leads to a system of SODEs of the form

$$\frac{d\boldsymbol{v}}{dt} = \mathbb{P}\left[\boldsymbol{S}_{\boldsymbol{v}}\left(\boldsymbol{v}\right)\boldsymbol{v} + \nu\boldsymbol{L}_{\boldsymbol{v}}\boldsymbol{v} + \left(\frac{2\nu k_B T}{\rho\Delta V}\right)^{\frac{1}{2}}\boldsymbol{D}_{\boldsymbol{w}}\boldsymbol{\mathcal{W}}_{\boldsymbol{v}}\left(t\right)\right], \tag{3.27}$$

where $\boldsymbol{S}_{\boldsymbol{v}}\left(\boldsymbol{v}\right)$ denotes a discretization of the advective operator $-\left(\boldsymbol{v} \cdot \boldsymbol{\nabla}\right)$, $\Delta V$ is the volume of a hydrodynamic cell, and $\boldsymbol{\mathcal{W}}_{\boldsymbol{v}}\left(t\right)$ is a collection of white-noise processes [39]. Here $\boldsymbol{D}_{\boldsymbol{w}}$ a tensor divergence operator that applies the conservative discrete vector divergence operator $\boldsymbol{D}$ independently for each coordinate, $\boldsymbol{L}_{\boldsymbol{v}}$ is a discrete (vector) Laplacian, and $\mathbb{P} = \boldsymbol{I} - \boldsymbol{G}\left(\boldsymbol{D}\boldsymbol{G}\right)^{-1}\boldsymbol{D}$ is a *discrete projection* operator, where $\boldsymbol{G}$ is a discrete scalar gradient operator. The imposed periodic, no-slip or free-slip boundary conditions are encoded in the specific forms of the discrete difference operators near the boundaries of the domain.

Let us first focus on creeping Stokes flow, where the advective term $\boldsymbol{v} \cdot \boldsymbol{\nabla}\boldsymbol{v}$ is neglected. Following the same procedure as we employed for the fluctuating Burgers equation in Section 3.2.2, the spatial discretization is constructed to obey a discrete fluctuation-dissipation balance principle. This relies on several key properties of the staggered difference operators. Importantly, the discrete gradient and divergence operators obey the duality relation $\boldsymbol{G} = -\boldsymbol{D}^\star$, just as the continuum operators. The resulting scalar Laplacian $\boldsymbol{L}_s = \boldsymbol{D}\boldsymbol{G} = -\boldsymbol{D}\boldsymbol{D}^\star$ is the standard $(2d + 1)$-point discrete Laplacian, which is also applied to each (staggered) component of the velocity to form $\boldsymbol{L}_{\boldsymbol{v}} = -\boldsymbol{D}_{\boldsymbol{w}}\left(\boldsymbol{D}_{\boldsymbol{w}}\right)^\star$ (see Ref. [39] for a discussion of modifications near physical boundaries). Because of the duality between $\boldsymbol{D}$ and $\boldsymbol{G}$ the MAC projection is self-adjoint, $\mathbb{P}^\star = \mathbb{P}$, and idempotent, $\mathbb{P}^2 = \mathbb{P}$, just like the continuum projection operator. From these properties and Eq. (2.22) it follows (see Appendix in Ref. [39] for details) that the equilibrium covariance of the fluctuating velocities is

$$\langle \boldsymbol{v}\boldsymbol{v}^\star \rangle = \frac{k_B T}{\rho\Delta V}\mathbb{P} \tag{3.28}$$

This means that when an equilibrium snapshot of the velocity is expressed in any orthonormal basis for the subspace of discretely divergence-free vector fields, the coefficients are i.i.d. Gaussian random variables with mean zero and variance $\rho^{-1}k_BT/\Delta V$. This is the expression of discrete fluctuation-dissipation balance for the case of incompressible flow.

The addition of the nonlinear advective term does not affect the discrete fluctuation-dissipation balance since the advective term is skew-adjoint, $\boldsymbol{S}_{\boldsymbol{v}}^{\star} = -\boldsymbol{S}_{\boldsymbol{v}}$, just like the discretization (3.22) of the term $uu_x$ for the one-dimensional case. Specifically, in two dimensions, for a given $\boldsymbol{u}$ such that $\boldsymbol{Du} = 0$, the spatial discretization of the advective term described in Refs. [78, 39] leads to

$$
\begin{aligned}
[\boldsymbol{S}_{\boldsymbol{v}}\left(\boldsymbol{u}\right)\boldsymbol{v}]_{i+\frac{1}{2},j}^{(x)} = & -(4\Delta x)^{-1}\left[\left(u_{i+\frac{3}{2},j}^{(x)} + u_{i+\frac{1}{2},j}^{(x)}\right)v_{i+\frac{3}{2},j}^{(x)} - \left(u_{i-\frac{1}{2},j}^{(x)} + u_{i+\frac{1}{2},j}^{(x)}\right)v_{i-\frac{1}{2},j}^{(x)}\right] \\
& -(4\Delta y)^{-1}\left[\left(u_{i,j+\frac{1}{2}}^{(y)} + u_{i+1,j+\frac{1}{2}}^{(y)}\right)v_{i+\frac{1}{2},j+1}^{(x)} - \left(u_{i,j-\frac{1}{2}}^{(y)} + u_{i+1,j-\frac{1}{2}}^{(y)}\right)v_{i+\frac{1}{2},j-1}^{(x)}\right].
\end{aligned}
$$

This can easily be shown to be a skew-adjoint discretization, $[\boldsymbol{S}_{\boldsymbol{v}}\left(\boldsymbol{u}\right)\boldsymbol{v}] \cdot \boldsymbol{w} = -[\boldsymbol{S}_{\boldsymbol{v}}\left(\boldsymbol{u}\right)\boldsymbol{w}] \cdot \boldsymbol{v}$, for either periodic, free-slip and no-slip conditions (or any combination thereof). Furthermore, this discretization leads to Hamiltonian dynamics for inviscid flow, i.e., the phase-space flow generated by the advective term is incompressible,

$$
\frac{\partial}{\partial\boldsymbol{v}} \cdot \boldsymbol{S}_{\boldsymbol{v}}\left(\boldsymbol{v}\right) = \boldsymbol{0}.
$$

A good temporal integrator should preserve this special structure of the equations and reproduce the correct velocity fluctuations for reasonably large time step sizes.

Note that the addition of a passively-advected scalar field poses no additional difficulties if $c$ is discretized on the regular (non-staggered) grid underlying the (staggered) velocity grid. Specifically, the spatial discretization of (3.25) that we employ is a scalar equivalent of (3.27),

$$
\frac{d\boldsymbol{c}}{dt} = \boldsymbol{S}_c\left(\boldsymbol{v}\right)\boldsymbol{c} + \chi\boldsymbol{L}_c\boldsymbol{c} + \left(\frac{2\epsilon\chi}{\Delta V}\right)^{\frac{1}{2}}\boldsymbol{D}\mathcal{W}_c\left(t\right), \tag{3.29}
$$

where $\boldsymbol{S}_c\left(\boldsymbol{v}\right)$ is a cell-centered conservative and skew-adjoint discretization of the advection operator $-\left(\boldsymbol{v}\cdot\boldsymbol{\nabla}\right)$,

$$
[\boldsymbol{S}_c\left(\boldsymbol{u}\right)\boldsymbol{c}]_{i,j} = -(2\Delta x)^{-1}\left(u_{i+\frac{1}{2},j}^{(x)}c_{i+1,j} - u_{i-\frac{1}{2},j}^{(x)}c_{i-1,j}\right) - (2\Delta y)^{-1}\left(u_{i,j+\frac{1}{2}}^{(y)}c_{i,j+1} - u_{i,j-\frac{1}{2}}^{(y)}c_{i,j-1}\right),
$$

and $\boldsymbol{L}_c$ is equivalent to $\boldsymbol{L}_s = \boldsymbol{DG}$ except near boundaries. The semi-discrete equation (3.29) obeys a discrete fluctuation-dissipation balance principle [39]. Specifically, at thermodynamic equilibrium the fluctuations in the concentration are Gaussian with covariance

$$
\langle\boldsymbol{cc}^{\star}\rangle = \frac{\epsilon}{\Delta V}\boldsymbol{I}, \tag{3.30}
$$

and also uncorrelated with the velocity fluctuations.

The coupled velocity-concentration equation system of SODEs (3.27,3.29) can be written in the generic Langevin form (2.1). Note that the concentration-dependent term in the velocity equation that ought to be included to preserve the skew-symmetry of the non-diffusive terms can be written in the form of a projected *discrete* gradient of a scalar, $\mathbb{P}\boldsymbol{G}\left(c^2/2\right)$, which vanishes identically. This shows that in two dimensions the system (3.27,3.29) is time reversible with respect to the equilibrium Gibbs-Boltzmann distribution with the separable discrete Hamiltonian

$$
H\left(\boldsymbol{v},c\right) = \frac{\rho\Delta V}{2}\sum_{i,j}\left[\left(v_{i+\frac{1}{2},j}^{(x)}\right)^2 + \left(v_{i,j+\frac{1}{2}}^{(y)}\right)^2\right] + \frac{k_BT\Delta V}{2\epsilon}\sum_{i,j}c_{i,j}^2.
$$

Note that the Gibbs-Boltzmann distribution is constrained to the linear subspace of discretely divergence-free vector fields,

$$
\left(\boldsymbol{Dv}\right)_{i,j} = \Delta x^{-1}\left(v_{i+\frac{1}{2},j}^{(x)} - v_{i-\frac{1}{2},j}^{(x)}\right) + \Delta y^{-1}\left(v_{i,j+\frac{1}{2}}^{(y)} - v_{i,j-\frac{1}{2}}^{(y)}\right) = 0,
$$

and with periodic boundaries both the average momentum and average concentration are conserved by the dynamics.

### 3.3.3 Temporal Discretization

In our initial discussion of temporal integration schemes for (3.27) we will neglect the advective term and focus on creeping Stokes flow, thus avoiding technical details while preserving the essential features of the problem. There

is a vast literature on deterministic temporal integration of the incompressible Navier-Stokes equations, and, in particular, the handling of the $\nabla \pi$ term. One of the most popular class of methods are splitting or *projection methods*, such as the prototype projected Euler-Maruyama method,

$$\boldsymbol{v}^{n+1} = \boldsymbol{v}^n + \nu \Delta t \, \mathbb{P} \boldsymbol{L_v} \boldsymbol{v}^n + (2\nu \Delta t)^{\frac{1}{2}} \, \mathbb{P} \boldsymbol{D_w} \boldsymbol{W_v^n}, \tag{3.31}$$

where we set $\rho^{-1} k_B T / \Delta V = 1$ for simplicity and $\boldsymbol{W_v^n}$ are i.i.d. standard normal random variates generated independently at each time step. Note that in practice, due to roundoff errors and the use of inexact Poisson solvers in the projection operation, it is preferable to apply $\mathbb{P}$ to $\boldsymbol{v}^n$ as well.

As explained in Addendum 3.7 (see also Appendix B in Ref. [39]), the iteration (3.31) gives a steady-state covariance that is a first-order accurate approximation to the continuum result (3.28),

$$\boldsymbol{C_v} = \langle \boldsymbol{v}^n \, (\boldsymbol{v}^n)^\star \rangle = \mathbb{P} + \Delta t \, \Delta \boldsymbol{C_v} + O\left(\Delta t^2\right).$$

In Addendum 3.7 we consider approximate projection methods [83, 84] and find that they do not satisfy this requirement. The scheme (3.31) can be seen as a direct application of the Euler-Maruyama method to (3.27). Note that any purely explicit scheme can be applied to (3.27) by simply performing a projection operation after every stage of the scheme.

Semi-implicit schemes can also be applied to (3.27). As a prototype example, let us consider the implicit midpoint method (2.24),

$$\boldsymbol{v}^{n+1} = \boldsymbol{v}^n + \frac{\nu \Delta t}{2} \, \mathbb{P} \boldsymbol{L_v} \left(\boldsymbol{v}^n + \boldsymbol{v}^{n+1}\right) + (2\nu \Delta t)^{\frac{1}{2}} \, \mathbb{P} \boldsymbol{D_w} \boldsymbol{W_v^n}. \tag{3.32}$$

At first sight, it appears that solving (3.32) requires the application of $\left[\boldsymbol{I} - (\nu \Delta t/2) \, \mathbb{P} \boldsymbol{L_v}\right]^{-1}$. However, it is not hard to see that solving (3.32) is equivalent to solving the following linear system for the velocity $\boldsymbol{v}^{n+1}$ and the pressure $\boldsymbol{\pi}^{n+\frac{1}{2}}$,

$$
\begin{aligned}
\left(\boldsymbol{I} - \frac{\nu \Delta t}{2} \boldsymbol{L_v}\right) \boldsymbol{v}^{n+1} + \Delta t \, \boldsymbol{G} \boldsymbol{\pi}^{n+\frac{1}{2}} &= \left(\boldsymbol{I} + \frac{\nu \Delta t}{2} \boldsymbol{L_v}\right) \boldsymbol{v}^n + (2\nu \Delta t)^{\frac{1}{2}} \, \boldsymbol{D_w} \boldsymbol{W_v^n} \\
\boldsymbol{D} \boldsymbol{v}^{n+1} &= 0.
\end{aligned}
\tag{3.33}
$$

This coupled velocity-pressure *Stokes linear system* can be solved efficiently even in the presence of non-periodic boundaries by using a preconditioned Krylov iterative solver, as described in detail in Ref. [85]. The scheme (3.32) reproduces the static covariance of the velocity fluctuations exactly, $\boldsymbol{C_v} = \mathbb{P}$, for *any* time step. A more intuitive approach to analyzing the scheme (3.33) based on computing the modes of the spatial discretization is described in Addendum 3.8.

Having illustrated how the implicit midpoint rule (2.24) can be applied to the time-dependent Stokes equations, it is simple to modify the implicit-explicit predictor-corrector schemes described in Section 2.2 to account for incompressibility. In Ref. [39] the implicit trapezoidal predictor-corrector scheme (2.31) was used to solve (3.24,3.25), but only tested in an essentially linearized context. Here we also consider the implicit midpoint predictor-corrector scheme (2.33), for which the predictor stage consists of solving the linear system for $\tilde{\boldsymbol{v}}^{n+\frac{1}{2}}$, $\tilde{\boldsymbol{\pi}}^{n+\frac{1}{2}}$ and $\tilde{\boldsymbol{c}}^{n+\frac{1}{2}}$,

$$
\begin{aligned}
\left(\boldsymbol{I} - w_1 \nu \Delta t \, \boldsymbol{L_v}\right) \tilde{\boldsymbol{v}}^{n+\frac{1}{2}} + \Delta t \, \boldsymbol{G} \tilde{\boldsymbol{\pi}}^{n+\frac{1}{2}} &= \frac{\Delta t}{2} \boldsymbol{S_v} \left(\boldsymbol{v}^n\right) \boldsymbol{v}^n + \left[\boldsymbol{I} + \left(\frac{1}{2} - w_1\right) \nu \Delta t \, \boldsymbol{L_v}\right] \boldsymbol{v}^n \\
&\quad + (\nu \Delta t)^{\frac{1}{2}} \, \boldsymbol{D_w} \left(\boldsymbol{W_v^n}\right)_1 \\
\left(\boldsymbol{I} - w_1 \chi \Delta t \, \boldsymbol{L_c}\right) \tilde{\boldsymbol{c}}^{n+\frac{1}{2}} &= \frac{\Delta t}{2} \boldsymbol{S_c} \left(\boldsymbol{v}^n\right) \boldsymbol{c}^n + \left[\boldsymbol{I} + \left(\frac{1}{2} - w_1\right) \chi \Delta t \, \boldsymbol{L_c}\right] \boldsymbol{c}^n \\
&\quad + (\epsilon \chi \Delta t)^{\frac{1}{2}} \, \boldsymbol{D} \left(\boldsymbol{W_c^n}\right)_1 \\
\boldsymbol{D} \tilde{\boldsymbol{v}}^{n+\frac{1}{2}} &= 0,
\end{aligned}
$$

and similarly for the corrector stage. The concentration equation is decoupled from the velocity equation and can be solved using standard techniques, e.g., multigrid methods. Note that in practice it is better to rewrite the linear systems in terms of the increments $\tilde{\boldsymbol{v}}^{n+\frac{1}{2}} - \boldsymbol{v}^n$ and $\tilde{\boldsymbol{c}}^{n+\frac{1}{2}} - \boldsymbol{c}^n$. This is because for weak fluctuations the terms involving the identity matrix may dominate the right-hand side and compromise the accuracy of the linear solvers, unless special care is taken in choosing the termination criteria for the iterative linear solvers.

## 3.4 Fluctuating Hydrodynamics of Binary Fluid Mixtures

In this section we apply the techniques we developed in Sections 2.2 and 2.3 to the fluctuating hydrodynamics problems described in Section 3.1.1. In the example considered here many of the stochastic drift terms present in the more general case are not present. In Chapter 4, we present a numerical method for performing Brownian dynamics for particles suspended in a fluid, based on treating the fluid velocity as a fast degree of freedom compared to the positions of the particles. That example includes the majority of the stochastic drift terms that appear in a general setting, and employs our midpoint scheme for overdamped dynamics essentially in its full generality (the only difference is that the block $C$ from Section 2.3 is constant).

We model the diffusion of a concentration field that is passively advected by the randomly fluctuating fluid velocity, as we first discussed in Section 3.1.1. In the nonlinear overdamped setting, the methods presented here can be used to model diffusion of labeled or tracer particles in liquids over a broad range of length scales, as we did in Ref. [23]. In the linearized setting, the same methods can be used to study the spatio-temporal spectrum of Gaussian fluctuations around steady or dynamic deterministic flows [26], as we first did in Ref. [39] for a steady state and extend in this work to a dynamic setting in Section 3.5.3.1. In Section 3.5.3.2 we present an application of the methods developed here to study the dynamic structure factors in binary fluid mixtures subjected to a small temperature gradient, in the presence of gravity and confinement [71].

We consider the velocity-concentration system (3.2,3.3) in a simplified setting in which the noise in the concentration equation is additive and we omit the nonlinear term $\boldsymbol{v} \cdot \boldsymbol{\nabla} \boldsymbol{v}$,

$$\partial_t \boldsymbol{v} = \boldsymbol{\mathcal{P}} \left( \nu \boldsymbol{\nabla}^2 \boldsymbol{v} + \sqrt{2\rho^{-1}\nu k_B T}\, \boldsymbol{\nabla} \cdot \boldsymbol{\mathcal{W}} - \beta c\, \boldsymbol{g} \right),$$

$$\partial_t c = -\boldsymbol{\nabla} \cdot (c\boldsymbol{v}) + \chi_0 \boldsymbol{\nabla}^2 c + \boldsymbol{\nabla} \cdot \left( \sqrt{2\chi_0 \vartheta_0}\, \boldsymbol{\mathcal{W}}_c \right), \tag{3.34}$$

where $\nu = \eta/\rho$ and $\vartheta_0 = \rho^{-1} m c_0$, where $m$ is the mass of the tracer particles and $c_0$ is a reference concentration. For simplicity we have replaced $\boldsymbol{u} = \boldsymbol{\sigma} \star \boldsymbol{v}$ by $\boldsymbol{v}$, assuming that the filtering is done by an implicit truncation of the SPDE at small scales; this is naturally performed in the finite-volume discretizations of this system described in Section 3.3.2. Note that for incompressible $\boldsymbol{v}$ we have $\boldsymbol{\nabla} \cdot (c\boldsymbol{v}) = \boldsymbol{v} \cdot \boldsymbol{\nabla} c$. In (3.34) the constraint $\boldsymbol{\nabla} \cdot \boldsymbol{v} = 0$ is enforced by the Helmholtz projection operator $\boldsymbol{\mathcal{P}} = \boldsymbol{I} - \boldsymbol{\mathcal{G}} (\boldsymbol{\mathcal{D}} \boldsymbol{\mathcal{G}})^{-1} \boldsymbol{\mathcal{D}}$, where $\boldsymbol{\mathcal{D}} \equiv \boldsymbol{\nabla} \cdot$ denotes the divergence operator and $\boldsymbol{\mathcal{G}} \equiv \boldsymbol{\nabla}$ the gradient operator with the appropriate boundary conditions taken into account. The equations introduced in this section are similar in many ways to the equations in Section 3.3, but there exist several subtle key differences. Here we focus on the practical simulation of the diffusive mixing of a binary fluid which can be studied in experiments. We assume the noise is weak at the observed scale, and linearize around the deterministic steady state of zero velocity, neglecting the higher order advection term. The concentration in a binary fluid mixture affects the motion of the fluid due to buoyancy, and we include a Boussinesq approximation in the equation for the evolution of velocity. Additionally, we assume a large separation of timescales between the evolution of velocity and concentration, requiring the use of the fast-slow integrators developed in Section 2.3.

The coupled velocity-concentration system (3.34) can be written as an infinite-dimensional system of the form (2.43) with the identification $\boldsymbol{v} \equiv \boldsymbol{y}$ as the (potentially) fast variable and $c \equiv \boldsymbol{x}$ as the slow variable. We have a quadratic (Gaussian) coarse-grained energy *functional* that includes a contribution due to the (excess) gravitational potential energy of the tracer particles of excess mass (over the solvent) of $\beta m$,

$$U\left[\boldsymbol{v}\left(\cdot\right), c\left(\cdot\right)\right] = \frac{\rho}{2} \int v^2\left(\boldsymbol{r}\right)\, d\boldsymbol{r} + \beta\rho \int c\left(\boldsymbol{r}\right)\left(\boldsymbol{r} \cdot \boldsymbol{g}\right)\, d\boldsymbol{r} + \frac{k_B T}{2\vartheta_0} \int c^2\left(\boldsymbol{r}\right)\, d\boldsymbol{r}, \tag{3.35}$$

which corresponds to $\bar{\boldsymbol{y}} \equiv \bar{\boldsymbol{v}} = \boldsymbol{0}$, $\boldsymbol{\Psi}\left(\boldsymbol{x}\right) \equiv \rho \boldsymbol{I}/2$ a multiple of the identity, and quadratic $U\left(\boldsymbol{x}\right) \equiv (2\vartheta_0)^{-1} k_B T \int c^2\left(\boldsymbol{r}\right)\, d\boldsymbol{r}$. The mobility [1] and noise operators can be taken to be

$$\boldsymbol{N}\left[c\left(\cdot\right)\right] = \begin{bmatrix} \boldsymbol{A} & \boldsymbol{B} \\ -\boldsymbol{B}^{\star} & \boldsymbol{C} \end{bmatrix} \equiv - \begin{bmatrix} (k_B T)^{-1} \chi_0 \vartheta_0 \boldsymbol{\nabla}^2 & -\rho^{-1} \boldsymbol{\nabla} \cdot c\boldsymbol{\mathcal{P}} \\ -\rho^{-1} \boldsymbol{\mathcal{P}} c\boldsymbol{\nabla} & \rho^{-1} \nu \left(\boldsymbol{\mathcal{P}} \boldsymbol{\nabla}^2 \boldsymbol{\mathcal{P}}\right) \end{bmatrix}$$

and

$$\boldsymbol{M}_{\frac{1}{2}}\left[c\left(\cdot\right)\right] = \begin{bmatrix} \boldsymbol{A}_{\frac{1}{2}} & \boldsymbol{0} \\ \boldsymbol{0} & \epsilon^{-1} \boldsymbol{C}_{\frac{1}{2}} \end{bmatrix} = \begin{bmatrix} \sqrt{\chi_0 \vartheta_0 / k_B T}\, \boldsymbol{\nabla} \cdot & \boldsymbol{0} \\ \boldsymbol{0} & \sqrt{\rho^{-1}\nu}\, \boldsymbol{\mathcal{P}} \boldsymbol{\nabla} \cdot \end{bmatrix},$$

where differential operators act on everything to their right and we note that only the operator $\boldsymbol{B}\left[c\left(\cdot\right)\right]$ is a functional of the slow variable $c$. The diagonal blocks of the mobility operator $\boldsymbol{N}$ generate momentum and (bare)

---

[1]Note that the advective part of the mobility operator we use here is slightly different from that in Section 3.3.2 because here we use the conservative $\boldsymbol{\nabla} \cdot (c\boldsymbol{v})$ rather than the advective form $\boldsymbol{v} \cdot \boldsymbol{\nabla} c$, as required for momentum conservation in the presence of gravity.

mass diffusion and the corresponding noise terms. The upper right block of $\boldsymbol{N}$ generates the advective term $-\boldsymbol{v} \cdot \boldsymbol{\nabla} c$ in the concentration equation, while the lower left block of $\boldsymbol{N}$ generates the gravity term in the velocity equation,

$$-\rho^{-1} \boldsymbol{\mathcal{P}} c \boldsymbol{\nabla} \left( \rho \beta \left( \boldsymbol{r} \cdot \boldsymbol{g} \right) + \frac{k_B T}{2 \vartheta_0} c \right) = -\beta \boldsymbol{\mathcal{P}} c \boldsymbol{g} - \rho^{-1} \boldsymbol{\mathcal{P}} \boldsymbol{\nabla} \left( \frac{c^2}{2} \right) = -\beta \boldsymbol{\mathcal{P}} c \boldsymbol{g},$$

where we used the fact that projection eliminates pure gradients. This last property allows for a key simplification, namely, the stochastic drift term involving $\partial_{\boldsymbol{x}} \cdot \boldsymbol{B}^{\star} \equiv \partial_{\boldsymbol{c}} \cdot \boldsymbol{B}^{\star} \left[ c \left( \cdot \right) \right]$ can be omitted, and there is no difference between a kinetic and a Stratonovich interpretation of the overdamped dynamics [23]. We take advantage of these properties in the algorithms presented next. It is important to note that these simplifying properties are also valid after (careful) spatial discretization of the SPDEs (See Section 3.3.2). Also note that spatially-discretized white noise acquires an additional factor of $\Delta V^{-\frac{1}{2}}$, where $\Delta V$ is the volume of the grid cells.

Note that a more complete but formal calculation [24] using the true ideal gas entropy functional (3.5) would set $\boldsymbol{A} = \chi_0 m / \left( \rho k_B T \right) \boldsymbol{\nabla} \cdot c \boldsymbol{\nabla}$, where all differential operators act to their right, and obtain multiplicative noise as well as an additional *barodiffusion* term in the concentration equation,

$$\partial_t c = -\boldsymbol{\nabla} \cdot (c \boldsymbol{v}) + \boldsymbol{\nabla} \cdot \left[ \chi_0 \left( \boldsymbol{\nabla} c + \frac{\beta m \boldsymbol{g}}{k_B T} c \right) \right] + \boldsymbol{\nabla} \cdot \left( \sqrt{2 \chi_0 \rho^{-1} m c} \, \boldsymbol{\mathcal{W}}_c \right). \tag{3.36}$$

The barodiffusion term is only important in the presence of very high gravitational energies such as in ultracentrifuges, and we will neglect it here and use (3.3) instead.

### 3.4.1 Inertial Equations

For the full inertial dynamics (3.34), applying our predictor-corrector methods would require treating the diffusion of both momentum and mass with the same scheme, i.e., both would need to treated implicitly or both treated explicitly. Similarly, if a semi-implicit method is used, two linear solves would be required, one for the predictor and one for the corrector stage. However, we can take specific advantage of the structure of (3.34) and use a *split* approach, in which we handle concentration and velocity differently, for example, we can treat viscosity implicitly (since velocity is a faster variable) and treat mass diffusion explicitly (since concentration is a slower variable). In Algorithm 3.1 we present an optimized split scheme for integrating (3.34), which only requires a single fluid solve per time step. Note that this scheme can be made second-order accurate deterministically for the fully nonlinear Navier-Stokes equation by using a time-lagged (multi-step) scheme for the advective term $\rho \boldsymbol{v} \cdot \boldsymbol{\nabla} \boldsymbol{v} = \rho \boldsymbol{\nabla} \cdot (\boldsymbol{v} \otimes \boldsymbol{v})$. Here we treat concentration implicitly but an explicit treatment is also possible. In Section 3.5.3.2 we use Algorithm 3.1 to study the difference between the inertial and overdamped dynamics for a problem involving a fluid sample subjected to a concentration gradient, in the presence of gravity.

The analysis presented in this work does not directly apply to split schemes and confirming second-order weak accuracy requires custom analysis. Empirical order of accuracy tests can also be used but note that these can be misleading since error terms that dominate for very small time step sizes may be negligible for time step sizes of interests. For very small $\Delta t$, statistical errors are often much larger than the truncation errors, making empirical convergence studies computationally infeasible.

For completeness, in Algorithm 3.2 we apply our implicit trapezoidal integrator (2.31) to the variable-coefficient inertial equations (3.6); this integrator requires two concentration and two velocity (Stokes) linear solves per time step. Our analysis shows that this is a second-order weak integrator for the *linearized* inertial equations. We do not use this integrator in this work because a constant-coefficient incompressible approximation is appropriate in the (passive tracer) applications we study here. Note that for incompressible $\boldsymbol{v}$ the conservative and advective forms are equivalent, $\boldsymbol{\nabla} \cdot (c \boldsymbol{v}) = \boldsymbol{v} \cdot \boldsymbol{\nabla} c$; in the numerical schemes it is preferred to use the conservative form to ensure strict conservation of mass and momentum even when imposing the divergence-free constraint on the velocity only to some finite threshold. Note that the nonlinear advective terms can alternatively be handled using a midpoint rule following (2.32). For example, $\left[ (c\boldsymbol{v})^n + (c\boldsymbol{v})^{p,n+1} \right] / 2$ can be replaced by

$$\left( \frac{c^n + c^{p,n+1}}{2} \right) \left( \frac{\boldsymbol{v}^n + \boldsymbol{v}^{p,n+1}}{2} \right),$$

without affecting the order of accuracy.

**Algorithm 3.1** Split integrator for the inertial dynamics (3.34), as implemented in the IBAMR software framework [86].

1. In the predictor step for concentration, solve for $c^{p,n+1}$,

$$\frac{c^{p,n+1} - c^n}{\Delta t} = -\boldsymbol{v}^n \cdot \boldsymbol{\nabla} c^n + \chi_0 \boldsymbol{\nabla}^2 \left( \frac{c^n + c^{p,n+1}}{2} \right) + \boldsymbol{\nabla} \cdot \left( \sqrt{\frac{2\chi_0 \vartheta_0}{\Delta t \Delta V}} \, \boldsymbol{W}_c^n \right).$$

2. Solve the time-dependent Stokes or Navier-Stokes system for $\boldsymbol{v}^{n+1}$ and $\pi^{n+\frac{1}{2}}$,

$$\rho \frac{\boldsymbol{v}^{n+1} - \boldsymbol{v}^n}{\Delta t} + \rho \left( \boldsymbol{v} \cdot \boldsymbol{\nabla} \boldsymbol{v} \right)^{n+\frac{1}{2}} + \boldsymbol{\nabla} \pi^{n+\frac{1}{2}} = \eta \boldsymbol{\nabla}^2 \left( \frac{\boldsymbol{v}^{n+1} + \boldsymbol{v}^n}{2} \right) + \boldsymbol{\nabla} \cdot \left( \sqrt{\frac{2\eta \, k_B T}{\Delta t \Delta V}} \, \boldsymbol{W}^n \right)$$

$$- \rho \beta \left( \frac{c^n + c^{p,n+1}}{2} \right) \boldsymbol{g}$$

$$\boldsymbol{\nabla} \cdot \boldsymbol{v}^{n+1} = 0.$$

The nonlinear advective term $(\boldsymbol{v} \cdot \boldsymbol{\nabla} \boldsymbol{v})^{n+\frac{1}{2}}$ can be omitted in the Stokes limit, or approximated to second-order accuracy using an Adams-Bashforth approach.

3. Correct the concentration by solving

$$\frac{c^{n+1} - c^n}{\Delta t} = -\left( \frac{\boldsymbol{v}^{n+1} + \boldsymbol{v}^n}{2} \right) \cdot \boldsymbol{\nabla} \left( \frac{c^n + c^{p,n+1}}{2} \right) + \chi_0 \boldsymbol{\nabla}^2 \left( \frac{c^n + c^{n+1}}{2} \right) + \boldsymbol{\nabla} \cdot \left( \sqrt{\frac{2\chi_0 \vartheta_0}{\Delta t \Delta V}} \, \boldsymbol{W}_c^n \right).$$

---

### 3.4.2  Overdamped Equations

The overdamped limit of (3.34) is the Stratonovich SPDE [23]

$$\begin{aligned}
\partial_t c &= \beta \rho \eta^{-1} \left( \boldsymbol{G} \star c \boldsymbol{g} \right) \cdot \boldsymbol{\nabla} c + \sqrt{2\eta^{-1} k_B T} \left( \boldsymbol{G}_{\frac{1}{2}} \boldsymbol{\mathcal{W}} \right) \odot \boldsymbol{\nabla} c \qquad (3.37) \\
&+ \chi_0 \boldsymbol{\nabla}^2 c + \boldsymbol{\nabla} \cdot \left( \sqrt{2\chi_0 \vartheta_0} \, \boldsymbol{\mathcal{W}}_c \right),
\end{aligned}$$

where the notation is explained in Section 3.1.1.1. In Algorithm 3.3 we give a temporal integrator for this equation, which we first proposed in Appendix B of Ref. [23]. This algorithm can be seen as an application of the implicit trapezoidal method (2.32) to (3.37), with the identifications

$$\boldsymbol{L} \equiv \chi_0 \boldsymbol{\nabla}^2, \quad \text{and} \quad \boldsymbol{g} \left[ c \left( \cdot \right) \right] = \beta \rho \eta^{-1} \left( \boldsymbol{G} \star c \boldsymbol{g} \right) \cdot \boldsymbol{\nabla} c,$$

and

$$\boldsymbol{K} \left[ c \left( \cdot \right) \right] \circ \boldsymbol{\mathcal{W}} \left( t \right) \equiv \sqrt{2\eta^{-1} k_B T} \left( \boldsymbol{G}_{\frac{1}{2}} \boldsymbol{\mathcal{W}} \right) \odot \boldsymbol{\nabla} c + \boldsymbol{\nabla} \cdot \left( \sqrt{2\chi_0 \vartheta_0} \, \boldsymbol{\mathcal{W}}_c \right).$$

Note that the advective term in the corrector stage can alternatively be treated using an explicit trapezoidal rule, as in (2.31), without affecting the formal order of accuracy of the scheme.

Algorithm 3.3 is weakly first-order accurate for the nonlinear overdamped dynamics, and second-order accurate for the linearized overdamped dynamics (3.13). Therefore, this method "kills two birds with one stone" and can be used for either strong (nonlinear) [23] or weak (linearized) noise settings. In Section 3.5.3.1 we use Algorithm 3.3 to study the dynamics of the development of giant concentration fluctuations in the absence of gravity.

## 3.5  Numerical Results

In this section we numerically study the schemes introduced in sections 2.2 and 2.3. First, we investigate the behavior of the mixed explicit-implicit trapezoidal (2.31) and midpoint (2.33) schemes on the fluctuating Burgers and Navier-Stokes equations. We focus here on the behavior of the equilibrium distribution of the fluctuating fields for large fluctuations and large time step sizes. The discrete spectrum of the equilibrium fluctuations is one of the most important properties of a numerical scheme for long-time simulations.

**Algorithm 3.2** Unsplit implicit trapezoidal temporal integrator for the variable-coefficient inertial equations (3.6).

1. In the predictor step for concentration, solve for $c^{p,n+1}$,

$$\frac{c^{p,n+1} - c^n}{\Delta t} = -\boldsymbol{\nabla} \cdot (c\boldsymbol{v})^n + \frac{1}{2}\boldsymbol{\nabla} \cdot \left[\chi^n \left(\boldsymbol{\nabla}c^n + \boldsymbol{\nabla}c^{p,n+1}\right)\right] + \boldsymbol{\nabla} \cdot \left(\sqrt{\frac{2\left(\chi\rho^{-1}\mu_c^{-1}\right)^n k_B T}{\Delta t \Delta V}}\, \boldsymbol{W}_c^n\right),$$

and solve (independently) the variable-coefficient Stokes system for $\boldsymbol{v}^{p,n+1}$ and $\pi^{p,n+\frac{1}{2}}$ [87],

$$\rho\frac{\boldsymbol{v}^{p,n+1} - \boldsymbol{v}^n}{\Delta t} + \boldsymbol{\nabla}\pi^{p,n+\frac{1}{2}} = -\rho\boldsymbol{\nabla} \cdot (\boldsymbol{v} \otimes \boldsymbol{v})^n - \beta\rho c^n \boldsymbol{g}$$

$$+ \boldsymbol{\nabla} \cdot \left[\frac{\eta^n}{2}\left(\bar{\boldsymbol{\nabla}}\boldsymbol{v}^n + \bar{\boldsymbol{\nabla}}\boldsymbol{v}^{p,n+1}\right) + \sqrt{\frac{2\eta^n k_B T}{\Delta t \, \Delta V}}\, \boldsymbol{W}^n\right]$$

$$\boldsymbol{\nabla} \cdot \boldsymbol{v}^{p,n+1} = 0.$$

2. Correct the concentration by solving,

$$\frac{c^{n+1} - c^n}{\Delta t} = -\frac{1}{2}\boldsymbol{\nabla} \cdot \left[(c\boldsymbol{v})^n + (c\boldsymbol{v})^{p,n+1}\right] + \frac{1}{2}\boldsymbol{\nabla} \cdot \left[\chi^n \boldsymbol{\nabla}c^n + \chi^{p,n+1}\boldsymbol{\nabla}c^{n+1}\right]$$

$$+ \frac{1}{2}\boldsymbol{\nabla} \cdot \left[\left(\sqrt{\frac{2\left(\chi\rho^{-1}\mu_c^{-1}\right)^n k_B T}{\Delta t \Delta V}} + \sqrt{\frac{2\left(\chi\rho^{-1}\mu_c^{-1}\right)^{p,n+1} k_B T}{\Delta t \Delta V}}\right)\boldsymbol{W}_c^n\right],$$

and correct the velocity by solving (independently) the the variable-coefficient Stokes system for $\boldsymbol{v}^{n+1}$ and $\pi^{n+\frac{1}{2}}$ [87],

$$\rho\frac{\boldsymbol{v}^{n+1} - \boldsymbol{v}^n}{\Delta t} + \boldsymbol{\nabla}\pi^{n+\frac{1}{2}} = -\frac{\rho}{2}\boldsymbol{\nabla} \cdot \left[(\boldsymbol{v} \otimes \boldsymbol{v})^n + (\boldsymbol{v} \otimes \boldsymbol{v})^{p,n+1}\right] - \frac{\beta\rho}{2}\left(c^n + c^{p,n+1}\right)\boldsymbol{g}$$

$$+ \frac{1}{2}\boldsymbol{\nabla} \cdot \left(\eta^n \bar{\boldsymbol{\nabla}}\boldsymbol{v}^n + \eta^{p,n+1}\bar{\boldsymbol{\nabla}}\boldsymbol{v}^{n+1}\right) +$$

$$+ \frac{1}{2}\boldsymbol{\nabla} \cdot \left[\left(\sqrt{\frac{2\eta^n k_B T}{\Delta t \, \Delta V}} + \sqrt{\frac{2\eta^{p,n+1} k_B T}{\Delta t \, \Delta V}}\right)\boldsymbol{W}^n\right]$$

$$\boldsymbol{\nabla} \cdot \boldsymbol{v}^{n+1} = 0.$$

---

**Algorithm 3.3** Implicit trapezoidal integrator for the limiting (overdamped) equation (3.37), as implemented in the IBAMR software framework [86].

---

1. In the predictor stage, solve the steady Stokes equation with random forcing,

$$\boldsymbol{\nabla}\pi^n = \eta\boldsymbol{\nabla}^2\boldsymbol{v}^n + \boldsymbol{\nabla}\cdot\left(\sqrt{\frac{2\eta\,k_BT}{\Delta t\Delta V}}\,\boldsymbol{W}^n\right) - \rho\beta c^n\boldsymbol{g}$$

$$\boldsymbol{\nabla}\cdot\boldsymbol{v}^n = 0.$$

2. Do a predictor step for (3.7) by solving for $c^{p,n+1}$,

$$\frac{c^{p,n+1} - c^n}{\Delta t} = -\boldsymbol{v}^n\cdot\boldsymbol{\nabla}c^n + \chi_0\boldsymbol{\nabla}^2\left(\frac{c^n + c^{p,n+1}}{2}\right) + \boldsymbol{\nabla}\cdot\left(\sqrt{\frac{2\chi_0\vartheta_0}{\Delta t\Delta V}}\,\boldsymbol{W}_c^n\right).$$

3. Solve the corrector steady Stokes equation

$$\boldsymbol{\nabla}\pi^{n+\frac{1}{2}} = \eta\left(\boldsymbol{\nabla}^2\boldsymbol{v}^{n+\frac{1}{2}}\right) + \boldsymbol{\nabla}\cdot\left(\sqrt{\frac{2\eta\,k_BT}{\Delta t\Delta V}}\,\boldsymbol{W}^n\right) - \rho\beta\left(\frac{c^n + c^{p,n+1}}{2}\right)\boldsymbol{g}$$

$$\boldsymbol{\nabla}\cdot\boldsymbol{v}^{n+\frac{1}{2}} = 0.$$

   Note that the same random stress is used here as in the predictor, so that if there is no gravity, we can set $\boldsymbol{v}^{n+\frac{1}{2}} = \boldsymbol{v}^n$. In general if an iterative solver is used the solution from the predictor $\boldsymbol{v}^n$ should be used as an initial guess to speed up the convergence.

4. Take a corrector step for concentration to compute $c^{n+1}$,

$$\frac{c^{n+1} - c^n}{\Delta t} = -\boldsymbol{v}^{n+\frac{1}{2}}\cdot\boldsymbol{\nabla}\left(\frac{c^n + c^{p,n+1}}{2}\right) + \chi_0\boldsymbol{\nabla}^2\left(\frac{c^n + c^{n+1}}{2}\right) + \boldsymbol{\nabla}\cdot\left(\sqrt{\frac{2\chi_0\vartheta_0}{\Delta t\Delta V}}\,\boldsymbol{W}_c^n\right).$$

---

Our spatial discretizations were constructed to obey a discrete fluctuation-dissipation balance principle, which means that for sufficiently small time steps the numerical schemes will produce the correct equilibrium fluctuations even when the nonlinear terms are important. In the absence of advection, the schemes (2.31) and (2.33) reduce to the implicit midpoint rule, which was designed to produce the correct equilibrium fluctuations for *any* time step. What is not obvious is how increasing the time step size affects the long-time behavior of schemes in the presence of the nonlinear advective terms, which are treated explicitly. We study this question numerically in this section.

In fluctuating hydrodynamics, the magnitude of the equilibrium fluctuations is controlled by the degree of coarse graining, more specifically, by the average number of particles $N_p$ (microscopic degrees of freedom) per hydrodynamic cell (macroscopic degree of freedom). In particular, the law of large numbers suggests that the Gaussian fluctuations at equilibrium have a variance inversely proportional to the volume of a hydrodynamic cell $\Delta V$. In order to model the effect of the degree of coarse graining we can introduce a parameter $\epsilon \sim N_p^{-1}$ that measures the strength of the fluctuations, with $\epsilon \sim 1$ indicating very strong fluctuations, i.e., minimal coarse graining. While we cannot expect Markovian SPDE models to really be a good approximation to reality in the absence of coarse-graining, from a numerical analysis perspective it is important to understand how robust the numerical schemes are to increased magnitude of the fluctuations. We note that the types of schemes we use here may have uses in other fields such as turbulence, where reproducing the correct spectrum of fluctuations is also important.

In section 3.5.3, we investigate the diffusive mixing of a binary liquid when subjected to a temperature gradient. In particular, we study the noneqilibrum fluctuations in concentration induced by advection by the fluctuating velocity field. We perform simulations in the absence of gravity and in the presence of Earth's gravity, and we determine that the assumption of uniform separation of timescales between concentration and velocity fails for sufficiently small wavenumbers when gravity is present.

### 3.5.1 Fluctuating Burgers Equation

We first turn our attention to the fluctuating Burgers equation. For simplicity, we take $c = 1$ and consider a periodic system with zero total momentum (no macroscopic advection),

$$\partial_t u + u\,\partial_x u = \nu\,\partial_{xx}^2 u + (2\epsilon\nu)^{1/2}\,\partial_x \mathcal{W}.$$

When the spatial discretization (3.23) is used, the coarse-grained velocities $u_j$ have Gaussian equilibrium fluctuations with mean zero and covariance

$$\langle u_i u_j \rangle = \frac{\epsilon}{\Delta x}\delta_{ij}.$$

The equilibrium magnitude of the advection velocities is therefore $|u| \approx \sqrt{\epsilon/\Delta x}$, which is a measure of the typical magnitude of the advection velocity.

#### 3.5.1.1 Dimensionless Numbers

In deterministic fluid dynamics, the dimensionless number that describes how well advection is resolved by the time step size is the advective CFL number

$$\alpha = \frac{|u|\,\Delta t}{\Delta x} \approx \Delta t \epsilon^{\frac{1}{2}} \Delta x^{-\frac{3}{2}}.$$

Traditional wisdom says that for schemes that handle advection explicitly $\Delta t$ should be chosen such that $\alpha \lesssim 1$. The presence of diffusion, however, stabilizes numerical schemes by adding dissipation and introduces the viscous CFL number $\beta$ and the cell Reynolds number $r$,

$$\beta = \frac{\nu\Delta t}{\Delta x^2}, \quad r = \frac{\alpha}{\beta} = \frac{|u|\,\Delta x}{\nu} \approx \epsilon^{\frac{1}{2}}\nu^{-1}\Delta x^{\frac{1}{2}}.$$

Note that the cell Reynolds number measures the relative importance of the nonlinear term (advection) versus the linear term (diffusion), and is independent of $\Delta t$. In the deterministic setting, standard von Neumann stability analysis for the Euler scheme applied to the advection-diffusion equation suggests that our centered discretization of advection is stable if $\alpha^2/2 \le \beta \le 1/2$. This suggests that the dimensionless number

$$\gamma = \frac{\alpha^2}{\beta} = r^2\beta = \frac{|u|^2\,\Delta t}{\nu} \sim \frac{\epsilon\Delta t}{\nu\Delta x}$$

may be important in controlling the behavior of our spatio-temporal discretizations.

For weak fluctuations ($\epsilon \ll 1$) or strong dissipation ($r \ll 1$), both of which are typically true for realistic fluids at small scales and sufficient levels of coarse-graining ($N_p \gg 1$), the accuracy is controlled by the viscous CFL number $\beta$. In particular, if $\beta \ll 1$ we can be confident that the numerical scheme resolves the dynamics of the fluctuations accurately. However, running with small viscous CFL numbers is often impractical. Our semi-implicit schemes are designed to be stable and also to correctly reproduce the equilibrium fluctuations even for large time steps, $\beta \gg 1$, at least as long as $\alpha \ll 1$. An important question, which is difficult to analyze with existing analytical tools, is how large the time step can be before the explicit handling of the nonlinear advective term $u\,\partial_x u$ introduces large errors. We study this question here by examining the equilibrium fluctuations for strong fluctuations, $\epsilon \gtrsim 1$, and large time steps, $\beta \gg 1$.

### 3.5.1.2 Static Structure Factors

In order to study the behavior of the equilibrium fluctuations we follow the approach used in Ref. [42]. In this approach, instead of studying the fluctuations in the actual (real space) variables $u_j$, we study the equilibrium discrete Fourier spectrum of the fluctuating variables, defined as

$$S_\kappa = N\epsilon^{-1}\Delta x \, \langle \hat{u}_k \hat{u}_k^\star \rangle \,.$$

Here the discrete Fourier transform is defined as

$$\hat{u}_k = N^{-1} \sum_{j=0}^{N} u_{j+1} e^{-ij\Delta k},$$

where $0 \leq \kappa \leq \lfloor N/2 \rfloor$ is the waveindex and $\Delta k = 2\pi\kappa/N \leq \pi$ is the dimensionless wavenumber. This quantity $S_\kappa$ is a dimensionless discrete version of what is called the *static structure factor* $S(k)$ in the physics literature, where $k = \Delta k/\Delta x$ is the physical wavenumber. For fluctuating hydrodynamics, at thermodynamic equilibrium

$$S_\kappa = 1 \text{ for all } \kappa \neq 0,$$

which is a re-statement of the discrete fluctuation-dissipation balance principle.

For periodic systems, due to translational invariance the quantity $S_\kappa$ contains the same statistics about the equilibrium fluctuations as the $N \times N$ covariance matrix $C_{j,j'} = \langle u_j u_{j'} \rangle$. The advantage of using the Fourier description is that it illustrates the behavior at different physical length scales. It is expected that any numerical scheme will produce some artifacts at the largest wavenumbers because of the strong corrections due to the discretization; however, small wavenumbers, $\Delta k \ll 1$, ought to have much smaller errors because they evolve over time scales and length scales much larger than the discretization step sizes $\Delta x$ and $\Delta t$. A scheme or choice of time step size that produces a *discrete structure factor* $S_\kappa$ much different from one at small wavenumbers must be rejected as unphysical. It is important to emphasize, however, that getting a good equilibrium spectrum for the fluctuations is not a guarantee that a scheme accurately models the *dynamics* of the fluctuations.

### 3.5.1.3 Numerical Results

In Fig. 3.1 we show numerical results for the equilibrium structure factor $S_\kappa$ for a periodic system with $\nu = 1$ and $\Delta x = 1$ and zero total momentum, $\langle u_j \rangle = 0$. To illustrate the importance of using a Hamiltonian discretization of advection in the nonlinear setting, we consider a scheme where the advective term $uu_x$ is handled using the conservative but non-Hamiltonian discretization

$$(\boldsymbol{Su})_j = \frac{u_{j+\frac{1}{2}}^2 - u_{j-\frac{1}{2}}^2}{2\Delta x} = \frac{u_{j+1}^2 - u_{j-1}^2}{4\Delta x}, \text{ where } u_{j+\frac{1}{2}}^2 = \frac{u_j^2 + u_{j+1}^2}{2}, \tag{3.38}$$

instead of the conservative Hamiltonian discretization (3.22). We recall that the correct answer is $S_\kappa = 1$ for all wavenumbers. The results in the left panel of Fig. 3.1 illustrate that for weak fluctuations (i.e., nearly linear equations), the correct spectrum is obtained. However, for strong fluctuations (i.e., nonlinear equations), $\epsilon = 4$, the non-Hamiltonian scheme produces the wrong static spectrum of fluctuations at small wavenumbers, and reducing $\Delta t$ does not help.

On the other hand, the Hamiltonian discretization gives small errors in the spectrum even for the larger time step size. In the right panel of Fig. 3.1 we zoom in to show the magnitude and form of the errors in the structure factors for the explicit-implicit trapezoidal scheme (2.31) and for the midpoint scheme (2.33) with $w_1 = 1/2$ and with $w_1 = 1/4$. We see that all three schemes show similarly small errors in the spectrum. Reducing $\Delta t$ by an
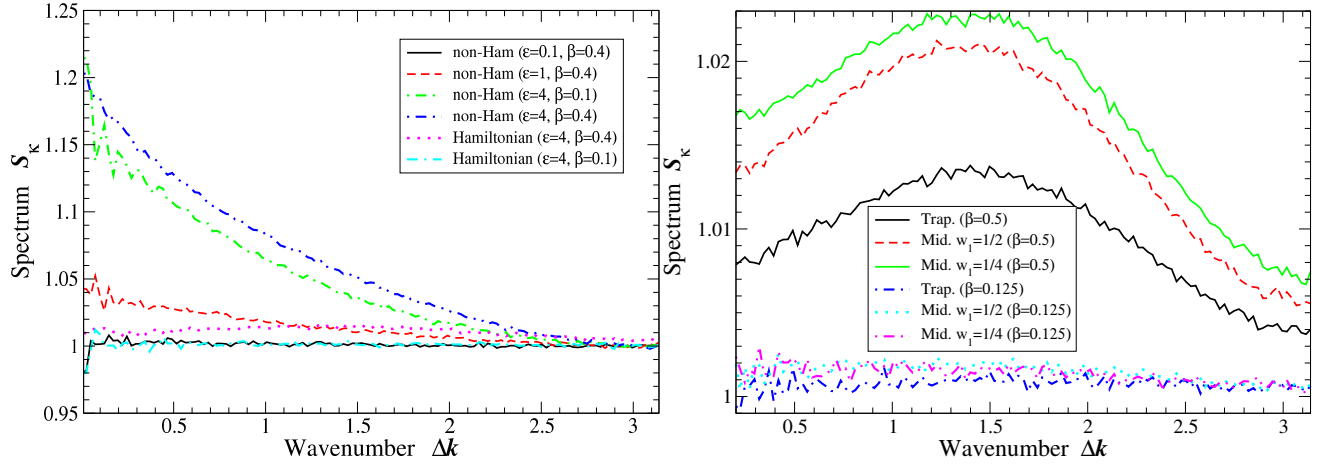
Figure 3.1: Static structure factor $S_\kappa$ for a periodic system of 256 cells at thermodynamic equilibrium in the case of strong fluctuations, $\epsilon = 4$. (*Left panel*) Midpoint scheme (2.33) with $w_1 = 1/2$ and non-Hamiltonian advection (3.38) for time step size $\beta = 0.4$ for weak fluctuations $\epsilon = 0.1$ ($\alpha \approx 0.13$), medium fluctuations $\epsilon = 1$ ($\alpha = 0.4$) and strong fluctuations $\epsilon = 4$ ($\alpha = 0.8$). For $\epsilon = 4$, reducing the time step to $\beta = 0.1$ ($\alpha = 0.2$) does not significantly improve the accuracy and even if $\Delta t \to 0$ the wrong spectrum of fluctuations is obtained. Switching to the Hamiltonian discretization (3.22) significantly lowers the errors. (*Right panel*) Comparison between the trapezoidal scheme (2.31) and for the midpoint scheme (2.33) with $w_1 = 1/2$ and with $w_1 = 1/4$ for $\epsilon = 4$ for large time step $\beta = 0.5$ ($\alpha = 1$) and small time step $\beta = 0.05$ ($\alpha = 0.1$). Advection is discretized in a Hamiltonian manner.

order of magnitude makes the error statistically insignificant. We have verified that the errors are of second order in the time step size $\Delta t$ for all three schemes.

In Fig. 3.2 we show numerical results for the static structure factor in the case of weaker fluctuations, $\epsilon = 0.1$ and $\epsilon = 0.01$, but large time step size. This is a typical scenario for fluctuating hydrodynamics in practice, since for reasonable degree of coarse graining the fluctuations would be small and the behavior of the equations would be close to that of the linearized equations. In the absence of the advective nonlinearity our schemes are stable for arbitrary viscous CFL number $\beta$. Under equilibrium conditions the semi-implicit predictor-corrector schemes we consider are observed to be stable up to rather large $\Delta t$ as measured in the advective CFL $\alpha$, and even the dimensionless number $\gamma = \alpha^2/\beta$. However, for sufficiently large $\Delta t$ the nonlinearities are expected to play some role, and one cannot expect to be able to increase the time step up to the stability limit and still maintain reasonable accuracy. The results in Fig. 3.2 show that for large $\Delta t$ there appear significant artifacts in the static structure factor for the trapezoidal scheme (2.31) and for the midpoint scheme (2.33) with $w_1 = 1/4$. While the magnitude of the errors is small, the problematic observation is that the errors have a peak at the smallest wavenumbers, where we, in fact, expect schemes to closely mimic the continuum equations.

The above observations lead us to select the midpoint scheme (2.33) with $w_1 = 1/2$ as the most robust temporal integrator for the fluctuating Burgers equation. At the same time, we should recognize that the best choice of scheme will depend on the quantity of interest and the particular problem under consideration. All schemes are observed to produce equilibrium fluctuations that are rather robust under the presence of strong non-linearities if a Hamiltonian advection of discretization is employed. In the next section we confirm that this conclusion also holds for the fluctuating Navier-Stokes equation.

### 3.5.2 Fluctuating Navier-Stokes Equation with Passive Tracer

We now turn our attention to the fluctuating Navier-Stokes equations with a passively-advected scalar, eq.(3.24) and (3.25). Here we set $\rho^{-1}k_B T = \epsilon$ so that $\epsilon$ controls the magnitude of both the velocity and the concentration fluctuations. The implementation of our spatio-temporal discretizations and their accuracy in the linearized setting (weak fluctuations) is discussed in more detail in Ref. [39]. Our implementation is integrated into the the IBAMR software framework [86], an open-source library for developing fluid-structure interaction models that use the immersed boundary method. Based on our experience with the fluctuating Burgers equation, we focus our attention on the mixed explicit-implicit trapezoidal scheme (2.31) and the midpoint scheme (2.33) with $w_1 = 1/2$. For simplicity, here we focus on two spatial dimensions, but emphasize that our formulation, numerical schemes, implementation, and conclusions, apply to three spatial dimensions as well.
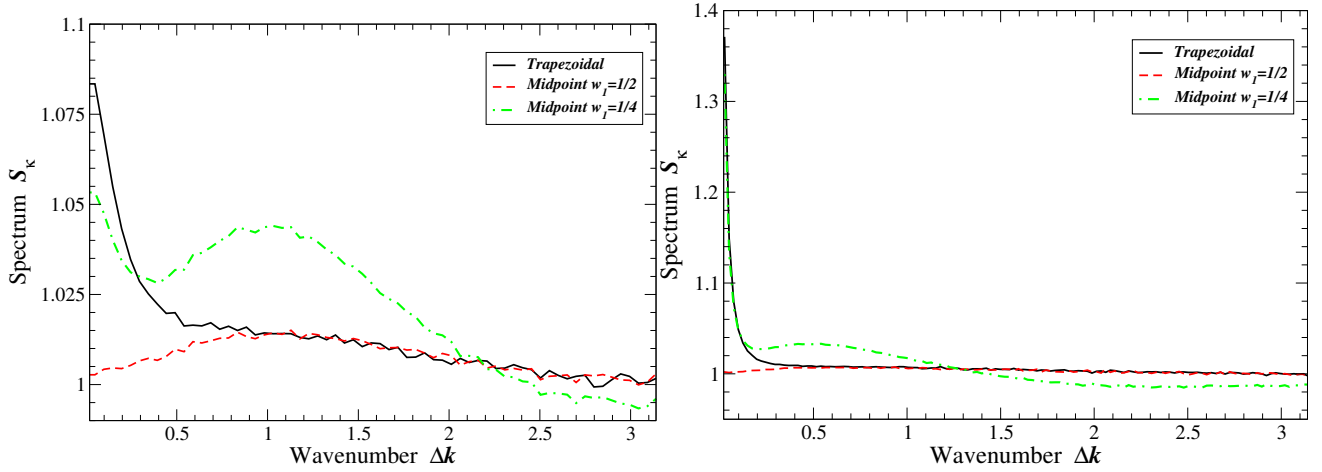
Figure 3.2: Static structure factor $S_\kappa$ at thermodynamic equilibrium in the case of weaker fluctuations and large time step sizes, for the trapezoidal scheme (2.31) and for the midpoint scheme (2.33) with $w_1 = 1/2$ and with $w_1 = 1/4$. (*Left panel*) Moderate fluctuations, $\epsilon = 0.1$, for time step size $\beta = 10$, $\alpha \approx 3.2$, $\gamma = 1$. (*Right panel*) Weak fluctuations, $\epsilon = 0.01$ and time time step size, $\beta = 100$, $\alpha = 10$, $\gamma = 1$.

For simplicity, in our numerical tests we set $\Delta x = \Delta y = 1$. The diffusion coefficients for momentum and concentration are set to $\nu = 1$ and $\chi = 0.25$, and a grid of size $64 \times 64$ is employed. The same dimensionless numbers as for the Burgers equation apply, with the difference that there is a separate diffusive CFL for the concentration, $\beta_c = \chi\beta/\nu$, and therefore the cell Peclet number $r_c = |u|\Delta x/\chi$ is four times larger than the cell Reynolds number $r$ (in practice, the Schmidt number $S_c = \nu/\chi \gg 1$).

### 3.5.2.1   Static Structure Factors

The equilibrium fluctuations in velocity and concentration are characterized by the static structure factors, which are the equilibrium average of the discrete Fourier spectrum of the fluctuating velocities and concentrations. Concentration fluctuations are characterized via

$$S_{\boldsymbol{\kappa}}^{(c)} = N\epsilon^{-1}\Delta V \left\langle \hat{c}\hat{c}^\star \right\rangle,$$

where $\Delta V = \Delta x\,\Delta y$ is the volume of the hydrodynamic cells. For the velocity fluctuations, we calculate the spectrum of the fluctuations of a variable related to vorticity [39],

$$S_{\boldsymbol{\kappa}}^{(\Omega)} = N\epsilon^{-1}\Delta V \left\langle \hat{\Omega}\hat{\Omega}^\star \right\rangle,$$

where $\hat{\Omega}$ is obtained from the discrete Fourier spectrum of the velocity components as

$$\hat{\Omega} = k^{-1}\left(k_x\hat{v}_y - k_y\hat{v}_x\right),$$

and $k = \sqrt{k_x^2 + k_y^2}$ is the wavenumber. Note that $S_{\boldsymbol{\kappa}}^{(\Omega)}$ fully characterizes the covariance of the velocity fluctuations since our scheme ensures the velocity is discretely divergence free at all times and $k^{-1}\left(-k_y, k_x\right)$ spans the subspace of divergence-free velocities in Fourier space. For staggered variables the shift between the corresponding grids should be taken into account as a phase shift in Fourier space, for example, $\exp\left(k_x\Delta x/2\right)$ for $v_x$. Additionally, the wavenumber $\boldsymbol{k} = (k_x, k_y)$ should be replaced by the effective wavenumber $\tilde{\boldsymbol{k}}$ that takes into account the centered discretization of the projection operator, for example,

$$\tilde{k}_x = \frac{\exp\left(ik_x\Delta x/2\right) - \exp\left(-ik_x\Delta x/2\right)}{i\Delta x} = k_x\frac{\sin\left(k_x\Delta x/2\right)}{\left(k_x\Delta x/2\right)}. \tag{3.39}$$

One can additionally define and measure the cross-correlation between concentration and velocity fluctuations via the cross-correlation static structure factor

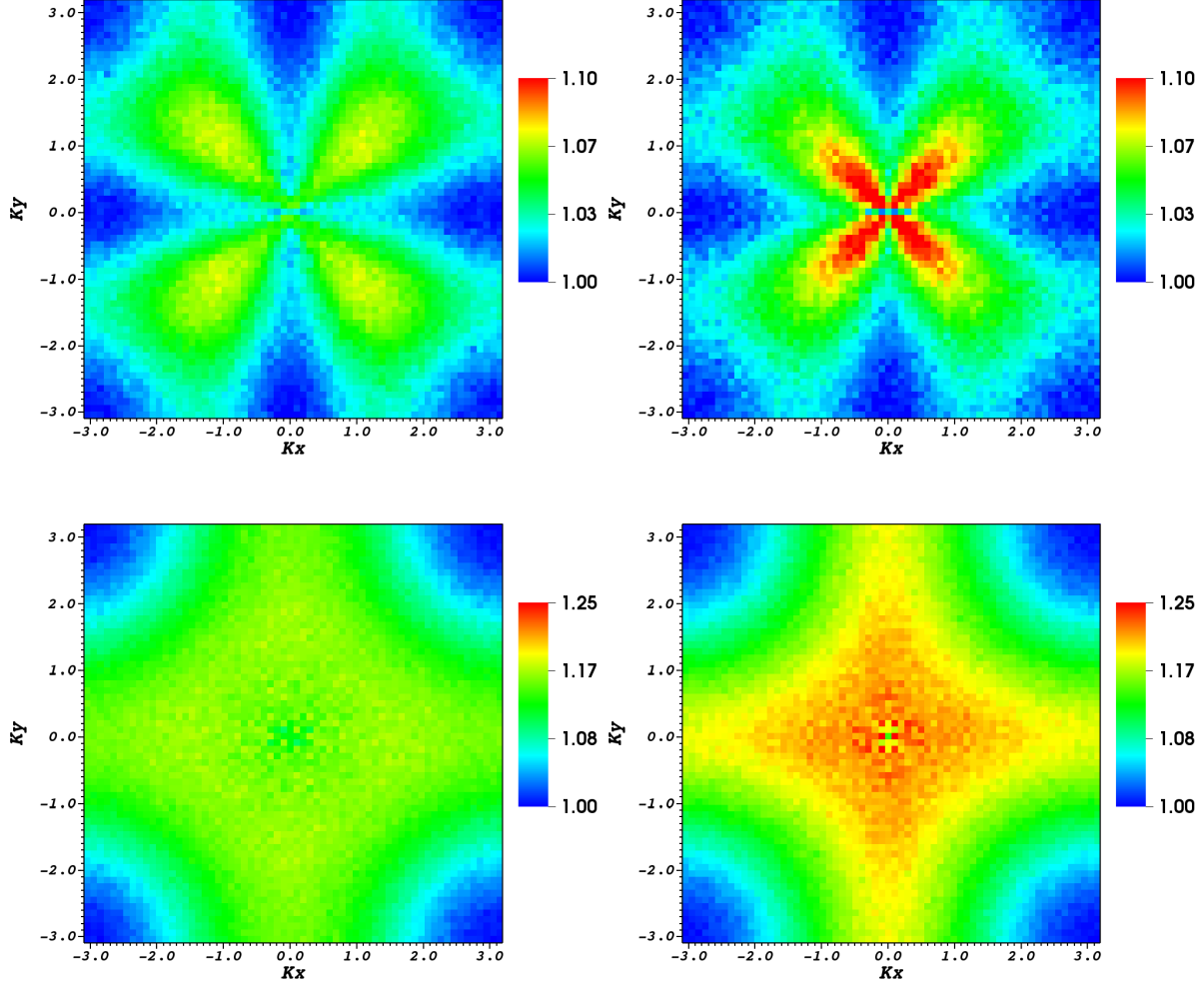$$S_{\boldsymbol{\kappa}}^{(c,\Omega)} = N\epsilon^{-1}\Delta V \left\langle \hat{c}\hat{\Omega}^\star \right\rangle,$$

47

Figure 3.3: Discrete structure factors $S_{\boldsymbol{\kappa}}^{(\Omega)}$ (top) and $S_{\boldsymbol{\kappa}}^{(c)}$ (bottom) for the midpoint scheme (2.33) with $w_1 = 1/2$ on the left and for the trapezoidal scheme (2.31) on the right, for the case of large fluctuations $\epsilon = 4$. (*Top row*) For velocity spectra the time step size is such that $\beta = 0.5$, and the advective CFL is $\alpha = 1$. (*Bottom row*) For concentration spectra the diffusive CFL $\beta_c = \chi\beta/\nu = 0.0625$ and advective CFL $\alpha = 0.5$.

which is in general a complex number.

Discrete fluctuation-dissipation balance in the coupled velocity-concentration equations requires that $S_{\boldsymbol{\kappa}}^{(c)} = S_{\boldsymbol{\kappa}}^{(\Omega)} = 1$ and $S_{\boldsymbol{\kappa}}^{(c,\boldsymbol{v})} = 0$ for all nonzero wavenumbers. Deviations from these values indicate a violation of discrete fluctuation-dissipation balance and can be used to numerically access the behavior of the schemes in the nonlinear setting, as we do next.

### 3.5.2.2 Numerical Results

In 3.3 we show numerical results for the spectrum of the fluctuations in the solenoidal modes of velocity and concentration for strong fluctuations, $\epsilon = 4$. We see that, just as for the fluctuating Burgers equation, both the trapezoidal and the midpoint scheme show artifacts in the spectra, especially for concentration and for the trapezoidal scheme. The cross-correlation $S_{\boldsymbol{\kappa}}^{(c,\Omega)}$ is found to be small and difficult to measure due to large statistical errors.

We have verified that as the time step is reduced, both schemes give the correct spectrum even for strong fluctuations (i.e., strong nonlinearities). In Fig. 3.4 we show the average error in the equilibrium spectrum $\langle |S_{\boldsymbol{\kappa}} - 1| \rangle$ for vorticity and concentration. The second-order weak accuracy of the error is clearly seen in Fig. 3.2 for both velocity and concentration and for both the midpoint and the trapezoidal scheme.
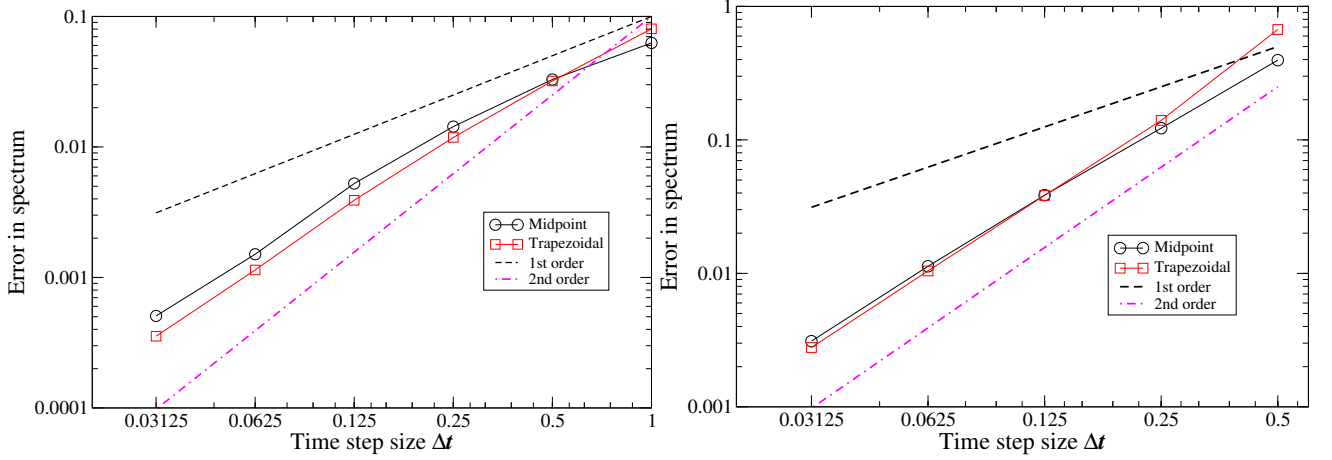
Figure 3.4: Average error in the structure factor for several time step sizes for the trapezoidal scheme (2.31) and for the midpoint scheme (2.33) with $w_1 = 1/2$, for the case of large fluctuations $\epsilon = 4$. First- and second-order error trends are indicated, showing the second-order asymptotic accuracy. Error bars are comparable to the symbol size and not shown. (Left panel) $\left\langle S_{\boldsymbol{\kappa}}^{(\Omega)} - 1 \right\rangle$. (Right panel) $\left\langle S_{\boldsymbol{\kappa}}^{(c)} - 1 \right\rangle$.

In Fig. 3.5 we show the spectrum of concentration fluctuations $S_{\boldsymbol{\kappa}}^{(c)}$ for the case of weak fluctuations, $\epsilon = 0.01$, and large time step size, viscous CFL $\beta = 50$ and diffusive CFL $\beta_c = 12.5$, and advective CFL $\alpha = 5$. We see a large error for small wavenumbers for the trapezoidal scheme. A similar but weaker artifact is seen for the velocity spectrum $S_{\boldsymbol{\kappa}}^{(\Omega)}$ as well, indicating that the trapezoidal scheme violates fluctuation-dissipation balance at small wavenumbers for large $\Delta t$. The midpoint scheme is seen to be much more accurate for both $S_{\boldsymbol{\kappa}}^{(c)}$ and $S_{\boldsymbol{\kappa}}^{(\Omega)}$. These investigations confirm that the midpoint scheme (2.33) with $w_1 = 1/2$ is the more robust temporal integrator for fluctuating hydrodynamics.

### 3.5.3 Giant Concentration Fluctuations

In this section we apply our temporal integrators to the study of diffusive mixing in binary liquid mixtures in the presence of a temperature gradient and gravity. These simulations were run by Yifei Sun using the IBAMR software [86] which implements the temporal integrators introduced in Section 2.2, and we are grateful for the time and effort he dedicated to producing these results. The equations for the velocity $\boldsymbol{v}\left(\boldsymbol{r}, t\right)$ and mass concentration $c\left(\boldsymbol{r}, t\right)$ for a mixture of two fluids can be approximated as

$$\rho \partial_t \boldsymbol{v} + \boldsymbol{\nabla}\pi = \eta \boldsymbol{\nabla}^2 \boldsymbol{v} + \boldsymbol{\nabla} \cdot \left( \sqrt{2\eta k_B T_0}\, \boldsymbol{\mathcal{W}} \right) - \rho \beta c \boldsymbol{g} \tag{3.40}$$

$$\boldsymbol{\nabla} \cdot \boldsymbol{v} = 0$$

$$\partial_t c + \boldsymbol{v} \cdot \boldsymbol{\nabla} c = \chi \boldsymbol{\nabla} \cdot \left( \boldsymbol{\nabla} c + c\left(1 - c\right) S_T \boldsymbol{\nabla} T \right), \tag{3.41}$$

where $\boldsymbol{\mathcal{W}}$ denotes white-noise stochastic forcing for the thermal fluctuations and $\boldsymbol{g}$ is gravity. Here we have ignored the stochastic forcing term $\boldsymbol{\nabla} \cdot \left( \sqrt{2\chi_0 c_0}\, \boldsymbol{\mathcal{W}}_c \right)$, which is responsible for equilibrium fluctuations in the concentration, since our focus will be on the much larger nonequilibrium fluctuations induced by the coupling to the velocity equation via the advective term $\boldsymbol{v} \cdot \boldsymbol{\nabla} c$. The shear viscosity $\eta = \nu \rho$, mass diffusion coefficient $\chi$, solutal expansion coefficient $\beta$, and Soret coefficient $S_T$, are assumed to be given material constants independent of concentration. Furthermore, the density $\rho$ is taken to be constant in a Boussinesq approximation. Temperature fluctuations are not considered in a large Lewis number (very fast temperature dynamics) approximation [88]. We assume that the applied temperature gradient $\boldsymbol{\nabla} T$ is weak and approximate $T \approx T_0 = \text{const}$. In principle there is no difficulty in making the temperature be spatially-dependent, however, our simplifying approximation is justified because the typical relative temperature difference across the sample is not large.

These equations are extremely difficult to integrate numerically for large Schmidt number, $S_c = \nu/\chi \gg 1$, if one wants to get dynamics correct. Therefore, we actually take a limit of the above equations $S_c \to \infty$ and integrate the resulting dynamics numerically. In a linearized setting, $c = \bar{c} + \delta c$ and $\boldsymbol{v} \equiv \delta \boldsymbol{v}$, the overdamped equations are
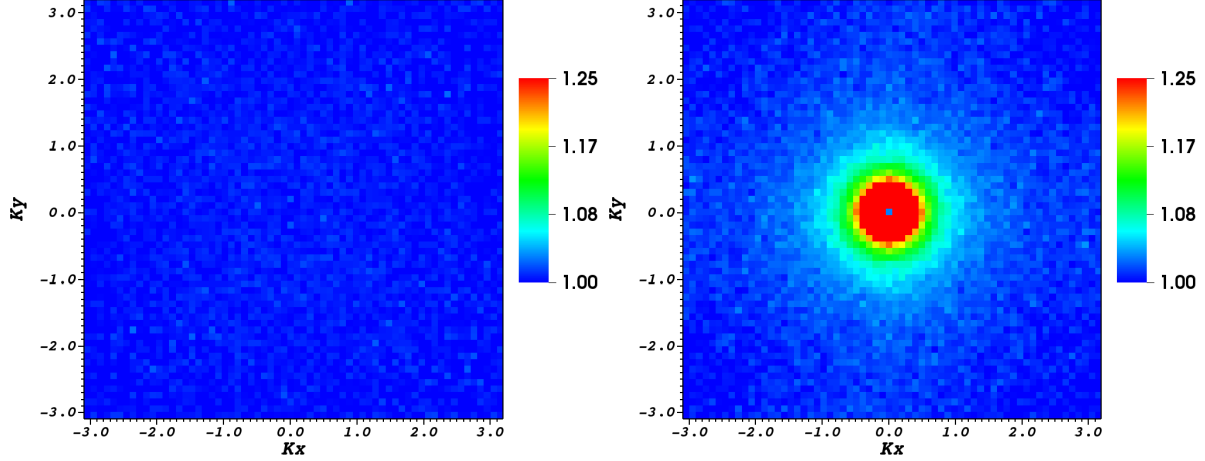
Figure 3.5: Discrete structure factor for concentration $S_\kappa^{(c)}$ for the midpoint scheme (2.33) with $w_1 = 1/2$ on the left and for the trapezoidal scheme (2.31) on the right, for the case of weak fluctuations, $\epsilon = 0.01$, and large time step, $\beta = 50$, $\beta_c = 12.5$, $\alpha = 5$.

written in [88] as a large Schmidt and large Lewis number approximation to the complete system of equations,

$$\nabla \pi = \eta \nabla^2 \boldsymbol{v} + \nabla \cdot \left( \sqrt{2\eta k_B T_0}\, \boldsymbol{\mathcal{W}} \right) - \rho \beta \left( \delta c \right) \boldsymbol{g} \tag{3.42}$$

$$\nabla \cdot \boldsymbol{v} = 0$$

$$\partial_t \left( \delta c \right) + \boldsymbol{v} \cdot \boldsymbol{h} = \chi \nabla^2 \left( \delta c \right),$$

where $\boldsymbol{h} = \nabla \bar{c}$ is the concentration gradient imposed by the applied temperature gradient. Theoretical analysis is based on the simplified linearized equations (3.42) under the assumption that the applied gradient $\boldsymbol{h}$ is constant and weak. The theory predicts the *steady-state* spectrum of the concentration fluctuations at wave number $\boldsymbol{k}$ to be [88]

$$S\left( \boldsymbol{k} \right) = \left\langle \left( \widehat{\delta c}\left( \boldsymbol{k} \right) \right) \left( \widehat{\delta c}\left( \boldsymbol{k} \right) \right)^\star \right\rangle = \frac{k_B T_0}{\left( \eta \chi k_\perp^4 - g \rho \beta h_\parallel \right)} h_\parallel^2, \tag{3.43}$$

where $\perp$ and $\parallel$ denote the perpendicular and parallel component relative to gravity, respectively. The characteristic $k_\perp^4$ power-law divergence of the spectrum at large wavenumbers is a signature of long-ranged nonequilibrium fluctuations and leads to a dramatic increase in the magnitude and correlation length of the fluctuations compared to systems in thermodynamic equilibrum; this effect has been termed *giant fluctuations* [51, 53]. The expression (3.43) shows that fluctuations at wavenumbers below the critical (rollover) wave number $k_c^4 = g\rho\beta h_\parallel / (\eta\chi)$ are suppressed by gravity. Henceforth we will assume that the gradient is parallel to gravity, $h_\parallel = h$.

For the dynamics of vertically-averaged concentration, i.e., for $k_\parallel = 0$, $k_\perp = k$, the linearization (3.42) predicts an exponential time correlation function

$$S\left( k, t \right) = \left\langle \left( \widehat{\delta c}\left( k, t \right) \right) \left( \widehat{\delta c}\left( k, 0 \right) \right)^\star \right\rangle = S\left( k \right) e^{-t/\tau} \tag{3.44}$$

with decay time

$$\tau^{-1} = \chi k^2 \left[ 1 + \left( \frac{k_c}{k} \right)^4 \right]. \tag{3.45}$$

The relaxation has a minimum at $k = k_c$ with value $\tau_{\min}^{-1} = 2\chi k_c^2$. For smaller wavenumbers $\tau$ becomes the smallest time scale and limits the stability of the simulations. As we discuss in Section 3.5.3.2, at small wavenumbers the separation of time scales used to justify the overdamped limit fails and the fluid inertia has to be taken into account. In the absence of gravity, however, as we discuss in Section 3.5.3.1, the separation of time scales is uniform across all length scales and the overdamped limit can be used.

50

### 3.5.3.1 Giant Fluctuations in Microgravity

In this section we perform computer simulations of diffusive mixing in microgravity, recently studied aboard a satellite in orbit around the Earth during the GRADFLEX experiment [53]. The experimental configuration consists of a dilute solution of polystyrene in toluene with average concentration $c_0 = 0.018$, confined between two parallel transparent plates that are a distance $H = 1$mm apart. A temperature gradient $\boldsymbol{\nabla} T = \Delta T / H$ is imposed along the $y$ axes via the plates at time $t = 0$. At long times, the weak temperature gradient leads to a strong concentration gradient $\boldsymbol{\nabla} \bar{c} = \bar{c} S_T \boldsymbol{\nabla} T$ due to the Soret effect, giving rise to an exponential steady-state concentration profile $\bar{c}(y)$. Quantitative shadowgraphy is used to observe and measure the strength of the fluctuations in the concentration around $\bar{c}$ via the change in the refraction index. Some of us already modeled the *steady-state* fluctuations in the GRADFLEX experiment using the inertial equations (3.40,3.41) in previous work [39]. Here we extend this study to also model the *dynamics* of the concentration fluctuations following the time when the temperature gradient is first applied (to a uniform sample), before the steady state is reached. In future work we will compare our numerical results to experimental measurements.

In the actual experiments reported in Ref. [53], concentration diffusion is much slower than momentum diffusion, corresponding to Schmidt number $S_c = \nu / \chi \approx 3 \cdot 10^3$. This level of stiffness makes direct simulation of the temporal dynamics of the fluctuations infeasible, as long averaging is needed to obtain accurate steady-state spectra, especially for small wavenumbers. In order to bypass this problem, in our previous work [39] we artificially increased $\chi$ and decreased $\nu$ to reduce the Schmidt number, while keeping the product $\chi \nu$ fixed. This is exactly the scaling in which one can formally derive the limiting overdamped dynamics (3.7) [23], and from (3.43) we see that the static structure factor depends only on the product $\chi \nu$ when $\nu \gg \chi$. In fact, artificially decreasing the Schmidt number while keeping $\chi \nu$ fixed, and rescaling time appropriately, can be seen as an instance of the *seamless* multiscale method presented in Ref. [89]. Here we take the overdamped limit and solve the limiting equations numerically, thus completely avoiding the stiffness issue. This allows us to take a much larger time step size, related to the time scale of mass diffusion, rather than the fast momentum diffusion.

For the GRADLEX experiments we can assume $c \ll 1$ and thus $c(1 - c) \approx c$ to make the Soret term linear in concentration and treat the Soret flux as advection by a Soret velocity $\boldsymbol{v}_s = -\chi S_T \boldsymbol{\nabla} T$, to obtain the concentration equation employed in our numerical method,

$$\partial_t c + \boldsymbol{\nabla} \cdot (c (\boldsymbol{v} - \chi S_T \boldsymbol{\nabla} T)) = \chi \boldsymbol{\nabla}^2 c. \tag{3.46}$$

We integrate the overdamped limit of (3.40,3.46) for $g = 0$ in time using Algorithm 3.3. The spatial discretization and the physical parameters are essentially identical to those used in incompressible simulations in our previous work, see Section V in [39]. An important improvement is that we now handle both the Soret term and the boundary condition for concentration implicitly, thus ensuring strict conservation of the total solutal mass. The domain is periodic in the directions parallel to the boundaries. At the top and bottom boundaries a no-flux boundary condition is imposed for the concentration, and a no-slip boundary condition is imposed for velocity. The observed light intensity, once corrected for the optical transfer function of the equipment, is proportional to the intensity of the fluctuations in the concentration averaged along the gradient,

$$c_\perp(x, z; t) = H^{-1} \int_0^H c(x, y, z; t) dy,$$

and this is the main quantity of interest in our simulations. What is actually measured experimentally is the static structure factor, which is the Fourier transform $\widehat{\delta c}_\perp$ of the concentration fluctuations averaged along the gradient direction,

$$S(k_x, k_z; t) = \left\langle \left( \widehat{\delta c}_\perp \right) \left( \widehat{\delta c}_\perp \right)^\star \right\rangle.$$

Because of the increase in the time step afforded by the use of the overdamped integrator, we are able here to perform fully three-dimensional simulations on a domain of dimensions $(4 \times 1 \times 4)$ mm, discretized on a $256 \times 64 \times 256$ grid with uniform grid spacing $\Delta x = 1/64$ mm. Here the thickness of the sample is $H = 1$ mm and corresponds to the experimental setup, and the lateral extend is set to $L = 4$ mm. The structure factors $S(k_x, k_z; t)$ were averaged radially to obtain $S(k; t)$, where $k = \sqrt{k_x^2 + k_z^2}$. Note that in this case it is possible to obtain the same results using two-dimensional simulations ($k_z = 0$) because of the symmetries of the linearized equations, nevertheless, we chose to obtain three-dimensional results directly comparable to experiments. The key physical parameters are $\rho = 0.858 \, \text{g/cm}^3$, $\chi = 1.97 \cdot 10^{-6} \, \text{cm}^2/\text{s}$, $\nu = 6.07 \cdot 10^{-3} \, \text{cm}^2/\text{s}$, $T_0 = 300 \, \text{K}$, $S_T = 0.06486 \, \text{K}^{-1}$, and the temperature difference is $\Delta T = 17.4 \, \text{K}$. Additional details of the experimental setup and parameters are given in Ref. [53]. The time step size was $\Delta t \approx 10 \, \text{s}$, corresponding to a diffusive Courant number $\chi \Delta t / \Delta x^2 \approx 8$, and the results were
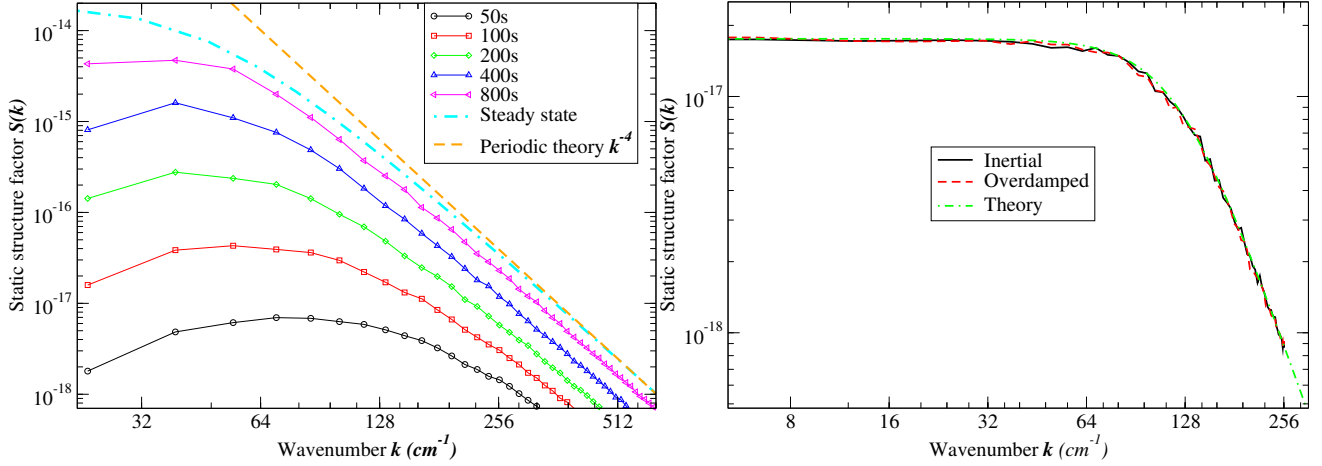
Figure 3.6: (Color online) (Left) Time evolution of the static structure factor $S(k;t)$ in the GRADFLEX experiment [53]. The steady-state spectrum, studied in more detail in Section V in [39], is also shown, and compared to the simple quasi-periodic theory (3.43). At smaller wavenumbers the steady-state fluctuations are damped due to confinement effects. (Right) Static structure factor $S(k)$ of concentration fluctuations in a binary liquid mixture subjected to a steady temperature gradient [71]. In order to account for spatial discretization artifacts, on the $x$ axes we show the modified wave number $\sin(k\Delta x/2)/(\Delta x/2)$ [39]. The theory (3.43) is shown for comparison.

averaged over 32 simulations. To obtain the static structure factor at steady state, we used a time step size that was twice larger, and averaged over 32 runs of length $140,000$ s, skipping the initial $14,000$ s in the analysis.

In the left panel of Fig. 3.6 we show the static structure factor as a function of time, along with the steady state asymptotic value. We observe that it takes a long time, on the time scale of the macroscopic diffusive mixing, to actually establish the steady state. This is in contrast to experiments performed in gravity, where gravity accelerates the dynamics of the concentration fluctuations at the smaller wavenumbers, as seen in (3.45). This was used in Refs. [90, 73] to construct a simple but approximate theory for the time evolution of the static structure factor during free diffusive mixing of two miscible liquids. Such a simple theory cannot be developed in microgravity because there is no separation of time scales between the dynamics of the mean and the dynamics of the fluctuations around the mean, and computer simulations become indispensable.

### 3.5.3.2 Giant Fluctuations in Earth Gravity

In this section we consider giant fluctuations in the presence of gravity. We model the experiments used in Ref. [71] to measure the Soret and diffusion coefficients in binary mixtures using a setup similar to that in the GRADFLEX experiment described in the previous section. A notable difference is that the average concentration $c_0 \approx 0.5$ is much larger than in the GRADFLEX setup, and only a small relative concentration difference is induced by an applied modest temperature gradient. We therefore approximate $c(1-c) \approx c_0(1-c_0)$ in (3.41), giving a constant mass Soret flux. In this example, because we want to accurately resolve the decay of the time correlation functions over several orders of magnitude, we perform two dimensional simulations. As we already explained, there is no difference between two and three dimensional simulations because of the simple one-dimensional geometry of the deterministic solution [26].

By linearizing the inertial dynamics (3.40,3.41) and taking a spatio-temporal Fourier transform we can obtain an approximate theory for the spatio-temporal correlation functions for the concentration fluctuations. This straightforward analysis predicts that the static factor $S(k)$ continues to follow (3.43) if $\nu \gg \chi$, but the time correlation function, unlike the overdamped result (3.47), is found to be a sum of two modes

$$S(k,t) = S_0 \exp\left(-\frac{t}{\tau_1}\right) + (S(k) - S_0)\exp\left(-\frac{t}{\tau_2}\right),\tag{3.47}$$

where we omit the long formula for $S_0$ and just quote the relaxation times

$$\tau_{1/2}^{-1} = \frac{1}{2}(\nu + \chi)k^2 \pm \frac{1}{2}\sqrt{k^4(\nu - \chi)^2 - 4\beta g h}.$$

In the limit $\nu/\chi \to \infty$, we get the diffusive relaxation time (3.45) if we use the minus sign, $\tau_\chi^{-1} \approx \chi k^2$, and for the plus sign we get the viscous relaxation time

$$\tau_\nu^{-1} = \nu k^2 \left[ 1 - \frac{\beta g h}{\nu \chi k^4} \right] \approx \nu k^2. \tag{3.48}$$

where $\nu = \eta/\rho$.

Note however that the relaxation times become complex-valued for

$$k_p \lesssim \left( \frac{4\beta g h}{\nu^2} \right)^{\frac{1}{4}} = \left( 4 \frac{\chi}{\nu} \right)^{\frac{1}{4}} k_c = \sqrt{2}\, S_c^{-\frac{1}{4}} k_c,$$

indicating the appearance of *propagative* rather than diffusive modes for small wavenumbers. Because of the fourth root power, for realistic values of $S_c \sim 10^4$, propagative modes appear at wavenumbers that are, in principle, observable in experiments via very low-angle light scattering and shadowgraph techniques, although, to our knowledge, experimental observation of propagative modes has only been reported for temperature fluctuations [91]. This shows that there is a *qualitative* difference between the inertial and overdamped dynamics in this example. This comes because of the lack of separation between the relaxation times associated with mass ($\tau_\chi$) and momentum diffusion ($\tau_\nu$) for wavenumbers $k \lesssim k_p$. In order to obtain accurate results over the whole range of wavenumbers observed in experiments, we need to account for the fluid inertia and integrate the system in time using Algorithm (3.1). For comparison we also numerically take the overdamped limit and use Algorithm (3.3) for the temporal integration.

In our simulations we use a grid of $128 \times 128$ cells, with grid spacing $\Delta x = \Delta y = 1/128$ cm. This corresponds to thickness of the sample of $H = L = 1$ cm. The physical parameters correspond to the THN-C12 mixture studied in [71], $\rho = 0.8407\,\text{g/cm}^3$, $\chi = 6.21 \cdot 10^{-6}\,\text{cm}^2/\text{s}$, $\nu = 1.78 \cdot 10^{-2}\,\text{cm}^2/\text{s}$, $T_0 = 300\,\text{K}$, $S_T = 9.5 \cdot 10^{-3}\,\text{K}^{-1}$, $\beta = 0.27$, $g = 981\,\text{cm/s}^2$, and the temperature difference across the sample is $\Delta T = 40\,\text{K}$. To obtain the time-correlation functions we analyze a single run corresponding to $3,125$ s of physical time, skipping the initial $625$ s. The time step used in both the inertial and overdamped integrators is $\Delta t = 5 \cdot 10^{-3}$ s, giving a viscous Courant number $\nu \Delta t/\Delta x^2 = 1.5$. This means that the viscous dynamics is well-resolved by this small time step and there is no real benefit from using the overdamped equations. A larger time step cannot be used here even in the overdamped limit because the relaxation time (3.45) for the smallest wave number $k \approx 6.28\,\text{cm}^{-1}$ is $\tau = 0.025$ s, and therefore resolving the dynamics of the concentration requires a rather small time step.

In the right panel of Fig. 3.6 we show numerical results for the static structure factor $S(\boldsymbol{k})$, while in Fig. 3.7 we show results for the dynamic structure factor $S(\boldsymbol{k}, t)$. While the static factor shows no difference between the inertial and overdamped integrators, the dynamic factor clearly shows the appearance of oscillations (propagative modes) for the smallest wavenumbers when inertia is accounted for. For comparison, in Fig. 3.7 we also plot the theory (3.47). We see a qualitative but not a quantitative agreement between the numerical results and the theory. This mismatch can be attributed to the effects of confinement by the two no-sip boundaries, which is not taken into account in the simple quasi-periodic theory used to derive (3.47). This effect becomes stronger the smaller the value of the dimensionless product $kH$. Constructing analytical theories in the presence of confinement and inertial effects is quite challenging and computer simulations are required to study these effects.

## 3.6 Conclusion

In this chapter, we focused on fluctuating hydrodynamics, specifically, we considered numerical methods for solving the fluctuating Burgers equation in one dimension, the fluctuating Navier-Stokes equations in two dimensions, and the fluctuating hydrodynamics equations describing diffusive mixing in binary fluids in three dimensions. In these equations, fluctuation-dissipation balance is obtained from the balance of the dissipative (self-adjoint) diffusive terms and the stochastic forcing. The advection terms are non-dissipative (skew-adjoint) and do not affect the equilibrium distribution. We employed the temporal integrators described in Chapter 2, obtaining second order weak accuracy for linearized fluctuating hydrodynamics, and took advantage of the fast-slow temporal integrator to use a large time step size for problems that exhibit a large separation of timescales.

## 3.7 Addendum: Approximate Projection Methods

Here we consider a generalization of the projected Euler-Maruyama scheme (3.31),

$$\boldsymbol{v}^{n+1} = \widetilde{\mathbb{P}} \left[ \boldsymbol{v}^n + \nu \Delta t\, \boldsymbol{L_v} \boldsymbol{v}^n + (2\nu \Delta t)^{\frac{1}{2}}\, \boldsymbol{D_w} \boldsymbol{W}_{\boldsymbol{v}}^n \right], \tag{3.49}$$
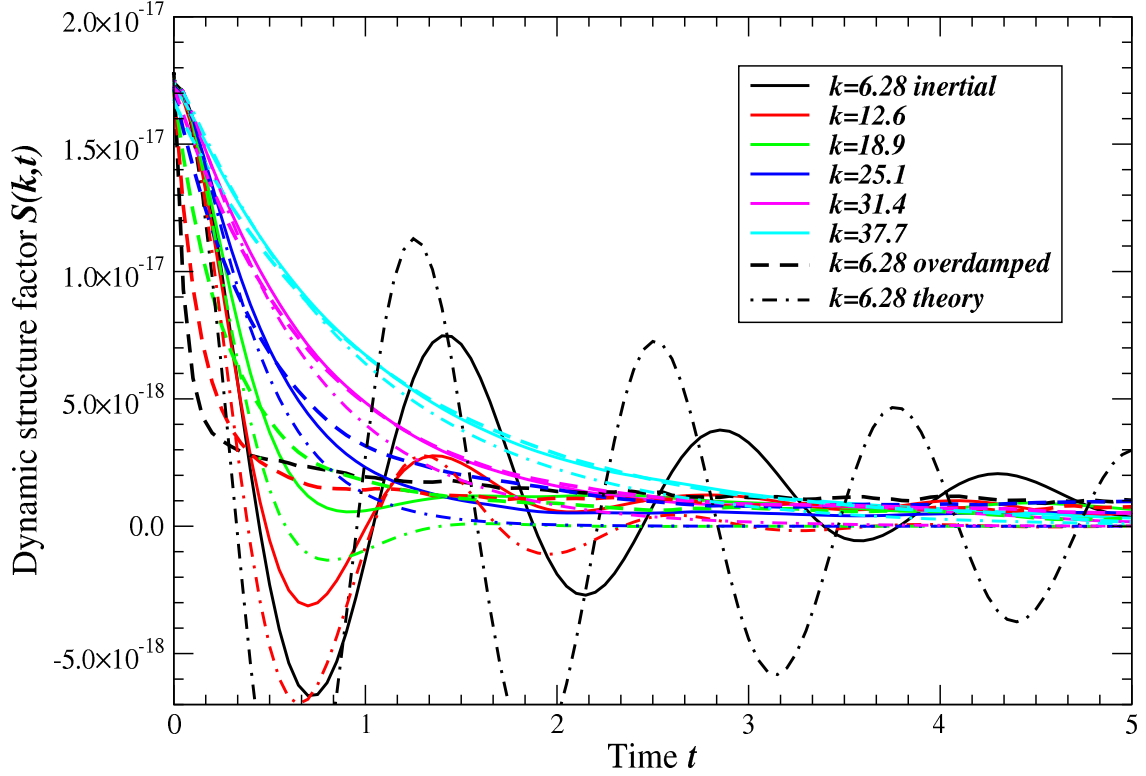
53

Figure 3.7: (Color online) Time correlation functions $S(k,t)$ of concentration fluctuations for concentration fluctuations in a binary liquid mixture subjected to a temperature gradient [71], for the first few wavenumbers (listed in the legend in cm$^{-1}$). Solid lines are obtained using the inertial equations, while dashed lines of the same color are obtained using the overdamped approximation. For the smallest two wavenumbers clear oscillations are observed indicating the appearance of propagative modes. These are not captured correctly in the overdamped approximation, and are only qualitatively described by the simple theory (3.47), shown with dashed-dotted lines.

where $\widetilde{\mathbb{P}}$ an approximation to the discrete projection $\mathbb{P}$, for example, $\mathbb{P} = I - GL_p^{-1}D$. Here $L_p$ is a discrete pressure Laplacian operator that may, in general, be different from $L_s = DG$. For example, with spatial discretizations of the incompressible (Navier-)Stokes equations that use cell-centered velocities, $L_s$ possesses a non-trivial nullspace and the corresponding exact projection methods (in which $\widetilde{\mathbb{P}} = \mathbb{P}$) suffer from the so-called checkerboard instability. Approximate projection methods have been developed to overcome these difficulties of exact cell-centered projection methods [83]. One of the simplest approximate projection methods is (3.49) with $L_p$ being the standard second-order Laplacian stencil [84]. For the staggered-grid spatial discretization we employ, however, it is straightforward to invert $L_s$ and approximate projection methods are not used in practice.

The steady-state covariance of the iteration (3.49) should be a consistent approximation to the continuum result (3.28). Specifically, we ask that to leading order in the time step size

$$C_v = \left\langle v^{n+1} \left(v^{n+1}\right)^\star \right\rangle = \left\langle v^n \left(v^n\right)^\star \right\rangle = \mathbb{P} + \Delta t\, \Delta C_v + O\left(\Delta t^2\right).$$

Substituting (3.49) in this condition and equating the leading-order terms we obtain the condition

$$\widetilde{\mathbb{P}}\mathbb{P}\widetilde{\mathbb{P}}^\star = \mathbb{P}.$$

This condition is satisfied for *exact projection* methods, $\widetilde{\mathbb{P}} = \mathbb{P}$, but not for approximate projection methods, $\widetilde{\mathbb{P}} \neq \mathbb{P}$. Assuming the initial condition is discretely divergence-free, for exact projection (3.49) is equivalent to (3.31).

## 3.8  Addendum: Mode Analysis

It is instructive to describe a framework for analyzing schemes such as (3.33), following the mode analysis used to study splitting errors in projection methods in the deterministic context [92, 93]. This analysis can in principle produce explicit expressions for the spectrum of velocity fluctuations for the types of schemes we consider here. It also illustrates clearly the role of the pressure and, in particular, the difficulties with applying semi-*implicit* projection (splitting) methods in the context of the fluctuating Navier-Stokes equations.

A mode of the spatially-discretized unforced time-dependent (creeping) Stokes flow equation

$$\partial_t v + G\pi = \nu L_v v, \text{ s.t. } Dv = 0 \tag{3.50}$$

is an exponentially-decaying solution of the form

$$v(t) = v_0 e^{-\sigma t} \text{ and } \pi(t) = \nu\pi_0 e^{-\sigma t}.$$

Here $\sigma \geq 0$ is the decay rate associated with the spatial mode $\{v_0, \pi_0\}$, which is a normalized solution to the eigen-problem

$$\left(L_v + \nu^{-1}\sigma I\right) v_0 + G\pi_0 = 0 \text{ and } Dv_0 = 0. \tag{3.51}$$

These modes diagonalize the creeping Stokes flow dynamics and form a complete orthonormal basis for the space of divergence-free velocity fields. This can be seen by eliminating the pressure to obtain the classical eigenvalue problem in the subspace of discretely divergence-free velocity fields

$$\left[L_v - L_v^{-1}G\left(DL_v^{-1}G\right)^{-1}DL_v^{-1}\right] v_0 = -\nu^{-1}\sigma v_0.$$

In the presence of a stochastic forcing, we can express any solution in a basis formed by the modes $\left\{v_0^1, v_0^2, \dots\right\}$,

$$v(t) = \sum_k \upsilon_k(t)\, v_0^k,$$

where the mode amplitudes $\upsilon_k(t)$ are scalar stochastic processes. The stochastic forcing

$$(2\nu)^{\frac{1}{2}}\, D_w \mathcal{W}_v(t)$$

in the momentum equation can be projected onto $v_0^k$ to obtain the amplitude of the stochastic forcing for mode $k$,

$$w_k(t) = (2\nu)^{\frac{1}{2}}\left(v_0^k\right)^\star\left(D_w\mathcal{W}_v(t)\right),$$

which is a scalar white-noise process with covariance

$$\langle w_k(t) \, w_k^\star(t') \rangle = 2\nu \left(v_0^k\right)^\star \left[D_w \langle \mathcal{W}_v(t) \mathcal{W}_v^\star(t') \rangle D_w^\star \right] \left(v_0^k\right) = -2\nu \left(v_0^k\right)^\star L_v \left(v_0^k\right) \delta(t-t'),$$

where we made use of the discrete fluctuation-dissipation balance between the viscous dissipation and the stochastic forcing, $L_v = -D_w \left(D_w\right)^\star$. From (3.51) we can express

$$-2\nu \left(v_0^k\right)^\star L_v \left(v_0^k\right) = -2\nu \left(v_0^k\right)^\star \left(G\pi_0 - \nu^{-1}\sigma_k v_0^k\right) = 2\nu \left(Dv_0^k\right)^\star \pi_0 + 2\sigma_k \left\|v_0^k\right\|^2 = 2\sigma_k,$$

where we again made use of the duality relation $G = -D^\star$. This simple calculation shows that in the mode representation the linearized fluctuating Navier-Stokes equation becomes a collection of decoupled scalar Langevin equations driven by standard Wiener processes,

$$\frac{dv_k}{dt} = -\sigma_k v_k + (2\sigma_k)^{\frac{1}{2}} \mathcal{W}_v(t). \tag{3.52}$$

The fluctuation-dissipation balance is most clearly revealed in this representation.

Temporal discretizations can be analyzed by projecting the numerical solution onto a set of *discrete* modes. For the implicit midpoint discretization (3.33), the modes are decaying solutions of the form

$$v_k^{n+1} = v_k^n e^{-\tilde{\sigma}_k \Delta t} \text{ and } \pi_k^{n+\frac{1}{2}} = \nu \pi_k^n e^{-\tilde{\sigma}_k \Delta t/2},$$

where $\tilde{\sigma}_k \approx \sigma_k$ is the numerical decay rate. The spatial structure of the mode $\{v_k^n, \pi_k^n\}$ is the solution to the discrete eigen-problem

$$\left[L_v + \nu^{-1}\left(\frac{2}{e^{-\tilde{\sigma}_k \Delta t} + 1}\right)\left(\frac{1-e^{-\tilde{\sigma}_k \Delta t}}{\Delta t}\right) I\right] v_k^n + \left(\frac{2}{e^{-\tilde{\sigma}_k \Delta t} + 1}\right) e^{-\tilde{\sigma}_k \Delta t/2} G\pi_k^n = v_k^n.$$

Comparison to (3.51) shows that the spatial modes are the same as for the semi-continuum (3.50), and the temporal decay rate is second-order accurate in the time step,

$$\sigma_k = \left(\frac{2}{e^{-\tilde{\sigma}_k \Delta t} + 1}\right)\left(\frac{1-e^{-\tilde{\sigma}_k \Delta t}}{\Delta t}\right) = \tilde{\sigma}_k \left(1 - \frac{\tilde{\sigma}_k^2 \Delta t^2}{12}\right) + O\left(\Delta t^3\right).$$

When the stochastic forcing is included, the discrete velocity can be represented in the basis formed by the discrete modes just as we did above for the time-continuous equations. In the mode representation the scheme (3.33) is seen to be nothing more than the implicit midpoint method (2.24) applied to the system of decoupled SDEs (3.52).

The mode analysis reveals that semi-implicit projection (splitting) methods have a significant shortcoming not seen for explicit methods. A Crank-Nicolson projection method for (3.50) consists of first solving the following linear system for the velocity $v^{n+1}$ with a time-lagged pressure [94],

$$\left(I - \frac{\nu\Delta t}{2}\right)\tilde{v}^{n+1} + \Delta t \, G\pi^{n-\frac{1}{2}} = \left(I + \frac{\nu\Delta t}{2}\right)v^n,$$

and then projecting the intermediate velocity $\tilde{v}^{n+1}$ to enforce the divergence-free constraint, $v^{n+1} = \mathbb{P}\tilde{v}^{n+1}$, by solving a linear system for the pressure correction

$$v^{n+1} = \tilde{v}^{n+1} - \Delta t \, G\Delta\pi^n, \text{ s.t. } Dv^{n+1} = 0.$$

Repeating the discrete mode calculation reveals that the spatial modes for the above temporal discretization are not the same as for the semi-continuum (3.50), specifically, the gradient of pressure term in (3.51) is modified by a term involving the Laplacian $L_v$. For periodic systems the discrete gradient and vector Laplacian commute, $L_v G = GL_s$, and modes have the correct spatial structure. However, for non-periodic systems the splitting of the pressure and velocity equations introduces a commutator error that leads to the appearance of "spurious" or "parasitic" modes [93]. For deterministic solutions and moderate time step sizes, spatio-temporal smoothness of the solution usually makes these commutator errors acceptably small. In the stochastic context, however, all modes are stochastically forced and have a non-negligible amplitude, including the parasitic modes. For this reason, we chose to use (3.33) and solve a coupled Stokes linear system for *both* pressure and velocity, and only use the projection method as a preconditioner for the required Krylov solver [85]. We emphasize again that for purely explicit time stepping scheme the spatial structure of the modes is preserved and projection methods can be used in the stochastic setting as well.

# Chapter 4

# Brownian Dynamics without Green's functions

The presence of suspended particles is a common feature of complex fluids. At small scales, the motion of immersed particles is driven by thermal fluctuations, giving rise to Brownian motion strongly affected by hydrodynamic effects. Fluctuating hydrodynamics has been shown to be a useful tool in modeling the dynamics of colloidal particles and polymer chains suspended in a fluid [95, 96, 97, 98, 99, 100, 101, 102, 103, 104, 105, 106]. By coupling a fluctuating fluid solver with immersed particles one can model the Brownian dynamics from the short time scales, at which sound waves play a role [104], to longer times, at which the velocity correlations decay in a power-law manner due to viscous dissipation. At the same time, the dynamics of interest in many problems is the diffusive (Brownian) dynamics of the immersed structures, which happens at much longer times due to the very small Reynolds numbers, or more precisely, the very large Schmidt numbers present in typical applications.

In the limit of zero Reynolds number, or more precisely, infinite Schmidt number, the methods of Brownian [12, 13, 107, 108, 109, 110, 111] and Stokesian dynamics [112, 11] have dominated in chemical engineering, and related techniques have been used in biochemical engineering [15, 16, 17, 18]. In this work we focus on Brownian dynamics, which can be seen as a simplified version of Stokesian dynamics that does not include second-order multipole terms (rotlets and stresslets) or lubrication effects in the hydrodynamic interactions among the immersed particles. A key common feature of this class of methods is that they simulate the overdamped (diffusive) dynamics of the particles by using Green's functions for steady Stokes flow to capture the effect of the fluid. While this sort of *implicit solvent* approach works very well in many situations, it has several notable technical difficulties: achieving near linear scaling for many-particle systems is technically challenging [109, 112, 111], handling non-trivial boundary conditions (bounded systems) is complicated [110] and has to be done on a case-by-case basis [108, 11, 10, 113, 97], and including Brownian motion requires additional specialized treatment [12, 13]. Notably, combining all components together and performing Brownian or Stokesian dynamics in complex geometry with accurate hydrodynamics, thermal fluctuations, and near-linear scaling requires a rather sophisticated set of tools. This is evidenced by the fact that existing Stokesian dynamics simulations of Brownian suspensions in even the simplest confined geometry, a slit channel, have relied on several uncontrolled approximations [114], even though all of the expressions and tools have, in principle, been developed [115, 10].

At first sight, it may appear that there is a conceptual gap between methods based on fluctuating hydrodynamics and those based on Green's functions. The fluid inertia, or, more precisely, the momentum diffusion is inherently part of the fluctuating hydrodynamics formulation of Brownian motion [116, 117, 118, 119], while it does not appear in the equations of Brownian or Stokesian dynamics. For example, particles suspended in a fluctuating fluid with inertial memory exhibit a well-known power-law decay of the velocity auto-correlation function (VACF) [118], which is not present in Brownian dynamics (BD) because BD is meant to describe longer time scales, at which the VACF looks like a Dirac delta function. In order to access the diffusive scaling, methods based on fluctuating hydrodynamics, such as Lattice-Boltzmann (LB) techniques [99], must ensure that the Schmidt number Sc is sufficiently large [120], though in practice Sc is always limited by computational efficiency considerations. Extensive testing has confirmed that with proper care a match can be achieved between results obtained using LB and BD methods [97, 98, 121].

Nevertheless, there remains a gap in the range of accessible Reynolds/Schmidt numbers between the two classes of methods. We close this gap in this work by designing a Fluctuating Immersed Boundary (FIB) method that solves the overdamped (inertia-less) equations of Brownian dynamics using an *explicit solvent* representation of the

fluid hydrodynamics. Importantly, the FIB method includes confinement in nontrivial geometries and Brownian motion consistently and with a controlled accuracy, and has linear complexity in the number of immersed particles. The key observation underlying the FIB method is that analytical Green's functions can be replaced by a steady Stokes solver with a stochastic stress tensor, as dictated by fluctuating hydrodynamics. Specifically, the action of the required response functions (on both deterministic and stochastic terms) is computed "on the fly" rather than pre-computed analytically. The fluid solver can be used to handle nontrivial boundary conditions, including cases where the concentration of chemical reactants affects the fluid flow via osmo-phoretic effects [122, 123]. The stochastic increments required to simulate the Brownian motion are generated by the fluctuating Stokes solver with no additional effort, in arbitrary domains with a combination of standard periodic, no-slip or slip boundaries [85]. Because in confined systems the mobility strongly depends on the positions of the particles relative to the boundaries, we pay special attention to correctly capturing the well-known stochastic drift term proportional to the divergence of the configuration-dependent mobility matrix. In particular, we develop a random finite difference approach that is related, but distinct from, the traditional Fixman midpoint method.

Rather closely related to our proposal is the work on the Stochastic Immersed Boundary Method (SIBM) and its generalization the Stochastic Eulerian Lagrangian Method (SELM) developed by Atzberger and collaborators [124, 100], as well as the work of Maxey and collaborators on the Force Coupling Method (FCM) [125, 126, 127]. In work independent from ours, Keaveny has recently included thermal fluctuations in the fluctuating FCM method [103], and also accounted for stresslet and rotlet terms (which are not included in our FIB method). While inertia can be included easily in both SELM and FCM, as it can be in the Inertial Coupling Method (ICM) [102] very closely-related to the FIB method, both methods can also be used in the steady Stokes limit [103]. At the level of the mathematical (continuum) formulation the SELM, fluctuating FCM and FIB methods are very similar, though the numerical techniques used to discretize and solve the equations of motion are rather distinct, leading to several crucial differences between the work presented here and existing work. Specifically, we develop novel temporal integrators that efficiently account for the dependence of the mobility on configuration, which is crucial in confined geometries. Crucially, we do not assume specific forms of the boundary conditions when solving the fluid (steady or unsteady) Stokes equations, and, in particular, we do not rely on periodic boundary conditions and using a Fourier basis (and the associated FFTs) to diagonalize the Stokes operator [124, 103]. Furthermore, we do not use Gaussian kernels as in the FCM, rather, we employ the compact-support kernels Peskin specifically constructed for immersed-boundary discretizations that employ a finite-difference-type discretization of the fluid equations [128]. Note also that we handle domain boundaries (for both deterministic *and* stochastic terms) directly in the finite-volume fluctuating Stokes solver, unlike recent extensions to BD [110] that handle complex boundaries by discretizing the boundary using immersed-boundary techniques. Independently of our work, an extension to SELM to nonperiodic domains, but using a finite-element rather than a finite-volume Stokes solver, has recently been developed [129]. We will defer a more detailed comparison with this related but distinct work until the concluding section, after we present the technical details of the FIB method.

This chapter is organized as follows. In the remainder of this section we summarize the well-known and widely-used method of Brownian dynamics, to the extent necessary for subsequent comparison with our FIB method. In Section 4.2 we discuss the equations of motion solved in the FIB method at the continuum level, and explain the relation to the equations of Brownian dynamics. Then, we explain how we discretize those equations in both space (Section 4.3) and time (Section 4.4). In Section 4.5 we perform a series of validation tests confirming the accuracy and robustness of the FIB method on a variety of tests of increasing complexity. Several technical derivations are detailed in the Addendums.

## 4.1 Brownian Dynamics

The equations of Brownian Dynamics (BD) model the diffusive dynamics of the positions $\boldsymbol{q}(t) = \{\boldsymbol{q}_1(t), \ldots, \boldsymbol{q}_N(t)\}$ of a collection of $N$ particles via the Ito system of stochastic differential equations,

$$\frac{d\boldsymbol{q}}{dt} = \boldsymbol{M}\boldsymbol{F} + \sqrt{2k_BT}\boldsymbol{M}^{\frac{1}{2}}\widetilde{\boldsymbol{\mathcal{W}}}(t) + k_BT\left(\partial_{\boldsymbol{q}} \cdot \boldsymbol{M}\right), \tag{4.1}$$

where $\boldsymbol{M}(\boldsymbol{q}) \succeq \boldsymbol{0}$ is the symmetric positive semidefinite (SPD) mobility matrix, relating the applied forces, $\boldsymbol{F}(\boldsymbol{q}) = -\partial U(\boldsymbol{q})/\partial\boldsymbol{q}$ with $U(\boldsymbol{q})$ a conservative potential, to the resulting (deterministic) velocity. For notational brevity we will often omit the explicit dependence on the configuration $\boldsymbol{q}$ or time $t$. The stochastic forcing $\widetilde{\boldsymbol{\mathcal{W}}}(t)$ denotes a vector of independent white noise process, formally time derivatives of independent Wiener processes. The "square root" of the mobility $\boldsymbol{M}^{\frac{1}{2}}$ is a matrix (not necessarily square) which satisfies the fluctuation dissipation balance

condition

$$M^{\frac{1}{2}} \left( M^{\frac{1}{2}} \right)^{\star} = M. \tag{4.2}$$

We use a superscript star throughout to denote the adjoint of a linear operator for a suitably-weighted inner product (conjugate transpose for matrices for the standard inner product). Throughout this paper we will rewrite the equations of motion (4.1) to eliminate the final "thermal", "stochastic" or "spurious" drift term $k_B T \left( \partial_{\boldsymbol{q}} \cdot \boldsymbol{M} \right)$ by using the *kinetic* interpretation of the stochastic integral [5], denoted in this paper by the stochastic product symbol $\diamond$,

$$\frac{d\boldsymbol{q}\,(t)}{dt} = \boldsymbol{M}(\boldsymbol{q})\boldsymbol{F}(\boldsymbol{q}) + \sqrt{2k_B T}\boldsymbol{M}^{\frac{1}{2}}(\boldsymbol{q}) \diamond \widetilde{\boldsymbol{\mathcal{W}}}(t). \tag{4.3}$$

Condition (4.2) insures that the dynamics (4.3) is time-reversible with respect to the Gibbs-Boltzmann distribution

$$P_{eq}(\boldsymbol{q}) = Z^{-1} \exp\left(-U(\boldsymbol{q})/k_B T\right), \tag{4.4}$$

where $Z$ is a normalization constant. This may be seen by examining the Fokker-Planck equation for the evolution of the probability distribution for observing the state $\boldsymbol{q}$ at time $t$ corresponding to (4.1) or (4.3),

$$\frac{\partial P}{\partial t} = \frac{\partial}{\partial \boldsymbol{q}} \cdot \left\{ \boldsymbol{M} \left[ \frac{\partial U}{\partial \boldsymbol{q}} P + (k_B T) \frac{\partial P}{\partial \boldsymbol{q}} \right] \right\}, \tag{4.5}$$

and noting that the term in square brackets vanishes when $P = P_{eq}$.

Developing schemes to simulate Brownian dynamics has several challenges. One such challenge is evaluating, or more precisely, applying the mobility matrix, which contains all of the information about hydrodynamic interactions between the particles. This can be non-trivial to achieve analytically even in relatively simple geometries, and the mobility is generally approximated via a multipole expansion or infinite series of images. Special care must be taken to insure that the truncation of these infinite series result in a positive-semidefinite matrix [11, 10]. Even if an efficient application of the action of the mobility matrix is available, one still must also be able to generate the action of $\boldsymbol{M}^{\frac{1}{2}}$, typically approximated by Chebyshev polynomials as originally proposed by Fixman [130]. Finally, the stochastic drift term $k_B T\, \partial_{\boldsymbol{q}} \cdot (\boldsymbol{M}(\boldsymbol{q}))$ must be calculated or approximated in some way. This amounts to consistently discretizing the kinetic interpretation of the stochastic integral, which is traditionally-accomplished by using the Fixman midpoint algorithm [5]. Note however that the Fixman method (and in general the use of the kinetic stochastic integral) requires handling the inverse of the mobilty matrix, which can add substantial complication and cost [103].

### 4.1.1 Mobility Matrix

For two well-separated spherical particles $i$ and $j$, we can approximate the pairwise mobility, which determines the velocity on particle $i$ resulting from a force on particle $j$, with [98, 11]

$$\begin{aligned} \boldsymbol{\mathcal{M}}_{ij} = \boldsymbol{\mathcal{M}}_{ji} = \\ \eta^{-1} \left( \boldsymbol{I} + \frac{a^2}{6} \boldsymbol{\nabla}_{\boldsymbol{r}}^2 \right) \left( \boldsymbol{I} + \frac{a^2}{6} \boldsymbol{\nabla}_{\boldsymbol{r}'}^2 \right) \boldsymbol{K}(\boldsymbol{r}, \boldsymbol{r}')|_{\boldsymbol{r}'=\boldsymbol{q}_i}^{\boldsymbol{r}=\boldsymbol{q}_j}, \end{aligned} \tag{4.6}$$

where $a$ is the radius of the particles. Here $\boldsymbol{K}$ is the Green's function for the steady Stokes problem with unit viscosity, with the appropriate boundary conditions such as no-slip on the boundaries of the domain. The differential operator $\boldsymbol{I} + \left(a^2/6\right) \boldsymbol{\nabla}^2$ is called the Faxen operator [98] and leads to the well-known Faxen correction to the Stokes drag law. Note that the form of (4.6) guarantees that an SPD mobility matrix is obtained by construction.

#### 4.1.1.1 Unconfined systems

For a three dimensional unbounded domain with fluid at rest at infinity, $\boldsymbol{K}(\boldsymbol{r}, \boldsymbol{r}') = \boldsymbol{K}(\boldsymbol{r} - \boldsymbol{r}')$ is isotropic and given by the Oseen tensor,

$$\boldsymbol{K}(\boldsymbol{r}) = \boldsymbol{O}(\boldsymbol{r}) = \frac{1}{8\pi r} \left( \boldsymbol{I} + \frac{\boldsymbol{r} \otimes \boldsymbol{r}}{r^2} \right).$$

For many particles in an unbounded domain, applying (4.6) to the Oseen tensor yields the far-field expression of the Rotne-Prager-Yamakawa (RPY) tensor [131], commonly used in Brownian dynamics simulations. A correction

needs to be introduced when particles are close to each other in order to produce a mobility which is positive definite [131],

$$\boldsymbol{M}_{ij} = \frac{1}{6\pi\eta a} \begin{cases} C_1(r_{ij})\boldsymbol{I} + C_2(r_{ij})\frac{\boldsymbol{r}_{ij}\otimes\boldsymbol{r}_{ij}}{r_{ij}^2}, & r_{ij} > 2a \\ C_3(r_{ij})\boldsymbol{I} + C_4(r_{ij})\frac{\boldsymbol{r}_{ij}\otimes\boldsymbol{r}_{ij}}{r_{ij}^2}, & r_{ij} \leq 2a \end{cases} \tag{4.7}$$

where $\boldsymbol{r}_{ij} = \boldsymbol{q}_i - \boldsymbol{q}_j$ is the vector connecting the particles, and $r_{ij}$ is its length, and

$$C_1(r_{ij}) = \frac{3a}{4r_{ij}} + \frac{a^3}{2r_{ij}^3} \qquad C_2(r_{ij}) = \frac{3a}{4r_{ij}} - \frac{3a^3}{2r_{ij}^3}$$

$$C_3(r_{ij}) = 1 - \frac{9r_{ij}}{32a} \qquad C_4(r_{ij}) = \frac{3r_{ij}}{32a}.$$

The diagonal blocks of the mobility matrix, i.e., the self-mobility can be obtained by setting $r_{ij} = 0$ (giving $C_3(0) = 1$ and $C_4(0) = 0$) to obtain $\boldsymbol{M}_{ii} = (6\pi\eta a)^{-1}\boldsymbol{I}$, which matches the Stokes solution for the drag for flow around a sphere. It is important physically that $\boldsymbol{M}_{ij} = \boldsymbol{M}_{ii}$ when $r_{ij} = 0$ since two perfectly overlapping particles must behave as if there is only a single particle at that location.

For a single particle in an unbounded domain it is obvious that $\boldsymbol{M}_{ii}$ is constant and thus has vanishing divergence. For the RPY mobility it can be shown that $\partial_{\boldsymbol{q}} \cdot (\boldsymbol{M}(\boldsymbol{q})) = \boldsymbol{0}$ even for multi-particle systems (this is in fact a rather generic consequence of the incompressibility of the flow [23]). Note, however, that when stresslet terms are included the mobility becomes a complicated function of configuration and the stochastic drift term must be accounted for [103].

#### 4.1.1.2   Confined systems

In the presence of boundaries, the Green's function may be decomposed as

$$\boldsymbol{K}(\boldsymbol{r}, \boldsymbol{r}') = \boldsymbol{O}(\boldsymbol{r} - \boldsymbol{r}') + \boldsymbol{K}^w(\boldsymbol{r}, \boldsymbol{r}'), \tag{4.8}$$

where $\boldsymbol{K}^w$ is the Green's function for a disturbance velocity field enforcing the no-slip condition at the walls. One can approximate the pairwise far-field mobility by using (4.6) and applying the Faxen operators to $\boldsymbol{O}$ and $\boldsymbol{K}^w$ separately [11]. For the diagonal blocks, we have to consider the self-mobility in an unbounded domain separately, and only use (4.6) with $\boldsymbol{K}$ replaced by $\boldsymbol{K}^w$ in order to account for the disturbance velocity from the boundary conditions [11] (equivalently, to account for the hydrodynamic interactions with the image particles),

$$\boldsymbol{M}_{ii} = \frac{1}{6\pi\eta a}\boldsymbol{I}$$
$$+ \eta^{-1}\left(\boldsymbol{I} + \frac{a^2}{6}\boldsymbol{\nabla}_{\boldsymbol{r}}^2\right)\left(\boldsymbol{I} + \frac{a^2}{6}\boldsymbol{\nabla}_{\boldsymbol{r}'}^2\right)\boldsymbol{K}^w(\boldsymbol{r}, \boldsymbol{r}')\big|_{\substack{\boldsymbol{r}=\boldsymbol{q}_i \\ \boldsymbol{r}'=\boldsymbol{q}_i}}.$$

Note that this approach requires knowing the Green's function for the particular geometry in question. For a single no-slip wall $\boldsymbol{K}^w$ was obtained by Blake [132], but for a slit channel with two no-slip walls there is no manageable analytical form [10].

It is important to note that even for a single particle near a boundary the mobility strongly depends on the position of the particle relative to the boundary and therefore the thermal drift $k_B T\,\partial_{\boldsymbol{q}} \cdot \boldsymbol{M}$ must be accounted for [10].

## 4.2   Fluctuating Immersed Boundary Method

In this section we present the continuum formulation of the equations of motion as employed in the FIB method. At the same time, we use operator notation that generalizes to spatially-discretized equations, by simply replacing the continuum integro-differential operators with sums and differences (matrices), see the discussion of Atzbeger [100] for more details. This makes the majority of this section directly transferable to the semi-discrete setting presented in Section 4.3. The operator notation we employ also enables us to treat in a unified way different boundary conditions without requiring a specific basis for the solution of the Stokes equations.

We consider $n$ spherical neutrally-buoyant particles of radius $a$ in $d$ dimensions, having spatial positions $\boldsymbol{q} = \{\boldsymbol{q}_1, \ldots, \boldsymbol{q}_N\}$ with $\boldsymbol{q}_i = (q_i^{(1)}, \ldots, q_n^{(d)})$. These particles are immersed in an incompressible fluid of constant density

$\rho$, temperature $T$, and viscosity $\eta$, and described by the fluctuating time dependent Stokes equations for the fluid velocity $\boldsymbol{v}(\boldsymbol{r}, t)$,

$$\rho \partial_t \boldsymbol{v} + \boldsymbol{\nabla} \pi = \eta \boldsymbol{\nabla}^2 \boldsymbol{v} + \boldsymbol{f} + \sqrt{2\eta k_B T}\, \boldsymbol{\nabla} \cdot \boldsymbol{\mathcal{Z}}$$
$$\boldsymbol{\nabla} \cdot \boldsymbol{v} = 0, \tag{4.9}$$

along with appropriate boundary conditions. Here $\boldsymbol{f}(\boldsymbol{r}, t)$ is a force density applied to the fluid, $k_B$ is Boltzmann's constant, and $\boldsymbol{\mathcal{Z}}(\boldsymbol{r}, t)$ is a random Gaussian tensor field whose components are white in space and time with mean zero [26],

$$\langle \mathcal{Z}_{ij}(\boldsymbol{r}, t) \mathcal{Z}_{kl}(\boldsymbol{r}', t') \rangle = (\delta_{ik}\delta_{jl} + \delta_{il}\delta_{jk})\, \delta(t - t')\delta(\boldsymbol{r} - \boldsymbol{r}'). \tag{4.10}$$

The coupling between the fluid and particles employed here is used in a large number of other methods and related prior work. In particular, the same basic equations are employed in SIBM [124, 133] and SELM [100]. In the deterministic setting, Maxey and collaborators have developed in extensive detail the use of smooth envelope or kernel function to represent particles in flow in the context of the Force Coupling Method (FCM) [126, 125, 134]. Recently, Keaveny has included fluctuations in the description in a manner fully consistent with our presentation [103]. Similar representations of particles have also been used with the Lattice Boltzmann method [135, 99]. Both Atzberger [133] and Keaveny [103] have already noted the relation to Brownian and Stokesian dynamics. Nevertheless, for completeness and clarity and the benefit of the reader, here we present a unified view of these somewhat disjoint works and point out some less-appreciated but important features.

### 4.2.1 Fluid-Particle Interaction

In the FIB method, the shape of the particle and its effective interaction with the fluid is captured through a smooth kernel function $\delta_a(\boldsymbol{r})$ that integrates to unity and whose support is localized in a region of size $a$. This kernel is used to mediate two crucial operations. First, it is used to transfer (spread) the force exerted on the particle to the fluid. Second, it is used to impose a minimally-resolved form of the no-slip constraint stating that the velocity of the particle equals the local velocity of the fluid. Following Refs. [136, 102, 137, 104] we term this diffuse (rather than "point") particle a *blob* for lack of better terminology (in polymer modeling the term bead is used for the same concept [99]).

In order to couple the fluid velocity field to the motion of immersed particles, we introduce composite local averaging $\boldsymbol{\mathcal{J}}(\boldsymbol{q})$ and spreading $\boldsymbol{\mathcal{S}}(\boldsymbol{q})$ operators. The operator $\boldsymbol{\mathcal{J}}(\boldsymbol{q})$ takes a continuous velocity field $\boldsymbol{v}(\boldsymbol{r})$ and computes its local average at the position of each particle, while $\boldsymbol{\mathcal{S}}(\boldsymbol{q})$ takes the forces $\boldsymbol{F} = \{\boldsymbol{F}_1, \ldots, \boldsymbol{F}_N\}$ applied on the particles and computes a smooth force density field,

$$(\boldsymbol{\mathcal{J}}(\boldsymbol{q})\boldsymbol{v}(\boldsymbol{r}))_i = \int \delta_a(\boldsymbol{q}_i - \boldsymbol{r})\boldsymbol{v}(\boldsymbol{r})d\boldsymbol{r} \tag{4.11}$$

$$(\boldsymbol{\mathcal{S}}(\boldsymbol{q})\boldsymbol{F})(\boldsymbol{r}) = \sum_i \delta_a(\boldsymbol{q}_i - \boldsymbol{r})\boldsymbol{F}_i. \tag{4.12}$$

Note that $\boldsymbol{\mathcal{J}}$ is dimensionless, and $\boldsymbol{\mathcal{S}}$ has units of inverse volume. The blobs are assumed to move with the locally-averaged fluid velocity,

$$\frac{d\boldsymbol{q}(t)}{dt} = \boldsymbol{\mathcal{J}}(\boldsymbol{q})\boldsymbol{v}(\boldsymbol{r}, t), \tag{4.13}$$

which is a minimally-resolved representation of the *no-slip constraint* [136, 102]. Furthermore, the applied forces $\boldsymbol{F}$ affect the motion of the fluid through the addition of a continuous force density to the fluid equation (4.9),

$$\boldsymbol{f} = \boldsymbol{\mathcal{S}}(\boldsymbol{q})\boldsymbol{F} + \boldsymbol{f}_{\text{th}}, \tag{4.14}$$

where $\boldsymbol{f}_{\text{th}}$ is a thermal or stochastic forcing that we discuss shortly. It is crucial for energy conservation and fluctuation-dissipation balance that the coupling operators are adjoints of one another [100, 126, 102], $\boldsymbol{\mathcal{J}} = \boldsymbol{\mathcal{S}}^\star$, as follows from

$$\sum_i (\boldsymbol{\mathcal{J}}\boldsymbol{v})_i \cdot \boldsymbol{u}_i = \int \boldsymbol{v} \cdot (\boldsymbol{\mathcal{S}}\boldsymbol{u})\, d\boldsymbol{r} = \int \sum_i \delta_a(\boldsymbol{q}_i - \boldsymbol{r})(\boldsymbol{v} \cdot \boldsymbol{u}_i)\, d\boldsymbol{r} \tag{4.15}$$

In this work we focus on suspensions of spherical particles (blobs), for which the kernel function $\delta_a(\boldsymbol{r}) \equiv \delta_a(r)$ should be taken to be a spherically-symmetric function of width $\sim a$. In our computational algorithm we employ the compact-support kernels of Peskin [128], which are of the tensor product form $\delta_a(\boldsymbol{r}) = \prod_{\alpha=1}^d \delta_a(r_\alpha)$ and are specifically designed to work well in the discrete context, as discussed further in Section 4.3. Note that a Gaussian

kernel, as used in FCM [126, 125], has the special property that it is of the tensor product form while also being isotropic. It should be noted, however, that much more general forms of the local interpolation and spreading operators are possible [100]; this has been successfully used to generalize FCM to non-spherical particles [127] and can also be used to further extend our FIB method. The local averaging and spreading operators have to be modified near physical boundaries, specifically, when the support of the kernel $\delta_a$ overlaps with a boundary. A proposal for how to do that has been developed by Yeo and Maxey [134], and an alternative proposal is developed in the context of the immersed boundary method in Ref. [138]. In this work we impose a repulsive potential between the boundaries and the particles, which keeps the kernels from overlapping the walls. Therefore, no modification of (4.11,4.12) is required for our purposes and we do not discuss this issue further in this work.

In order to ensure that the system of equations (4.9,4.13,4.14) obeys fluctuation-dissipation (i.e., that the dynamics is time reversible with respect to an appropriate Gibbs-Boltzmann distribution), the thermal forcing

$$\boldsymbol{f}_{\text{th}} = (k_B T) \, \partial_{\boldsymbol{q}} \cdot \boldsymbol{\mathcal{S}} \qquad (4.16)$$

should be included in the fluid equations, as derived by Atzberger [100] and also discussed from a different perspective in Appendix B in Ref. [102] and Ref. [104]. Here we use the convention that the contraction in the divergence of an operator is on the second index, $f_i^{\text{th}} = k_B T \, \partial_j \mathcal{S}_{ij}$, consistent with Ref. [100] but not with Ref. [102]; to avoid confusion we will write things out in indicial notation when necessary[1]. For a translationally-invariant (e.g., periodic) system and kernel, this term can be omitted. Namely, from the definition (4.12) it follows that $\boldsymbol{f}_{\text{th}} = - (k_B T) \, \boldsymbol{\nabla}_{\boldsymbol{r}} \sum_i \delta \left( \boldsymbol{q}_i - \boldsymbol{r} \right)$, and the solution of the incompressible velocity equations is not affected by the addition of a gradient of a scalar. This is not strictly true in the discrete setting (see Section 4.5.3.1) and may not generalize to confined (i.e., not translationally-invariant) systems for particles in the vicinity of boundaries. The term (4.16) is therefore, in general, required in order to obtain discrete fluctuation-dissipation balance and is included in our temporal integrator.

## 4.2.2 Overdamped Limit

Equations (4.9), (4.13), and (4.14) together constitute a physically-realistic description which obeys fluctuation-dissipation balance [100], including in the presence of additional particle inertia [102, 139]. Here we are interested in the inertia-less or overdamped limit, where the momentum of the fluid may be eliminated as a fast variable. More precisely, we assume that the Schmidt number is very large, $\text{Sc} = \eta / (\rho \chi) \gg 1$, where $\chi \approx k_B T / (6\pi\eta a)$ is a typical value of the diffusion coefficient of the particles [120].

Following the notation developed in Chapter 3, here we use $\boldsymbol{\mathcal{Z}} \left( \boldsymbol{r}, t \right)$ to denote an infinite-dimensional standard white-noise field, use $\boldsymbol{\mathcal{W}} \left( t \right)$ to denote a finite dimensional collection of standard white noise processes that represents a spatial discretization of $\boldsymbol{\mathcal{Z}} \left( \boldsymbol{r}, t \right)$, and use $\boldsymbol{W}$ to denote a collection of standard (mean zero and unit variance) Gaussian variates that appears when $\boldsymbol{\mathcal{W}} \left( t \right)$ is discretized in time. For notational clarity, and to emphasize that we also consider spatially-discretized operators in the following calculations, we introduce symbols for the various differential operators: $\boldsymbol{D}$ for the divergence, $\boldsymbol{G} = -\boldsymbol{D}^\star$ for the gradient, $\boldsymbol{L}$ for the vector Laplacian, and $\widetilde{\boldsymbol{D}}$ for the divergence operator acting on the stochastic tensor. In the infinite-dimensional (continuum) setting these are differential operators, while in the finite dimensional (discrete) setting they are matrices that approximate the corresponding differential operators (for example, using finite differences), taking into account the boundary conditions [39]. Note that the operator $\widetilde{\boldsymbol{D}}$ does not have to be a consistent representation of the tensor divergence, rather, all that matters is that the covariance of the stochastic fluid forcing $\widetilde{\boldsymbol{D}} \boldsymbol{\mathcal{W}}$ obey the fluctuation-dissipation property $\boldsymbol{L} = -\widetilde{\boldsymbol{D}} \langle \boldsymbol{\mathcal{W}} \boldsymbol{\mathcal{W}}^\star \rangle \widetilde{\boldsymbol{D}}^\star$ [39, 129]. For notational simplicity, here we assume that the components of $\boldsymbol{\mathcal{W}}$ are independent, $\langle \boldsymbol{\mathcal{W}} \boldsymbol{\mathcal{W}}^\star \rangle = \boldsymbol{I}$, with the understanding that some modifications of either the covariance of $\boldsymbol{\mathcal{W}}$, or, equivalently, the operator $\widetilde{\boldsymbol{D}}$, may be necessary near boundaries to preserve fluctuation-dissipation balance for confined systems [39].

To obtain the asymptotic dynamics in the limit $\text{Sc} \to \infty$ heuristically, we delete the inertial term $\rho \partial_t \boldsymbol{v}$ in (4.9) to obtain the (potentially discretized) fluctuating steady Stokes equations for the velocity $\boldsymbol{v}$ and the pressure $\pi$,

$$\begin{aligned} \boldsymbol{G}\pi - \eta \boldsymbol{L} \boldsymbol{v} &= \boldsymbol{g} = \boldsymbol{\mathcal{S}} \boldsymbol{F} + \sqrt{2 k_B T \eta} \, \widetilde{\boldsymbol{D}} \boldsymbol{\mathcal{W}} \\ \boldsymbol{D} \boldsymbol{v} &= 0, \end{aligned} \qquad (4.17)$$

with appropriate boundary conditions. For periodic systems we additionally constrain the average velocity $\langle \boldsymbol{v} \rangle = 0$ to eliminate the non-trivial nullspace. In the following we will denote with $\boldsymbol{\mathcal{L}}^{-1}$ the (continuum or discrete) Stokes

---

[1]Note that the mobility is symmetric so there is no notational ambiguity in $\partial_{\boldsymbol{q}} \cdot \boldsymbol{M}$.

solution operator for the system (4.17) with unit viscosity, $\boldsymbol{v} = \eta^{-1}\boldsymbol{\mathcal{L}}^{-1}\boldsymbol{g}$. Note that $\boldsymbol{\mathcal{L}}^{-1} \succeq \boldsymbol{0}$ is SPD because the Stokes problem (4.17) is symmetric by virtue of the adjoint relation $\boldsymbol{G} = -\boldsymbol{D}^{\star}$ and the Laplacian operator $\boldsymbol{L}$ is symmetric negative semi-definite.

In the overdamped regime, the (fast) fluid velocity evolves instantaneously to its steady state and may be viewed as a random function of the particles' positions, which are the relevant (slow) variables. Heuristically, one expects that the Brownian dynamics of the particles is described by $d\boldsymbol{q}/dt = \boldsymbol{v} = \eta^{-1}\boldsymbol{\mathcal{J}}\boldsymbol{\mathcal{L}}^{-1}\boldsymbol{g}$. A rigorous adiabatic mode elimination procedure [45, 37] informs us that the correct interpretation of the noise term in this equation is the kinetic one, leading to the overdamped Langevin equation

$$\frac{d\boldsymbol{q}(t)}{dt} = \boldsymbol{\mathcal{J}}(\boldsymbol{q})\boldsymbol{\mathcal{L}}^{-1}\left[\frac{1}{\eta}\boldsymbol{\mathcal{S}}(\boldsymbol{q})\boldsymbol{F}(\boldsymbol{q}) + \sqrt{\frac{2k_BT}{\eta}}\,\widetilde{\boldsymbol{D}} \diamond \boldsymbol{\mathcal{W}}(t)\right]. \tag{4.18}$$

This is the rigorous asymptotic limit of (4.9,4.13,4.14) as $\mathrm{Sc} \to \infty$ [140] and it is the equation of motion in the FIB method.

### 4.2.3 Relation to Brownian Dynamics

A key observation is that (4.18) is a specific instance of the equation of Brownian dynamics (4.3), with the identification

$$\boldsymbol{M} = \eta^{-1}\boldsymbol{\mathcal{J}}\boldsymbol{\mathcal{L}}^{-1}\boldsymbol{\mathcal{S}} \quad \text{and} \quad \boldsymbol{M}^{\frac{1}{2}} = \eta^{-\frac{1}{2}}\boldsymbol{\mathcal{J}}\boldsymbol{\mathcal{L}}^{-1}\widetilde{\boldsymbol{D}}. \tag{4.19}$$

To demonstrate that this choice satisfies the fluctuation dissipation balance condition (4.2), note the adjoint relations $\boldsymbol{\mathcal{J}} = \boldsymbol{\mathcal{S}}^{\star}$ and $\boldsymbol{L} = -\widetilde{\boldsymbol{D}}\widetilde{\boldsymbol{D}}^{\star}$. It is important to point out that the spatially-discretized operators we employ obey these properties even in the presence of nontrivial boundary conditions [39]. Observe also that

$$-\boldsymbol{\mathcal{L}}^{-1}\boldsymbol{L}\boldsymbol{\mathcal{L}}^{-1} = \boldsymbol{\mathcal{L}}^{-1} \tag{4.20}$$

as seen from their action on an arbitrary vector $\boldsymbol{g}$,

$$\begin{aligned}-\boldsymbol{\mathcal{L}}^{-1}\boldsymbol{L}\boldsymbol{\mathcal{L}}^{-1}\boldsymbol{g} &= -\boldsymbol{\mathcal{L}}^{-1}\eta\boldsymbol{L}\boldsymbol{v} = \\ \boldsymbol{\mathcal{L}}^{-1}\left(-\boldsymbol{G}\pi + \boldsymbol{g}\right) &= \boldsymbol{\mathcal{L}}^{-1}\boldsymbol{g},\end{aligned}$$

where we used the fact that $\boldsymbol{\mathcal{L}}^{-1}\boldsymbol{G} = \boldsymbol{0}$ since adding a gradient forcing to the Stokes equations does not affect the velocity. This gives

$$\begin{aligned}\boldsymbol{M}^{\frac{1}{2}}\left(\boldsymbol{M}^{\frac{1}{2}}\right)^{\star} &= \eta^{-1}\boldsymbol{\mathcal{J}}\boldsymbol{\mathcal{L}}^{-1}\left(\widetilde{\boldsymbol{D}}\widetilde{\boldsymbol{D}}^{\star}\right)\boldsymbol{\mathcal{L}}^{-1}\boldsymbol{\mathcal{S}} = \\ -\eta^{-1}\boldsymbol{\mathcal{J}}\left(\boldsymbol{\mathcal{L}}^{-1}\boldsymbol{L}\boldsymbol{\mathcal{L}}^{-1}\right)\boldsymbol{\mathcal{S}} &= \eta^{-1}\boldsymbol{\mathcal{J}}\boldsymbol{\mathcal{L}}^{-1}\boldsymbol{\mathcal{S}} = \boldsymbol{M}.\end{aligned} \tag{4.21}$$

Also note that the mobility (4.19) is guaranteed to be positive-semidefinite by virtue of (4.2).

More explicitly, (4.19) gives a pairwise mobility[2] that only depends on the position of the pair of particles under consideration [133],

$$\boldsymbol{M}_{ij} = \eta^{-1}\int \delta_a(\boldsymbol{q}_i - \boldsymbol{r})\boldsymbol{K}(\boldsymbol{r},\boldsymbol{r}')\delta_a(\boldsymbol{q}_j - \boldsymbol{r}')\,d\boldsymbol{r}d\boldsymbol{r}' \tag{4.22}$$

where we recall that $\boldsymbol{K}$ is the Green's function for the Stokes problem with unit viscosity and the specified boundary conditions. Note that in our approach the self-mobility $\boldsymbol{M}_{ii}$ is also given by the same formula (4.22) with $i = j$ and does not need to be treated separately. In fact, the self-mobility of a particle in an unbounded three-dimensional domain *defines* the effective hydrodynamic radius $a$ of a blob,

$$\boldsymbol{M}_{ii} = \boldsymbol{M}_{\mathrm{self}} = \frac{1}{6\pi\eta a}\boldsymbol{I} =$$

$$\eta^{-1}\int \delta_a(\boldsymbol{q}_i - \boldsymbol{r})\boldsymbol{O}(\boldsymbol{r} - \boldsymbol{r}')\delta_a(\boldsymbol{q}_i - \boldsymbol{r}')\,d\boldsymbol{r}d\boldsymbol{r}'.$$

The value of $a$ will therefore depend on the specific kernel used, as discussed further in section 4.3.1. In two dimensions, the self-mobility $\boldsymbol{M}_{\mathrm{self}} = \mu\boldsymbol{I}$ of a disk of radius $a$ in a periodic domain (equivalently, a periodic array of

---

[2]Note that this is an approximation and in practice the mobility is not pairwise additive if higher-order multipoles such as stresslets are accounted for.

infinite cylinders) grows logarithmically with the length of the square periodic cell $L$ as $\mu = (4\pi\eta)^{-1}\ln{(L/3.708a)}$ [141]. The same scaling with the system size holds for a blob and can be used to define an effective hydrodynamic radius for a two-dimensional blob [120]. Note that in two dimensions the mobility diverges for an infinite domain, in agreement with Stokes's paradox.

Maxey [126] observed that (4.22) consistently includes the Faxen correction to the mobility of two well-separated particles. Let $\boldsymbol{J}(\boldsymbol{q}_i)$ denote the local averaging operator for a particle $i$, $\boldsymbol{J}(\boldsymbol{q}_i)\boldsymbol{v} \equiv (\boldsymbol{\mathcal{J}}(\boldsymbol{q})\boldsymbol{v})_i$. For a smooth velocity field, we can perform a second order Taylor expansion of the velocity field,

$$
\begin{aligned}
\boldsymbol{J}(\boldsymbol{q}_i)\boldsymbol{v}(\boldsymbol{r}) &= \int \delta_a(\boldsymbol{q}_i - \boldsymbol{r})\boldsymbol{v}(\boldsymbol{r})d\boldsymbol{r} \\
&\approx \left[\boldsymbol{I} + \left(\int \frac{x^2}{2}\delta_a(x)\,dx\right)\boldsymbol{\nabla}^2\right]\boldsymbol{v}(\boldsymbol{r})\,\big|_{\boldsymbol{r}=\boldsymbol{q}_i} \\
&= \left(\boldsymbol{I} + \frac{a_F^2}{6}\boldsymbol{\nabla}^2\right)\boldsymbol{v}(\boldsymbol{r})\,\big|_{\boldsymbol{r}=\boldsymbol{q}_i},
\end{aligned}
$$

where we assumed a spherical blob, $\delta_a(\boldsymbol{r}) \equiv \delta_a(r)$. This shows that we can approximate the local averaging operator by a differential operator that is identical in form to the Faxen operator appearing in (4.6), if we define the "Faxen" radius of the blob $a_F \equiv \left(3\int x^2\delta_a(x)\,dx\right)^{1/2}$ through the second moment of the kernel function. In general, $a_F \neq a$, but for a suitable choice of the kernel one can accomplish $a_F \approx a$ and thus accurately obtain the Faxen correction for a rigid sphere (for example, for a Gaussian $a/a_F = \sqrt{3/\pi}$ [126]). Interestingly, it has been shown that the leading-order Faxen corrections to the linear and angular velocities of an ellipsoidal particle can also be captured remarkably accurately (to within 5%) by using a stretched and rotated Gaussian for the kernel function [127].

The calculations above show that the mobility tensor for a pair of blobs (4.22) is a good approximation to (4.6) for well-separated blobs and thus correctly captures the mobility up to the Rotne-Prager level even in the presence of confinement. This can also be seen from (4.22) by noting that when the two particles are well separated, $\boldsymbol{K}$ is a smooth function, and is well approximated by a Taylor series, giving

$$
\boldsymbol{M}_{ij} \approx \eta^{-1}\left(\boldsymbol{I} + \frac{a_F^2}{6}\boldsymbol{\nabla}_{\boldsymbol{r}}^2\right)\left(\boldsymbol{I} + \frac{a_F^2}{6}\boldsymbol{\nabla}_{\boldsymbol{r}'}^2\right)\boldsymbol{K}(\boldsymbol{r}-\boldsymbol{r}')\big|_{\boldsymbol{r}'=\boldsymbol{q}_i}^{\boldsymbol{r}=\boldsymbol{q}_j},
$$

which matches the expression (4.6) for well-separated rigid spheres. At smaller distances the mobility is mollified (regularized) in a natural way without requiring any special handling of the case $r_{ij} < 2a$ as in the traditional RPY tensor (4.7). Furthermore, a positive definite mobility tensor is obtained by construction. Most importantly, the same continues to hold in the presence of confinement (nontrivial boundary conditions). The boundary conditions are taken into account by the fluid solver when computing the action of the Green's function (4.8), while the regularization and the Faxen corrections are handled via the local averaging and spreading operators. This inherent self-consistency of the formulation is inherited from the underlying fluctuating hydrodynamics formulation (4.9,4.13,4.14) [102].

### 4.2.4 Stochastic Drift

One key difference between the inertial formulation (4.9,4.13,4.14) and the overdamped limit (4.18) is the fact that the noise in (4.18) is multiplicative and therefore the stochastic interpretation matters and affects the temporal discretization. Methods for integrating (4.3) have been developed in the Brownian Dynamics literature, however, here we propose to use the more efficient Random Finite Difference (RFD) approach outlined in Section 2.1.1.2. We believe this approach will find uses in Brownian Dynamics simulations as well as related methods for fluctuating hydrodynamics [103, 129]. We therefore explain it here in the more general setting of solving (4.3), of which (4.18) is a special instance. A detailed description of predictor-corrector schemes to solve (4.18) is given in Section 4.4.

Of course, one can use the Ito equation (4.1) with integrators based on the Euler-Maruyama scheme. This, however, requires computing the stochastic drift term $k_B T\,(\partial_{\boldsymbol{q}} \cdot \boldsymbol{M})$, which is difficult in general. First, we summarize the well-known Fixman midpoint approach to approximating $\partial_{\boldsymbol{q}} \cdot \boldsymbol{M}(\boldsymbol{q})$, and use it to construct an RFD approach that works better in the context of our explicit fluid method. Below we use the superscript to denote the time step level at which quantities are evaluated, for example, $\boldsymbol{M}^n \equiv \boldsymbol{M}(\boldsymbol{q}^n)$ denotes the mobility evaluated at the beginning of time step $n$, while $\boldsymbol{M}^{n+\frac{1}{2}} \equiv \boldsymbol{M}\left(\boldsymbol{q}^{n+\frac{1}{2}}\right)$ denotes a midpoint approximation of the mobility during time step $n$.

#### 4.2.4.1 Fixman's Method

The Fixman midpoint scheme used to capture the stochastic drift [12, 13] can be seen as corresponding to a direct discretization of the kinetic stochastic integral [5], see also (2.1),

$$
\begin{aligned}
\boldsymbol{q}^{n+\frac{1}{2}} &= \boldsymbol{q}^n + \frac{\Delta t}{2} \boldsymbol{M}^n \boldsymbol{F}^n \\
&\quad + \sqrt{\frac{\Delta t\, k_B T}{2}} \left(\boldsymbol{M}^n\right)^{\frac{1}{2}} \boldsymbol{W}^n \\
\boldsymbol{q}^{n+1} &= \boldsymbol{q}^n + \Delta t \boldsymbol{M}^{n+\frac{1}{2}} \boldsymbol{F}^{n+\frac{1}{2}} \\
&\quad + \sqrt{2\Delta t\, k_B T} \boldsymbol{M}^{n+\frac{1}{2}} \left(\boldsymbol{M}^n\right)^{-\frac{1}{2}} \boldsymbol{W}^n,
\end{aligned}
\tag{4.23}
$$

where $\boldsymbol{W}^n$ is a vector of i.i.d. standard Gaussian variables and

$$
\left(\boldsymbol{M}^n\right)^{-\frac{1}{2}} \left(\left(\boldsymbol{M}^n\right)^{-\frac{1}{2}}\right)^{\star} = \left(\boldsymbol{M}^n\right)^{-1}.
$$

While the Fixman method is quite elegant and has been widely used with notable success, it requires handling the inverse of the mobility matrix, which would add significant complication to our method [103].

In order to show that (4.23) is consistent with (4.3) one has to show that the first and second moments of the increment $\boldsymbol{q}^{n+1} - \boldsymbol{q}^n$ are $O(\Delta t)$ with coefficients matching the drift and diffusion terms in the Ito equation (4.18), and higher moments should be of higher order in $\Delta t$. The only nontrivial component is the stochastic drift term $k_B T\, \partial_{\boldsymbol{q}} \cdot \boldsymbol{M}(\boldsymbol{q})$. In order to compact the notation, henceforth we will index matrices and vectors without regard for the physical particles represented. For example, we will write $q_i$ to represent the scalar that is the $i$th entry of the length $nd$ vector of positions $\boldsymbol{q}$, disregarding which particle this entry describes. We will likewise consider the mobility $\boldsymbol{M}$ as a matrix of scalars $\mathcal{M}_{ij}$. This allows us to use Einstein summation notation and indicial algebra. We can show that the Fixman algorithm (4.23) generates the correct stochastic drift term from

$$
\lim_{\Delta t \to 0} \frac{1}{\Delta t} \Bigg\langle \mathcal{M}_{ij} \left(q_p^n + \sqrt{\frac{\Delta t\, k_B T}{2}} \left(\mathcal{M}_{pr}^n\right)^{\frac{1}{2}} W_r^n\right) \times
$$

$$
\sqrt{2\Delta t\, k_B T} \left(\mathcal{M}_{jk}^n\right)^{-\frac{1}{2}} W_k^n \Bigg\rangle = k_B T\, \partial_j \mathcal{M}_{ij}(\boldsymbol{q}^n),
\tag{4.24}
$$

where the average is over realizations of $\boldsymbol{W}$ and the shorthand $\partial_j$ denotes a partial derivative with respect to the $j$th component of $\boldsymbol{q}$.

#### 4.2.4.2 Random Finite Difference

The equivalence (4.24) only relies on the covariance structure of $\boldsymbol{W}^n$, and there is no reason that we must use an increment that is related in any way to the noise term in (4.3). As shown in section 2.1.1.2, one can use a RFD approach to generate the stochastic drift without having to apply the inverse of the mobility. The following centered difference gives the correct term with a second order truncation error,

$$
\frac{1}{\delta} \left\langle \left(\mathcal{M}_{ij}\left(q_k^n + \frac{\delta}{2}\widetilde{W}_k\right) \widetilde{W}_j - \mathcal{M}_{ij}\left(q_k^n - \frac{\delta}{2}\widetilde{W}_k\right) \widetilde{W}_j\right) \right\rangle
$$

$$
= \partial_j \mathcal{M}_{ij}(\boldsymbol{q}^n) + O(\delta^2),
\tag{4.25}
$$

where $\widetilde{\boldsymbol{W}}$ is a vector of $dn$ i.i.d. standard Gaussian random variables and $\delta$ is a small parameter.

While expression (4.25) could be used to approximate the drift term and may be a useful alternative to the Fixman scheme in related methods such as the fluctuating FCM [103], using an RFD of the form (4.25) requires at least one more Stokes solve per time step in order to evaluate the action of $\boldsymbol{M}(\boldsymbol{q} + \epsilon \Delta \boldsymbol{q})$. It is, however, possible to avoid the second Stokes solve by splitting the divergence of the mobility into two pieces,

$$
\eta\, \partial_{\boldsymbol{q}} \cdot \boldsymbol{M} = \partial_{\boldsymbol{q}} \cdot \left(\boldsymbol{J} \boldsymbol{\mathcal{L}}^{-1} \boldsymbol{S}\right) = (\partial_{\boldsymbol{q}} \boldsymbol{J}) : \left(\boldsymbol{\mathcal{L}}^{-1} \boldsymbol{S}\right) + \boldsymbol{J} \boldsymbol{\mathcal{L}}^{-1} \left(\partial_{\boldsymbol{q}} \cdot \boldsymbol{S}\right),
$$

where colon denotes a double contraction, see (4.31). We approximate the first term involving the gradient $\partial_{\boldsymbol{q}} \boldsymbol{J}$ using a standard two-stage Runge-Kutta (predictor-corrector) approach, and use an RFD to approximate $\partial_{\boldsymbol{q}} \cdot \boldsymbol{S}$, as explained in detail in Section 4.4.

## 4.3 Spatial Discretization For The Fluctuating Immersed Boundary Method

In this section we describe our spatial discretization of (4.18), which is constructed from components described in extensive detail in prior work by some of us; here we only briefly summarize the key points. The finite-volume solver used here to solve the fluctuating Stokes equations in confined domains is taken from Ref. [39], while the discretization of the fluid-particle interaction operators is based on the immersed-boundary method [128] and is described in extensive detail in Ref. [102]. The key novel component here is the use of a steady Stokes fluid solver to generate a fluctuating velocity, as also done in Refs. [106, 103, 129] using different techniques.

We discretize the fluid equation (4.9) using a standard staggered "marker and cell" (MAC) grid with uniform mesh width $h$ in a rectangular domain with an arbitrary combination of periodic, no-slip, or free-slip boundaries (see Section 3.3.2). The differential operators $\boldsymbol{D}$, $\boldsymbol{G}$, and $\boldsymbol{L}$ are discretized on the staggered grid using standard second order centered differences. The stochastic stress tensor $\boldsymbol{\mathcal{Z}}\left(\boldsymbol{r},t\right)$ is discretized as $\Delta V^{-\frac{1}{2}}\boldsymbol{\mathcal{W}}\left(t\right)$, where the additional factor of $\Delta V^{-\frac{1}{2}}$ comes from the fact that $\boldsymbol{\mathcal{Z}}$ is white in space. Adjustments to the stochastic increments are made near boundaries to preserve the fluctuation-dissipation relation $-\widetilde{\boldsymbol{D}}\widetilde{\boldsymbol{D}}^{T} = \boldsymbol{L}$ (more precisely, to ensure that $\boldsymbol{L} = -\widetilde{\boldsymbol{D}}\left\langle\boldsymbol{\mathcal{W}}\boldsymbol{\mathcal{W}}^{T}\right\rangle\widetilde{\boldsymbol{D}}^{T}$) [39].

### 4.3.1 Discrete Local Averaging and Spreading

The discrete operator (matrix) $\boldsymbol{\mathcal{J}}$ averages velocities on the staggered mesh by discretizing the integral $\int\delta_a(\boldsymbol{q}_i - \boldsymbol{r})\boldsymbol{v}(\boldsymbol{r})d\boldsymbol{r}$ using a simple quadrature

$$(\boldsymbol{\mathcal{J}}\boldsymbol{v})_i^\alpha = \sum_k \delta_a\left(\boldsymbol{q}_i - \boldsymbol{r}_k^\alpha\right)v_k^\alpha\Delta V,$$

where the sum is taken over faces $k$ of the grid, and $\Delta V$ is the volume of a grid cell. Here $\alpha$ indexes coordinate directions $(x, y, z)$ as a superscript, $\boldsymbol{r}_k^\alpha$ is the center of the grid face $k$ in the direction $\alpha$, and $v_k^\alpha \equiv v^{(\alpha)}\left(\boldsymbol{r}_k\right)$ is the staggered velocity field. Likewise, $\boldsymbol{\mathcal{S}}$ spreads forces to the staggered grid, and its expression remains identical to (4.11), but is evaluated only at faces of the staggered grid normal to the component of force being spread,

$$(\boldsymbol{\mathcal{S}}\boldsymbol{F})_k^\alpha = \sum_i F_i^\alpha\,\delta_a\left(\boldsymbol{q}_i - \boldsymbol{r}_k^\alpha\right),$$

where now the sum is over the particles.

For a uniform grid, the matrices representing the discrete local averaging and spreading operators are scaled transposes of each other, $\boldsymbol{\mathcal{J}}^T = \Delta V\,\boldsymbol{\mathcal{S}}$. Note that these discrete operators are adjoints like their continuum counterparts, $\boldsymbol{\mathcal{J}} = \boldsymbol{\mathcal{S}}^\star$, but in an inner product that includes an appropriate weighting [100] because the integral over the domain in (4.15) is replaced by a sum over grid points $k$,

$$\begin{aligned}
\sum_i (\boldsymbol{\mathcal{J}}\boldsymbol{v})_i \cdot \boldsymbol{F}_i &= \sum_{k,\alpha} v_k^\alpha (\boldsymbol{\mathcal{S}}\boldsymbol{F})_k^\alpha \Delta V \\
&= \sum_{i,k,\alpha} \delta_a\left(\boldsymbol{q}_i - \boldsymbol{r}_k^\alpha\right)v_k^\alpha F_i^\alpha\Delta V.
\end{aligned} \tag{4.26}$$

In the majority of the simulations we use the four-point kernel of Peskin [128] to discretize the kernel $\delta_a$, although in some cases we employ the three-point discrete kernel function of Roma and Peskin [142, 136]. The effective hydrodynamic radius $a$ for a given discrete kernel function can be obtained from the self-mobility of a blob in a periodic domain. For large periodic domains in three dimensions we numerically estimate the effective hydrodynamic (rigid sphere) radius to be $a = (0.91 \pm 0.01)\,h$ for the three-point kernel [136, 102], and $a = (1.255 \pm 0.005)\,h$ for the four-point kernel [137]. In two dimensions, the effective (rigid disk) hydrodynamic radii are estimated to be $a = (0.72 \pm 0.01)\,h$ for the three point and $a = (1.04 \pm 0.005)\,h$ for the four point kernel [120]. Note that the spatial discretization we use is not perfectly translationally invariant and there is a small variation of $a$ (quoted above as an error bar) as the particle moves relative to the underlying fixed fluid grid [102, 137]. By using the Peskin four-point kernel instead of the three-point discrete kernel function the translational invariance of the spatial discretization can be improved, however, at a potentially significant increase in computational cost, particularly in three dimensions.

It is important to note that, perhaps unexpectedly, these Peskin kernels give close agreement between the hydrodynamic and the Faxen radii of the blob. For example, in three dimensions, the three-point kernel gives $a_F \approx 0.93h$ (this number is again not exactly constant due to the imperfect translational invariance), as compared

to $a \approx 0.91h$. Using the four-point kernel gives an even better agreement, with $a \approx a_F \approx 1.25h$. In particular, it is important to choose a kernel with a nonzero second moment in order to capture the Faxen corrections in a physically-realistic manner; this eliminates the Peskin six-point kernel [128] from consideration.

### 4.3.2 Stokes Solver

In the FIB method we obtain the fluid velocity $\boldsymbol{v} = \eta^{-1}\boldsymbol{\mathcal{L}}^{-1}\boldsymbol{g}$ by numerically solving the discrete steady Stokes equation

$$
\begin{aligned}
\boldsymbol{G}\pi - \eta\boldsymbol{L}\boldsymbol{v} &= \boldsymbol{g} = \boldsymbol{\mathcal{S}}\boldsymbol{F} + \sqrt{\frac{2k_B T \eta}{\Delta V}}\,\widetilde{\boldsymbol{D}}\boldsymbol{\mathcal{W}} \qquad (4.27) \\
\boldsymbol{D}\boldsymbol{v} &= 0
\end{aligned}
$$

using a preconditioned Krylov iterative solver [85]. Note that we can explicitly write $\boldsymbol{\mathcal{L}}^{-1}$ using the Schur complement of (4.27),

$$
-\boldsymbol{\mathcal{L}}^{-1} = \boldsymbol{L}^{-1} - \boldsymbol{L}^{-1}\boldsymbol{G}\left(\boldsymbol{D}\boldsymbol{L}^{-1}\boldsymbol{G}\right)^{-1}\boldsymbol{D}\boldsymbol{L}^{-1}. \qquad (4.28)
$$

In the continuum setting, and also in the discrete setting with periodic boundary conditions, the various operators commute and one can simplify $\boldsymbol{\mathcal{L}}^{-1} = -\boldsymbol{P}\boldsymbol{L}^{-1}$, where $\boldsymbol{P} = \boldsymbol{I} - \boldsymbol{G}(\boldsymbol{D}\boldsymbol{G})^{-1}\boldsymbol{D}$ is the $L_2$ projection operator onto the subspace of (discretely) divergence free vector fields. In general, however, for many spatial discretizations, including the one we use, the operators do *not* commute and one must keep the full form (4.28) [1, 39].

### 4.3.3 Discrete Fluctuation Dissipation Balance

The spatially-discretized equation of motion for the particles has the same form as the continuum (4.18), and is an instance of (4.3) with the identification

$$
\begin{aligned}
\boldsymbol{M} &= \eta^{-1}\boldsymbol{\mathcal{J}}\boldsymbol{\mathcal{L}}^{-1}\boldsymbol{\mathcal{S}} \qquad (4.29) \\
\boldsymbol{M}^{\frac{1}{2}} &= (\eta\Delta V)^{-\frac{1}{2}}\,\boldsymbol{\mathcal{J}}\boldsymbol{\mathcal{L}}^{-1}\widetilde{\boldsymbol{D}}.
\end{aligned}
$$

Note that the key relation (4.20) continues to hold, $-\boldsymbol{\mathcal{L}}^{-1}\boldsymbol{L}\boldsymbol{\mathcal{L}}^{-1} = \boldsymbol{\mathcal{L}}^{-1}$, which follows directly from (4.28). This can be used to show that (4.2) is satisfied

$$
\begin{aligned}
\boldsymbol{M}^{\frac{1}{2}}&\left(\boldsymbol{M}^{\frac{1}{2}}\right)^T \qquad\qquad (4.30)\\
&= -(\eta\Delta V)^{-1}\left[\boldsymbol{\mathcal{J}}\boldsymbol{\mathcal{L}}^{-1}\left(\widetilde{\boldsymbol{D}}\widetilde{\boldsymbol{D}}^T\right)\boldsymbol{\mathcal{L}}^{-1}\left(\Delta V\,\boldsymbol{\mathcal{S}}\right)\right]\\
&= -\eta^{-1}\boldsymbol{\mathcal{J}}\left(\boldsymbol{\mathcal{L}}^{-1}\boldsymbol{L}\boldsymbol{\mathcal{L}}^{-1}\right)\boldsymbol{\mathcal{S}} = \eta^{-1}\boldsymbol{\mathcal{J}}\boldsymbol{\mathcal{L}}^{-1}\boldsymbol{\mathcal{S}} = \boldsymbol{M},
\end{aligned}
$$

where we made use of $\boldsymbol{\mathcal{J}}^T = \Delta V\,\boldsymbol{\mathcal{S}}$. Note that these relations are independent of the boundary conditions and thus (4.30) holds in confined systems.

## 4.4 Temporal Discretization

In this section we introduce our approach for temporal integration of the spatially-discretized equations of motion. A significant challenge is accurately capturing the stochastic drift present in the Ito interpretation, $\partial_{\boldsymbol{q}} \cdot \boldsymbol{M}(\boldsymbol{q})$, without which the system would not obey fluctuation-dissipation balance. This requires consistently discretizing the kinetic integral, which can be done in multiple dimensions using a Fixman predictor corrector scheme [5]. The Fixman scheme, however, requires applying the action of the inverse of the mobility (or, equivalently, the action of the square root of the inverse of the mobility), which is a complicating and a potentially expensive step [103]. Note that in certain cases, notably, for translationally-invariant situations such as periodic systems, the divergence of mobility vanishes and one can use a simple Euler-Maruyama integrator, as done in the work of Atzberger and collaborators [100]. This is not applicable to confined systems, however, and here we employ the Random Finite Difference (RFD) approach introduced in Section 2.1.1.2.

While the techniques in this chapter are introduced as direct discretizations of eq. (4.1), note that in the regime we are considering, the velocity of the fluid evolves much faster than the positions of the particles, and the system is an example of the those studied in section 2.3. This is a more natural way to think of this system, since

the equations of Brownian dynamics are in fact the overdamped limit of the inertial equations coupling the fluid and particle motion. The temporal integrators introduced in Section 2.3 can be applied directly to this problem. However, the Stokes solve required for the application of the mobility in this scenario is independent of configuration, and we can improve efficiency by developing a specialized temporal integrator for the FIB method which requires only one Stokes solve per time step.

Below we use the superscript $n$ to denote the current time step and quantities evaluated at the beginning of the current time step, and superscript $n+1$ for the updated quantities at the end of the time step. Quantities estimated at the midpoint of the time step are denoted with superscript $n + \frac{1}{2}$. For example, $\boldsymbol{M}^{n+\frac{1}{2}} \equiv \boldsymbol{M}\left(\boldsymbol{q}^{n+\frac{1}{2}}\right)$ denotes a midpoint approximation of the mobility. We develop two temporal integrators, a first-order simple midpoint method that requires only a single Stokes solve per time step, and an improved midpoint midpoint scheme that achieves second-order accuracy in the additive-noise (linearized) case at the cost of requiring two Stokes solves per time step. Which scheme allows for better tradeoff between accuracy and efficiency will depend on the specific problem at hand, and in particular, on the time step limitations imposed by stability considerations.

### 4.4.1 Simple midpoint scheme

A direct application of the RFD approach to integrating (4.18) would require evaluating the action of the mobility at two different configurations and thus at least two Stokes solves per time step. In order to avoid using a separate Stokes solver just to obtain the stochastic drift term, we take an alternative approach and split the stochastic drift into two pieces,

$$
\begin{aligned}
\eta \, \partial_j \mathcal{M}_{ij}\left(\boldsymbol{q}\right) = \partial_j \left( \mathcal{J}_{ik}(\boldsymbol{q}) \mathcal{L}_{kl}^{-1} \mathcal{S}_{lj}(\boldsymbol{q}) \right) = \\
\left( \partial_j \mathcal{J}_{ik}(\boldsymbol{q}) \right) \mathcal{L}_{kl}^{-1} \mathcal{S}_{lj}(\boldsymbol{q}) + \mathcal{J}_{ik}(\boldsymbol{q}) \mathcal{L}_{kl}^{-1} \left( \partial_j \mathcal{S}_{lj}(\boldsymbol{q}) \right),
\end{aligned}
\tag{4.31}
$$

where we use the implied summation convention. The two pieces can be handled separately, and only require the derivatives of $\boldsymbol{\mathcal{J}}$ and $\boldsymbol{\mathcal{S}}$. We approximate the term $\partial_j \mathcal{J}_{ik}(\boldsymbol{q})$ using a predictor-corrector approach in the spirit of Runge-Kutta algorithms such as the Euler-Heun temporal integrator for Stratonovich equations [38]. We use an RFD of the form (2.14) with $\Delta \boldsymbol{q} \sim \Delta \boldsymbol{p}$ to calculate the term $\partial_j \mathcal{S}_{lj}(\boldsymbol{q})$.

Our basic temporal integrator for the spatially-discretized equations (4.18) consists of first solving the steady Stokes equations with a random forcing,

$$
\begin{aligned}
-\eta \boldsymbol{L} \boldsymbol{v} + \boldsymbol{G} \pi = \boldsymbol{\mathcal{S}}^n \boldsymbol{F}^n + \sqrt{\frac{2 \eta k_B T}{\Delta t \Delta V}} \widetilde{\boldsymbol{D}} \boldsymbol{W}^n \\
+ \frac{k_B T}{\delta} \left[ \boldsymbol{\mathcal{S}}\left( \boldsymbol{q}^n + \frac{\delta}{2} \widetilde{\boldsymbol{W}}^n \right) - \boldsymbol{\mathcal{S}}\left( \boldsymbol{q}^n - \frac{\delta}{2} \widetilde{\boldsymbol{W}}^n \right) \right] \widetilde{\boldsymbol{W}}^n,
\end{aligned}
\tag{4.32}
$$

and then advecting the particles with the computed velocity field using a midpoint predictor-corrector scheme,

$$
\begin{aligned}
\boldsymbol{q}^{n+\frac{1}{2}} &= \boldsymbol{q}^n + \frac{\Delta t}{2} \boldsymbol{\mathcal{J}}^n \boldsymbol{v} \tag{4.33} \\
\boldsymbol{q}^{n+1} &= \boldsymbol{q}^n + \Delta t \boldsymbol{\mathcal{J}}^{n+\frac{1}{2}} \boldsymbol{v}. \tag{4.34}
\end{aligned}
$$

Here $\boldsymbol{W}^n$ is a random vector of i.i.d. standard Gaussian random numbers that represent stochastic fluxes of momentum, with $\boldsymbol{W}^n / \sqrt{\Delta t}$, loosely speaking, being a temporal discretization of $\boldsymbol{\mathcal{W}}(t)$. The auxiliary displacement $\widetilde{\boldsymbol{W}}^n$ is a vector of $nd$ i.i.d. standard Gaussian variates. The parameter $\delta$ should be as small as possible while still resolving to numerical roundoff the length scale over which $\boldsymbol{\mathcal{S}}$ varies; we use $\delta \approx 10^{-6} h$, where $h$ is the grid spacing.

The first-order midpoint temporal integrator (4.32)-(4.34) has the advantage that we can recreate the stochastic drift $\partial_{\boldsymbol{q}} \cdot \boldsymbol{M}$ by performing only two additional spreading operations and one local averaging operation per time step, in addition to the required Stokes solve. We use a midpoint corrector step (4.34) because in the absence of the RFD term it gives the correct diffusion coefficient for freely-diffusing single particles, *regardless* of the time step size. Namely, for any choice of $\Delta t$, the second moment of the stochastic increment of the particle positions is in agreement with the Einstein formula for the diffusion coefficient,

$$
\begin{aligned}
\mathrm{Var}\left( \boldsymbol{q}^{n+1} - \boldsymbol{q}^n \right) &= 2 \Delta t \, k_B T \eta^{-1} \left( \boldsymbol{\mathcal{J}}^{n+\frac{1}{2}} \boldsymbol{\mathcal{L}}^{-1} \boldsymbol{\mathcal{S}}^{n+\frac{1}{2}} \right) \\
&= 2 \Delta t \, k_B T \, \boldsymbol{M}^{n+\frac{1}{2}},
\end{aligned}
\tag{4.35}
$$

up to correction terms coming from the RFD term in the second line of (4.32). In section 4.5.2, we confirm that this property continues to hold to very high accuracy when the RFD is included, even for relatively large $\Delta t$. Note that a trapezoidal scheme that replaces the term $\boldsymbol{\mathcal{J}}^{n+\frac{1}{2}}\boldsymbol{v}$ in (4.34) with $\left(\boldsymbol{\mathcal{J}}^n + \boldsymbol{\mathcal{J}}^{n+1}\right)\boldsymbol{v}/2$ does not have the property (4.35) and only gives the correct diffusion coefficient for small $\Delta t$.

The predictor corrector steps (4.33)-(4.34) reproduce the first term on the right hand side of (4.31). The added stochastic force in the Stokes solve generates the thermal forcing (4.16), which appears in the second term on the right hand side of (4.31), in expectation to order $\delta^2$,

$$
\begin{aligned}
\frac{k_B T}{\delta} &\left\langle \mathcal{S}_{lj}\left(\boldsymbol{q}^n + \frac{\delta}{2}\widetilde{\boldsymbol{W}}^n\right)\widetilde{W}_j^n - \mathcal{S}_{lj}\left(\boldsymbol{q}^n - \frac{\delta}{2}\widetilde{\boldsymbol{W}}^n\right)\widetilde{W}_j^n \right\rangle \\
&= k_B T\left(\partial_k \mathcal{S}_{lj}\left(\boldsymbol{q}^n\right)\right)\left\langle \widetilde{W}_k^n \widetilde{W}_j^n \right\rangle + O\left(\delta^2\right) \\
&= k_B T\, \partial_j \mathcal{S}_{lj}\left(\boldsymbol{q}^n\right) + O\left(\delta^2\right).
\end{aligned}
\tag{4.36}
$$

In Section 4.7 we demonstrate that the simple midpoint scheme (4.32)-(4.34) is a first-order weak integrator for the equations of Brownian dynamics (4.18).

### 4.4.2 Improved midpoint scheme

It is possible to obtain second order accuracy in the additive-noise (linearized) approximation by using an additional Stokes solve in the corrector stage, as summarized by

$$
\begin{aligned}
&-\eta \boldsymbol{L}\boldsymbol{v} + \boldsymbol{G}\pi = \boldsymbol{\mathcal{S}}^n \boldsymbol{F}^n + \sqrt{\frac{4\eta k_B T}{\Delta t \Delta V}}\widetilde{\boldsymbol{D}}\boldsymbol{W}^{n,1} \\
&\boldsymbol{D}\boldsymbol{v} = 0 \\
&\boldsymbol{q}^{n+\frac{1}{2}} = \boldsymbol{q}^n + \frac{\Delta t}{2}\boldsymbol{\mathcal{J}}^n \boldsymbol{v} \quad \text{(predictor)} \\
&-\eta \boldsymbol{L}\tilde{\boldsymbol{v}} + \boldsymbol{G}\tilde{\pi} = \boldsymbol{\mathcal{S}}^{n+\frac{1}{2}}\boldsymbol{F}^{n+\frac{1}{2}} + \sqrt{\frac{\eta k_B T}{\Delta t \Delta V}}\widetilde{\boldsymbol{D}}\left(\boldsymbol{W}^{n,1} + \boldsymbol{W}^{n,2}\right) \\
&+\frac{k_B T}{\delta}\left[\boldsymbol{\mathcal{S}}\left(\boldsymbol{q}^n + \frac{\delta}{2}\widetilde{\boldsymbol{W}}^n\right) - \boldsymbol{\mathcal{S}}\left(\boldsymbol{q}^n - \frac{\delta}{2}\widetilde{\boldsymbol{W}}^n\right)\right]\widetilde{\boldsymbol{W}}^n \\
&\boldsymbol{D}\tilde{\boldsymbol{v}} = 0 \\
&\boldsymbol{q}^{n+1} = \boldsymbol{q}^n + \Delta t \boldsymbol{\mathcal{J}}^{n+\frac{1}{2}}\tilde{\boldsymbol{v}} \quad \text{(corrector)}.
\end{aligned}
\tag{4.37}
$$

Here the independent random variables $\boldsymbol{W}^{n,1}$ and $\boldsymbol{W}^{n,2}$ represent the two independent Wiener increments over each half of the time step. Note that by using a midpoint corrector step we ensure that the property (4.35) continues to hold. Here we only include an RFD term in the corrector step and use the initial position of the particle in the RFD term. One can also use $\boldsymbol{q}^{n+\frac{1}{2}}$ instead of $\boldsymbol{q}^n$ but this gains no additional accuracy.

Note that the scheme (4.37) is still only first order weakly accurate (see Section 4.7) because the noise in (4.18) is multiplicative. Achieving second-order weak accuracy in the nonlinear case requires more sophisticated stochastic Runge-Kutta schemes [32]. However, we will demonstrate in Sec. 4.5.4 that the improved midpoint scheme can sometimes give results which are significantly more accurate because the scheme (4.37) can be shown to be second order weakly accurate for the linearized (additive-noise) equations of Brownian dynamics [1]. The improved midpoint scheme may also give improved stability in certain cases, as we observe numerically in Section 4.5.5. Note, however, that both midpoint schemes are explicit and are thus subject to stability limits on $\Delta t$, dictated by the stiffness of the applied forces $\boldsymbol{F}(\boldsymbol{q})$.

## 4.5 Numerical Simulations

In this section we test the performance of the FIB by simulating a number of scenarios of increasing complexity. We start by confirming that our spatial discretization gives a mobility in agreement with known results for a single particle in a slit channel. We then confirm that our temporal integrators preserve the correct Gibbs-Boltzmann distribution for both single and multiparticle systems. After also verifying that the FIB method correctly reproduces the dynamical correlations between particles in the presence of shear flow and hydrodynamic interactions, we compare our method to standard Brownian Dynamics on the nonequilibrium dynamics of a colloidal cluster. Unless otherwise mentioned, the tests were conducted using the simple midpoint temporal integrator (4.32)-(4.34).

We have implemented the FIB algorithm in the open source code IBAMR [86], a parallel implementation of the immersed boundary method. The state-of-the-art multigrid-based iterative Stokes solvers [85] implemented in IBAMR enable us to efficiently solve the steady Stokes equations for any combination of periodic, no-slip or free-slip boundaries on the side of a rectangular domain, including in the presence of thermal fluctuations [39]. Although IBAMR supports adaptive mesh refinement (AMR) for deterministic time-dependent problems, at present only uniform grids are supported for steady-state flows with fluctuations. Unless otherwise specified, the simulations reported here were performed using the IBAMR implementation of the FIB method.

For periodic domains, no iterative solvers are necessary for uniform grids since the discrete Fourier transform diagonalizes the discrete Stokes equations and the Fast Fourier Transform (FFT) can be used to solve the steady Stokes equations very efficiently. This was used by some of us to solve the inertial fluid-particle equations efficiently on Graphical Processing Units (GPUs), as implemented in the open-source *fluam* CUDA code [102]. Implementing the FIB method in *fluam* amounted to simply changing the temporal integration scheme (for both the fluid and the particle dynamics) to the midpoint scheme (4.32)-(4.34), while reusing the core numerical implementation. Note that we only use FFTs as a linear solver for the discrete Stokes equations, similar to what is done in SIBM [124]. This means that the IBAMR and *fluam* codes give the same results for periodic systems to within solver tolerances. For periodic systems at zero Reynolds number flow a much higher (spectral) spatial accuracy can be accomplished by using a Fourier representation of the velocity and pressure, as done by Keaveny [103]. In fact, with proper care in choosing the number of Fourier modes kept and the help of the non-uniform FFT algorithm [143] one can construct a spatial discretization where the truncation error is at the level of roundoff tolerance [23]. In the presence of simple confinement such as a slit channel with only two walls, a Fourier representation can be used in the directions parallel to the channel walls, along with a different basis for the direction perpendicular to the walls. Here we do not explore such specialized geometries and use a finite-volume Stokes solver to handle more general combinations of boundary conditions.

While the different tests performed have different relevant timescales, there is an important common timescale of diffusion given by the typical time it takes a free particle to diffuse a distance $h$, where $h$ is the grid spacing. The typical value of the diffusion coefficient of a single spherical particle in a translationally-invariant system can be obtained from the mobility $\mu$ via the Stokes-Einstein relation, $\boldsymbol{\chi}_{\text{self}} = k_B T \boldsymbol{M}_{\text{self}} = k_B T \mu \boldsymbol{I} = \chi \boldsymbol{I}$, and leads to $\chi \approx k_B T / (6\pi\eta a)$ in three dimensions, and $\chi \approx k_B T \left(4\pi\eta\right)^{-1} \ln\left(L/3.708a\right)$ in two dimensions [120], where we recall that $a$ is the effective hydrodynamic radius of a blob and $L$ is the length of the periodic domain. In three dimensions there are well-known finite size corrections to the mobility that are taken into account in the calculations below [141, 99, 102, 137]. Based on the estimated diffusion coefficient we can define a dimensionless time step size through the diffusive Courant number

$$\beta = \frac{2\chi}{h^2}\Delta t.$$

This dimensionless number should be kept small (e.g., $\beta \lesssim 0.25$) in order to prevent a particle from jumping more than one grid cell during a single time step. Note that this time step limitation is much weaker than the corresponding limitation in methods that resolve the inertial dynamics, such as the Inertial Coupling method [102]. Resolving the time scale of the momentum diffusion requires keeping $\beta_\nu = 2\nu\Delta t/h^2 = \text{Sc}\,\beta$ small, which requires a time step on the order of $\text{Sc} \sim 10^3 - 10^4$ smaller than the FIB method. Note, however, that in applications the time step may further be limited by other factors such as the presence of stiff inter-particle potentials, as we discuss further in Section 4.5.5.

## 4.5.1   Mobility in a Slit Channel

The mobility of a single particle in a slit channel is affected by the presence of the two walls. We estimate this effect by placing a particle at multiple points across a $128h\text{x}128h\text{x}32h$ channel with planar no-slip walls at $z = 0$ and $z = 32h$, and periodic boundaries along the $x$ and $y$ directions. For each position of the blob, a unit force is applied either parallel and perpendicular to the wall, the Stokes system (4.17) without the stochastic momentum flux is solved, and the resulting particle velocity is calculated, giving the parallel $\mu_\parallel$ and perpendicular $\mu_\perp$ mobilities. The results of these calculations are reported in Fig. 4.1.

Unlike the case of a single no-slip boundary [11], writing down an analytical solution for slit channels is complex and requires numerically-evaluating the coefficients in certain series expansions [10]. For the parallel component of
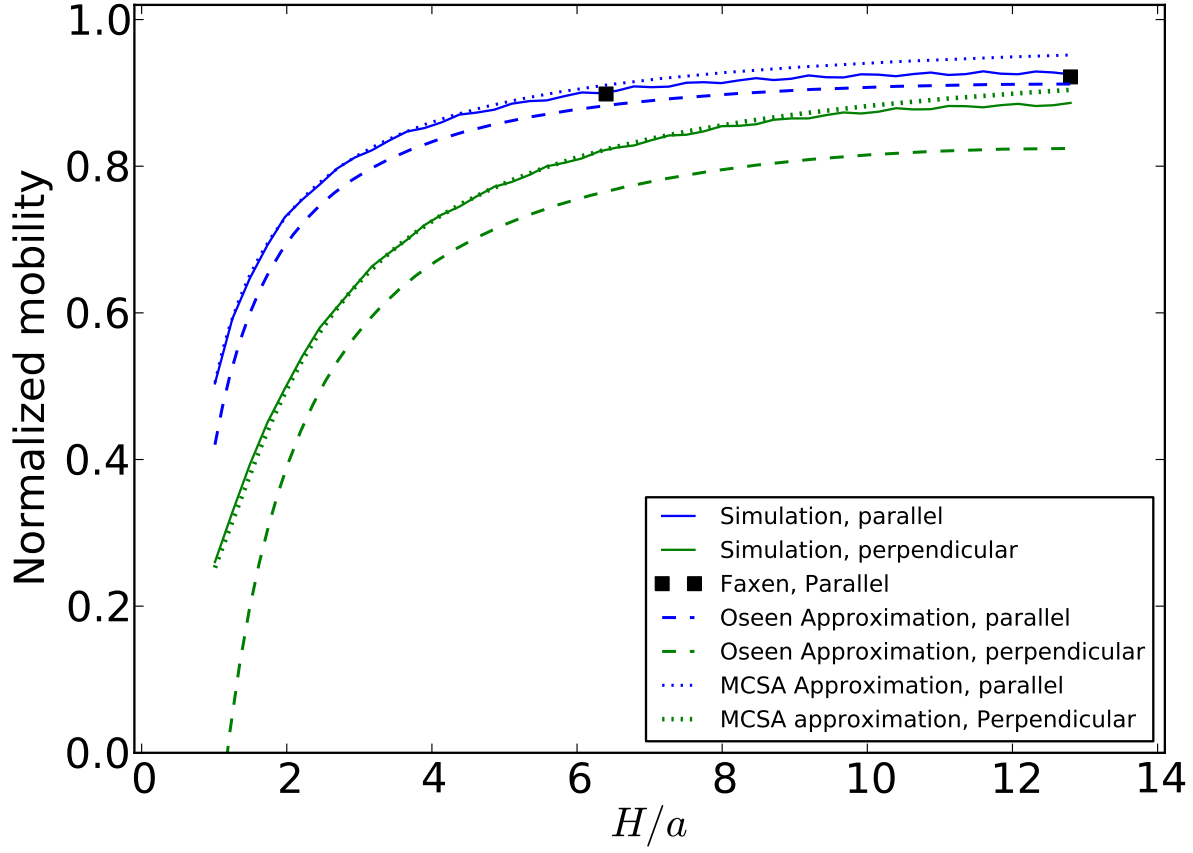
Figure 4.1: Mobility of a blob in a slit channel (relative to unbounded flow) in the directions parallel (blue lines and symbols) and perpendicular (green lines) to the confining no-slip walls as a function of the distance $H$ to the wall (expressed here in terms of the blob hydrodynamic radius $a$), in three dimensions. Note that small oscillations appear due to numerical grid artifacts. For the parallel mobility, simulation is in excellent agreement with two exact results obtained by Faxen (symbols), and over the whole range of distances the results are in good agreement with the Oseen [144] (dashed lines) and the more accurate MCSA (dotted lines) approximation [145].

the mobility, Faxen has obtained exact series expansions for the mobility at the half and quarter channel locations,

$$\mu_{\parallel}\left(H = \frac{L}{2}\right) = \frac{1}{6\pi\eta a}\left[1 - 1.004\frac{a}{H} + 0.418\frac{a^3}{H^3}\right.$$

$$\left. + 0.21\frac{a^4}{H^4} - 0.169\frac{a^5}{H^5} + \ldots\right]$$

$$\mu_{\parallel}\left(H = \frac{L}{4}\right) = \frac{1}{6\pi\eta a}\left[1 - 0.6526\frac{a}{H} + 0.1475\frac{a^3}{H^3}\right.$$

$$\left. - 0.131\frac{a^4}{H^4} - 0.0644\frac{a^5}{H^5} + \ldots\right]$$

where $H$ denotes the distance from the blob to the nearest wall, and $L$ is the distance between the walls. Here we neglect the corrections coming from the use of periodic boundary conditions in the $x$ and $y$ directions. As seen in Fig. 4.1, the exact results of Faxen are in excellent agreement with the numerical mobilities.

For other positions of the blob, we employ two different approximations. First we calculate an Oseen approximation [146] consisting of a heuristic superposition of two single-wall mobilities (c.f. Eqs. (1a,1b) of Ref. [145]). This is only an approximation to the correct result, but it provides an estimate of the trend in mobility across the channel and has been found to be in reasonable agreement with experimental results [144]. We expect this trend will underestimate the exact mobility because the superposition of single wall results will give a fluid velocity on the boundary moving against the direction of the applied force. Figure 4.1 shows that the Oseen approximation also underestimates our numerical results slightly, but exhibits similar qualitative behavior across the channel, giving evidence that the mobility calculated with our methods correctly captures the effects of no-slip boundaries. A more accurate approximation to the unwieldy full expression for the mobility [10] is given by the Modified Coherent Superposition Assumption (MCSA), which considers an infinite sum of reflections of the single-wall solutions in another wall [145]. In Fig. 4.1 we show an MCSA approximation which we evaluated using (c.f. Eq. (9) in Ref. [145])

$$
\frac{\mu^{(2)}}{\mu_0} = \left\{ 1 + \sum_{n=0}^{\infty} (-1)^n \left[ \frac{\mu_0}{\mu^{(1)}(nL + H)} - 1 \right] + \right.
$$
$$
\left. + \sum_{n=1}^{\infty} (-1)^n \left[ \frac{\mu_0}{\mu^{(1)}\left((n+1)L - H\right)} - 1 \right] \right\}^{-1} \tag{4.38}
$$

where $\mu^{(2)}$ is either the parallel $\mu_{\parallel}^{(2)}$ or the perpendicular $\mu_{\perp}^{(2)}$ mobility in the slit channel, $\mu_0$ is the mobility in an unbounded domain, and the parallel or perpendicular single-wall mobility $\mu^{(1)}$ is given by well-known expansions truncated at the fifth-order term [11, 10],

$$
\frac{\mu_{\perp}^{(1)}(H)}{\mu_0} = 1 - \frac{9a}{8H} + \frac{a^3}{2H^3} - \frac{a^5}{8H^5} \tag{4.39}
$$
$$
\frac{\mu_{\parallel}^{(1)}(H)}{\mu_0} = 1 - \frac{9a}{16H} + \frac{2a^3}{16H^3} - \frac{a^5}{16H^5},
$$

Note that $\mu^{(2)} \approx \mu^{(1)}$ when the distance between the walls is very large, $L \gg H \gg a$, as it must. The MCSA (4.38) is seen to be in very good agreement with our numerical results in Fig. 4.1. Both the MCSA and Oseen approximations are for an infinite slit geometry, whereas we use periodic boundary conditions in the directions parallel to the walls; we expect this has a small effect on the value of the mobility calculated due to hydrodynamic screening, as evidenced by the match with the exact results by Faxen.

## 4.5.2 Diffusion Coefficient

As explained in Section 4.4.1, we chose the midpoint form of the predictor corrector (4.33,4.34), because this gives an accurate diffusion coefficient even for large time step size $\Delta t$. Here we confirm this by numerically estimating the time-dependent diffusion coefficient of a single freely-diffusing particle in a two dimensional periodic domain

$$
\chi(s) = \frac{1}{2ds} \left\langle \|\boldsymbol{q}(t+s) - \boldsymbol{q}(t)\|^2 \right\rangle
$$

for a range of time step sizes. For comparison, we also try a simple trapezoidal predictor-corrector scheme that replaces (4.33,4.34) with

$$
\boldsymbol{q}^{\star,n+1} = \boldsymbol{q}^n + \Delta t \boldsymbol{\mathcal{J}}^n \boldsymbol{v}
$$
$$
\boldsymbol{q}^{n+1} = \boldsymbol{q}^n + \frac{\Delta t}{2} \left( \boldsymbol{\mathcal{J}}^n + \boldsymbol{\mathcal{J}}^{\star,n+1} \right) \boldsymbol{v}. \tag{4.40}
$$

This scheme is also a first-order weakly accurate integrator, but does not satisfy the property (4.35).

Figure 4.2 shows that the midpoint predictor corrector (4.33,4.34) gives a diffusion coefficient that agrees with the theoretical result $\chi(s) = k_B T \mu$ independent of $s$ to within statistical error for time step sizes as large as $\beta = \Delta t / \tau = 2\chi \Delta t / h^2 = 1.43$, where $\tau$ is the natural diffusive time scale for this test. By contrast, the trapezoidal scheme (4.40) introduces a measurable truncation error already for $\beta \gtrsim 0.2$. Both schemes include an RFD term to approximate the (small) drift term present due to the discretization showing that the RFD term does not ruin the accuracy of the diffusion coefficient for the midpoint scheme.
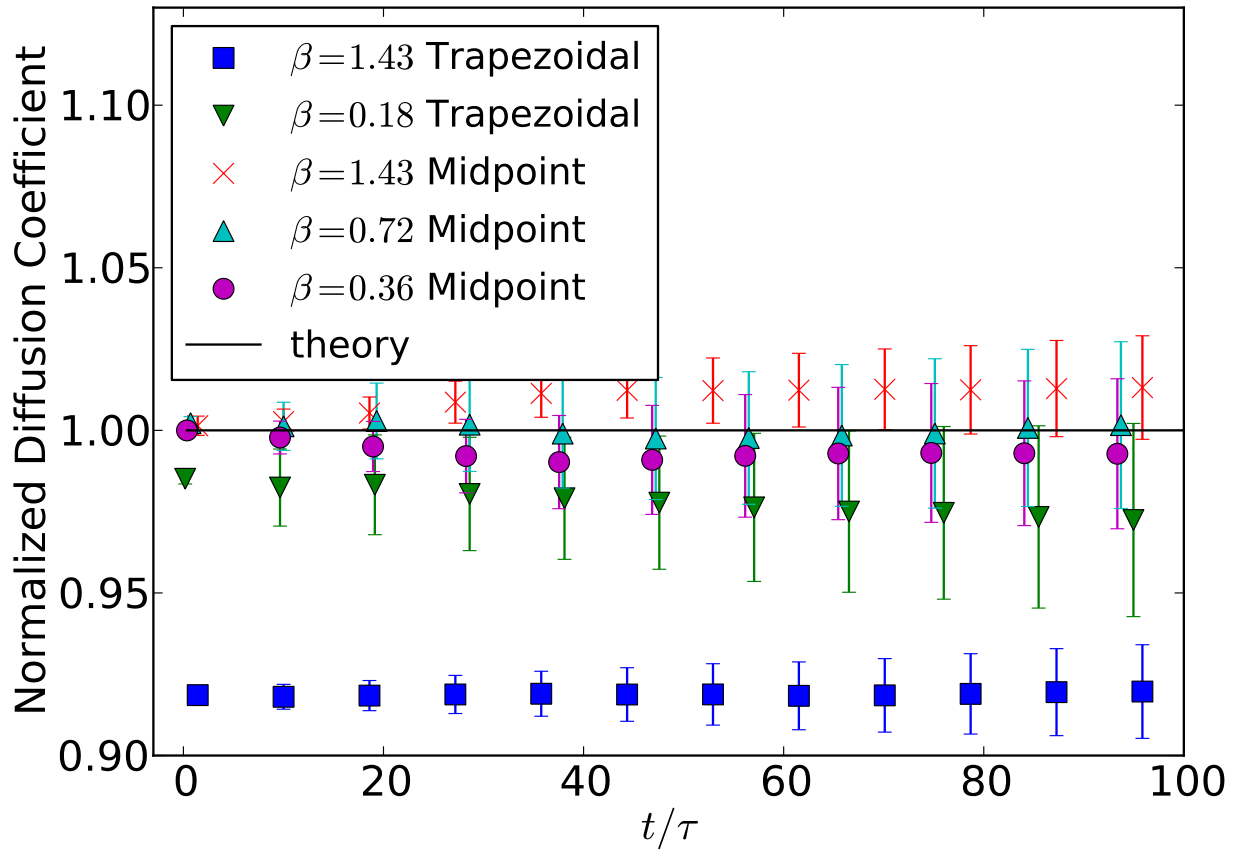
Figure 4.2: Normalized diffusion coefficient for multiple time step sizes using the midpoint (4.33,4.34) or the trapezoidal (4.40) predictor-corrector schemes.

### 4.5.3 Thermodynamic Equilibrium

One of the most important requirements on any scheme that couples fluctuating hydrodynamics to immersed particles is to reproduce the Gibbs-Boltzmann distribution (4.4) at thermodynamic equilibrium, independent of any dynamical parameters such as viscosity. In prior work [102], we confirmed that when fluid and particle inertia are consistently included in the formulation, the numerical method reproduces the correct equilibrium distribution for both the particle positions and the appropriate Maxwell-Boltzmann distribution for the particle velocities. In the overdamped limit considered here there are no velocity degrees of freedom, but the method should still reproduce the correct Gibbs-Boltzmann distribution (4.4) for sufficiently small time steps. In this section we consider several scenarios and verify that the FIB method correctly reproduces the theoretical equilibrium distribution. As we demonstrate next, in the case of a non-constant mobility this necessitates the proper inclusion of the stochastic drift terms using the specialized temporal integration techniques we developed in Section 4.4.

#### 4.5.3.1 Free Diffusion

In the continuum setting, for a single particle in a periodic system translational invariance implies that the mobility does not depend on the position of the particle, and therefore $\partial_{\boldsymbol{q}} \cdot \boldsymbol{M} = 0$. However, upon spatial discretization, translational invariance is broken by the presence of a fixed Eulerian grid on which the fluid equation is solved. Even though the Peskin kernels give excellent translational invariance of the mobility, there is still a fraction to a few percent (depending on the kernel) variation in the mobility as the particle position shifts relative to the underlying grid. Here we show that our midpoint temporal integrators correct for this and ensure a uniform equilibrium distribution for the position of freely-diffusing particles.

In this test, 3000 particles are allowed to diffuse freely in a periodic two-dimensional domain of size $16h \times 16h$. Because the particles do not exert forces on each other, each of the particles is statistically identical to an isolated particle diffusing in the same domain (even though the particles are not independent because of the hydrodynamic interactions [140]), and at equilibrium their positions should be independent and uniformly distributed in the periodic domain. A small time step size corresponding to $\beta \approx 0.01$ is used to approach the limit $\Delta t \to 0$. The three-point Peskin kernel is used in order to maximize the lack of translational invariance.

For testing purposes, we dropped the RFD and corrector stages in the simple midpoint scheme (4.32)-(4.34) to obtain the Euler-Maruyama integrator,

$$
\begin{aligned}
-\eta \boldsymbol{L}\boldsymbol{v} + \boldsymbol{G}\pi &= \boldsymbol{\mathcal{S}}^n \boldsymbol{F}^n + \sqrt{\frac{2k_B T}{\Delta t \Delta V}} \widetilde{\boldsymbol{D}} \boldsymbol{W}^n \\
\boldsymbol{D}\boldsymbol{v} &= 0 \\
\boldsymbol{q}^{n+1} &= \boldsymbol{q}^n + \Delta t \boldsymbol{\mathcal{J}}^n \boldsymbol{v}.
\end{aligned}
\tag{4.41}
$$

Note that this temporal integrator is inconsistent with the kinetic interpretation of the noise term, i.e., it is not consistent with the Fokker-Planck equation (2.5); it is biased even in the limit $\Delta t \to 0$.

The Euler-Maruyama method was compared with our midpoint scheme (4.32)-(4.34) by computing an empirical histogram for the equilibrium distribution of the position of a particle inside a cell (due to translational invariance of the periodic grid the distribution is the same in all grid cells). The results in Fig. 4.3 show small but clear artifacts in the equilibrium distribution when using the Euler-Maruyama (4.41) scheme, specifically, the particle is more likely to be found near the corners of the grid cell instead of the center of the grid cell. By contrast, our consistent integrator (4.32)-(4.34) give a uniform distribution for the position of the particle for sufficiently small time step sizes; the same is true for the improved integrator (4.37), not shown.

#### 4.5.3.2 Diffusion in a slit channel

One key strength of the FIB method is the ability to handle non-periodic boundary conditions. In this test particles are placed in a two-dimensional channel and allowed to diffuse freely. When a particle comes within a cutoff range $w$ from one of the two no-slip walls, it is repelled with a harmonic potential with spring stiffness $k$,

$$
U(H) = \frac{k}{2}(H - w)^2 \quad \text{if} \quad H \leq w \quad \text{and zero otherwise,}
\tag{4.42}
$$

where $H$ is the distance of the particle from the wall. The total potential for the equilibrium distribution is the sum of the top and bottom wall potentials. A long equilibrium run is performed in order to compute an empirical histogram for the marginal equilibrium distribution $P(H)$ for finding a particle at a given distance $H$ from the nearest wall (note that all particles are statistically identical). We perform the simulations in two dimensions in
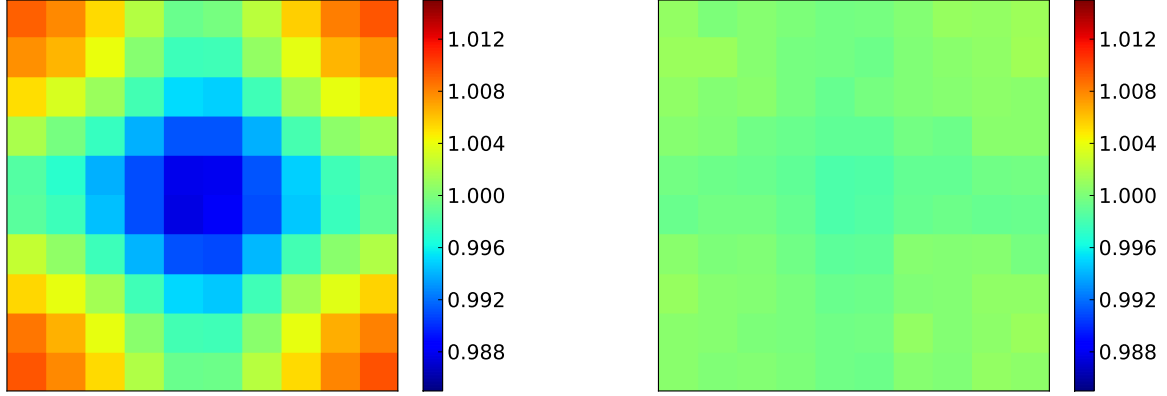
Figure 4.3: *(Left panel)* Normalized equilibrium probability distribution for finding a free particle at a particular position inside a grid cell when using the Euler-Maruyama scheme (4.41). A slightly nonuniform distribution is observed, in disagreement with the correct uniform Gibbs-Boltzmann distribution. This error does *not* vanish in the limit $\Delta t \to 0$. *(Right panel)* Using the midpoint scheme (4.32)-(4.34) preserves the correct distribution. The small residual artifacts disappear in the limit $\Delta t \to 0$. The same color scale (with variation in the range $0.985 - 1.015$) is used for both panels.

| Number of particles | 100 (midpoint) or 1 (Euler) |
|---|---|
| wall "spring" constant $k$ | $6 \left( k_B T / h^2 \right)$ |
| wall potential range $w$ | $7h$ |
| dimensionless time step size $\beta$ | 0.45 |
| domain width $L_x$ | $8h$ |
| domain height $L_y$ | $64h$ |

Table 4.1: Parameters used for the slit channel simulation results shown in Fig. 4.4.

order to maximize the statistical accuracy. The values of the simulation parameters are given in Table 4.1. Note that here we employ a relative large time step size in order to test the robustness of our temporal integrators.

As illustrated in Fig. 4.4, the results of the midpoint algorithm (4.32) with 100 particles compares favorably to the correct Gibbs-Boltzmann distribution $P(H) = Z^{-1} \exp\left(-U(H)/k_B T\right)$. We also test the biased Euler-Maruyama scheme (4.41) for a single particle. This scheme does not reproduce the stochastic drift term from Eq. (4.18), and thus yields an unphysical result where particles are more likely to be found near the boundaries (see also discussion in Section III.C in Ref. [10]).

In fact, the equilibrium distribution preserved by the biased scheme (4.41) in the limit $\Delta t \to 0$ can be calculated analytically for a single particle. For one particle in a slit channel, the $x$ and $y$ components of (4.1) decouple, and the only interesting dynamics occurs in the direction perpendicular to the channel walls. The Euler-Maruyama scheme (4.43) is consistent with the Ito equation

$$\frac{dH}{dt} = -\mu_\perp(H)\, U'(H) + \sqrt{2k_B T \mu_\perp(H)}\, \mathcal{W}_2\left(t\right). \tag{4.43}$$

By adding and subtracting $k_B T \mu'_\perp(H)$ we can convert this into the kinetic stochastic interpretation,

$$
\begin{aligned}
\frac{dH}{dt} &= -\mu_\perp(H)\, \widetilde{U}'(H) + \sqrt{2k_B T \mu_\perp(H)}\, \mathcal{W}_2\left(t\right) \\
&\quad + k_B T\, \mu'_\perp(H) \\
&= -\mu_\perp(H)\, \widetilde{U}'(H) + \sqrt{2k_B T \mu_\perp(H)} \diamond \mathcal{W}_2\left(t\right),
\end{aligned}
$$

where the biased potential is

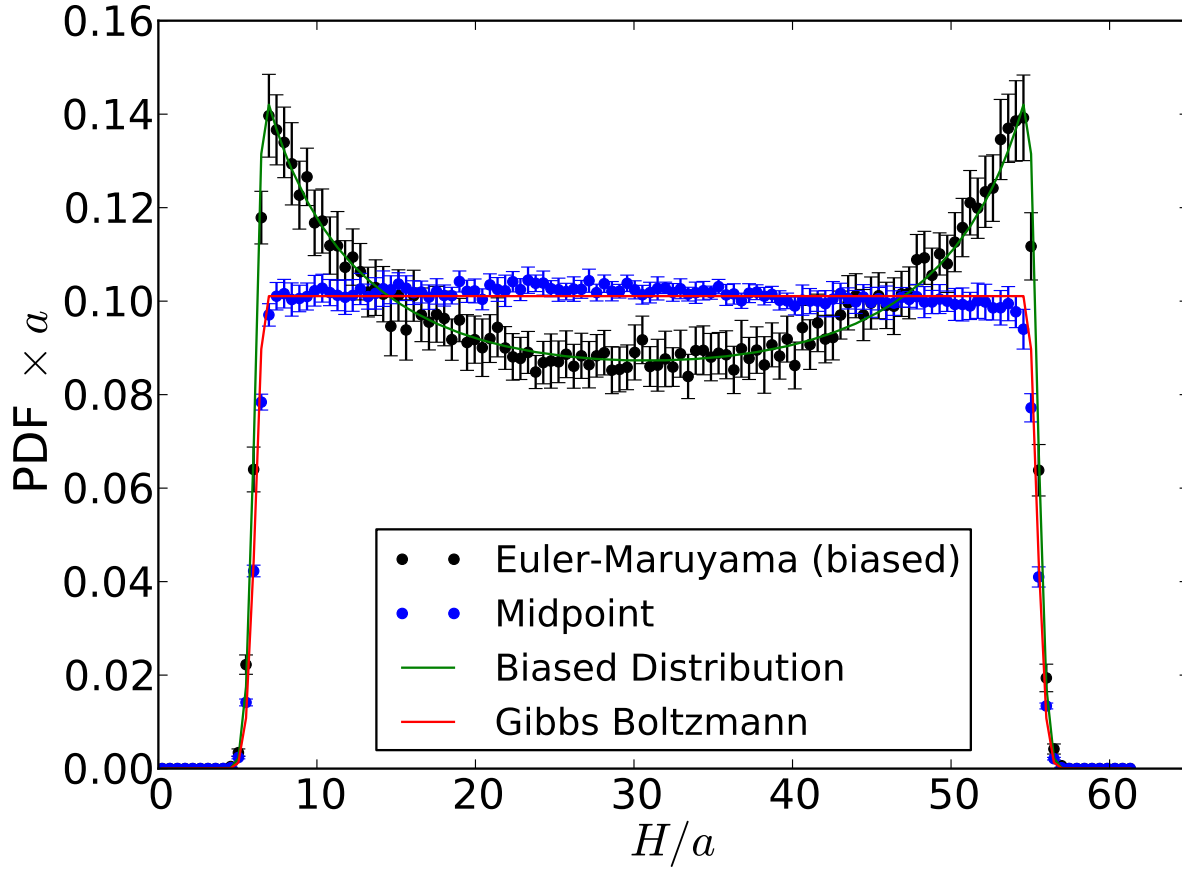$$\widetilde{U}(H) = U(H) + k_B T\, \ln(\mu_\perp(H)).$$

Figure 4.4: Probability distribution of the distance $H$ to one of the walls for a freely-diffusing single blob (Euler-Maruyama scheme (4.41)), as well as many non-interacting (midpoint scheme (4.32)) blobs, in a two dimensional slit channel. The correct (unbiased) (4.4) and the biased (4.44) Gibbs-Bolzmann distribution are shown for comparison.

| | |
|---|---|
| grid spacing $\Delta x$ | 1 |
| grid size | $32^3$ |
| shear viscosity $\eta$ | 1 |
| time step size $\Delta t$ | Variable |
| temperature $k_B T$ | $10^{-3}$ |
| LJ strength $\epsilon$ | $10^{-3}$ |
| LJ / hydro diameter $\sigma$ | 2 |
| number of particles $N$ | 1000 (dilute) or 3300 (dense) |

Table 4.2: Parameters used in the colloidal suspension equilibrium simulations shown in Fig. 4.5.

This shows that the Euler-Maruyama scheme (4.43) preserves the biased Gibbs-Boltzmann distribution corresponding to the biased potential $\widetilde{U}(H)$,

$$P_E(H) = \widetilde{Z}^{-1} \exp\left(-\frac{\widetilde{U}(H)}{k_B T}\right). \tag{4.44}$$

The biased distribution $P_E(H)$ is shown in Fig. 4.4 with $\mu_\perp$ calculated numerically (see Fig. 4.1). The biased distribution indeed matches the simulation results from the Euler-Maruyama scheme, confirming that the correct equilibrium distribution is not preserved without the RFD term and predictor-corrector steps. At the same time, we see that the temporal integrator (4.32)-(4.34) preserves the correct thermodynamic equilibrium distribution even in the presence of confinement.

### 4.5.3.3 Colloidal suspension

In this section we verify that our FIB algorithm gives the correct equilibrium distribution $P(\boldsymbol{q})$ for a multi-particle system by computing the radial (pair) distribution function (RDF) $g(r)$ for a periodic collection of $N$ colloidal particles interacting with a pairwise repulsive truncated Lennard-Jones (LJ) potential $V(r)$,

$$U(\boldsymbol{q}) = \sum_{i,j=1}^{N} V\left(\left\|\boldsymbol{q}_i - \boldsymbol{q}_j\right\|\right),$$

as described in more detail in Section 4.1 in Ref. [102]. The parameters used for these simulations are given in Table 4.2, and the GPU-based code *fluam* with the three point kernel is used for these simulations [102]. We are grateful to Dr. Florencio Balboa Usabiaga for running the *fluam* simulations and providing the numerical results. In the left panel of Fig. 4.5 we compare $g(r)$ between a simulation where the particles are immersed in an incompressible viscous solvent, and a standard computation of the equilibrium RDF using a Monte Carlo algorithm to sample the equilibrium distribution (4.4). We test the FIB algorithm at two different densities, a dilute suspension corresponding to a packing fraction based on the LJ diameter of $\phi \approx 0.13$, and a dense suspension (close to the freezing point) at packing fraction $\phi \approx 0.42$. Note that while the minimally-resolved model here cannot accurately model the dynamics (hydrodynamic interactions) at high packing fractions [112, 125], we do obtain the correct equilibrium properties because our formulation and numerical scheme obey discrete fluctuation-dissipation balance for any interaction potential and any viscosity.

As seen in Fig. 4.5, we obtain excellent agreement with the Monte Carlo calculations even for time steps close to the stability limit. The Brownian time scale here is[3]

$$\tau_B = \frac{a^2}{\chi} = \frac{6\pi a^3 \eta}{k_B T} \approx 2 \cdot 10^4,$$

and the time step size is primarily limited (to $\Delta t \lesssim 100$, corresponding to $\beta = 0.005$, for the dilute suspension, and $\Delta t \lesssim 50$ for the denser suspension) by stability requirements relating to the presence of the stiff LJ repulsion between the particles. Note that the time step size in these simulations is substantially larger than those required in the Inertial Coupling scheme developed by some of us in Ref. [102] (there, a time step of $\Delta t = 1$ was used).

---

[3]Perhaps a more relevant diffusive length scale to use is the typical inter-particle gap, which can be substantially smaller than $a$ for dense suspensions.
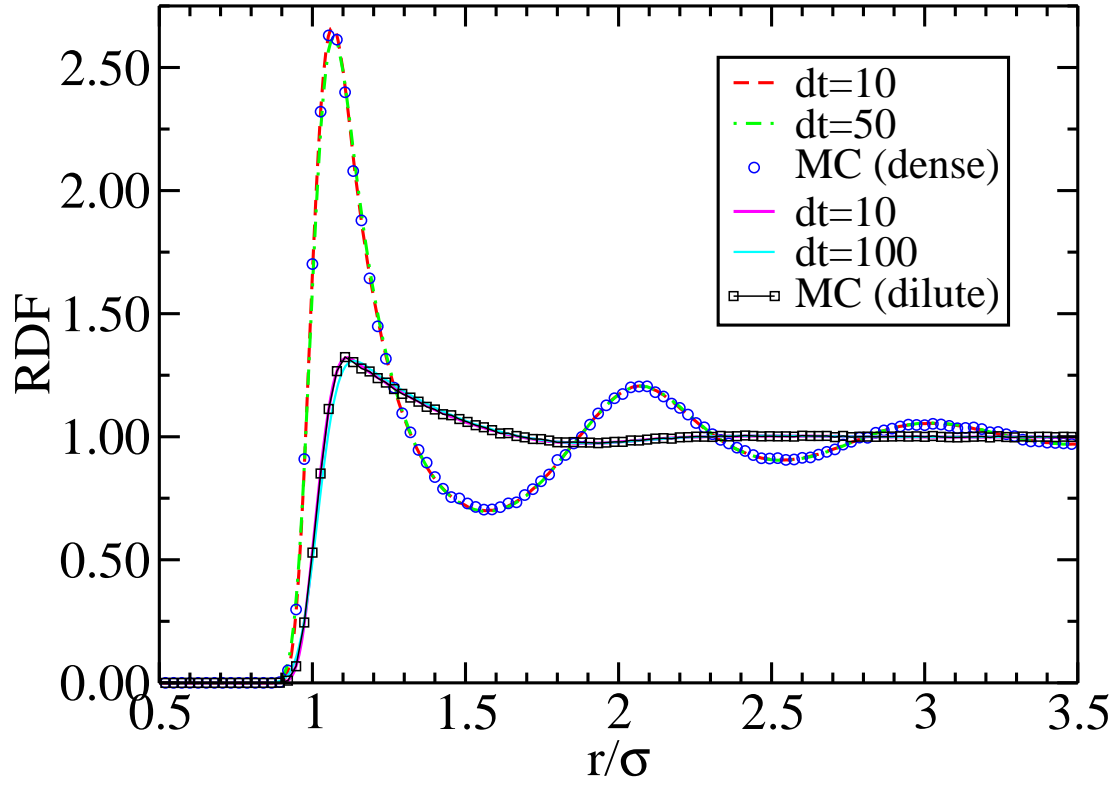
Figure 4.5: Radial pair correlation function $g(r)$ for a suspension of particles interacting with repulsive Lennard-Jones potentials at packing fractions $\phi \approx 0.13$ (dilute) and $\phi \approx 0.42$ (dense). Results from two different time step sizes are compared to Monte Carlo (MC) simulations.

| domain width, $L$ | $64h$ |
|---|---|
| hydrodynamic radius, $a$ | $1.04h$ |
| spring constant, $k$ | $1\left(k_B T/h^2\right)$ |
| time step size $\frac{\Delta t}{\tau}$ | 0.22, 0.11, 0.02 |
| diffusive CFL number $\beta$ | 0.45, 0.22, 0.05 |
| Weissenberg number | 1.0 |

Table 4.3: Parameters for the simulation of a single particle in shear flow.

| domain width, $L$ | $32h$ |
|---|---|
| well separation, $b$ | $5h$ |
| hydrodynamic radius, $a$ | $1.25h$ |
| spring constant, $k$ | $10\left(k_B T/h^2\right)$ |
| time step size $\frac{\Delta t}{\tau}$ | 0.3, 0.08 |
| diffusive CFL number$\beta$ | 0.06, 0.015 |
| Weissenberg number | 1.0 |

Table 4.4: Parameters for the simulation of two particles in shear flow.

## 4.5.4 Particles in Shear Flow

In this section we verify the the FIB method correctly models the *dynamics* of hydrodynamically-interacting Brownian particles by computing time correlation functions of the positions of particles in shear flow. Particles are anchored with a harmonic spring to their initial locations and subjected to shear flow, as can be experimentally realized by using optical tweezers to apply the potential [147]. Brammert, Holzer, and Zimmerman have performed theoretical analysis of this system [148, 149] and provide explicit expressions used to test the accuracy of our scheme. The numerical results presented below demonstrate the ability of our midpoint schemes to correctly reproduce the effect of hydrodynamic interactions between distinct immersed particles.

Note that it is not possible to have an unbounded system in a finite-volume approach; a finite system is necessary and it is most convenient to use a large but finite periodic system [4]. In these tests, we add a background shear flow with velocity $\boldsymbol{u}$ to the *periodic* fluctuating component $\boldsymbol{v}$ calculated by the steady Stokes solver; this mimics common practice in Brownian dynamics simulations of polymer chains in flow [107]. We will define $y$ as the direction of shear, and $x$ as the direction of flow. The background flow is of the form $\boldsymbol{u}(x,y) = (\dot{\gamma}y, 0, 0)$ for some constant $\dot{\gamma}$. Note that the total flow $\boldsymbol{u} + \boldsymbol{v}$ is a solution to the Stokes equations with the same forces that generated $\boldsymbol{v}$, but with boundary conditions modified to match the added background flow. The resulting velocity of the particle is then $\boldsymbol{\mathcal{J}}(\boldsymbol{q})\boldsymbol{v} + \boldsymbol{\mathcal{J}}(\boldsymbol{q})\boldsymbol{u}$. With a spherically symmetric kernel and the constant-shear flow $\boldsymbol{u}$, we have $\boldsymbol{\mathcal{J}}(\boldsymbol{q})\boldsymbol{u} = \boldsymbol{u}(\boldsymbol{q})$. To implement the addition of the background flow, we calculate $\boldsymbol{\mathcal{J}}\boldsymbol{v}$ without any modification for the shear flow, and then separately add $\boldsymbol{u}(\boldsymbol{q})$. The temporal scheme is then the same as (4.32)-(4.34) but with $\boldsymbol{\mathcal{J}}^n\boldsymbol{v}$ replaced by $\boldsymbol{\mathcal{J}}^n\boldsymbol{v} + \boldsymbol{u}(\boldsymbol{q}^n)$ and likewise $\boldsymbol{\mathcal{J}}^{n+\frac{1}{2}}\boldsymbol{v}$ is replaced by $\boldsymbol{\mathcal{J}}^{n+\frac{1}{2}}\boldsymbol{v} + \boldsymbol{u}\left(\boldsymbol{q}^{n+\frac{1}{2}}\right)$. Note that here $\boldsymbol{q}$ is the position of the particle not on the periodic torus but in an unbounded domain obtained by periodically replicating the fixed unit cell. In our tests the particles are localized to a single unit cell and do not interact with periodic image particles; in more general situations such as sheared suspensions more complicated approaches (reminiscent of Lees-Edwards boundary conditions commonly employed in molecular dynamics) are necessary to account for the lack of periodicity in shear flow [151]. Alternatively, one can use periodic flows of the form $u_x \sim \sin ky$ with $k$ sufficiently small (i.e., periodic box sufficiently large) to approach the limit $k \to 0$.

### 4.5.4.1 A Single Particle

In this simulation, a single particle is placed in a background shear flow and is attached to an anchor location, $\boldsymbol{q}_0$, by a harmonic spring with potential $U = (k/2)\left\|\boldsymbol{q} - \boldsymbol{q}_0\right\|^2$. The strength of the shear flow relative to the harmonic force is measured with the dimensionless Weissenberg number, $\mathrm{Wi} = \dot{\gamma}\tau$, where $\tau = (\mu k)^{-1}$ is the timescale of the particle's relaxation to its anchor location due to the harmonic spring. Theoretical results are given for three

---

[4]In Green's function's based approaches there is no difficulty in dealing with unbounded three dimensional systems (at rest at infinity) since the Oseen tensor is the required response function and is easy to compute. Note however that when simulating periodic domains (e.g., colloidal suspensions) one requires the Green's functions for Stokes flow in a periodic domain, and these are *not* simple to compute [150, 109], unlike in our approach, which handles boundary conditions naturally.
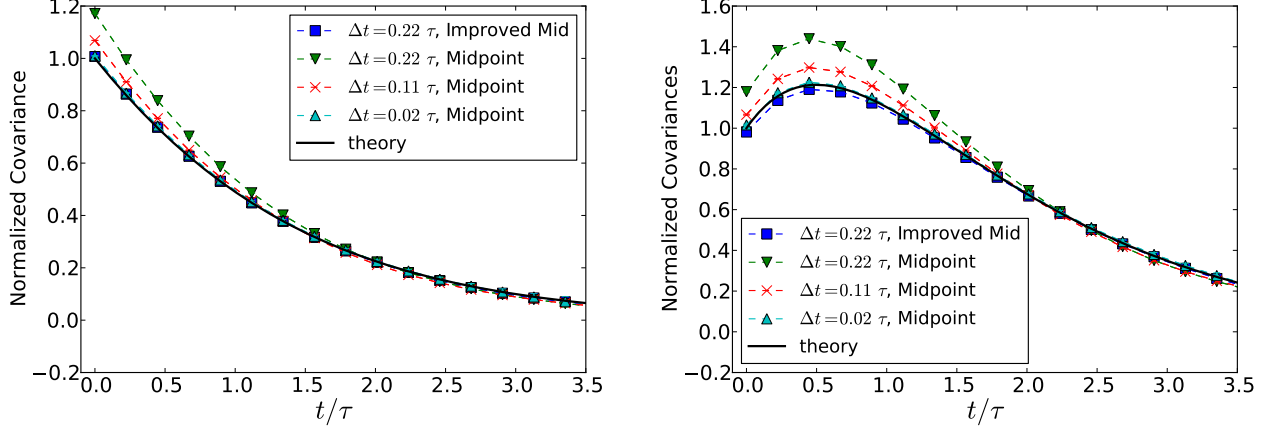
Figure 4.6: Normalized time correlation functions for a single particle in a harmonic potential in the presence of shear flow. As the time step size is reduced, the numerical results converge to the theoretical expressions, substantially faster for the improved midpoint algorithm. Error bars of two standard deviations are drawn, and are generally on the order of symbol size. *(Left panel)* Autocorrelation of the displacement of the particle in the direction of flow, $\langle \tilde{x}(t)\tilde{x}(0)\rangle$. *(Right panel)* Cross correlation of the displacements in flow and shear directions, $\langle \tilde{x}(t)\tilde{y}(0)\rangle$.

dimensions in Ref. [148], but the analysis also holds in two dimensions with the appropriate diffusion coefficient. We perform the single-particle tests in two dimensions and the two-particle tests in three dimensions.

The simulation parameters are given in Table 4.3. The strength of the spring is such that the equilibrium Gaussian distribution for $\|\boldsymbol{q} - \boldsymbol{q}_0\|$ has a standard deviation of $h$ (one grid cell). We define the fluctuation $\tilde{x} = x - \langle x \rangle$, where $\langle x \rangle$ is the average position, and similarly for $y$. The time correlations $C_{xx}(t) = \langle \tilde{x}(t)\tilde{x}(0)\rangle$, $C_{yy}(t) = \langle \tilde{y}(t)\tilde{y}(0)\rangle$, and $C_{xy}(t) = \langle \tilde{x}(t)\tilde{y}(0)\rangle$ are then calculated and compared to the known theoretical results [148],

$$\hat{C}_{xx}(t) \quad := \quad \frac{k_B T}{k}\left[1 + \frac{Wi^2}{2}\left(1 + \frac{|t|}{\tau}\right)\right]e^{-|t|/\tau}$$

$$\hat{C}_{xy}(t) \quad := \quad \frac{k_B T}{k}\frac{Wi}{2}\left(1 + 2\frac{t}{\tau}H(t)\right)e^{-t/\tau},$$

where $H(t)$ is the Heaviside function. The time correlations in the direction of shear, $C_{yy}(t)$, are not influenced by the background flow and are omitted. It can be seen in Fig. 4.6 that the simulation results converge to the correct time correlations as the time step size is reduced, which confirms that the FIB method's accurately captures the dynamics of an immersed particle subject to external forcing and flow.

Significantly more accurate time correlation functions can be obtained by using the improved midpoint scheme (4.37). Because the equations of motion of a single blob in shear flow are additive-noise equations, the improved midpoint scheme is second-order accurate. This is confirmed in Fig. 4.6 where we see that the second-order scheme is able to obtain the same accuracy as the first-order scheme with a time step that is an order of magnitude larger.

### 4.5.4.2    Two Particles

In the previous section, we tested the ability of our algorithm to reproduce the dynamics of a single particle. We now test the ability of our approach also correctly capture the hydrodynamic interactions between particles. We extend the previous simulation to include two particles, each in its own harmonic potential with minima separated by vector of length $b$ in the direction of flow, $U(\boldsymbol{q}) = (k/2)\|\boldsymbol{q} - \boldsymbol{q}_{\min}\|^2$, where $\boldsymbol{q}_{\min}$ are the positions of the minima of the two harmonic wells. The shear flow used is the same as in the previous section. In this simulation we study the correlations between the motion of particle 1 and particle 2 (cross-correlations), as well as correlations of particle 1 with itself (self-correlations). The self-correlations are different from the single-particle case due to the disturbances in the fluid caused by the presence of the second particle.

Theoretical results are calculated in Ref. [149] for an infinite domain by linearizing the equations around the equilibrium location of the particles $\bar{\boldsymbol{q}}$ (which is in general different from $\boldsymbol{q}_{\min}$) and forming equations of motion for the fluctuations $\tilde{\boldsymbol{q}} = \boldsymbol{q} - \bar{\boldsymbol{q}}$ under the assumption that $\tilde{\boldsymbol{q}}$ is small. This leads to a simple Ornstein-Uhlenbeck process

| | |
|---|---|
| grid spacing $\Delta x$ | 3.27 |
| grid size | $32^3$ |
| shear viscosity $\eta$ | 1 |
| time step size $\Delta t$ | 0.05 (simple) or 0.1 (improved) |
| temperature $k_B T$ | 12.3 |
| LJ strength $\epsilon$ | 10 |
| LJ / hydro diameter $\sigma$ | 6.4 |
| number of particles $N$ | 13 |

Table 4.5: Parameters used in the colloidal cluster collapse simulations shown in the right panel of Fig. 4.5. These are chosen to match those in Ref. [152] as closely as possible.

[149]

$$\frac{d\tilde{\boldsymbol{q}}}{dt} = \boldsymbol{A}\tilde{\boldsymbol{q}} - k\boldsymbol{M}(\bar{\boldsymbol{q}})\tilde{\boldsymbol{q}} + \boldsymbol{B}\tilde{\boldsymbol{q}} + \boldsymbol{M}^{\frac{1}{2}}(\bar{\boldsymbol{q}})\boldsymbol{\mathcal{W}}(t), \tag{4.45}$$

where $\boldsymbol{A}$ is the shear rate tensor, $A_{12} = A_{45} = \dot{\gamma}$ and all other entries are zero, and $\boldsymbol{B}_{ij} = \partial_j \boldsymbol{M}_{ik}(\bar{\boldsymbol{q}}) \left( \boldsymbol{q}_{\min}^{(k)} - \bar{\boldsymbol{q}}^{(k)} \right)$. Because we have chosen to have the shear flow in the direction that separates the wells, we have that $\bar{\boldsymbol{q}} = \boldsymbol{q}_{\min}$ if we choose $\bar{\boldsymbol{q}}_1^{(2)} = \bar{\boldsymbol{q}}_2^{(2)} = 0$, and therefore $\boldsymbol{B} = \boldsymbol{0}$ and no derivatives of the mobility are required. Since we employ periodic boundary conditions for the velocity in our simulations, we approximate $\boldsymbol{M}(\bar{\boldsymbol{q}})$ using a periodic correction to the Rotne-Prager-Yamakawa tensor calculated with an Ewald sum [150] and evaluated at position $\bar{\boldsymbol{q}}$.

The simulation was run using a periodic three dimensional domain, and the temperature was set such that the standard deviation of the particles' displacements was $\sqrt{10}h$, keeping the particles near the potential minima and thus giving better agreement with the linearized theoretical calculations. The simulation parameters are given in Table 4.4. The numerical time correlation functions shown in Figs. 4.7, 4.8 and 4.9 are in good agreement with the theoretical results for the moderate time step size. The error is improved as the time step size is decreased to better resolve the relevant timescale. Note that the improved midpoint scheme (4.37) gives better agreement with theoretical results, as it is second-order accurate for this example because the equations of motion are essentially linear. Note that a visible mismatch with the theoretical curve is seen for the cross-correlation $\langle \tilde{y}_1(t)\tilde{y}_2(0) \rangle$ in the right panel of Fig. 4.8; since the two midpoint schemes are in agreement with each other this mismatch comes from the approximations made in the theory.

### 4.5.5 Colloidal Gelation

In this section, we confirm that the FIB method correctly reproduces the dynamical effect of multi-particle hydrodynamic interactions for a collection of colloidal particles interacting via excluded-volume (non-bonded) interactions with an attractive tail. It has been demonstrated that hydrodynamic interactions play a significant role in the process of colloidal gelation [152]. Here we use the FIB method to study a model test example of colloidal cluster dynamics, and compare the FIB results to those of traditional Brownian Dynamics (with hydrodynamic interactions).

As a simple test problem illustrating the effect of hydrodynamics on gelation, a 13-particle colloidal cluster collapse example has been constructed in Ref. [152]. The physical system consists of 13 blobs initially placed at the vertices of an icosahedron (see Fig. 4 in Ref. [152]), and then released to relax toward the thermodynamically-preferred collapsed (bound) cluster of 13 spheres. In the absence of hydrodynamic interactions the collapse is rapid. In the presence of hydrodynamic interactions, however, the cluster undergoes a slow rearrangement process through multiple elongated configurations (see Fig. 4 in Ref. [152]) before it collapses. This results in a dramatic slowing down of the collapse when hydrodynamics is accounted for.

The collapse of the cluster can be monitored via the radius of gyration of the cluster $R_g(t)$. An ensemble average $\langle R_g(t) \rangle$ over 64 trajectories obtained using the FIB method is shown in Fig. 4.10. In the first set of simulations, we employ periodic boundary conditions with a grid of $32^3$ cells and use the GPU-based code *fluam* with the three-point Peskin kernel [102] and the simple midpoint integrator. The *fluam* simulations were run by Dr. Florencio Balboa Usabiaga, and we thank him for providing these numerical results. The second set of simulations were performed using IBAMR on a periodic grid of $64^3$ cells with the four-point kernel and the improved midpoint integrator. We use the Asakura-Oosawa depletion force with a repulsive Lennard-Jones interaction, following Ref. [152]. Important parameters of our simulations are summarized in Table 4.5.

It is important to note that the time step size used for these simulations is much smaller than the Brownian time scale $\tau_B = a^2/\chi \approx 50$. This is because the time step size here is severely limited by stability considerations.
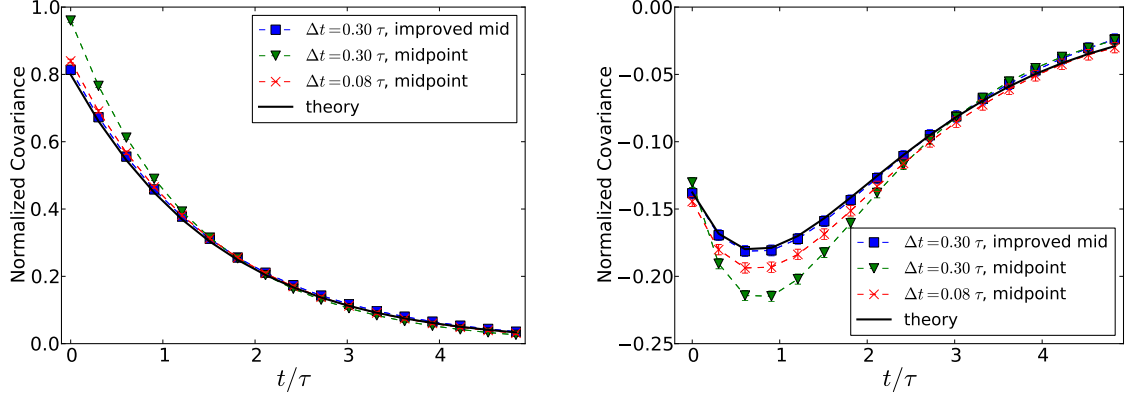
Figure 4.7: Time correlation functions for two particles bound by harmonic potentials in the presence of shear flow. *(Left panel)* Autocorrelation of the displacement of one of the particles in the direction of flow, $\langle \tilde{x}_1(t)\tilde{x}_1(0)\rangle$. *(Right panel)* Correlation of the displacements of the two particles in the direction of flow, $\langle \tilde{x}_1(t)\tilde{x}_2(0)\rangle$.
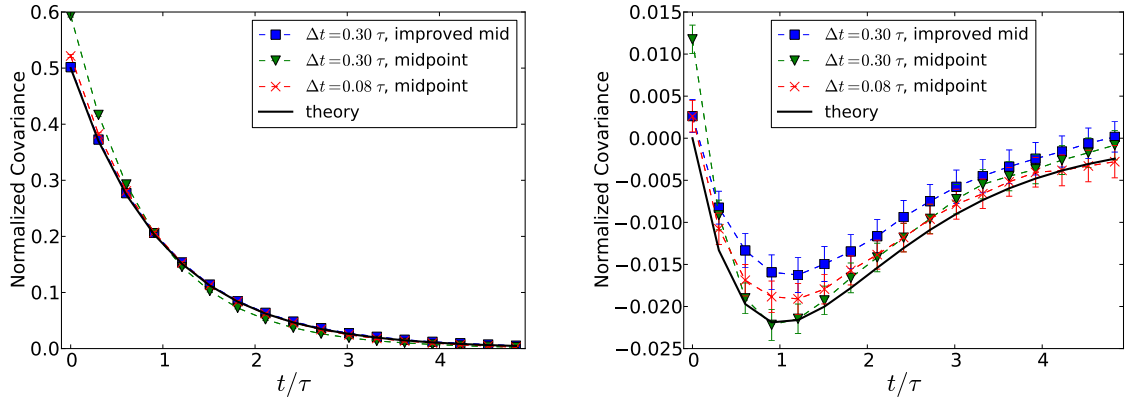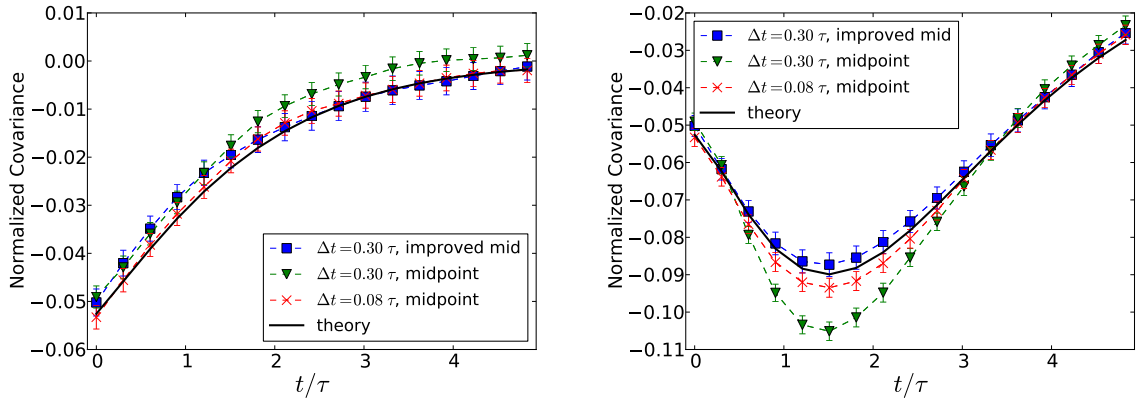


Figure 4.8: *(Left panel)* Autocorrelation of the displacement of one of the particles in the direction of shear $\langle \tilde{y}_1(t)\tilde{y}_1(0)\rangle$. *(Right panel)* Correlation of the displacements of the two particles in the direction of the shear, $\langle \tilde{y}_1(t)\tilde{y}_2(0)\rangle$.



Figure 4.9: Cross correlation of the displacements of the two particles in the shear and flow directions, $\langle \tilde{y}_2(t)\tilde{x}_1(0)\rangle$ (left panel) and $\langle \tilde{x}_1(t)\tilde{y}_2(0)\rangle = \langle \tilde{y}_2(-t)\tilde{x}_1(0)\rangle$ (right panel).
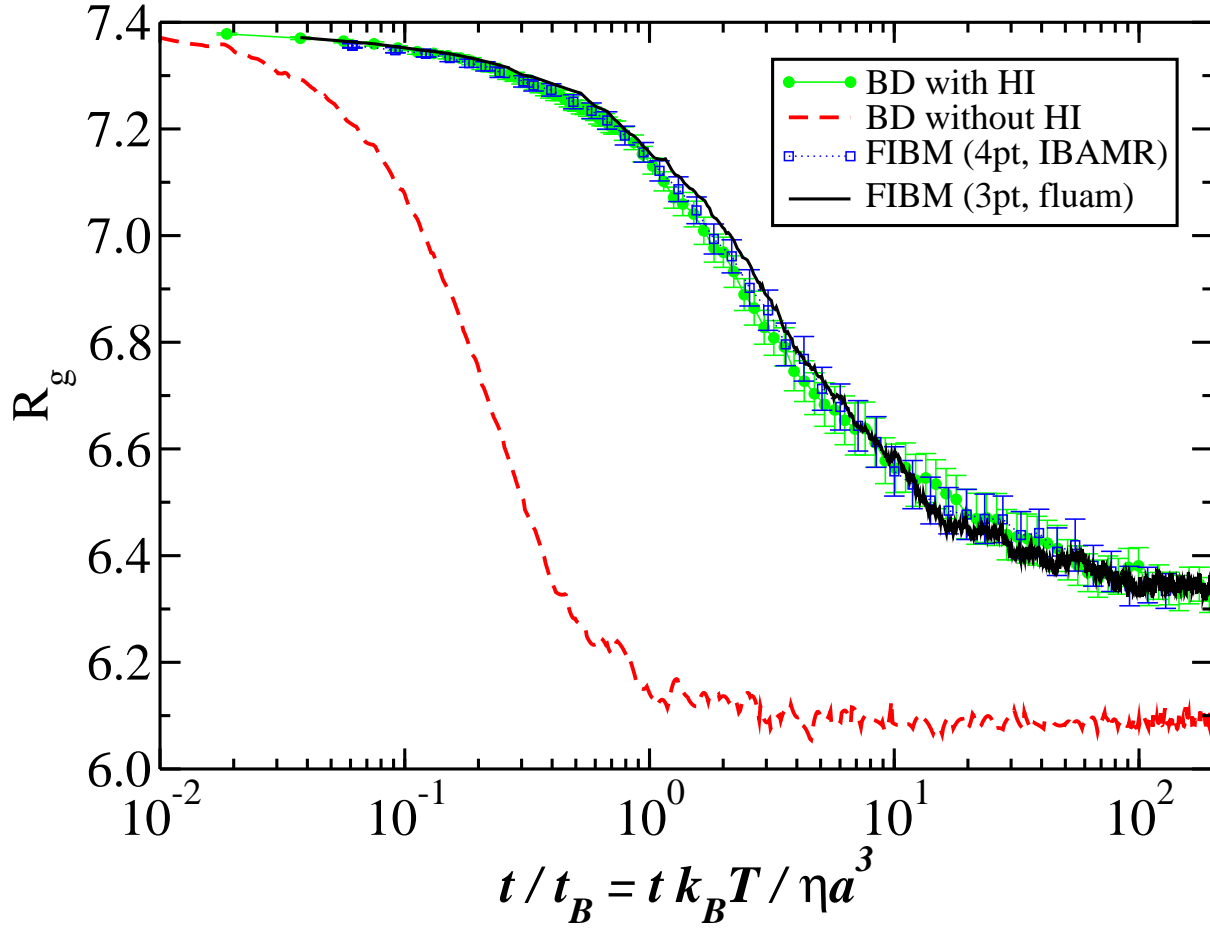
Figure 4.10: Relaxation of the radius of gyration of a colloidal cluster of 13 spheres toward equilibrium, as obtained by averaging 64 independent simulations. The FIB method is compared to traditional Brownian Dynamics (BD) with and without hydrodynamic interactions (HI). For comparison, FIB simulations were performed both using the *fluam* code with the three-point kernel and a domain of $32^3$ grid cells, as well as using the IBAMR code with the four-point kernel and $64^3$ grid cells.

The stiff hard-core repulsion between the particles and the fact that the particles are close to each other due to the attractive tail combine to make the simple midpoint scheme unstable for $\Delta t > 0.05$ (determined empirically). The improved midpoint scheme shows slightly improved stability and we have successfully used it for $\Delta t = 0.1$, however, the cost per time step is approximately doubled so this improvement is not substantial. Achieving larger time step sizes and avoiding exploding (unstable) trajectories requires specialized temporal integration methods such as Metropolization[5] [153]. Note that in a small fraction of the trajectories (we only observed two such trajectories) the cluster dissolves instead of collapsing. This could be the signature of a rare event but it could also be an artifact of numerical instabilities arising from the stiff interparticle potentials; lacking better statistics we have excluded these trajectories from the averages.

In Ref. [152], the authors compare their method to BD without hydrodynamic interactions (HI) (i.e., employ a mobility that it a diagonal matrix), but do not compare to BD with hydrodynamic interactions. In the right panel of Fig. 4.10 we compare the results from the FIB method to BD with and without HI. We included hydrodynamics using the free-space Rotne-Prager-Yamakawa (RPY) mobility (4.7), and employed a simple Euler-Maruyama integrator with time step size $\Delta t = 0.05$ instead of the Fixman method since the divergence of the free-space RPY mobility

---

[5]Note, however, that Metropolization of even the simple midpoint scheme is a rather nontrivial task because the mobility matrix is never formed or factorized in FIB.

vanishes identically. The results in Fig. 4.10 demonstrate that both BD-with HI and the FIB method reproduce the slowing down (relative to BD without HI) in the cluster collapse and agree with each other. While inclusion of higher-order effects such as stresslets and lubrication , may lead to some quantitative differences, our results are already in good agreement with those in Fig. 4 in Ref. [152] and indicate that the primary effect comes from the far-field hydrodynamic interactions.

## 4.6  Conclusion

In this chapter, we introduced the Fluctuating Immersed Boundary (FIB) method for Brownian Dynamics of confined suspensions of spherical particles. The key idea is to use a numerical fluctuating Stokes fluid solver combined with an immersed boundary representation of the particles in order to compute the action of the mobility on the fly, thus eliminating the need to derive an analytic approximation for each separate geometry. This approach is very similar to the Fluctuating Force Coupling Method [125, 126, 127] and Stochastic Eularian Lagrangian Method [124, 100, 129], but uses different numerical methods to discretize and integrate the equations of motion. In particular, we employ a specialized temporal integrator that makes use of a Random Finite Difference term to handle the thermal drift in a computationally efficient manner. We introduce a weakly first order accurate scheme that requires only one Stokes solve per time step. Our methods are validated on a number of test problems, comparing to available theory.

## 4.7  Addendum: Weak Temporal Accuracy of Brownian Dynamics schemes

In this section, we show that the algorithms outlined in Section 4.4 are first order weakly accurate temporal integrators for the system (4.18). It suffices to show that the first three moments of the numerical one-step increment in time match to first order the moments of the exact increment [22]. Without loss of generality, we consider the case $\eta = 1$ for this analysis. The RFD term (4.36) introduces an error proportional to $\delta^2$. This is a spatial truncation error and will be ignored in the context of temporal accuracy. Note that in practice, $\delta$ will be a very small fixed value that introduces a negligible truncation error to the approximation of the stochastic drift.

For the continuous equation, we have, to first order,

$$
\begin{aligned}
\Delta_\alpha^q &\equiv q_\alpha((n+1)\Delta t) - q_\alpha(n\Delta t) \\
&= \Delta t (\mathcal{J}_{\alpha\mu}^n \mathcal{L}_{\mu\nu}^{-1} \mathcal{S}_{\nu\beta}^n) F_\beta^n \\
&\quad + \sqrt{2k_B T} \int_{t'}^{t} \mathcal{J}_{\alpha\mu}^n \mathcal{L}_{\mu\nu}^{-1} \widetilde{D}_{\nu\beta} d\mathcal{W}_\beta \\
&\quad + \Delta t\, k_B T \partial_\gamma \cdot (\mathcal{J}_{\alpha\mu}^n \mathcal{L}_{\mu\nu}^{-1} \mathcal{S}_{\nu\gamma}^n) + O\left(\Delta t^{\frac{3}{2}}\right),
\end{aligned}
\tag{4.46}
$$

where $\mathcal{J}$, $\mathcal{S}$ and $\boldsymbol{F}$ are evaluated at the beginning of the time step. The first moment of the true increment is

$$
\begin{aligned}
E[\Delta_\alpha^q] &\equiv \Delta t\, \mathcal{J}_{\alpha\mu}^n \mathcal{L}_{\mu\nu}^{-1} \mathcal{S}_{\nu\beta}^n F_\beta^n + O\left(\Delta t^2\right) \\
&\quad + \Delta t\, k_B T \left[ \mathcal{J}_{\alpha\mu}^n \mathcal{L}_{\mu\nu}^{-1} \partial_\gamma (\mathcal{S}_{\nu\gamma}^n) + \partial_\gamma (\mathcal{J}_{\alpha\mu}^n) \mathcal{L}_{\mu\nu}^{-1} \mathcal{S}_{\nu\gamma}^n \right].
\end{aligned}
$$

### 4.7.1  First Order Midpoint Scheme

Looking at the discrete increment to first order, we get,

$$
\begin{aligned}
\bar{\Delta}_\alpha^q &\equiv q_\alpha^{n+1} - q_\alpha^n = \Delta t\, \mathcal{J}_{\alpha\mu}^n \mathcal{L}_{\mu\nu}^{-1} \mathcal{S}_{\nu\beta}^n F_\beta^n \\
&\quad + \Delta t\, \mathcal{J}_{\alpha\mu}^n \mathcal{L}_{\mu\nu}^{-1} \frac{k_B T}{\delta} [\mathcal{S}_{\nu\beta}(\boldsymbol{q}^n + \frac{\delta}{2}\widetilde{\boldsymbol{W}}^n)\widetilde{W}_\beta^n - \mathcal{S}_{\nu\beta}(\boldsymbol{q}^n - \frac{\delta}{2}\widetilde{\boldsymbol{W}}^n)\widetilde{W}_\beta^n] \\
&\quad + (\Delta t)^{\frac{1}{2}} \left(\frac{k_B T}{2\Delta V}\right)^{\frac{1}{2}} \partial_\gamma (\mathcal{J}_{\alpha\mu}^n)(q_\gamma^{n+\frac{1}{2}} - q_\gamma^n) \mathcal{L}_{\mu\nu}^{-1} \widetilde{D}_{\nu\beta} W_\beta^n \\
&\quad + \sqrt{\frac{2k_B T \Delta t}{\Delta V}} \mathcal{J}_{\alpha\mu} \mathcal{L}_{\mu\nu}^{-1} \widetilde{D}_{\nu\beta} W_\beta^n + O\left(\Delta t^{\frac{3}{2}}\right).
\end{aligned}
$$

Inserting the expression for the predictor increment $\boldsymbol{q}^{n+\frac{1}{2}} - \boldsymbol{q}^n$, simplifying and ignoring terms of order $\Delta t^2$, along with terms of order $\Delta t^{\frac{3}{2}}$ with zero expectation, and terms of order $\delta^2$, we obtain

$$
\begin{aligned}
\bar{\Delta}_\alpha^q &= \Delta t \, \mathcal{J}_{\alpha\mu}^n \mathcal{L}_{\mu\nu}^{-1} \mathcal{S}_{\nu\beta}^n F_\beta^n \\
&+ \Delta t \, k_B T \, \mathcal{J}_{\alpha\mu}^n \mathcal{L}_{\mu\nu}^{-1} \partial_\gamma (\mathcal{S}_{\nu\beta}^n) \widetilde{W}_\gamma^n \widetilde{W}_\beta^n \\
&+ \frac{\Delta t \, k_B T}{\Delta V} \partial_\gamma (\mathcal{J}_{\alpha\mu}^n) \left( \mathcal{J}_{\gamma\epsilon} \mathcal{L}_{\epsilon\zeta}^{-1} \widetilde{D}_{\zeta\eta} W_\eta^n \right) \mathcal{L}_{\mu\nu}^{-1} \widetilde{D}_{\nu\beta} W_\beta^n \\
&+ \sqrt{\frac{2 k_B T \Delta t}{\Delta V}} \mathcal{J}_{\alpha\mu} \mathcal{L}_{\mu\nu}^{-1} \widetilde{D}_{\nu\beta} W_\beta^n + O\left(\Delta t^{\frac{3}{2}}\right).
\end{aligned}
$$

The first moment of this increment is obtained by using the adjoint relation $\mathcal{J}_{\gamma\epsilon} = \mathcal{S}_{\epsilon\gamma} \Delta V$, as well as $\mathcal{L}_{\epsilon\zeta}^{-1} \widetilde{D}_{\zeta\eta} \mathcal{L}_{\mu\nu}^{-1} \widetilde{D}_{\nu\beta} \left\langle W_\eta^n W_\beta^n \right\rangle = \mathcal{L}_{\epsilon\zeta}^{-1} \widetilde{D}_{\zeta\eta} \widetilde{D}_{\nu\eta} \mathcal{L}_{\mu\nu}^{-1} = \mathcal{L}_{\mu\epsilon}^{-1}$ by virtue of (4.20),

$$
\begin{aligned}
E[\bar{\Delta}_\alpha^q] &= \Delta t \, \mathcal{J}_{\alpha\mu}^n \mathcal{L}_{\mu\nu}^{-1} \mathcal{S}_{\nu\beta}^n F_\beta^n + O\left(\Delta t^2\right) \\
&+ \Delta t \, k_B T \left[ \mathcal{J}_{\alpha\mu}^n \mathcal{L}_{\mu\nu}^{-1} \partial_\gamma (\mathcal{S}_{\nu\gamma}^n) + \partial_\gamma (\mathcal{J}_{\alpha\mu}^n) \mathcal{L}_{\mu\epsilon}^{-1} \mathcal{S}_{\epsilon\gamma}^n \right],
\end{aligned}
$$

which matches the $O(\Delta t)$ terms in the continuous increment (4.46).

The second moment of the discrete increment,

$$
E[\bar{\Delta}_\alpha^q \bar{\Delta}_\eta^q] = 2 \Delta t \, k_B T \, \mathcal{J}_{\alpha\mu} \mathcal{L}_{\mu\nu}^{-1} \mathcal{S}_{\nu\eta} + O(\Delta t^2),
$$

also matches the continuous second moment to second order. Finally the third moments are both $O(\Delta t^2)$, because the order $\Delta t^{\frac{3}{2}}$ terms are mean zero.

## 4.7.2   Improved Midpoint Scheme

We show here that the scheme given by Eq. (4.37) is also first order weakly accurate. The discrete increment for this scheme to first order is

$$
\begin{aligned}
\bar{\Delta}_\alpha^q &\equiv q_\alpha^{n+1} - q_\alpha^n = \Delta t \, \mathcal{J}_{\alpha\mu}^n \mathcal{L}_{\mu\nu}^{-1} \left[ \mathcal{S}_{\nu\beta}^n F_\beta^n + \sqrt{\frac{k_B T}{\Delta V \Delta t}} \widetilde{D}_{\nu\beta} \left( W_\beta^{n,1} + W_\beta^{n,2} \right) \right] \\
&+ \sqrt{\frac{\Delta t \, k_B T}{\Delta V}} \partial_\eta \left( \mathcal{J}_{\alpha\mu}^n \right) \left( q_\eta^{n+\frac{1}{2}} - q_\eta^n \right) \mathcal{L}_{\mu\nu}^{-1} \widetilde{D}_{\nu\beta} \left( W_\beta^{n,1} + W_\beta^{n,2} \right) \\
&+ \frac{\Delta t \, k_B T}{\delta} \mathcal{J}_{\alpha\mu}^n \mathcal{L}_{\mu\nu}^{-1} \left[ \mathcal{S}_{\nu\beta}(\boldsymbol{q}^n + \frac{\delta}{2} \widetilde{\boldsymbol{W}}^n) \widetilde{W}_\beta^n - \mathcal{S}_{\nu\beta}(\boldsymbol{q}^n - \frac{\delta}{2} \widetilde{\boldsymbol{W}}^n) \widetilde{W}_\beta^n \right] + O\left(\Delta t^{\frac{3}{2}}\right).
\end{aligned}
$$

Inserting the expression for the predictor increment and removing terms that are either $O(\Delta t^2)$, $O(\Delta t^{\frac{3}{2}})$ with mean zero, or $O(\delta^2)$, we get,

$$
\begin{aligned}
\bar{\Delta}_\alpha^q &= \Delta t \mathcal{J}_{\alpha\mu}^n \mathcal{L}_{\mu\nu}^{-1} \mathcal{S}_{\nu\beta}^n F_\beta^n \\
&+ \frac{\Delta t \, k_B T}{\Delta V} \partial_\eta \left( \mathcal{J}_{\alpha\mu}^n \right) \left( \mathcal{J}_{\eta\kappa}^n \mathcal{L}_{\kappa\rho}^{-1} \widetilde{D}_{\rho\zeta} W_\zeta^{n,1} \right) \mathcal{L}_{\mu\nu}^{-1} \widetilde{D}_{\nu\beta} \left( W_\beta^{n,1} + W_\beta^{n,2} \right) \\
&+ \Delta t \, k_B T \, \mathcal{J}_{\alpha\mu}^n \mathcal{L}_{\mu\nu}^{-1} \partial_\beta (\mathcal{S}_{\nu\beta}^n) \\
&+ \sqrt{\frac{\Delta t \, k_B t}{\Delta V}} \mathcal{J}_{\alpha\mu}^n \mathcal{L}_{\mu\nu}^{-1} \widetilde{D}_{\nu\beta} \left( W_\beta^{n,1} + W_\beta^{n,2} \right) + O\left(\Delta t^{\frac{3}{2}}\right).
\end{aligned}
$$

The second and third terms on the right hand side of this expression give us the stochastic drift. The first moment is identical to that of the simple scheme to $O(\Delta t)$, as is the second moment. The third moments of both the discrete and continuous terms are already each $O(\Delta t^2)$. Note that for the special case of additive noise, such as for example the linearized equation (4.45), the improved midpoint scheme can be shown to match the first five moments of the true increment to $O(\Delta t^2)$, and is thus weakly second-order accurate (see Appendix A1 in [1]).

### 4.7.3 Second Order Deterministic scheme

We show here that the scheme given by Eq. (4.37) is first order weakly accurate. The discrete increment for this scheme to first order is

$$
\begin{aligned}
\bar{\Delta}_\alpha^q := q_\alpha^{n+1} - q_\alpha^n \;=\; \Delta t \quad & J_{\alpha\mu}^n \mathcal{L}_{\mu\nu}^{-1} \left[ S_{\nu\beta}^n F_\beta^n + \sqrt{\frac{k_B T}{\Delta V \Delta t}} \widetilde{D}_{\nu\beta} \left( W_\beta^{n,1} + W_\beta^{n,2} \right) \right] \\
& + \sqrt{\frac{\Delta t k_B T}{\Delta V}} \partial_\eta \left( \mathcal{J}_{\alpha\mu}^n \right) \left( q_\eta^{n+\frac{1}{2}} - q_\eta^n \right) \mathcal{L}_{\mu\nu}^{-1} \widetilde{D}_{\nu\beta} \left( W_\beta^{n,1} + W_\beta^{n,2} \right) \\
& + \frac{k_B T}{\delta} \Delta t \, J_{\alpha\mu}^n \mathcal{L}_{\mu\nu}^{-1} \left[ \mathcal{S}_{\nu\beta}(q_\eta^n + \tfrac{\delta}{2} \widetilde{W}_\eta^n) \widetilde{W}_\beta^n - \mathcal{S}_{\nu\beta}(q_\eta^n - \tfrac{\delta}{2} \widetilde{W}_\eta^n) \widetilde{W}_\beta^n \right] \\
& + O(\Delta t^{3/2}).
\end{aligned}
$$

Simplifying this expression, and removing terms that are both high order and mean zero, as well as terms of order $\delta^2$, we get

$$
\begin{aligned}
\bar{\Delta}_\alpha^q := q_\alpha^{n+1} - q_\alpha^n \;=\; & \Delta t J_{\alpha\mu}^n \mathcal{L}_{\mu\nu}^{-1} S_{\nu\beta}^n F_\beta^n \\
& + \frac{\Delta t k_B T}{\Delta V} \partial_\eta \left( \mathcal{J}_{\alpha\mu}^n \right) \left( \mathcal{J}_{\eta\kappa}^n \mathcal{L}_{\kappa\rho}^{-1} \widetilde{D}_{\rho\zeta} W_\zeta^{n,1} \right) \mathcal{L}_{\mu\nu}^{-1} \widetilde{D}_{\nu\beta} \left( W_\beta^{n,1} + W_\beta^{n,2} \right) \\
& + k_B T \Delta t \, J_{\alpha\mu}^n \mathcal{L}_{\mu\nu}^{-1} \partial_\beta (\mathcal{S}_{\nu\beta}^n) \\
& + \sqrt{k_B t \Delta t} J_{\alpha\mu}^n \mathcal{L}_{\mu\nu}^{-1} \widetilde{D}_{\nu\beta} \left( W_\beta^{n,1} + W_\beta^{n,2} \right).
\end{aligned}
$$

The middle two deterministic terms from this expression give us the stochastic drift. Looking at the first moment, we have

$$
\begin{aligned}
E\left[ \bar{\Delta}_\alpha^q \right] := E\left[ q_\alpha^{n+1} - q_\alpha^n \right] \;=\; & \Delta t J_{\alpha\mu}^n \mathcal{L}_{\mu\nu}^{-1} S_{\nu\beta}^n F_\beta^n \\
& + kT \Delta t [\partial_\eta (J_{\alpha\mu}^n) \mathcal{L}_{\mu\nu}^{-1} S_{\nu\eta}^n + J_{\alpha\mu}^n \mathcal{L}_{\mu\nu}^{-1} \partial_\beta (S_{\nu\beta}^n)] \\
& + O(\Delta t^2),
\end{aligned}
$$

which matches the increment above to 1st order.

$$
\begin{aligned}
E[\Delta_\alpha^q] := E[q_\alpha((n+1)\Delta t) - q_\alpha(n\Delta t)] \;=\; & \Delta t \, J_{\alpha\mu}^n \mathcal{L}_{\mu\nu}^{-1} S_{\nu\beta}^n F_\beta^n \\
& + \Delta t kT \partial_\eta \cdot (J_{\alpha\mu} L_{\mu\nu}^{-1} S_{\nu\eta}).
\end{aligned}
$$

The second moment of this increment is just the square of the stochastic terms,

$$
E[\bar{\Delta}_\alpha^q \bar{\Delta}_\eta^q] \;=\; 2kT\Delta t \, J_{\alpha\mu} L_{\mu\nu}^{-1} \mathcal{S}_{\nu\eta} + O(\Delta t^2),
$$

which matches the continuous second moment to second order,

$$
E[\Delta_\alpha^q \Delta_\eta^q] \;=\; 2k_B T \Delta t J_{\alpha\mu} L_{\mu\nu}^{-1} \mathcal{S}_{\nu\eta} + O(\Delta t^2).
$$

The third moments of both the discrete and continuous terms are already each $O(\Delta t^2)$. The increments contain order $\Delta t^{\frac{3}{2}}$ terms, but all such terms have 0 expectation, and vanish when we look at the moment.

# Chapter 5

# Brownian Dynamics for Suspensions of Rigid Bodies

Brownian motion of rigid bodies suspended in a viscous solvent is one of the oldest problems in nonequilibrium statistical mechanics, and is of crucial importance in a number of applications in chemical engineering and materials science. Examples include the dynamics of passive [154, 155, 156, 157, 158, 159] or active [160, 123, 161, 162] particles in suspension, the dynamics of biomolecules in solution [17, 18, 163], the design of novel nano-colloidal materials [164], and others. At the mesoscopic scales of interest, the erratic motion of individual molecules in the solvent drives the diffusive motion of the suspended particles. The number of degrees of freedom necessary to simulate this motion directly using Molecular Dynamics (MD) is large enough to make this approach prohibitively expensive. Instead, the Brownian dynamics approach captures the effect of the solvent through a mobility operator, and thermal fluctuations are modeled using appropriate stochastic forcing terms. In Chapter 4 we used a computational fluid solver and immersed boundary techniques to simulate the diffusive motion of spherical particles including hydrodynamic interactions. This fluctuating immersed boundary method is suitable for minimally-resolved computations in which only the translational degrees of freedom are kept and hydrodynamics is resolved at a far-field level assuming the particles are spherical. However, in order to study more interesting systems, one is often required to model the behavior of particles with nontrivial shapes such as rigidly-fused colloidal clusters [157, 155] or colloidal boomerangs [154]. In this chapter, we show how to include rotational degrees of freedom in the overdamped Langevin equation, and develop specialized temporal integrators for this system.

One of the important goals of our work is to develop an overdamped formulation and associated numerical algorithms that apply when the hydrodynamic mobility (equivalently, resistance) functions depend strongly on the configuration. Many previous works have focused on the rotational diffusion of a single isolated rigid body in an unbounded domain. However, in practice, rigid particles diffuse either in a suspension, in which case they interact hydrodynamically with other particles, or near a boundary such as a microscope slip or the walls of a channel, in which case they interact hydrodynamically with the boundaries. Here we consider a general case of a rigid body performing translational and rotational Brownian motion in a confined system, specifically, we numerically study particles sedimented close to a single no-slip boundary. This is of particular relevance to recent experimental studies of the diffusive motion of colloidal particles that are much denser than water and thus sediment close to the microscope slip (glass plate) [155, 156, 154].

When writing the equations of motion for a rigid body one must first choose how to represent the orientation of the body. For bodies with a high degree of symmetry one can use simple representations of orientation, for example, for rigid rods in three dimensions one can use two polar angles to represent the orientation [14, 158]. More complex (biaxial or skewed) particle shapes, or asymmetrically patterned particles of symmetric shapes [156], as common in active particle suspensions [161], require describing the complete orientation of the rigid bodies. Mathematically, the orientation of a general rigid body in three dimensions is an element of the rotation group $SO(3)$; the group of unitary $3 \times 3$ matrices of unit determinant (rotation matrices). This group can be parameterized in a number of ways, the most fundamental one representing elements of this group by an orientated rotation angle, represented as a three-dimensional vector $\boldsymbol{\phi}$, the direction of which gives an axes of rotation relative to a reference configuration, and the magnitude of which gives an angle of rotation around that axes. Prior work on rotational Brownian motion in the overdamped regime has considered the use of Euler angles [162, 165], oriented rotation angles [166], as well as a number of other representations [167, 163]. Each of these representations has its own set of problems, notably, most of them have singularities or redundancies (which can be avoided in principle with sufficient care), lead to

complex analytical expressions involving potentially expensive-to-evaluate trigonometric functions, or require a large amount of storage (e.g., a rotation matrix with 9 elements). Furthermore, with the exception of [162, 166, 165], most prior work on rotational diffusion either assumes that the mobility does not depend on configuration [168], focuses on cases where tracking a single axes is sufficient to describe the Brownian motion [14, 158, 169], or is not careful in handling the stochastic drift terms necessary when the rotational mobility is dependent on the position and orientation of the body.

In molecular dynamics circles, it is well-known [170, 171] that a robust and efficient representation of orientation is provided by unit quaternions, which are unit vectors in *four* dimensions (i.e., points on the unit 4-sphere). This representation contains one redundant degree of freedom (four instead of the minimal required of three), however, it is free of singularities and thus numerically robust, and, as we will see, leads to a straightforward formulation that is simple to work with both analytically and numerically. In some sense, the quaternion representation is a direct generalization of the standard representation used in Brownian Dynamics of rigid rods [158], namely, a unit vector in *three* dimensions. That common representation is also redundant (only two polar angles are required to describe a direction in three dimensions), however, it offers many advantages over more compressed representations such as polar angles, and is thus the representation of choice.

We consider the overdamped regime, where the timescale of momentum diffusion in the fluid is much shorter than the timescale of the motion of the rigid bodies themselves. Formally, this regime corresponds to the limit of infinite Schmidt number [120]. Neglecting inertia, we track only the positions and orientations of the immersed bodies, deriving evolution equations for the quaternion representation. This Langevin system exhibits the correct deterministic dynamics and preserves the Gibbs-Boltzmann distribution in equilibrium, properly restricted to the unit quaternion 4-sphere. Integrating these equations proves challenging primarily due to the presence of the stochastic drift term that arises from the configuration dependent mobility. The standard approach to handling the stochastic drift term is Fixman's method, requiring a costly application of the inverse of the mobility which in some cases is not directly computable. We employ a Random Finite Difference (RFD) scheme [3, 2] for approximating the drift; this approach only requires application of the mobility and its "square root" but not the inverse of the mobility.

We perform a number of numerical experiments in which we simulate the Brownian motion of rigid particles sedimented near a wall in the presence of gravity, as inspired by recent experimental studies of the diffusion of asymmetric spheres [156], clusters of spheres [155, 157], and boomerang colloids [154, 159]. In the first example, we study the rotational and translational diffusion of an asymmetric colloidal sphere near a wall, modeling recently-manufactured "colloidal surfers" [123] in which a dense hematite cube is embedded in a polymeric spherical particle. In the second example, we study a tetramer formed by rigidly connecting four colloidal spheres near a planar boundary, modeling colloidal clusters that have been manufactured in the lab [155, 157]. In the last example we study the quasi two-dimensional diffusive motion of a dense boomerang colloid sedimented near a no-slip boundary, as inspired by recent experiments [154, 159]. We demonstrate the crucial importance of the choice of tracking point when computing the translational diffusion coefficient, and in particular, we demonstrate that with a suitable choice of the origin around which torques are expressed, one can obtain an approximate but relatively accurate formula for the effective diffusion coefficient in the directions parallel to the boundary. At the same time, however, our results indicate that there is no exact closed-form expression for the long-time quasi-two-dimensional coefficient, and our numerical methods for simulating trajectories are necessary in order to study the long-time diffusive dynamics of even a single rigid body in the presence of confinement.

This chapter is organized as follows. In Section 5.1, we formulate the equations of motion for rigid bodies with translation and rotation, giving a brief background on the use of quaternions to parameterize orientation. Chapter 5.2 introduces temporal integrators for these equations, including a Fixman scheme, as well as an RFD scheme that approximates the stochastic drift using only applications of the mobility. We perform numerical tests of our schemes in Section 5.3 to verify that we can correctly simulate the dynamics of a rigid body near a no-slip boundary. Finally, we give our concluding thoughts and remarks in Section 5.4. Technical details are handled in the Addendums.

## 5.1  Langevin equations for rigid bodies

In this section, we formulate Langevin equations for rigid bodies performing rotational and translational diffusion. We begin by focusing on formulating an overdamped Langevin equation for rotational diffusion using a unit quaternion representation of rigid-body orientation. For the remainder of this chapter, we will assume that we know how to compute the configuration dependent hydrodynamic mobilities needed for our equations. These mobility matrices are applied to vectors of forces and torques to compute the resulting linear and angular velocities of the immersed rigid bodies. In future work, we will develop algorithms for computing these objects on the fly using a

computational fluid solver as in our Fluctuating Immersed Boundary (FIB) method (see Chapter 4), as we discuss in more detail in Chapter 6.

Our goal is to formulate an equation for the evolution of the orientation of a rigid body. It is important that the resulting system has the right deterministic term, that it is time reversible with respect to the correct Gibbs-Boltzmann distribution in equilibrium, and that it preserves the constraint that the quaternion has unit norm.

### 5.1.1 Quaternions

Describing the orientation of a rigid body in three dimensions can be done in many ways. Rotation matrices are perhaps the most straightforward approach to accomplishing this task, but they require the use of 9 floating point numbers to parameterize a 3 dimensional space. Additionally, accumulation of numerical errors over many time steps can cause rotation matrices to lose their orthonormal properties. Euler angles suffer from gimbal lock, where at certain orientations, two Euler angles describe rotation about the same axis, and a degree of freedom is lost. Oriented angles are inconvenient to accumulate (in particular one cannot simply add oriented angles to represent successive rotations) and require the evaluation of trigonometric functions. In this work, we choose to use normalized quaternions, which require 4 floating point numbers to store, are easy to normalize, can be accumulated in a convenient manner, and avoid the need for (potentially expensive to evaluate) trigonometric functions.

A normalized quaternion can be used to represent a finite rotation relative to a given initial reference frame, and is specified by $\boldsymbol{\theta} = \{s, \boldsymbol{p}\}$, a combination of a scalar $s$ and a vector $\boldsymbol{p} \in \mathbb{R}^3$ that satisfy the unit-norm constraint

$$\|\boldsymbol{\theta}\|^2 = s^2 + \boldsymbol{p} \cdot \boldsymbol{p} = 1.$$

Quaternions can be combined via the operation of quaternion multiplication, whereby $\boldsymbol{\theta}_3 = \boldsymbol{\theta}_1 \cdot \boldsymbol{\theta}_2$ is defined via

$$\begin{bmatrix} s_3 \\ \boldsymbol{p}_3 \end{bmatrix} = \begin{bmatrix} s_1 s_2 - \boldsymbol{p}_1 \cdot \boldsymbol{p}_2 \\ s_1 \boldsymbol{p}_2 + s_2 \boldsymbol{p}_1 + \boldsymbol{p}_1 \times \boldsymbol{p}_2 \end{bmatrix}, \tag{5.1}$$

with $\boldsymbol{\theta}_i = \{s_i, \boldsymbol{p}_i\}$, $i = 1, 2, 3$. With this operation, the normalized quaternions form a group with identity $\boldsymbol{\theta}^I = \{1, \boldsymbol{0}\}$. Based on the definition of quaternion multiplication and the quaternion identity, it is clear that the inverse of a quaternion $\boldsymbol{\theta} = \{s, \boldsymbol{p}\}$ is given by $\boldsymbol{\theta}^{-1} = \{s, -\boldsymbol{p}\}$.

In this work, we will use normalized quaternions to represent the orientation of a body in three space dimensions. Any finite rotation can be defined by it's oriented angle, a vector $\boldsymbol{\phi}$, indicating a turn of $\phi = \|\boldsymbol{\phi}\|$ radians counterclockwise (i.e., using the right-hand convention) around an axis $\hat{\boldsymbol{\phi}} = \boldsymbol{\phi}/\phi$. This rotation can be associated with the quaternion

$$\boldsymbol{\theta}_{\boldsymbol{\phi}} = \{\cos(\phi/2), \sin(\phi/2)\hat{\boldsymbol{\phi}}\}, \tag{5.2}$$

i.e., $\boldsymbol{p}$ gives the axis of the rotation and the magnitude of $\boldsymbol{p}$ gives the angle of rotation; the inclusion of $s$ and the normalization constraint is thus not strictly necessary [172] but is useful numerically. Note that $\boldsymbol{\theta}$ and $-\boldsymbol{\theta}$ correspond to the same physical rotation/orientation. Performing a rotation on any three dimensional vector $\boldsymbol{r}$ gives a rotated vector $\boldsymbol{r}' = \boldsymbol{R}(\boldsymbol{\theta})\boldsymbol{r}$, where the rotation matrix

$$\boldsymbol{R}(\boldsymbol{\theta}) = 2 \left[ \boldsymbol{p}\boldsymbol{p}^T + s\boldsymbol{P} + \left(s^2 - \frac{1}{2}\right)\boldsymbol{I} \right].$$

Here $\boldsymbol{P}$ is a cross-product $3 \times 3$ matrix such that $\boldsymbol{P}\boldsymbol{x} = \boldsymbol{p} \times \boldsymbol{x}$ for any $\boldsymbol{x}$. Given two normalized quaternions $\boldsymbol{\theta}_1$ and $\boldsymbol{\theta}_2$, their rotation matrices satisfy the condition

$$\boldsymbol{R}(\boldsymbol{\theta}_1)\boldsymbol{R}(\boldsymbol{\theta}_2) = \boldsymbol{R}(\boldsymbol{\theta}_1 \boldsymbol{\theta}_2), \tag{5.3}$$

that is, the map $\boldsymbol{R}(\cdot)$ is a homomorphism. From (5.3), it is clear that subsequent rotations can be accumulated by multiplying their associated quaternions. In other words, if a rotation given by oriented angle $\boldsymbol{\phi}$ followed by a rotation $\boldsymbol{\psi}$ yields a total rotation $\boldsymbol{\zeta}$, then it holds that $\boldsymbol{\theta}_{\boldsymbol{\zeta}} = \boldsymbol{\theta}_{\boldsymbol{\psi}} \cdot \boldsymbol{\theta}_{\boldsymbol{\phi}}$. Note that, in principle, the formalism developed here can directly be applied to two dimensions by replacing quaternions with complex numbers; a rotation of $\phi$ radians in a counterclockwise direction is associated with the complex number $\theta_\phi = \exp(i\phi) = \cos\phi + i\sin\phi$.

Given an angular velocity, we can write the corresponding time derivative of orientation as

$$\dot{\boldsymbol{\theta}} = \boldsymbol{\Psi}\boldsymbol{\omega}, \tag{5.4}$$

where $\boldsymbol{\Psi}(\boldsymbol{\theta})$ is the $4 \times 3$ matrix

$$\boldsymbol{\Psi} = \frac{1}{2} \begin{bmatrix} -\boldsymbol{p}^T \\ s\boldsymbol{I} - \boldsymbol{P} \end{bmatrix},$$

and again $\boldsymbol{P}$ represents the matrix such that $\boldsymbol{Px} = \boldsymbol{p} \times \boldsymbol{x}$ for any $\boldsymbol{x}$. The matrix $\boldsymbol{\Psi}$ has many properties that will be useful when we formulate equations of motion for bodies with orientation. First, it satisfies the property

$$\boldsymbol{\Psi}^T \boldsymbol{\theta} = \frac{1}{2}\left(-s\boldsymbol{p} + s\boldsymbol{p}\right) = \boldsymbol{0}, \tag{5.5}$$

which together with the relation $\dot{\boldsymbol{\theta}} = \boldsymbol{\Psi}\boldsymbol{\omega}$, indicates that the deterministic evolution of orientation remains on the constraint. This property is used in Section 5.1 in showing that the Langevin equations presented in this work also preserve the constraint. Another useful relationship is the fact that

$$\partial_{\theta} \cdot \boldsymbol{\Psi}^T = 0 \quad \text{i.e.} \quad \partial_l\left(\Psi_{lk}\right) = 0. \tag{5.6}$$

which is clear because the $j$-th row of $\boldsymbol{\Psi}$ has no entries that depend on the $j$-th component of $\boldsymbol{\theta}$. This property allows us to immediately remove one of the three terms arising from a product rule expansion of the stochastic drift (See Appendix 5.7)

Describing the orientation of a body at several times $t^n$ requires choosing a single initial reference orientation associated with $\boldsymbol{\theta}^0 = \{1, \boldsymbol{0}\}$, and keeping a quaternion $\boldsymbol{\theta}^n$ for each $t^n$ that describes the rotation from the reference orientation to the orientation at instant $t^n$. Furthermore, if the body undergoes a rotation with constant angular velocity $\boldsymbol{\omega}$ from time $t^n$ to time $t^{n+1} = t^n + \Delta t$, we have that $\boldsymbol{\theta}^{n+1} = \boldsymbol{\theta}_{\boldsymbol{\omega}\Delta t} \cdot \boldsymbol{\theta}^n$. This leads to a natural recipe for tracking orientation using quaternions:

1. Given an angular velocity $\boldsymbol{\omega}$ and time step size$\Delta t$, construct the quaternion $\boldsymbol{\theta}_{\boldsymbol{\omega}\Delta t}$ using (5.2).

2. Update the quaternion, $\boldsymbol{\theta}^{n+1} \leftarrow \boldsymbol{\theta}_{\boldsymbol{\omega}\Delta t} \cdot \boldsymbol{\theta}^n$, using (5.1) for quaternion multiplication.

3. If the accumulation of numerical errors has caused$\left|\|\boldsymbol{\theta}^{n+1}\| - 1\right| > \epsilon$, for some tolerance $\epsilon$, renormalize the quaternion, $\boldsymbol{\theta}^{n+1} \leftarrow \boldsymbol{\theta}^{n+1}/\|\boldsymbol{\theta}^{n+1}\|$.

In the rest of this paper, we will refer to these three steps collectively as $\boldsymbol{\theta}^{n+1} = \text{Rotate}(\boldsymbol{\theta}^n, \boldsymbol{\omega}\Delta t)$. In constructing numerical schemes in Section 5.2, it will be necessary to consider the second order expansion of this rotate procedure

$$\text{Rotate}(\boldsymbol{\theta}, \boldsymbol{\omega}\Delta t) = \boldsymbol{\theta} + \boldsymbol{\Psi}\boldsymbol{\omega}\Delta t - \frac{(\boldsymbol{\omega} \cdot \boldsymbol{\omega})\Delta t^2}{8}\boldsymbol{\theta} + O\left(\Delta t^3\right), \tag{5.7}$$

as shown in Addendum (5.5).

## 5.1.2 Rotational Brownian Motion

For simplicity, we first consider a single rigid body fixed in space but free to rotate. We let the orientation of this body (relative to some fixed reference frame) be denoted by the quaternion $\boldsymbol{\theta}(t)$, and we suppose that the body is subjected to a torque $\boldsymbol{\tau}$ about a fixed point $\boldsymbol{q}$, generated by a given potential $U(\boldsymbol{\theta})$. It can be shown (see Addendum 5.6) the the torque generated by the potential is

$$\boldsymbol{\tau} = -\boldsymbol{\Psi}^T \partial_{\boldsymbol{\theta}} U \tag{5.8}$$

In practice, it is not necessary to formulate $U(\boldsymbol{\theta})$ and calculate $-\boldsymbol{\Psi}^T \partial U/\partial\boldsymbol{\theta}$ to obtain the torque. Often is is much more convenient to calculate torque directly based on the geometries of the rigid bodies and the forces applied to them. We will see that (5.8) will be a convenient relation for mathematically formulating the constrained equations of motion. The schemes that we develop will be able to simulate the motion of rigid bodies without direct knowledge of $U(\boldsymbol{\theta})$; they simply update the positions and orientations of the bodies based on the total forces and torques applied to each body.

### 5.1.2.1 Langevin Equation

We introduce the $3 \times 3$ symmetric positive semidefinite (SPD) rotational mobility matrix $\boldsymbol{M}_{\boldsymbol{\omega}\boldsymbol{\tau}}(\boldsymbol{\theta})$, which acts on torque to produce the resulting angular velocity, $\boldsymbol{\omega} = \boldsymbol{M}_{\boldsymbol{\omega}\boldsymbol{\tau}}\boldsymbol{\tau}$. Note that this operator contains all the effects of hydrodynamics, including the shape of the body, the hydrodynamic interactions with other bodies or boundaries, etc. In this section we will assume this matrix is known, and discuss ways to obtain it explicitly in Section 5.3. Using eq. (5.4) and (5.8), we can write down a deterministic equation of motion for the rigid body,

$$\frac{d\boldsymbol{\theta}}{dt} = \boldsymbol{\Psi}\boldsymbol{M}_{\boldsymbol{\omega}\boldsymbol{\tau}}\boldsymbol{\tau} = -\left(\boldsymbol{\Psi}\boldsymbol{M}_{\boldsymbol{\omega}\boldsymbol{\tau}}\boldsymbol{\Psi}^T\right)\partial_{\boldsymbol{\theta}}U = -\widetilde{\boldsymbol{M}}\,\partial_{\boldsymbol{\theta}}U,$$

where we have defined the $4 \times 4$ mobility matrix $\widetilde{\boldsymbol{M}} = \boldsymbol{\Psi} \boldsymbol{M}_{\boldsymbol{\omega\tau}} \boldsymbol{\Psi}^T$ . It is now straight forward to formulate an Ito Langevin equation for the rotational motion of this body

$$\frac{d\boldsymbol{\theta}}{dt} = -\widetilde{\boldsymbol{M}}\partial_{\boldsymbol{\theta}}U + \sqrt{2k_BT}\widetilde{\boldsymbol{M}}^{\frac{1}{2}}\boldsymbol{\mathcal{W}} + (k_BT)\,\partial_{\boldsymbol{\theta}}\cdot\widetilde{\boldsymbol{M}}, \tag{5.9}$$

where $\boldsymbol{\mathcal{W}}(t)$ is a collection of independent white noise processes. Here $\widetilde{\boldsymbol{M}}^{\frac{1}{2}} = \boldsymbol{\Psi} \boldsymbol{M}_{\boldsymbol{\omega\tau}}^{\frac{1}{2}}$, with the "square root" of the mobility $\boldsymbol{M}_{\boldsymbol{\omega\tau}}^{\frac{1}{2}}$ obeying the fluctuation-dissipation relation $\boldsymbol{M}_{\boldsymbol{\omega\tau}}^{\frac{1}{2}}\left(\boldsymbol{M}_{\boldsymbol{\omega\tau}}^{\frac{1}{2}}\right)^{\star} = \boldsymbol{M}_{\boldsymbol{\omega\tau}}$, for example, it could be the Cholesky factor of $\boldsymbol{M}_{\boldsymbol{\omega\tau}}$. Note that in (5.9) the covariance for the noise satisfies the fluctuation dissipation balance condition $\widetilde{\boldsymbol{M}}^{\frac{1}{2}}\left(\widetilde{\boldsymbol{M}}^{\frac{1}{2}}\right)^{\star} = \widetilde{\boldsymbol{M}}$. The $i$-th component of the stochastic drift term $\partial_{\boldsymbol{\theta}}\cdot\widetilde{\boldsymbol{M}}$ may be written in indicial notation as $\partial_j \widetilde{M}_{ij}(\boldsymbol{\theta})$, where $\partial_j \equiv \partial/\partial\theta_j$.

Using Ito's formula, we can show that the overdamped dynamics (5.9) strictly preserves the constraint that $\boldsymbol{\theta}$ have unit norm,

$$d\left(\boldsymbol{\theta}^T\boldsymbol{\theta}\right) = \boldsymbol{\theta}^T d\boldsymbol{\theta} + (k_BT)\,\boldsymbol{I} : \widetilde{\boldsymbol{M}} = (k_BT)\left(\boldsymbol{\theta}^T\left(\partial_{\boldsymbol{\theta}}\cdot\widetilde{\boldsymbol{M}}\right) + \boldsymbol{I} : \widetilde{\boldsymbol{M}}\right) = 0,$$

where we used (5.5), and the chain rule

$$\boldsymbol{\theta}^T\left(\partial_{\boldsymbol{\theta}}\cdot\widetilde{\boldsymbol{M}}\right) = \partial_{\boldsymbol{\theta}}\cdot\left(\boldsymbol{\theta}^T\widetilde{\boldsymbol{M}}\right) - \boldsymbol{I} : \widetilde{\boldsymbol{M}}.$$

Note that the stochastic drift term in (5.9) can be rewritten as (see Addendum 5.7),

$$\partial_{\boldsymbol{\theta}}\cdot\widetilde{\boldsymbol{M}} = \partial_{\boldsymbol{\theta}}\cdot\left(\boldsymbol{\Psi}\boldsymbol{M}_{\boldsymbol{\omega\tau}}\boldsymbol{\Psi}^T\right) = \boldsymbol{\Psi}\left(\partial_{\boldsymbol{\theta}}\boldsymbol{M}_{\boldsymbol{\omega\tau}}\right) : \boldsymbol{\Psi}^T - \frac{1}{4}\mathrm{Tr}\left(\boldsymbol{M}_{\boldsymbol{\omega\tau}}\right)\boldsymbol{\theta}, \tag{5.10}$$

where Tr denotes trace, and colon denotes double contraction; in index notation $\left(\boldsymbol{\Psi}\left(\partial_{\boldsymbol{\theta}}\boldsymbol{M}_{\boldsymbol{\omega\tau}}\right) : \boldsymbol{\Psi}^T\right)_i = \Psi_{ij}\partial_l\left(M_{\boldsymbol{\omega\tau}}\right)_{jk}\Psi_{lk}$ and $\{\mathrm{Tr}\left(\boldsymbol{M}_{\boldsymbol{\omega\tau}}\right)\boldsymbol{\theta}\}_i = \left(M_{\boldsymbol{\omega\tau}}\right)_{jj}\theta_i$ . We will see that this way of writing the drift is convenient when we consider numerical methods for integrating (5.9) in Section 5.2.

In the special case of a free particle with unit mobility, $\boldsymbol{M}_{\boldsymbol{\omega\tau}} = \boldsymbol{I}$, (5.9) degenerates to the Stratonovich equation (see (5.22))

$$\dot{\boldsymbol{\theta}} = (2k_BT)^{\frac{1}{2}}\boldsymbol{\Psi}\circ\boldsymbol{\mathcal{W}}_3, \tag{5.11}$$

where $\boldsymbol{\mathcal{W}}_3(t)$ is three-dimensional white noise. Recall that the infinitesimal change in orientation is given by the infinitesimal rotation $d\boldsymbol{\phi}$ in the axes-angle representation, where the direction of the vector $d\boldsymbol{\phi}$ is the axes around which the body is rotated by an angle $d\phi$. Also recall that the corresponding change in the quaternion is

$$d\boldsymbol{\theta} = \boldsymbol{\Psi}(\boldsymbol{\theta})\,d\boldsymbol{\phi},$$

at least deterministically. Since the standard rules of calculus apply in the Stratonovich interpretation, (5.11) is equivalent to

$$d\boldsymbol{\varphi} = (2k_BT)^{\frac{1}{2}}\,d\boldsymbol{\mathcal{B}} \tag{5.12}$$

where $\boldsymbol{\mathcal{B}}_3(t)$ is Brownian motion, formally $\boldsymbol{\mathcal{W}}_3 \equiv d\boldsymbol{\mathcal{B}}_3/dt$. This is a natural definition of isotropic rotational diffusion [172].

We can verify that (5.9) has the correct noise covariance when $\boldsymbol{M}_{\boldsymbol{\omega\tau}}$ is not a multiple of the identity by considering the rotational mean square displacement at short times. Let us consider a set of orthonormal vectors $\boldsymbol{u}_i(t)$ which are attached to the rigid body, and define the rotational displacement Kraft et al. [157],

$$\Delta\hat{\boldsymbol{u}}\left(\Delta t\right) \equiv \frac{1}{2}\sum_{i=0}^{3}\boldsymbol{u}_i(0)\times\boldsymbol{u}_i\left(\Delta t\right). \tag{5.13}$$

A straightforward calculation relates this rotational displacement to the total angle of rotation $\boldsymbol{\phi}_{\Delta t}$ relative to the the initial configuration,

$$\Delta\hat{\boldsymbol{u}}\left(\Delta t\right) = \sin\left(\phi_{\Delta t}\right)\hat{\boldsymbol{\phi}}_{\Delta t}, \tag{5.14}$$

which shows that the magnitude of the rotational displacement is insensitive to the choice of the initial triad $\boldsymbol{u}_i(0)$. If the covariance of the noise in (5.9) is correct, it should hold that (c.f. Eq. (1) in Ref. [157])

$$\frac{1}{2k_BT}\lim_{\Delta t\to 0}\frac{\langle\left(\Delta\hat{\boldsymbol{u}}\left(\Delta t\right)\right)\left(\Delta\hat{\boldsymbol{u}}\left(\Delta t\right)\right)^T\rangle}{\Delta t} = \frac{1}{2k_BT}\lim_{\Delta t\to 0}\left(\frac{\phi_{\Delta t}^2}{\Delta t}\hat{\boldsymbol{\phi}}_{\Delta t}\hat{\boldsymbol{\phi}}_{\Delta t}^T\right) = \boldsymbol{M}_{\boldsymbol{\omega\tau}}. \tag{5.15}$$

In Addendum 5.8 we confirm that (5.9) is consistent with the definition of the rotational diffusion coefficient (5.15), and therefore our equation has the same physical noise covariance as the equation in Ref. [157], only written in a different representation. In our numerical tests, we will use $\langle \Delta \hat{u}_i (\tau) \Delta \hat{u}_j (\tau) \rangle$ as a convenient definition of a rotational mean square displacement (RMSD) at time $\tau$.

### 5.1.2.2 Smoluchowski Equation

A key property of the overdamped Langevin equation (5.9) is that it is time reversible with respect to the Gibbs-Boltzmann equilibrium distribution

$$P_{\text{eq}} (\boldsymbol{\theta}) = Z^{-1} \exp (-U (\boldsymbol{\theta}) / k_B T) \, \delta \left( \boldsymbol{\theta}^T \boldsymbol{\theta} - 1 \right), \tag{5.16}$$

with $Z$ a normalization constant. The overdamped equation (5.9) has the structure of a generic Langevin equation (1.1); however, a crucial difference is that (5.9) is an SDE on a manifold, namely, the unit 4-sphere, rather than an SDE in Eucledian space. A discussion of overdamped Langevin equations constrained on a manifold can be found in Ref. [81]. As explained there, for general curved manifolds one has to carefully construct the stochastic drift terms in order to ensure consistency with the desired equilibrium distribution. A key difference between (5.9) and the types of constrained equations discussed in Ref. [81] is that in our case the original (true or physical) dynamics is unconstrained, and could, in principle, be described using a non-redundant parameterization of the rotation group such as Euler angles [162]; the unit norm constraint implicit in (5.9) arises because it is mathematically simpler to embed the unit 4-sphere in a four dimensional Euclidean space than to parameterize it directly. The geometric matrix $\boldsymbol{\Psi} (\boldsymbol{\theta})$ plays the role of the projection operator in Ref. [81], but unlike a projection operator, $\boldsymbol{\Psi}$ is not square and projects from the original (physical) three-dimensional space of angular velocity to the tangent space of the unit 4-sphere.

To see that (5.16) is indeed the correct distribution let us consider the case $U (\boldsymbol{\theta}) = 0$, which should correspond to uniform probability of all orientations. The uniform distribution over the space of orientations of a rigid body in three dimensions is the so-called Haar measure over the group $SO(3)$, and has been the subject of mathematical study [173, 174]. It is known that in the quaternion representation this Haar measure corresponds to a *constant* probability density over the surface of the unit 4-sphere, i.e., the Hausdorff measure on the unit 4-sphere [173, 175, 172]; generating random uniformly-distributed orientations amounts to simply generating a point uniformly sampled on the unit 4-sphere [1]. This uniform distribution over the unit quaternion sphere is captured in (5.16) by the term $\delta \left( \boldsymbol{\theta}^T \boldsymbol{\theta} - 1 \right)$, and the additional prefactor $\exp (-U (\boldsymbol{\theta}) / k_B T)$ captures the standard Gibbs-Boltzmann weighting of the configurations based on their potential energy. Note that more generally, for a manifold $\Sigma$ defined by the scalar constraint $g(\boldsymbol{\theta}) = 0$, the Hausdorff measure $d\sigma_\Sigma$ on the the surface contains a metric factor relative to the Lebesque measure $d\boldsymbol{\theta}$ in unconstrained coordinates, as given by the co-area formula [81],

$$d\sigma_\Sigma (\boldsymbol{\theta}) = \delta \left( g(\boldsymbol{\theta}) \right) \| \boldsymbol{\nabla} g(\boldsymbol{\theta}) \|_2 \, d\boldsymbol{\theta}.$$

In our case, however, $g(\boldsymbol{\theta}) = \boldsymbol{\theta}^T \boldsymbol{\theta} - 1$ and $\| \boldsymbol{\nabla} g(\boldsymbol{\theta}) \|_2 = \| \boldsymbol{\theta} \|_2 = 1$ is constant over the surface of the unit 4-sphere, and the metric factor can be absorbed into the normalization factor $Z$. The fact that no metric factors appear in the quaternion representation simplifies the equations; in other representations such as Euler angles or rotation angles the Gibbs-Boltzmann distribution is *not* uniform even in the absence of external potentials, and therefore "metric forces" need to be included in the stochastic drift terms to ensure the correct equilibrium distribution [166, 165]. This subtle point has been missed in many prior works even though the concept of metric forces is well understood for rather general constrained Langevin equations [176].

To demonstrate that (5.9) is the equilibrium distribution (invariant measure) for (5.16), we examine the Fokker-Planck equation for the probability density $P (\boldsymbol{\theta}, t)$,

$$\partial_t P = \partial_i \left\{ \widetilde{M}_{ij} \left[ (\partial_j U) P + (k_B T) \, \partial_j P \right] \right\}, \tag{5.17}$$

where $\partial_i$ represents a partial derivative with respect to the $i$th component of $\boldsymbol{\theta}$. Note that when $P$ is the Gibbs-Boltzmann distribution (5.16), we formally obtain

$$\left[ (\partial_j U) P_{\text{eq}} + (k_B T) \, \partial_j P_{\text{eq}} \right] \sim \exp (-U (\boldsymbol{\theta}) / k_B T) \, \delta' \left( \boldsymbol{\theta}^T \boldsymbol{\theta} - 1 \right) \theta_j.$$

---

[1]Numerically, a uniformly-distributed unit 4-vector can be generated by generating a vector of 4 standard Gaussian random variables and normalizing the result; to see this observe that the resulting distribution must be uniform by virtue of rotational invariance of the multivariate Gaussian distribution.

We can then use the fact that $\boldsymbol{\Psi}^T\boldsymbol{\theta} = 0$ to see that at thermodynamic equilibrium the thermodynamic driving force inside the square brackets in eq. (5.17) vanishes, which implies that the Gibbs-Boltzmann distribution is an equilibrium distribution; using standard tools it can also be shown that (5.16) is the *unique* invariant measure. Note that the calculation above is formal, but one can make a more precise argument by considering the backward Kolmogorov equation applied to $\mathbb{E}[f]$ for an arbitrary well behaved function $f$ and expressing expectation values as integrals over the unit 4-sphere, similar to the approach taken in [81]. A similar calculation can be used to show that the generator of the Markov diffusion process (5.9) is self-adjoint with respect to a dot product weighted by the invariant measure (5.16), which proves that the overdamped dynamics is time reversible with respect to (5.16).

We can compare the FPE (5.17) with the one given by [158] for rigid rods. A rigid rod can be parameterized with a unit 3-vector $\boldsymbol{p}$ indicating the orientation of the rod (this is not to be confused with $\boldsymbol{p}$, the vector component of a quaternion from Section 5.1.1). If we expand (5.17) and use the property (5.6), we obtain

$$
\begin{aligned}
\partial_t P =& \partial_i \left\{ \Psi_{ik} \left(M_{\boldsymbol{\omega\tau}}\right)_{kl} \Psi_{jl} \left[\left(\partial_j U\right) P + \left(k_B T\right) \partial_j P\right]\right\} \\
=& \Psi_{ik} \partial_i \left\{ \left(M_{\boldsymbol{\omega\tau}}\right)_{kl} \left(\Psi_{jl}\left(\partial_j U\right) P + \left(k_B T\right) \Psi_{jl} \partial_j P\right)\right\}.
\end{aligned}
$$

This FPE has exactly the same form as the rotational part of eq. (4.149) of [158], with the crucial difference that for rods $\boldsymbol{\Psi}$ is replaced by $\boldsymbol{P}$, the cross product matrix for $\boldsymbol{p}$. We see that (5.17) is a natural generalization of the standard Smoluckowski equation for uniaxial bodies to biaxial bodies.

### 5.1.3 Rotation-Translation Coupling

In order to describe Brownian motion of freely suspended particles, it is necessary to also include translation in our model of rigid body motion. We first consider tracking both the location and orientation of a single rigid body. To do this, we introduce a variable $\boldsymbol{q}(t)$ for the Cartesian coordinates of a fixed point on the rigid body (not necessarily the center of mass). We assume that we are given hydrodynamic information in the form of a known $\boldsymbol{N}(\boldsymbol{q}, \boldsymbol{\theta})$, the grand mobility, which is the linear mapping from given force $\boldsymbol{F}$ and torque $\boldsymbol{\tau}$ (about $\boldsymbol{q}$) to the resulting velocity $\boldsymbol{u} \equiv \dot{\boldsymbol{q}}$ and angular velocity $\boldsymbol{\omega}$,

$$
\left[\begin{array}{c} \boldsymbol{u} \\ \boldsymbol{\omega} \end{array}\right] = \boldsymbol{N} \left[\begin{array}{c} \boldsymbol{F} \\ \boldsymbol{\tau} \end{array}\right] = \left[\begin{array}{cc} \boldsymbol{M}_{\boldsymbol{uF}} & \boldsymbol{M}_{\boldsymbol{u\tau}} \\ \boldsymbol{M}_{\boldsymbol{\omega F}} & \boldsymbol{M}_{\boldsymbol{\omega\tau}} \end{array}\right] \left[\begin{array}{c} \boldsymbol{F} \\ \boldsymbol{\tau} \end{array}\right].
$$

where $\boldsymbol{M}_{\boldsymbol{u\tau}} = \boldsymbol{M}_{\boldsymbol{\omega F}}^{\star}$ is the translation-rotation coupling tensor, and $\boldsymbol{M}_{\boldsymbol{uF}}$ is the translation-translation mobility that we first introduced in Chapter 4. Let us suppose that the torque and force are generated from a conservative potential $U(\boldsymbol{q}, \boldsymbol{\theta})$. Then using the fact that $\dot{\boldsymbol{q}} = \boldsymbol{u}$, along with (5.4) and (5.8) we can write the full Langevin equation including translation as the Ito overdamped equation,

$$
\begin{aligned}
\boldsymbol{v} = \frac{d\boldsymbol{x}}{dt} =& -\widetilde{\boldsymbol{N}}\partial_{\boldsymbol{x}}U + \sqrt{2k_B T}\,\widetilde{\boldsymbol{N}}^{\frac{1}{2}}\boldsymbol{\mathcal{W}} + \left(k_B T\right)\partial_{\boldsymbol{x}} \cdot \widetilde{\boldsymbol{N}} \\
=& -\left(\boldsymbol{\Xi N \Xi^{\star}}\right)\partial_{\boldsymbol{x}}U + \sqrt{2k_B T}\,\boldsymbol{\Xi N}^{\frac{1}{2}}\boldsymbol{\mathcal{W}} + \left(k_B T\right)\partial_{\boldsymbol{x}} \cdot \left(\boldsymbol{\Xi N \Xi^{\star}}\right),
\end{aligned}
\tag{5.18}
$$

where $\boldsymbol{x} = (\boldsymbol{q}, \boldsymbol{\theta})^T$ and $\boldsymbol{v} = \left(\boldsymbol{u}, \dot{\boldsymbol{\theta}}\right)^T$ are composite vectors of the translational and rotational variables (and their velocities), and we have introduced the block matrix

$$
\boldsymbol{\Xi} = \left[\begin{array}{cc} \boldsymbol{I} & \boldsymbol{0} \\ \boldsymbol{0} & \boldsymbol{\Psi} \end{array}\right].
\tag{5.19}
$$

The "square root" of the mobility $\boldsymbol{N}^{\frac{1}{2}}$ satisfies the fluctuation-dissipation relation $\boldsymbol{N}^{\frac{1}{2}}\boldsymbol{N}^{\frac{1}{2}\star} = \boldsymbol{N}$. A similar computation to that given in Section 5.1.2 shows that (5.18) is time reversible with respect to the Gibbs-Boltzmann distribution,

$$
P_{\text{eq}}(\boldsymbol{q}, \boldsymbol{\theta}) = Z^{-1}\exp\left(-U\left(\boldsymbol{q}, \boldsymbol{\theta}\right)/k_B T\right)\delta\left(\boldsymbol{\theta}^T\boldsymbol{\theta} - 1\right).
\tag{5.20}
$$

## 5.2 Temporal Integrators

In this section we introduce temporal integrators for the equations of motion of immersed rigid bodies formulated in Section 5.1. We update the quaternion representation of orientation using the Rotate procedure introduced in Section 5.1.1, preserving the unit-norm constraint to numerical precision. The stochastic drift term in eq. (5.18) is approximated in two ways, using a Fixman midpoint scheme and a Random Finite Difference (RFD) scheme, see Section 2.1 for a comparison of the two approaches in the context of unconstrained overdamped Langevin equations.

### 5.2.1 Euler-Maruyama

For illustration purposes, we begin by considering a naive Euler-Maruyama (EM) scheme applied to a variant of (5.9), in which we do not carefully handle the stochastic drift term $(k_B T)\, \partial_{\boldsymbol\theta} \cdot \widetilde{\boldsymbol M}$,

$$\boldsymbol\omega^n = -\, \boldsymbol M_{\boldsymbol\omega\boldsymbol\tau}^n \boldsymbol\tau^n + \left(\frac{2 k_B T}{\Delta t} \boldsymbol M_{\boldsymbol\omega\boldsymbol\tau}^n\right)^{\frac{1}{2}} \boldsymbol W^n \tag{5.21}$$

$$\boldsymbol\theta^{n+1} = \text{Rotate}\left(\boldsymbol\theta^n,\, \boldsymbol\omega^n \Delta t\right),$$

where a superscript denotes the point in time at which a particular quantity is evaluated, e.g. $\boldsymbol\theta^n \approx \boldsymbol\theta(n\Delta t)$ and $\boldsymbol M_{\boldsymbol\omega\boldsymbol\tau}^n = \boldsymbol M_{\boldsymbol\omega\boldsymbol\tau}(\boldsymbol\theta^n)$. Here $\boldsymbol W^n$ is a collection of i.i.d. standard Gaussian variates generated using a pseudo-random number generator, and the Rotate procedure is defined in section 5.1.1. Here and henceforth, we have used (5.8) to express the updates directly in terms of torque $\boldsymbol\tau(\boldsymbol\theta)$. While the scheme (5.21) is not actually consistent with (5.9), it makes a natural starting point when discussing temporal integrators for (5.9).

Note that because we use the Rotate procedure, this update actually moves along the unit norm constraint of normalized quaternions, as opposed to stepping off of the constraint and then projecting back onto it [81]. This is a natural way to update orientation multiplicatively while still being consistent with the additive Langevin equations formulated in Section 5.1. We can expand the Rotate procedure using the Taylor series (5.7) and truncate the result at first order in $\Delta t$, to obtain an expression for the leading order change in $\boldsymbol\theta$,

$$\boldsymbol\theta^{n+1} - \boldsymbol\theta^n \approx \Delta t\, \boldsymbol\Psi^n \boldsymbol\omega^n - \Delta t^2 \frac{(\boldsymbol\omega^n \cdot \boldsymbol\omega^n)}{8} \boldsymbol\theta^n.$$

$$= \Delta t \boldsymbol\Psi^n \left(-\boldsymbol M_{\boldsymbol\omega\boldsymbol\tau}^n \boldsymbol\tau^n + (2 k_B T\, \boldsymbol M_{\boldsymbol\omega\boldsymbol\tau}^n)^{\frac{1}{2}} \boldsymbol W^n\right)$$

$$- \Delta t\, (k_B T) \frac{(\boldsymbol W^n)^T \boldsymbol M_{\boldsymbol\omega\boldsymbol\tau}^n \boldsymbol W^n}{4} \boldsymbol\theta^n + O\left(\Delta t^2\right).$$

Note that the last term is equal in expectation to $-\Delta t\, (\text{Tr}\,(\boldsymbol M_{\boldsymbol\omega\boldsymbol\tau}^n)/4)\, \boldsymbol\theta^n$, which gives us the second term in the stochastic drift on the right hand side of (5.10). Therefore, when constructing more sophisticated temporal integrators, we see that we only need to add Fixman or RFD terms that will generate the remaining stochastic drift term $k_B T \Delta t \left(\boldsymbol\Psi\, (\partial_{\boldsymbol\theta} \boldsymbol M_{\boldsymbol\omega\boldsymbol\tau}) : \boldsymbol\Psi^T\right)^n$ in the update $\boldsymbol\theta^{n+1} - \boldsymbol\theta^n$. Fortunately, adding this term to the orientation looks to first order like a Rotate procedure with angular velocity $k_B T \left((\partial_{\boldsymbol\theta} \boldsymbol M_{\boldsymbol\omega\boldsymbol\tau}) : \boldsymbol\Psi^T\right)^n$. With this in mind, we now construct first order weakly accurate temporal integrators for (5.9).

### 5.2.2 Fixman Scheme

The standard approach to handling the stochastic drift in overdamped Langevin equations is to use Fixman's scheme, see Section 2.1.1.1. Henceforth we consider the full equations (5.18) including translation and rotational diffusion. To apply the Fixman method to (5.18) we rewrite (5.18) in a split Strato-Ito form,

$$\frac{d\boldsymbol x}{dt} = -\left(\boldsymbol\Xi \boldsymbol N \boldsymbol\Xi^T\right) \frac{\partial U}{\partial \boldsymbol x} + (2 k_B T)^{\frac{1}{2}} \boldsymbol\Xi \boldsymbol N \circ \boldsymbol N^{-\frac{1}{2}} \boldsymbol{\mathcal W}, \tag{5.22}$$

where $\boldsymbol N^{-\frac{1}{2}}$ satisfies $\boldsymbol N^{-\frac{1}{2}} \left(\boldsymbol N^{-\frac{1}{2}}\right)^{\star} = \boldsymbol N^{-1}$. The term $\boldsymbol N^{-\frac{1}{2}} \boldsymbol{\mathcal W}$ can be thought of as a "random force and torque" [103] and is equivalent in law to $\boldsymbol N^{-1} \boldsymbol N^{\frac{1}{2}} \boldsymbol{\mathcal W}$. To show that this is equivalent to (5.9), we can use the general identity (2.7) to obtain

$$(2 k_B T)^{\frac{1}{2}} \boldsymbol\Xi \boldsymbol N \circ \boldsymbol N^{-\frac{1}{2}} \boldsymbol{\mathcal W} = (k_B T)\, \partial_x \cdot \left(\boldsymbol\Xi \boldsymbol N \boldsymbol\Xi^T\right) - (k_B T)\, \boldsymbol\Xi \boldsymbol N \left(\partial_x \cdot \boldsymbol\Xi^T\right) + (2 k_B T)^{\frac{1}{2}} \boldsymbol\Xi \boldsymbol N^{\frac{1}{2}} \boldsymbol{\mathcal W}$$

$$= (k_B T)\, \partial_x \cdot \left(\boldsymbol\Xi \boldsymbol N \boldsymbol\Xi^T\right) + (2 k_B T)^{\frac{1}{2}} \boldsymbol\Xi \boldsymbol N^{\frac{1}{2}} \boldsymbol{\mathcal W},$$

where we used (5.6).

It is now straightforward to apply Fixman's method with the Rotate procedure, yielding the predictor-corrector

temporal integrator,

$$\boldsymbol{v}^n = (\boldsymbol{u}^n, \boldsymbol{\omega}^n) = \left( \boldsymbol{N} \left[ \begin{array}{c} \boldsymbol{F} \\ \boldsymbol{\tau} \end{array} \right] \right)^n + \sqrt{\frac{2 k_B T}{\Delta t / 2}} \left( \boldsymbol{N}^{\frac{1}{2}} \right)^n \boldsymbol{W}^{n,1} \tag{5.23}$$

$$\boldsymbol{q}^{p,n+\frac{1}{2}} = \boldsymbol{q}^n + \frac{\Delta t}{2} \boldsymbol{u}^n$$

$$\boldsymbol{\theta}^{p,n+\frac{1}{2}} = \mathrm{Rotate}\left( \boldsymbol{\theta}^n, \frac{\Delta t}{2} \boldsymbol{\omega}^n \right)$$

$$\boldsymbol{v}^{p,n+\frac{1}{2}} = \left( \boldsymbol{N} \left[ \begin{array}{c} \boldsymbol{F} \\ \boldsymbol{\tau} \end{array} \right] \right)^{p,n+\frac{1}{2}} + \sqrt{\frac{k_B T}{\Delta t}} \boldsymbol{N}^{p,n+\frac{1}{2}} \left( \boldsymbol{N}^{-\frac{1}{2}} \right)^n \left( \boldsymbol{W}^{n,1} + \boldsymbol{W}^{n,2} \right)$$

$$\boldsymbol{q}^{n+1} = \boldsymbol{q}^n + \Delta t \, \boldsymbol{u}^{p,n+\frac{1}{2}}$$

$$\boldsymbol{\theta}^{n+1} = \mathrm{Rotate}\left( \boldsymbol{\theta}^n, \Delta t \boldsymbol{\omega}^{p,n+\frac{1}{2}} \right).$$

We show that this scheme produces the correct stochastic drift in Addendum 5.7, more precisely, the scheme (5.25) is a first-order weak integrator for (5.18). The Fixman scheme requires the application of $\boldsymbol{N}^{-\frac{1}{2}}$, or, equivalently, of $\boldsymbol{N}^{-1}$; this is computationally expensive in cases when only $\boldsymbol{N}$ is easy to compute, and it is prohibitive in cases when only the application of $\boldsymbol{N}$ and $\boldsymbol{N}^{\frac{1}{2}}$ to a vectors can be computed. In the examples we study here these matrices will be small and thus easy to compute using direct linear algebra, but this approach does not extend easily to suspensions of many rigid particles. In the next section, we show how to avoid using $\boldsymbol{N}^{-\frac{1}{2}}$ or $\boldsymbol{N}^{-1}$ by using a random finite difference (RFD) scheme.

It is important to observe that the Fixman scheme (5.23) is unaffected by the change of representations of orientations. All that needs to be changed to use other representations of orientations is to simply change the Rotate procedure. This point has already been intuited in prior works, where the standard Fixman method has been used for non-spherical bodies, such as, for example, work on Brownian dynamics for rigid rods [14]. The analytical simplicity of the quaternion representation makes it straightforward for us to prove first order weak accuracy for the Fixman scheme in the general case (see Addendum 5.7), although the key idea is in fact to write the dynamics in the split Ito-Strato form (5.22).

### 5.2.3 Random Finite Difference Scheme

To avoid the computation of $\boldsymbol{N}^{-\frac{1}{2}}$ or $\boldsymbol{N}^{-1}$, we formulate a random finite difference scheme by expanding the stochastic drift term into pieces. We use Einstein's implicit summation notation for clarity, where $i, n, m,$ and $p$ represent any component of $\boldsymbol{x}$, and $s, t,$ and $u$ represent indices that range over only the orientation components, i.e. components of $\boldsymbol{\theta}$ , obtaining (see Addendum 5.7)

$$\left\{ \partial_{\boldsymbol{x}} \cdot \left( \boldsymbol{\Xi} \boldsymbol{N} \boldsymbol{\Xi}^T \right) \right\}_i = \Xi_{im} \left( \partial_n N_{mp} \right) \Xi_{np} + \left[ \begin{array}{c} 0 \\ \left( \partial_s \Psi_{it} \right) \left( M_{\boldsymbol{\omega} \boldsymbol{\tau}} \right)_{tu} \Psi_{su} \end{array} \right]. \tag{5.24}$$

An Euler-Maryuama scheme such as (5.21) will, in expectation, produce a drift of

$$\left\{ \left( \partial_{\boldsymbol{\theta}} \boldsymbol{\Psi} \right) : \left( \boldsymbol{M}_{\boldsymbol{\omega} \boldsymbol{\tau}} \boldsymbol{\Psi}^T \right) \right\}_i = \left( \partial_s \Psi_{it} \right) \left( M_{\boldsymbol{\omega} \boldsymbol{\tau}} \right)_{tu} \Psi_{su}$$

in the orientation as we saw in Section 5.2.1. The remaining term

$$\left\{ \boldsymbol{\Xi} \left( \partial_{\boldsymbol{x}} \left( \boldsymbol{N} \right) : \boldsymbol{\Xi}^T \right) \right\}_i = \Xi_{im} \left( \partial_n N_{mp} \right) \Xi_{np}$$

can be approximated using an RFD correction to the velocity as follows,

$$\tilde{\boldsymbol{v}} = (\tilde{\boldsymbol{u}}^n, \tilde{\boldsymbol{\omega}}^n) = \widetilde{\boldsymbol{W}}^n \tag{5.25}$$

$$\tilde{\boldsymbol{q}} = \boldsymbol{q}^n + \delta \tilde{\boldsymbol{u}}^n$$

$$\tilde{\boldsymbol{\theta}} = \mathrm{Rotate}\left( \boldsymbol{\theta}^n, \delta \tilde{\boldsymbol{\omega}}^n \right)$$

$$\boldsymbol{v}^n = (\boldsymbol{u}^n, \boldsymbol{\omega}^n) = \left( \boldsymbol{N} \left[ \begin{array}{c} \boldsymbol{F} \\ \boldsymbol{\tau} \end{array} \right] \right)^n + \sqrt{\frac{2 k_B T}{\Delta t}} \left( \boldsymbol{N}^{\frac{1}{2}} \right)^n \boldsymbol{W}^n + \frac{k_B T}{\delta} \left( \widetilde{\boldsymbol{N}} - \boldsymbol{N}^n \right) \widetilde{\boldsymbol{W}}^n$$

$$\boldsymbol{q}^{n+1} = \boldsymbol{q}^n + \Delta t \boldsymbol{u}^n$$

$$\boldsymbol{\theta}^{n+1} = \mathrm{Rotate}\left( \boldsymbol{\theta}^n, \Delta t \boldsymbol{\omega}^n \right),$$

where $\widetilde{\boldsymbol{W}}^n$ is a collection of i.i.d. standard normal variates generated independently at each time step, and $\delta$ is a small parameter (see discussion in Section 2.1.1.2). This scheme only requires the application of $\boldsymbol{N}^n$, $\boldsymbol{N}^{\frac{1}{2}}$, and $\widetilde{\boldsymbol{N}}$, which can be a considerable advantage over the Fixman scheme in the case when $\boldsymbol{N}$ is expensive to invert. In Addendum 5.7 we show that this RFD approach does in fact generate the correct drift terms, and the scheme (5.25) is a first-order weak integrator for (5.18). Observe that the RFD scheme is also invariant under changes of representation for the orientation of the body; all that is required is an appropriate Rotate procedure.

## 5.2.4  Suspensions of Rigid Bodies

The temporal integration schemes presented above straightforwardly generalize to suspensions of more than one rigid body. The overdamped Langevin equation (5.18) continues to hold, but now $\boldsymbol{x}$ collects the positions and orientations of all bodies, and $\boldsymbol{v}$ collects the linear and angular velocities of all bodies, and $\boldsymbol{\Xi}$ is a block-diagonal matrix with one diagonal block (5.19) per body. We suppose that we are given the grand mobility tensor $\boldsymbol{N}$ for all of the bodies, which maps the forces and torques applied on the bodies to the resulting linear and angular velocities. The deterministic and stochastic terms are handled in a straightforward way; we accumulate deterministic velocities and angular velocities on each body using the grand mobility tensor, and the random velocities and angular velocities that the bodies experience are given by $\sqrt{2k_B T \Delta t} \boldsymbol{N}^{\frac{1}{2}} \boldsymbol{W}$ where $\boldsymbol{N}^{\frac{1}{2}} \left( \boldsymbol{N}^{\frac{1}{2}} \right)^T = \boldsymbol{N}$. Note that the direct computation of $\boldsymbol{N}^{\frac{1}{2}}$ can be expensive in the multi-body setting; a generalization of the fluctuating immersed boundary method [3] can however generate the stochastic forcing in essentially linear time by using a fluctuating hydrodynamic solver.

We focus here on generalizing the Fixman and RFD approximations of the stochastic drift term. The grand mobility $\boldsymbol{N}$ consists of blocks $\boldsymbol{N}_{AB}$ which take forces and torques on body $B$ and produce the resulting velocities and angular velocities on body $A$ (which can be the same as body $B$). We consider now the stochastic drift for a given body $A$, letting $\boldsymbol{x}_A = \{\boldsymbol{q}_A, \boldsymbol{\theta}_A\}$ denote the position and orientation of body $A$,

$$
\begin{aligned}
\frac{d\boldsymbol{x}_A}{dt} \text{ drift} &= (k_B T) \sum_B \partial_{\boldsymbol{x}_B} \cdot \left( \boldsymbol{\Xi}_A \boldsymbol{N}_{AB} \boldsymbol{\Xi}_B^T \right), \\
&= (k_B T) \sum_B \left[ (\partial_{\boldsymbol{x}_B} \boldsymbol{\Xi}_A) : \left( \boldsymbol{N}_{AB} \boldsymbol{\Xi}_B^T \right) + \boldsymbol{\Xi}_A \partial_{\boldsymbol{x}_B} \left( \boldsymbol{N}_{AB} \boldsymbol{\Xi}_B^T \right) \right] \\
&= (k_B T) (\partial_{\boldsymbol{x}_B} \boldsymbol{\Xi}_A) : \left( \boldsymbol{N}_{AA} \boldsymbol{\Xi}_A^T \right) + \sum_B \boldsymbol{\Xi}_A (\partial_{\boldsymbol{x}_B} \boldsymbol{N}_{AB}) : \boldsymbol{\Xi}_B^T.
\end{aligned} \tag{5.26}
$$

where the sums range over all bodies $B$. Here

$$
\boldsymbol{\Xi}_A = \begin{bmatrix} \boldsymbol{I} & \boldsymbol{0} \\ \boldsymbol{0} & \boldsymbol{\Psi}(\boldsymbol{\theta}_A) \end{bmatrix},
$$

and we used the fact that $\partial_{\boldsymbol{x}_B} \boldsymbol{\Xi}_A$ is nonzero only when $A = B$. The first term term on the right hand side of (5.26) is a local term that does not contain any many-body effects, and can therefore be approximated by using the Rotate procedure, as for a single body. The second term on the right hand side of (5.26) can be approximated using a random finite difference or Fixman approach in the same way as for a single body. This second term contains many-body interactions which are captured in the computation of $\boldsymbol{N}^{-\frac{1}{2}}$ in the Fixman approach, and in the RFD approach they are captured by randomly displacing *all* bodies together (rather than one by one).

## 5.3  Examples

In this section we apply the Fixman and RFD temporal integrators to some simple examples of a single rigid body immersed in a viscous fluid. Since we want to focus on examples with configuration-dependent mobilities, we examine rigid bodies in the vicinity of no-slip boundaries. We simulate the diffusive motion of an asymmetric sphere (Section 5.3.3), a tetramer of colloidal spheres (Section 5.3.4), and a colloidal boomerang (Section 5.3.5), in the presence of gravity and a no-slip wall located at the plane $z = 0$. There are two main quantities that we examine in these simulations, the first static and the second dynamic. The first quantity are various moments of the equilibrium distribution for the position and orientation of the rigid bodies, which we compare to moments of the expected Gibbs-Boltzmann distribution. The second quantity we study is the the mean square displacement of the rigid bodies, as we now explain in more detail.

### 5.3.1 Mean Square Displacement

We define the total mean square displacement (MSD) at time $\tau$ as the outer product

$$\boldsymbol{D}(\tau; \boldsymbol{x}) = \frac{1}{2} \langle \Delta \boldsymbol{X}(\tau) \left( \Delta \boldsymbol{X}(\tau) \right)^T \rangle_{\boldsymbol{x}} = \begin{bmatrix} \boldsymbol{D}_t & \boldsymbol{D}_c \\ \boldsymbol{D}_c^T & \boldsymbol{D}_r \end{bmatrix} (\tau; \boldsymbol{x}), \tag{5.27}$$

where $\Delta X(\tau; \boldsymbol{x}) = (\Delta \boldsymbol{q}(\tau; \boldsymbol{x}), \Delta \hat{\boldsymbol{u}}(\tau; \boldsymbol{x}))$, with position increment $\Delta \boldsymbol{q}(\tau) = \boldsymbol{q}(\tau) - \boldsymbol{q}(0)$ and orientation increment $\Delta \hat{\boldsymbol{u}}(\tau)$ as defined in (5.13). The average in (5.27) is taken over trajectories started at $\boldsymbol{x} = (\boldsymbol{q}(0), \boldsymbol{\theta}(0))$. Recall that the short-time diffusion coefficient is given by the mobility in agreement with the Stokes-Einstein relation (see eq. (2) of [157])

$$\frac{1}{2k_B T} \lim_{\tau \to 0} \frac{\boldsymbol{D}(\tau; \boldsymbol{x})}{\tau} = \boldsymbol{N}(\boldsymbol{x}), \tag{5.28}$$

where the grand mobility tensor $\boldsymbol{N}$ is the block matrix

$$\boldsymbol{N} = \begin{bmatrix} \boldsymbol{M}_{\boldsymbol{uF}} & \boldsymbol{M}_{\boldsymbol{u\tau}} \\ \boldsymbol{M}_{\boldsymbol{\omega F}} & \boldsymbol{M}_{\boldsymbol{\omega\tau}} \end{bmatrix}.$$

Our overdamped Langevin equation ensures consistency with this Stokes-Einstein relation, see (5.15) and Addendum 5.8 for the proof for the rotational component $\boldsymbol{D}_r$.

We can further define the *equilibrium* MSD via the ergodic average

$$\boldsymbol{D}(\tau) = \langle \boldsymbol{D}(\tau; \boldsymbol{x}) \rangle, \tag{5.29}$$

where the average is taken over $\boldsymbol{x}$ distributed according to the Gibbs-Boltzmann distribution (5.20). In practice, we estimate $\boldsymbol{D}(\tau)$ from our simulations by taking a time average over one long trajectory (using the ergodic property) with the initial condition distributed according to (5.20), as generated using an accept/reject Monte Carlo method. We estimate error bars by running an ensemble of statistically independent trajectories. The Stokes-Einstein relation (5.28) gives the *short-time* mean square displacement, which can be used to define a short-time translational diffusion tensor

$$\boldsymbol{\chi}_{st} = \frac{1}{2} \lim_{\tau \to 0} \frac{\langle \boldsymbol{D}_t(\tau; \boldsymbol{x}) \rangle}{\tau} = \langle \boldsymbol{M}_{\boldsymbol{uF}} \rangle.$$

In general, it is much harder to characterize the *long-time* diffusion coefficient

$$\boldsymbol{\chi}_{lt} = \frac{1}{2} \lim_{\tau \to \infty} \frac{\langle \boldsymbol{D}_t(\tau; \boldsymbol{x}) \rangle}{\tau},$$

even for a single body in the presence of confinement. The only simple case is when the MSD is *strictly* linear with time so that the long and short time diffusion coefficients are equal and one can just average the mobility over the Gibbs-Boltzmann distribution in order to obtain the diffusion coefficient.

The choice of the origin around which torques are expressed, which is the point on the body whose position we track, strongly affects the short-time mean square displacement. Given two fixed points on the body $\boldsymbol{q}_1$ and $\boldsymbol{q}_2$, it is straightforward to derive the following relationship between the blocks of $\boldsymbol{N}^1$ calculated using origin $\boldsymbol{q}_1$, and $\boldsymbol{N}^2$ calculated with origin $\boldsymbol{q}_2$[177],

$$\boldsymbol{M}_{\boldsymbol{\omega\tau}}^2 = \boldsymbol{M}_{\boldsymbol{\omega\tau}}^1 \tag{5.30}$$
$$\boldsymbol{M}_{\boldsymbol{\omega F}}^2 = \boldsymbol{M}_{\boldsymbol{\omega F}}^1 + \boldsymbol{M}_{\boldsymbol{\omega\tau}}^1 \times \boldsymbol{r}_{12}$$
$$\boldsymbol{M}_{\boldsymbol{uF}}^2 = \boldsymbol{M}_{\boldsymbol{uF}}^1 - \boldsymbol{r}_{12} \times \left( \boldsymbol{M}_{\boldsymbol{\omega\tau}}^1 \times \boldsymbol{r}_{12} \right) + \left( \boldsymbol{M}_{\boldsymbol{\omega F}}^1 \right)^T \times \boldsymbol{r}_{12} - \boldsymbol{r}_{12} \times \boldsymbol{M}_{\boldsymbol{\omega F}}^1,$$

where $\boldsymbol{r}_{12} = \boldsymbol{q}_2 - \boldsymbol{q}_1$. Cross-products between vectors and tensors are defined in Eqs. (4,5) in [177], with $\boldsymbol{A} \times \boldsymbol{b}$ corresponding to taking cross products between rows of $\boldsymbol{A}$ and $\boldsymbol{b}$, in index notation,

$$(\boldsymbol{A} \times \boldsymbol{b})_{ij} = (\boldsymbol{A}_{i,:} \times \boldsymbol{b})_j = \epsilon_{jkl} A_{ik} b_l,$$

where $\boldsymbol{\epsilon}$ is the Levi-Chivita tensor, and similarly,

$$(\boldsymbol{b} \times \boldsymbol{A})_{ij} = (\boldsymbol{b} \times \boldsymbol{A}_{:,j})_i = \epsilon_{ikl} b_k A_{lj}.$$

In general, the cross-coupling (translation-rotation) mobility tensors $\boldsymbol{M}_{\boldsymbol{\omega F}} = \boldsymbol{M}_{\boldsymbol{u\tau}}^T$ are not symmetric. However, it can be shown that for any body shape, there exists a unique point in the body called the center of diffusion or

center of mobility (CoM), such that, when that point is taken as the origin, the coupling tensors are symmetric, $\boldsymbol{M}_{\boldsymbol{\omega F}}^T = \boldsymbol{M}_{\boldsymbol{\omega F}} = \boldsymbol{M}_{\boldsymbol{u\tau}} = \boldsymbol{M}_{\boldsymbol{u\tau}}^T$. For some bodies of sufficient symmetry, there exists a point called the center of hydrodynamic stress (CoH) [177], where the cross-coupling vanishes, $\boldsymbol{M}_{\boldsymbol{\omega F}} = \boldsymbol{M}_{\boldsymbol{u\tau}} = 0$; note that if a CoH exists it is also the CoM. A CoH always exists in two dimensions [154, 159], however, for general skew bodies in three dimensions a CoH does not exist [177].

### 5.3.1.1  Free isotropic diffusion

For a freely-diffusing rigid body in an unbounded fluid in the absence of any external forces and torques, all orientations are equally likely. It is well-known that in the oriented angle representation the Haar measure over the rotation group corresponds to $\hat{\boldsymbol{\phi}}$ uniformly distributed over the unit 3-sphere, and a probability density $P(\phi) = (2/\pi)\sin^2(\phi/2)$ for the angle of rotation (see (14) in [174]). Combined with (5.14) this shows that for free isotropic rotational diffusion the asymptotic long-time value of the rotational MSD is finite,

$$\lim_{\tau \to \infty} \boldsymbol{D}_r(\tau) = \lim_{\tau \to \infty} \langle (\Delta \hat{\boldsymbol{u}}(\tau))(\Delta \hat{\boldsymbol{u}}(\tau))^T \rangle = \left\langle \hat{\boldsymbol{\phi}}\hat{\boldsymbol{\phi}}^T \right\rangle \frac{2}{\pi} \int_0^\pi \sin^2(\phi/2) \sin^2(\phi) \, d\phi \tag{5.31}$$

$$= \frac{1}{3}\boldsymbol{I} \cdot \frac{1}{2} = \frac{1}{6}\boldsymbol{I} \approx 0.167,$$

independent of the shape of the body.

When the CoM is used as the tracking point, the translational MSD for free isotropic diffusion is strictly linear in time (see (46) in [167]),

$$\boldsymbol{D}_t(\tau) = (2k_B T \tau) \cdot \frac{1}{d}\text{Tr}(\boldsymbol{M}_{\boldsymbol{uF}}) \boldsymbol{I}, \tag{5.32}$$

where $d$ is the dimensionality. This gives the effective long-time diffusion coefficient for the isotropic translational diffusion of the body $\chi_{lt} = \text{Tr}(\boldsymbol{M}_{\boldsymbol{uF}})/d$, which is independent of the orientation of the body used to evaluate $\text{Tr}(\boldsymbol{M}_{\boldsymbol{uF}})$.

### 5.3.1.2  Confined Diffusion

Our primary focus in this work is diffusion of rigid bodies in the presence of confinement and gravity, specifically, we consider diffusion in the vicinity of a no-slip boundary [11]. In typical experiments, the particles being tracked are substantially denser than the solvent and thus sediment close to the bottom microscope slip due to gravity [155, 156], or, the particles are confined in a narrow slit channel [154, 159]. In both cases the boundaries strongly modify the hydrodynamic response. Notably, the CoM will depend on the position of the body relative to the boundary, and for non-skew particles, there may not be a CoH in the presence of a boundary even if there is one in an unbounded domain. Note that in the presence of gravity the typical height of a rigid body above a plane wall is on the order of the gravitational height $h_g \sim k_B T/(m_e g)$, where $m_e$ is the excess mass of the particle relative to the solvent, and $g$ is the gravitational acceleration. The value of the gravitational height varies widely in experiments depending on the density of the colloidal particles and their size (volume), from tens of nanometers to tens of micrometers.

In the numerical studies that follow we examine the MSD of isolated rigid particles sedimented near a wall in the presence of gravity. We orient our coordinate system so that the $x$ and $y$ axes (first two axes) are parallel to the wall and the $z$ axis (third axis) is perpendicular to the wall. In experiments based on confocal or optical microscopy, only the motion of the particle parallel to the wall can be observed and measured, in particular, what is measured is the parallel mean square displacement

$$D_\parallel(\tau) = D_{11}(\tau) + D_{22}(\tau).$$

In our simulations, we apply no forces in the $x$ and $y$ directions, and at large times we expect that $D_\parallel(\tau)$ will grow linearly with slope proportional to the long-time quasi-two-dimensional diffusion coefficient $\chi_{2D}$ which can be measured from simulations or experiments,

$$D_\parallel(\tau) \sim 4\chi_{2D}\tau \quad \text{at long times.}$$

In general, we do not expect $D_\parallel(\tau)$ to be strictly linear in time. However, if it is, then the long-time diffusion coefficient is the same as the short-time diffusion coefficient, and can be obtained by averaging the parallel mobility over the equilibrium distribution,

$$\chi_{2D} = k_B T \left\langle M_\parallel \right\rangle = k_B T \left\langle \frac{M_{11} + M_{22}}{2} \right\rangle. \tag{5.33}$$

Observe that the long-time diffusion coefficient is independent of the choice of tracking point, but the short-time one is. The goal is therefore to identify a tracking point that makes $D_\parallel(\tau)$ as close to linear as possible, so that (5.33) is a good approximation. If this can be accomplished, then the long-time diffusion coefficient can be estimated from a purely equilibrium calculation, *without* requiring us to simulate long-time trajectories. If a CoH exists, and is *independent* of the configuration, then translational and rotational motion will decouple and (5.33) will be exact. In general, however, a CoH does not exist in three dimensions even in the absence of confinement. However, as argued in Refs. [154, 159], if the diffusion is strongly confined to be effectively two-dimensional, either because of strong gravity or because of the presence of two tightly-spaced confining walls, an approximate CoH will exist and therefore the parallel MSD will be essentially linear in time. We will examine these claims in greater detail in Section 5.3.5.

We also investigate the perpendicular mean square displacement for the height above the plane wall,

$$D_\perp(\tau) = D_{33}(\tau),$$

which we expect to reach a finite asymptotic value at large times due to the presence of gravity,

$$\lim_{\tau \to \infty} D_\perp(\tau) = \langle (z_1 - z_2)^2 \rangle_{(z_1, z_2)}. \tag{5.34}$$

where $z_1$ and $z_2$ are the heights of the tracking point for two configurations sampled uniformly and randomly from the Gibbs-Boltzmann distribution (5.20). A good generalization of the concept of a gravitational height for nonspherical particles is

$$h_g = \left( \lim_{\tau \to \infty} D_\perp(\tau) \right)^2 \sim f_g \left( \frac{k_B T}{m_e g} \right), \tag{5.35}$$

where $f_g$ is a geometric factor that is hard to compute analytically for a general body but can be computed using a Monte Carlo algorithm from (5.34). Note, however, that $f_g$ depends on the choice of the tracking point, and should therefore be associated with a particular fixed point on the body.

For rotation, we examine the diagonal components $D_{ii}(\tau)$, $i = 4, 5, 6$ of the rotational MSD, which must reach a finite asymptotic limit at large times since the rotational displacements are bounded,

$$\lim_{\tau \to \infty} \boldsymbol{D}_r(\tau) = \langle (\Delta \hat{\boldsymbol{u}}(\boldsymbol{\theta}_1, \boldsymbol{\theta}_2)) (\Delta \hat{\boldsymbol{u}}(\boldsymbol{\theta}_1, \boldsymbol{\theta}_2))^T \rangle_{(\boldsymbol{\theta}_1, \boldsymbol{\theta}_2)}, \tag{5.36}$$

where $\Delta \hat{\boldsymbol{u}}(\boldsymbol{\theta}_1, \boldsymbol{\theta}_2)$ is the rotational displacement (5.13) between two random orientations $\boldsymbol{\theta}_1$ and $\boldsymbol{\theta}_2$ sampled uniformly from the Gibbs-Boltzmann distribution (5.20).

In order to compute averages over the Gibbs-Boltzmann distribution (5.20), which includes the effects of gravity and steric repulsion from the wall, we use a Monte Carlo method to generate random samples distributed according to the equilibrium distribution. The simplest way to do this is an accept-reject method in which we first generate a random position $\boldsymbol{q}$ with uniform height and a uniform random orientation $\boldsymbol{\theta}$ of the body, and accept the random configuration $\boldsymbol{x}$ with probability $\exp(-U(\boldsymbol{x})/k_B T)$. Note that in principle this distribution is unbounded in the $z > 0$ direction, and cannot be captured entirely by such an accept-reject method with height distributed in a finite interval. However, since the probability decays monotonically in the tail as $\sim \exp(-m_e g h/k_B T)$ where $h$ is the height of the tracking point of the body, we can adjust the upper bound of the uniformly distributed height empirically to ensure that we are only neglecting an insignificant portion of the distribution. One can avoid this bias by using an exponential distribution as a proposal density in the accept/reject process, or by using Markov Chain Monte Carlo to generate samples from the Gibbs-Boltzmann distribution; we have found this to produce indistinguishable results for our purposes, while being significantly slower. We estimate asymptotic values of the MSD from (5.34) and (5.34) by using the Monte Carlo method to generate a large number of pairs of samples from the equilibrium distribution, calculating the mean square displacement between each pair, and averaging this value over all of the pairs.

When using discrete timesteps with stochastic forcing, it is possible for unphysical configurations to occur; this leads to a finite-time breakdown of explicit integrators [178, 153] such as our Fixman and RFD schemes. Specifically, in our numerical tests, it is possible for the stochastic terms to "kick" some part of the body through the wall; this invalidates the hydrodynamic calculations used to compute the mobility, or makes the mobility not positive-semidefinite. To handle this possibility in our simulations, after each configurational update (including the predictor step to the midpoint in the Fixman scheme), we check whether any of the blobs overlap the wall, and if the new configuration is not valid, we throw it away and start again at state $\boldsymbol{x}^n$ and repeat the time step, drawing new random numbers. This procedure is repeated until a valid new state is found (note that it is possible for multiple rejections to occur in one time interval). Because this rejection of invalid states changes the dynamics,

and therefore the statistics of the system, we ensure that the number of rejections is very low compared to the total number of steps taken. In the results presented in this section, the rejection rate (number of rejections divided by number of attempted steps) is never greater than $5 \times 10^{-5}$; in most cases it is zero.

### 5.3.2   Rigid multiblob models of rigid-body hydrodynamics

We discretize rigid bodies for the purposes of hydrodynamic calculations by constructing them out of multiple rigidly-connected spherical "blobs" (recall that blobs were first introduced in chapter 4) of hydrodynamic radius $a$. These blobs can be thought of as hydrodynamically minimally-resolved spheres forming a rigid conglomerate that approximates the hydrodynamics of the actual rigid object being studied. Several examples of such blob models of rigid particles are given in the top three panels (panels 1-3) of Fig. 5.1 and compared to an image of the actual physical object studied experimentally in prior work by others; these experiments inspired the work presented in this chapter. Note that the hydrodynamic fidelity of the rigid "multiblob" [179] models can be refined by increasing the number of blobs (and, of course, decreasing their hydrodynamic radius $a$ accordingly), as illustrated for a model of a lysozyme in the bottom panel (panel 4) of Fig. 5.1; of course, increasing the resolution comes at a significant increase in the computational cost of the method. Similar "bead" or "raspberry" models appear in a number of studies of hydrodynamics of particle suspensions [17, 18, 163, 20, 19, 180, 181, 15, 16, 182, 183, 179], either connected rigidly as we do here, or connected via stiff springs; in some models the fluid or particle inertia is included also. Since in this work we focus on the long-time diffusive dynamics it is crucial to use rigid rather than stiff springs, and to eliminate inertia in the spirit of the overdamped approximation, in order to allow for a sufficiently large time step to reach physical time scales of interest (seconds to minutes in actual experiments).

After discretizing a rigid body using $n$ blobs, we write down a system of equations that constrain the body to move rigidly. These intuitive equations are written in a large number of prior works [17, 18, 163, 181, 15, 16, 182] but we refer to [181] for a clear yet detailed exposition; the authors also provide associated computer codes in the supplementary material. Letting $\boldsymbol{\lambda} = \{\boldsymbol{\lambda}_1, \ldots, \boldsymbol{\lambda}_n\}$ be a vector of forces (Lagrange multipliers) that act on each blob to enforce the rigidity of the body, we have the linear system for $\boldsymbol{\lambda}_j$, $\boldsymbol{u}$ and $\boldsymbol{\omega}$,

$$\sum_j (\boldsymbol{M}_B)_{ij}\, \boldsymbol{\lambda}_j = \boldsymbol{u} + \boldsymbol{\omega} \times (\boldsymbol{r}_i - \boldsymbol{q}), \quad \forall i \tag{5.37}$$

$$\sum_i \boldsymbol{\lambda}_i = \boldsymbol{F}$$

$$\sum_i (\boldsymbol{r}_i - \boldsymbol{q}) \times \boldsymbol{\lambda}_i = \boldsymbol{\tau},$$

where $\boldsymbol{F}$ is the total force applied on the body, $\boldsymbol{u}$ is the velocity of point $\boldsymbol{q}$, $\boldsymbol{\omega}$ is the angular velocity of the body, $\boldsymbol{\tau}$ is the total torque applied to the body about point $\boldsymbol{q}$, and $\boldsymbol{r}_i$ is the position of blob $i$. Here the blob-blob mobility $\boldsymbol{M}_B$ describes the hydrodynamic relations between the blobs, accounting for the influence of the boundaries. The pairwise block $(\boldsymbol{M}_B)_{ij}$ computes the velocity of blob $i$ given forces on blob $j$ in the absence of all other blobs, and can be computed, in principle, using (4.6). In the presence of a single wall, an analytic approximation to $(\boldsymbol{M}_B)_{ij}$ is given by Swan and Brady [11], as a generalization of the Rotne-Prager tensor (4.7) to account for the no-slip boundary using Blake's image construction. In this work we utilize the translation-translation part of the Rotne-Prager-Blake mobility (see equations (B1) and (C2) in [11]) to compute $\boldsymbol{M}_B$, ignoring the higher order torque and stresslet terms in the spirit of the blob model [3]. Note that in a suitable limit of infinitely many blobs of appropriate radius, solving (5.37) computes the exact grand mobility for the rigid body (or bodies), even though only the lowest-order monopole approximation is used for $\boldsymbol{M}_B$ [184].

The solution of the linear system (5.37) defines a linear mapping from force and torque to velocity and angular velocity, and thus gives the grand mobility $\boldsymbol{N}$ (for explicit formulas, see [181]) as an explicit $6 \times 6$ matrix. In the examples considered in the work, the number of blobs is small and the system (5.37) can easily be solved by computing the Schur complement [181] and inverting it directly with dense linear algebra. The use of dense linear algebra allows us to focus our attention on the temporal integrators for the overdamped dynamics and not on linear algebra or hydrodynamics issues. In principle, our temporal integrators can be used with a variety of methods for computing the hydrodynamic mobility of suspensions of rigid bodies.

We compute the square root $\boldsymbol{N}^{\frac{1}{2}}$ by performing a dense Cholesky factorization on $\boldsymbol{N}$. It is important to note that if $\boldsymbol{M}_B$ is SPD, the grand mobility $\boldsymbol{N}$ computed by solving (5.37) is also SPD. Note that the Swan-Brady approximation to $\boldsymbol{M}_B$ [11] used here is based on the Rotne-Prager tensor and is thus only guaranteed to be positive definite when the blobs do not overlap each other or the wall, i.e, when no two blobs are closer than a distance $2a$
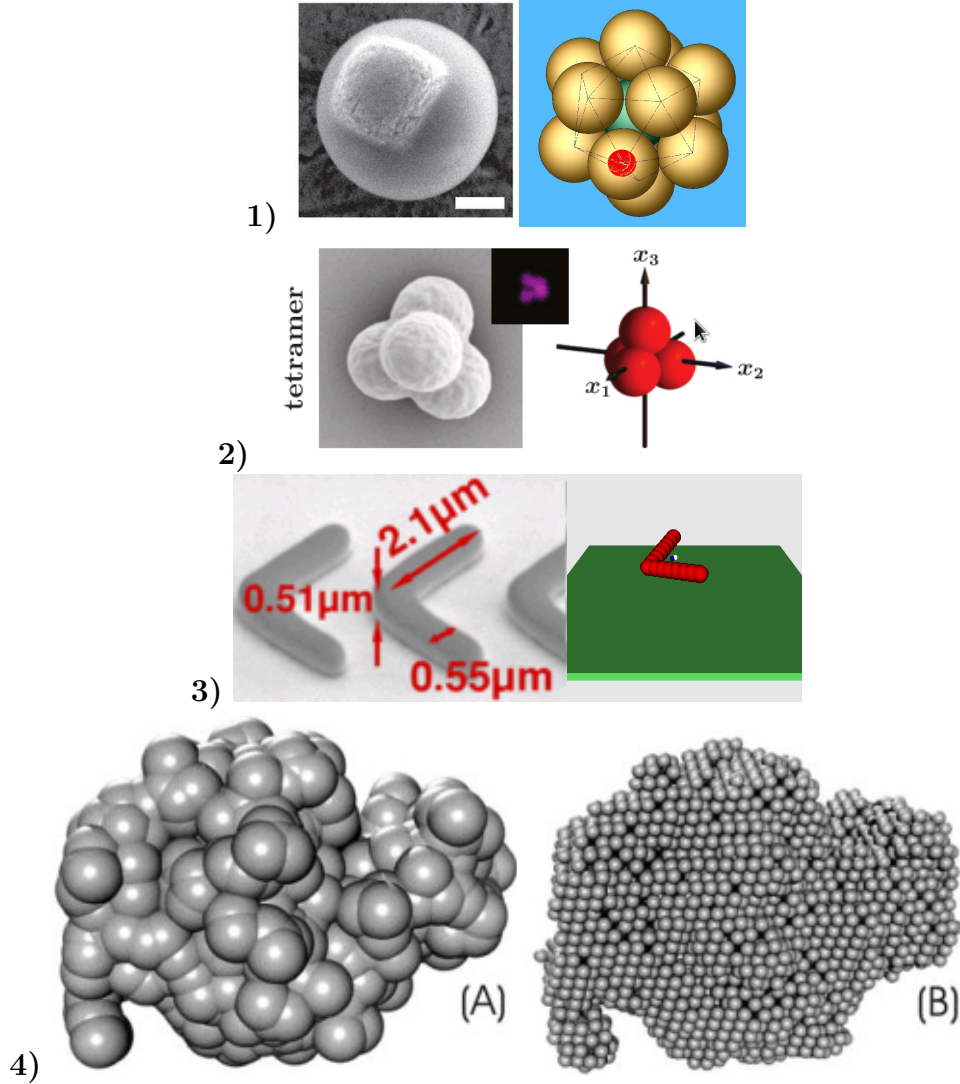
Figure 5.1: Rigid multi-blob or "raspberry" models of systems relevant in soft condensed matter physics, as well as chemical and biochemical engineering. In the top three panels, the left figure shows an experimental image of a colloidal particle manufactured in the lab in prior work by others, while the right panel shows the multiblob model that we use in this work. (Panel 1) A nearly spherical colloidal "surfer" that has a much denser metallic cube of hematite embedded in it, taken from the work of Palacci et al. [123]. In our computer simulations we model this as an icosahedron of rigidly-connected blobs, one of which (indicated by a red dot on the right) models the dense hematite and holds all of the mass of the particle. (Panel 2) A tetramer formed by connecting four colloidal particles using DNA bonding into a tetrahedron, taken from the work of Kraft et al. [157]. The multiblob model has four blobs rigidly placed at the vertices of a tetrahedron. (Panel 3) A right-angle boomerang colloid manufactured using lithography and studied in a slit channel formed by two microscope slips by Chakrabarty et al. [154]. Our 15-blob computational approximation (red spheres) of the boomerang models a dense boomerang sedimented near a single microscope slip (green plane). Additional smaller spheres show the location of the quasi-two-dimensional CoH (yellow) and CoM (blue) for our blob approximation in an unbounded fluid. (Panel 4) A rigid multiblob representation of a lysozyme taken from the work of de la Torre et al. [18], resolved more closely as a "bead" model (left) or more finely as a "shell" model (right).

and the distance of all blob centroids to the wall is greater than $a$. It is possible to generalize the Rotne-Prager-Yamakawa tensor for confined systems [185], thus guaranteeing an SPD $M_B$ even when blobs overlap each other or the wall (but of course their centroids must remain above the wall), but we know of no published explicit formula that accomplishes this even for the case of a single wall. Fortunately, for our model of boomerang-shaped particles we find an SPD mobility far from the wall even though blobs overlap each other.

### 5.3.3 Asymmetric sphere: Icosahedron

In this section we examine the diffusive motion of a rigid sphere whose center of mass is displaced away from the center in the presence of gravity and a bottom wall (no-slip boundary). This models recently manufactured colloidal "surfers" that become active when the particles sediment to a microscope slip [123]; here we consider a passive particle in the absence of chemical driving forces. Diffusive and rotational dynamics of a symmetric patterned (Janus) sphere near a boundary has been studied experimentally by Anthony et al. [156], and can be described well by theoretical approximations for the mobility of a rigid sphere near a planar wall [186]. It is therefore a good example to validate our methods on.

We construct a hydrodynamic model of an asymmetric rigid sphere of radius $a_I$ by rigidly constraining 12 blobs at the vertices of an icosahedron, as done using penalty springs in Ref. [179]. Note that we can also approximate the hydrodynamic response of a single sphere near a wall by using the Rotne-Prager-Blake translational and rotational mobilities computed by Swan and Brady [11], giving a minimally-resolved 1-blob model of a colloidal sphere near a boundary. However, note that the 12-blob icosahedron is a more accurate representation when the sphere comes close to the wall because the near-field hydrodynamics is better resolved; more accurate results can be obtained by using more blobs to construct a spherical shell [184].

Each blob has a hydrodynamics radius of $a = 0.175$ and is located a distance $2.5a$ from the center of the icosahedron, so that the minimal distance between two blobs is about $2.63a$. These parameters are chosen so that the icosahedron is almost rotationally invariant hydrodynamically, and has an effective translational hydrodynamic radius in bulk (i.e., far from the wall) of

$$a_I = \frac{1}{6\pi\eta\left(\text{Tr}\left(M_{uF}\right)/3\right)} \approx 2.86a = 0.5,$$

in some arbitrary units (e.g., microns). A gravitational force of $f = 0.5 = 1.25\,k_BT/a_I$ is applied to one of the 12 blobs, which represents the dense hematite cube embedded in a spherical colloidal surfer [123]. Gravity therefore generates a torque around the center of the sphere and causes the icosahedron to prefer orientations where the dense blob is facing down. A short-ranged repulsive force is added to keep the icosahedron from overlapping the wall, by using a combination of a Yukawa and a hard-sphere-like divergent potential,

$$U_{\text{wall}}(h) = \frac{\epsilon}{h - a_I}\,\exp\left(-\frac{h - a_I}{b}\right), \tag{5.38}$$

where $h$ is the distance from the center of the icosahedron to the wall, $\epsilon = 10k_BT$ is the repulsion strength, and $b = a_I$ to be the Debye length (these values are selected somewhat arbitrarily). This choice of parameters gives the center of the icosahedron a gravitational height (5.35) of $h_g \approx 1.36a_I$. Note that in this example the icosahedron is considered to be a hydrodynamic *approximation* of a physical sphere and therefore the repulsive force acts on the center of the sphere (thus not generating any torque), rather than acting on each of the 12 blobs individually (which would generate some small spurious torque).

#### 5.3.3.1 Equilibrium Distribution

We first investigate the equilbrium distribution $P_{eq}(q, \theta)$, examining the marginal distributions of height $h$ and orientation angle $\phi$, which is the angle between the $z$ axis and the vector connecting the center of the icosahedron to the blob to which we apply the gravitational force. In this simple example, we can compute the marginals of the equilibrium Gibbs-Boltzmann distribution analytically for both $h$ and $\phi$, and they are compared to numerical results in Fig. 5.2. We see that the RFD and Fixman schemes agree with each other and with theory. Due to the nonuniform gravitational forcing on the icosahedron, it prefers orientations with $\phi$ closer to zero, but the thermal fluctuations causes it to explore all values of $\phi$.

#### 5.3.3.2 Mean Square Displacement

To validate how well our scheme captures the dynamics of the system, we examine the mean square displacement of the geometric center of the icosahedron. We compare our results to the mean square displacement of a single
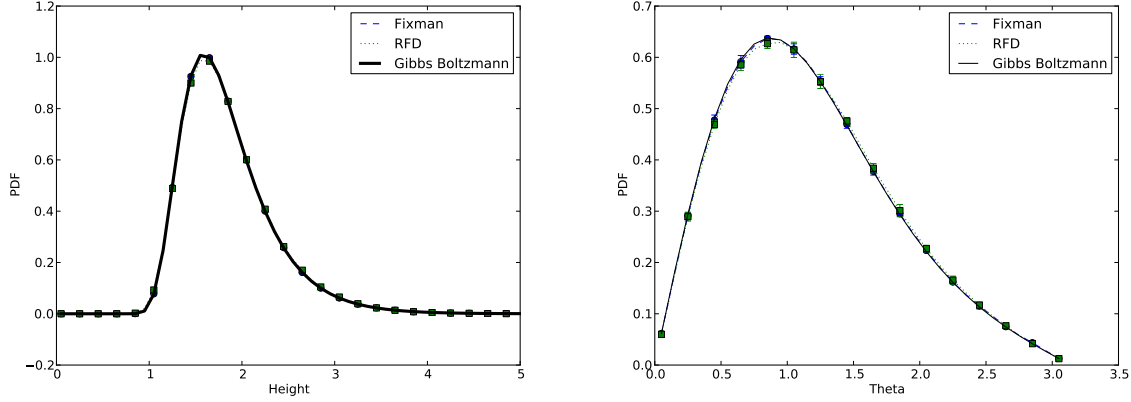
Figure 5.2: Equilibrium distribution for a rigid icosahedron of blobs compared to analytic expressions for the Gibbs-Boltzmann distribution. These figures were created using data from 6 independent runs of $4 \cdot 10^5$ time steps with a small time step size of $\Delta t = 0.04 \, (6\pi\eta a_I^3)/k_B T$ to avoid rejections; no rejections occcured during these simulations. *(Left)* Equilibrium distribution of the height $h$, the distance from the center of the icosahedron to the wall. *(Right)* Equilibrium distribution of the angle $\phi$, where $\phi = 0$ indicates that the heavy blob is at the bottom of the icosahedron, and $\phi = \pi$ indicates that it is at the top. As expected, we see the distribution skewed towards smaller values of $\phi$ due to the gravitational force.

blob with hydrodynamic radius $a = 0.5$. We apply torques and forces to the single blob that are identical to those applied to the icosahedron, and we use the formula from [11] for the translational and rotational mobility of blobs near a wall, excluding the stresslet terms. This tests allows us to both evaluate our temporal integration method, as well as to examine how well the 12-bead model approximates a single spherical particle. The results are shown in figure 5.3, and we see that the dynamics of the icosahedron is very similar to that of a single blob. Note that the icosahedron actually has a mobility that is closer to that of a real sphere than the single blob, but for this simulation the gravitational height is sufficiently large so that the icosahedron is far enough from the wall that this distinction is barely visible in Fig. 5.3.

Note that for a sphere the mobility does not depend on the orientation of the sphere. Furthermore, by symmetry, the gravitational force (perpendicular to the wall) cannot induce rotation of the sphere, and by symmetry, a torque cannot introduce vertical displacements. Because of these special symmetries it can be shown that the parallel MSD will be strictly linear and therefore (5.33) is an exact prediction for the effective quasi two-dimensional diffusion coefficient; this has in fact been confirmed experimentally with relatively good accuracy for spheres whose center of mass is very close to their geometric center [156]. In the left panel of Fig. 5.3 we show the straight-line theoretical prediction for the parallel MSD and find very good agreement with the numerical results.

### 5.3.4  Colloidal tetramer: Tetrahedron

In this section we study a tetramer formed by rigidly connecting four colloidal spheres at the vertices of a tetrahedron [157, 155], diffusing near a single no slip boundary. The tetrahedron is discretized in a minimally-resolved way using 4 blobs, one at each vertex of a regular tetrahedron. In some arbitrary units, each blob is a distance $d = 2$ away from all of the others and has a hydrodynamic radius of $a = 0.5$; this somewhat arbitrary choice makes the tetrahedron hydrodynamically quite different from a sphere.

The tetrahedron is allowed to translate and rotate freely in the presence of a no slip boundary at $z = 0$. To avoid symmetries and make the test more general, we assume each of the four spheres to have a different density; the gravitational forces on the vertices are set to $f_1 = 0.15 k_B T/a$, $f_2 = 0.1 k_B T/a$, $f_3 = 0.3 k_B T/a$ and $f_4 = 0.05 k_B T/a$. To prevent the tetrahedron from passing through the wall, we also include a repulsive potential (5.38) between each of the blobs and the wall, where $\epsilon = 10 k_B T$ and $b = 0.5a$. The total force and torque on the rigid tetramer is the sum of the forces and torques on the individual blobs. This choice of parameters gives the center of the tetrahedron a gravitational height (5.35) of $h_g \approx 2.47a$.

For comparison and validation, we also construct an approximation to the freely-moving rigid tetrahedron using four blobs connected by stiff springs, and then employ the FIB method described in Chapter 4 to simulate the diffusive motion; the same geometry and forces are used in both simulations. The FIB simulation was performed
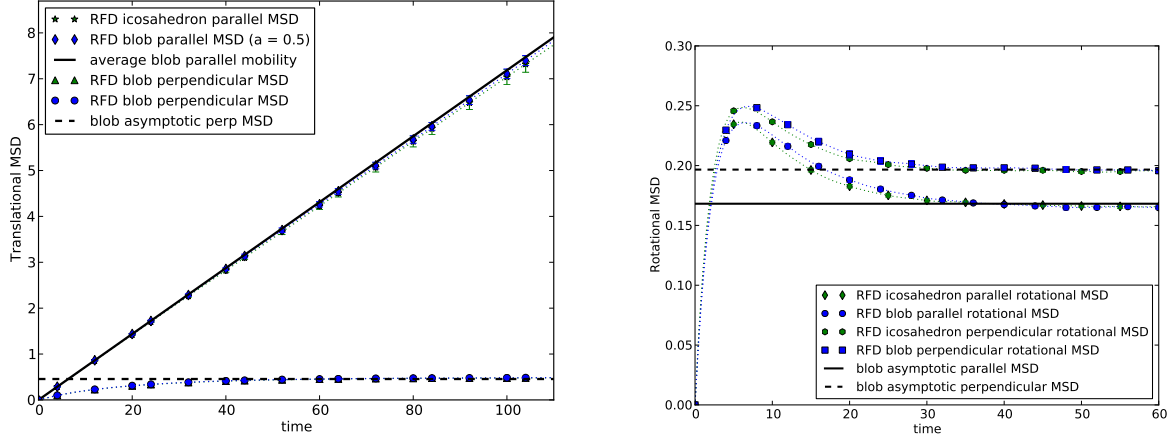
103

Figure 5.3: Mean square displacements for a sphere with nonuniform mass distribution diffusing near a planar boundary. Symbols show numerical results obtained by processing long equilibrium trajectories, while lines show theoretical predictions. These figures were generated using data from 16 independent trajectories of length $5 \cdot 10^5$ time steps, using a small time step size of $\Delta t = 0.004 \, (6\pi\eta a_I^3)/k_B T$ to eliminate rejections. *(Left)* Parallel $(D_\parallel(\tau))$ and perpendicular $(D_\perp(\tau))$ translational MSD of a single blob and a rigid icosahedron of blobs. Solid black lines show the theoretical parallel translational MSD for a single blob (solid line) predicted by (5.33), while the dashed line shows the asymptotic perpendicular translational MSD (5.34). As expected, the icosahedron behaves similarly to a blob with equal effective hydrodynamic radius. *(Right)* Parallel $(x - x$ and $y - y$, identical by symmetry) as well as perpendicular $(z - z)$ components of the rotational mean square displacement (5.29). The dashed line shows the asymptotic rotational MSD (5.36). We see that the rotational dynamics of the blob and the icosahedron are also in good agreement.

in a domain of $64 \times 64 \times 64$ cells of width $\Delta x = 0.796a$ using the 4-point Peskin kernel, which ensures that the effective hydrodynamic radius of the blobs is $a$. The boundaries on the top and bottom of the domain are both no-slip walls, which differs from the domain for the rigid body simulations, but since the center of the tetrahedron almost never goes past 20% of the channel width (see figure 5.4), the effect of the top wall is relatively minor. The spring stiffness was set to $k = 200 \, k_B T/a$ to keep the deformations of the tetrahedron small; this imposes a stringent limit on time step size. We are grateful to Florencio Balboa Usabiaga for running these FIB simulations using the IBAMR software framework [86].

### 5.3.4.1 Equilibrium Distribution

In this section we examine the equilibrium distribution for the colloidal tetramer. We use a Monte Carlo method to generate the marginal Gibbs-Boltzmann distribution for the height of the geometric center of the tetrahedron, and compare to our numerical results. We see in figure 5.4 that the Fixman (5.23) and RFD schemes (5.25) are in good agreement with the Gibbs-Boltzmann distribution. The Euler-Maruyama scheme (5.21, with the obvious additions to include translation), however, neglects parts of the stochastic drift and generates an equilibrium distribution which has clear errors that do not vanish as the time step is refined (not shown).

### 5.3.4.2 Mean Square Displacement

In this section, we examine the translational mean square displacement of the tetrahedron. In the left panel of Fig. 5.5 we examine the effect of the choice of tracking point on the parallel mean square displacement by comparing $D_\parallel(\tau)$ when tracking the geometric center of the tetrahedron, versus tracking one of the four vertices. In both cases (5.28) gives the initial slope of the MSD as it must, and these slopes are clearly different. Since at long times the slopes of the parallel MSD is independent of the choice of tracking point, the MSD cannot be linear at all times for both choices of tracking point. Indeed, the results in Fig. 5.5 show that the parallel MSD is only linear to within statistical and numerical truncation errors when the geometric center is tracked. By contrast, the rotational MSD is insensitive to the choice of tracking point, as seen in the right panel of Fig. 5.5.
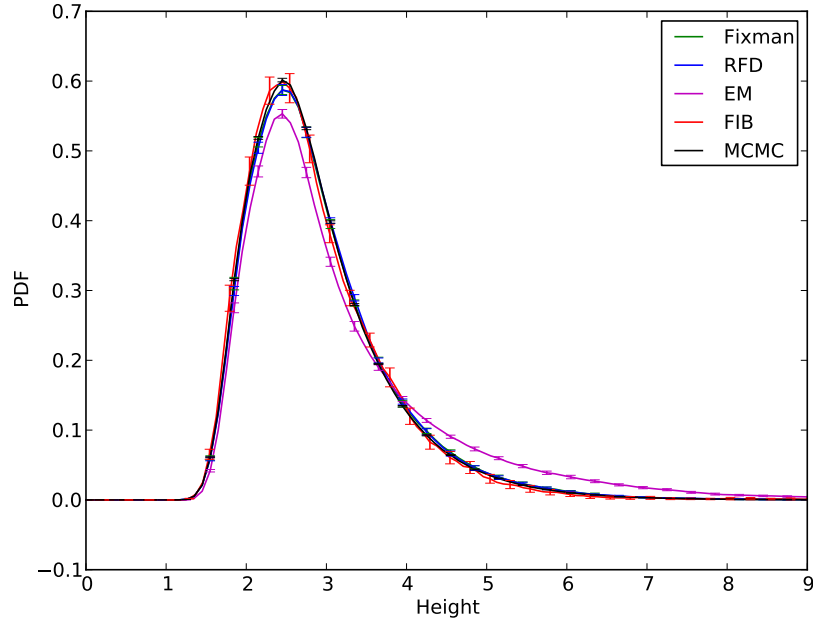
Figure 5.4: Equilibrium distribution for the height of the geometric center of the tetrahedron. The FIB method and the integrators from Sections 5.2.2 and 5.2.3 agree with the Gibbs-Boltzmann distribution generated using Monte Carlo sampling. The EM scheme (5.21) is shown as well to demonstrate that neglecting the stochastic drift term yields an incorrect equilibrium distribution. This plot is based on 16 runs for each of the RFD, Fixman, and EM schemes, with $300k$ time steps for each run, and a small time step size of $\Delta t \approx 0.0653 \left(6\pi\eta a^3/k_BT\right)$; no rejections were needed for this small time step in any of the runs.
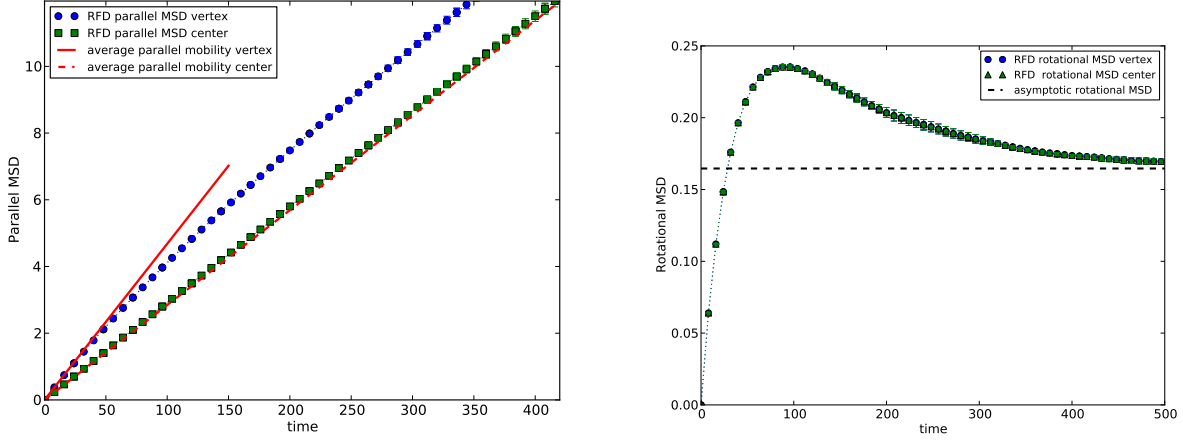
Figure 5.5: Mean square displacement for a colloidal tetramer sedimented near a bottom wall. The data for both figures is generated from 4 independent runs of $300k$ time steps with a time step of $\Delta t \approx 0.136 \left(6\pi\eta a^3/k_B T\right)$. The MSDs for each tracking point are calculated from the same trajectories. *(Left)* Comparison of parallel translational MSD $D_\parallel(\tau)$ when tracking the geometric center (green circles), versus when tracking the fourth vertex (blue diamonds). We see that at short times the slope agrees with (5.28), shown as a red dashed line for the geometric center, and as a red solid line for the vertex. *(Right)* Comparison of the $x - x$ component of the rotational mean square displacement using the two choices of tracking point. The asymptotic rotational MSD predicted by (5.36) is shown as a dashed line.

We note that far from the wall, torques applied about the center of the tetrahedron generate no translation, indicating that in the absence of confinement the geometric center is both the CoM and the exact three dimensional CoH (which does not exist for general rigid bodies). In the presence of the boundary, this is not guaranteed to be the case, but we nonetheless observe in Fig. 5.5 that the average parallel mobility evaluated using the center of the tetrahedron as an origin gives a good approximation to the long time quasi two-dimensional diffusion coefficient. This is perhaps not surprising due to the high symmetry of a tetrahedron, as the geometric center is the "obvious" point to track. Note, however, that in many practical situations only part of diffusing particle may be tracked, for example, a unit of a protein may be labeled by a fluorescent dye. In such cases, one must be very careful in interpreting the results for translational diffusion as if the particle were spherical and the center of the sphere were tracked. Furthermore, as we illustrate in the next section, there are many particle shapes for which there is no obvious geometric center and it is then not trivial to determine what the best point to track is, even if one can track an arbitrary point on the body.

In Figure 5.6 we compare results for the MSD obtained using the overdamped rigid-body integrators from Section 5.2 to results obtained using the FIB method and stiff springs. We examine the mean square translational displacement parallel and perpendicular to the wall, as well as the rotational MSD, and find that the behavior of the tetrahedron is the same for both the stiff and rigid simulations. However, due to the presence of the stiff springs, using the FIB method to simulate a rigid body requires a time step size that is much shorter; the FIB simulations used a time step size of $\Delta t \approx 0.004 \left(6\pi\eta a^3/k_B T\right)$, while the rigid body simulation used a time step size 32 times larger, $\Delta t \approx 0.136 \left(6\pi\eta a^3/k_B T\right)$. Due to the small time step size required for the tetrahedron constructed using rigid springs, and the high cost of solving a Stokes problem each time step, it is computationally impractical to study the long time diffusion coefficient using this approach, and we see that at long times the MSD calculated from FIB simulations is statistically inaccurate. The time step size for the rigid-body method could in principle be even larger and still resolve the dynamics of the body, but it is limited by the stiff potential used to repel the particle from the wall; we keep $\Delta t$ sufficiently small to strictly control the number of rejections of unphysical states where a blob gets too close to or passes through the wall. In Section 5.4 we address some ideas that may allow for the use of larger time step sizes even in the presence of these challenges.
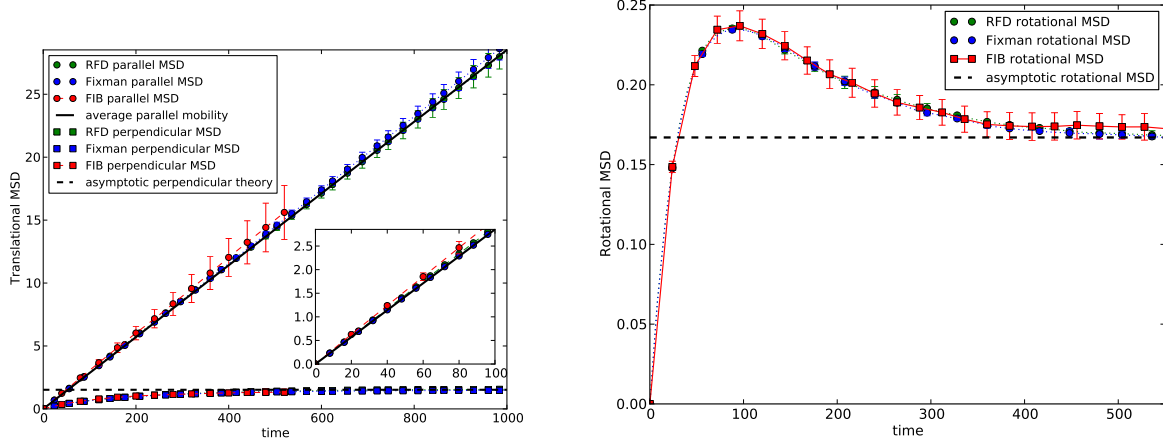
106

Figure 5.6: Comparison of the mean square displacement for a colloidal tetramer sedimented near a bottom wall, obtained by treating the body as rigid using the RFD and Fixman methods developed here, versus keeping it nearly rigid with stiff springs and using the FIB method. For the rigid-body simulations we used 4 independent runs of $300k$ timesteps each for both the Fixman and RFD schemes, and the highest rejection rate was $2.33 \times 10^{-5}$ (a total of 7 rejections). *(Left)* Parallel translational MSD when tracking the geometric center of the tetrahedron. The inset focuses on the short time diffusion, and shows a slight hydrodynamic difference between the rigid and semi-rigid models that is due to the different methods used to handle the hydrodynamics, as well as the slight flexibility of the tetrahedron in the FIB simulations. *(Right)* The parallel $((x - x)$ or $(y - y))$ component of the rotational MSD (5.15).

## 5.3.5 Colloidal Boomerang

The authors of reference [154] perform a detailed experimental study of the quasi-two-dimensional translational and rotational diffusion of lithographed symmetric right-angle boomerang colloids (see panel 3 in Fig. 5.1) confined between two microscope slips. Some theoretical analysis is also performed assuming that the overdamped dynamics of the particles is effectively two-dimensional. Subsequently this work was extended to asymmetric (L-shaped) right-angle boomerangs [159]. Of course, the actual dynamics of the particles is three dimensional, and a complete theoretical or numerical analysis of the diffusive dynamics requires the complete formalism developed in this Chapter.

In this section we examine a single symmetric boomerang near a single planar boundary (bottom wall) in the presence of gravity. We choose to study a single boundary rather than a slit channel as done in the experiments in order to simplify the hydrodynamic calculations of mobilities [11]; in principle one can construct tabulated approximations of blob mobilities in a slit channel but this is quite complex and expensive [10]. While we cannot make direct comparisons with the experimental values reported in Ref. [154], we can still address the fundamental questions about differences between fully three-dimensional and quasi two-dimensional diffusion. Specifically, by enlarging the gravitational force we apply to the boomerang (i.e., increasing its effective density mismatch with the solvent), we can cause the motion to be more or less confined to a two dimensional plane parallel to the bottom wall. In this section we use microns as the unit of length, seconds as the unit of time, and milligrams as the unit of mass.

For hydrodynamic calculations, we construct a blob model of a boomerang and try to match the physical parameters in the experiments [154] as close as possible. Our model of the boomerang particle is constructed by rigidly connecting 15 blobs, one at the cross point, and 7 for each arm, as illustrated in panel 3 in Fig. 5.1. Note that in this minimally-resolved blob model the cross-section of the arms of the boomerang is cylindrical rather than square, as would be more realistic for modeling the lithographed particles. Prior investigations in the context of the immersed boundary method [183], which we have also confirmed independently by using the Rotne-Prager tensor as the pairwise blob mobility, have shown that to construct a good hydrodynamic approximation of a rigid cylinder of radius $r$ using blobs, one should set the effective hydrodynamic radius of each blob to $a \approx \sqrt{3/2}\, r$, and place the blobs centers on a line at a distance of around $a$ (the precise value does not matter much). Following these recommendations, we set the blob radius to $a = 0.325$, which gives an effective cylinder radius of 0.265, and the blobs are spaced a distance 0.3 apart.

For a free boomerang far away from boundaries, there is a unique CoM that, due to symmetry, must lie on the
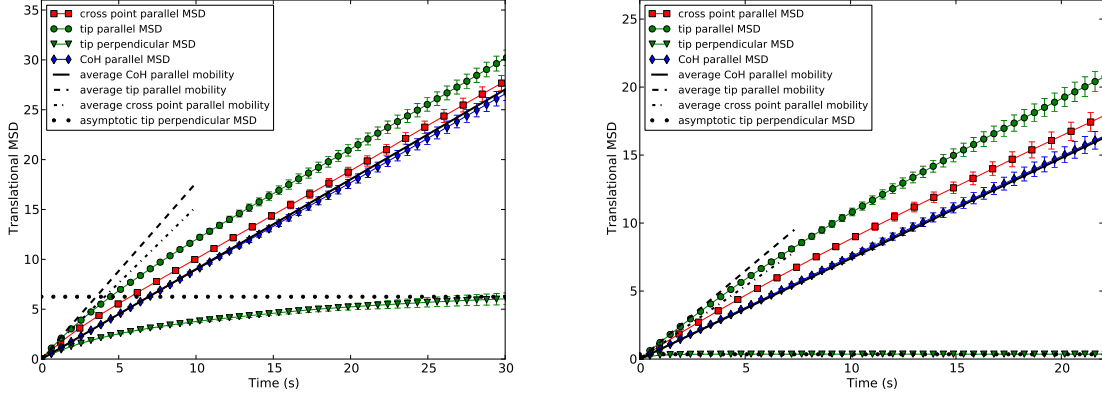
107

Figure 5.7: Translational MSD of the boomerang MSD for $g = 1$ (left panel) and $g = 20$ (right panel). We see that by calculating the MSD using the CoH, we get a short and long time diffusion coefficient which agree, allowing us to estimate the long-time quasi two dimensional diffusion coefficient of the boomerang using (5.33). This is not the case when tracking the cross point or the tip of one of the arms.

the line that bisects the boomerang arms. Also, there must be a unique point on the bisector for which there is no coupling between torque applied out of the plane of the boomerang and the translational motion in the plane of the boomerang. We can consider this point as the CoH for quasi-two-dimensional diffusion [154], although, as already explained, this point is not a CoH in the strict sense for three-dimensional diffusion. The locations of the bulk CoM and the bulk quasi-two-dimensional CoH, which we shall henceforth imprecisely refer to as just CoM and CoH, are shown in panel 3 of Fig. 5.1. For our blob model, we compute the CoH to be is about 1.075 microns away from the cross point (center of the intersection blob), and the CoM is 0.96 microns from the cross point. These numbers compare favorably to the experimental findings in [154], where the CoH is estimated to be a distance of 1.16 microns from the cross point. The difference between the CoH and CoM is too small for this specific particle shape for us to be able to tell the difference to within statistical errors; in future work we will consider asymmetric boomerangs, for which the difference may be more significant.

The total gravitational force applied to the body is $0.18 \times g$ $(k_BT/a)$ where $g$ is a parameter that we vary. This number is chosen so that $g = 1$ gives a rough approximation of the gravitational binding experienced by the actual lithographed particles, which have a density of $1.2\,\mathrm{g/cm^3}$. We split the gravitational force evenly among the 15 blobs. Each blob is also repelled from the wall using the potential (5.38) with screening length $b = 0.5a$ and strength $\epsilon = 7.5k_BT$. The gravitational height (5.35) for one of the two (equivalent) tips of the boomerang are shown in Table 5.1 for several values of $g$. Since the tips are the points that are most likely to venture further from the wall, these values give an indication of how close to two-dimensional the dynamics of the boomerang is.

In Fig. 5.7 we show the parallel and perpendicular translational MSDs of the boomerang for a weak $(g = 1)$ and a strong gravitational sedimentation $(g = 20)$, where strong here means that the gravity is sufficiently strong to keep the boomerang essentially flat against the surface. For the parallel MSD, we show results based on three different choices of the tracking point: 1) the CoH, 2) the center of the blob at the tip of one of the arms, and 3) the center of the blob at the cross point where the arms meet. For an unconfined boomerang, we expect that the parallel MSD measured using the CoM will be strictly linear in time. We also expect that for the boomerang confined to a plane by strong gravity and exhibiting quasi two dimensional diffusion, the MSD will be linear in time when tracking the CoH [154, 159]. However, in our simulations, we find that due to the close proximity of the CoH and the CoM, the MSD is identical to within statistical error independent of which of these two points was tracked. For clarity, we only include the MSD calculated from the CoH in our results, with the understanding that the CoM is indistinguishable at this level of accuracy. We see from the figure that by choosing the CoH as the tracking point, we obtain an MSD that is linear over all times up to statistical accuracy for both gravities. This means that we can get an accurate estimate of the long-time diffusion coefficient $\chi_{2D}$ by using equation (5.33) over a broad range of gravities; note however that this conclusion should be checked for other particle shapes such as asymmetric boomerangs before drawing broad conclusions.

In Table 5.1 we show the estimated long-time parallel diffusion coefficient $\chi_{2D}$ obtained from (5.33) for different strengths of the gravitational sedimentation. We find that, surprisingly, the presence of the boundary does not strongly reduce the effective short-time diffusion coefficient compared to bulk, except at the largest gravity. The

| $g$ | $\chi_{2D}(\mu m^2/s)$ | $\chi_{2D}/\chi_{3D}$ | $\chi_\theta\left(\mathrm{rad}^2/s\right)$ | $h_g(\mu m)$ |
|-----|------------------------|------------------------|---------------------------------------------|---------------|
| 1   | 0.226                  | 0.834                  | 2.51                                        | 2.5           |
| 10  | 0.194                  | 0.716                  | 1.37                                        | 0.855         |
| 20  | 0.185                  | 0.683                  | 0.44                                        | 0.592         |

Table 5.1: Long-time quasi two-dimensional diffusion coefficient $\chi_{2D}$ for the boomerang colloid at $g = 1, 10,$ and 20 estimated using (5.33) and tracking the CoH. The diffusion coefficient for a free boomerang in an unbounded fluid $\chi_{3D}$ is computed using (5.32). The rotational diffusion coefficient $\chi_\theta$ is calculated using (5.40). Effective gravitational heights (5.35) are also calculated for the tip of the boomerang, giving an indication of how flat the boomerang is against the wall.
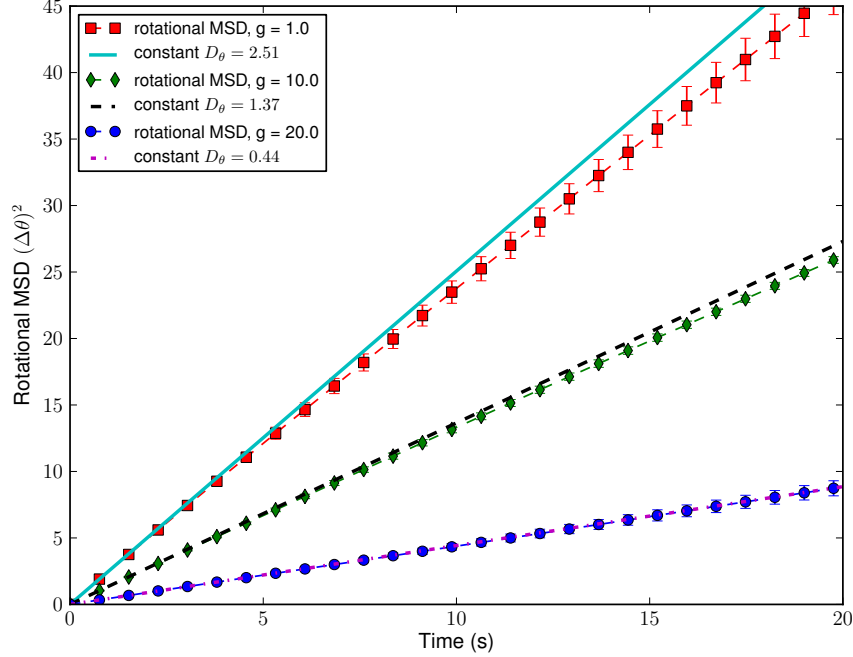


Figure 5.8: Planar rotational mean squared displacement (5.39) as a function of time for three different strengths of the gravitational confinement.

value of this quasi two dimensional diffusion coefficient is measured experimentally in Ref. [154] for the case of a boomerang particle in a microscope slip at a distance of $2\mu m$, and a value of $\chi_{2D}^{\mathrm{exp}} = 0.054\,\mu m^2/s$ is reported. This is lower than the values calculated here, which we expect is largely due to the absence of the top wall in our simulations, which is likely to significantly increase the drag on the boomerang. Another source of error is that we used a minimally-resolved blob model of the boomerang, which may not be sufficiently accurate when the boomerang spends a large fraction of time close to the wall. In order to keep the blobs away from the wall, here we added a Yukawa-like repulsion with a screening length that is probably unphysically large.

To estimate the two-dimensional rotational diffusion coefficient $\chi_\theta$, measured experimentally in Ref. [154], we project the bisector of the boomerang arms into the $x-y$ plane, and define $\theta(t)$ to be the angle of rotation around the $z$ axis between this projected vector at time $t$ and the initial projected bisector. We count each full counterclockwise rotation as an addition of $2\pi$, and similarly we subtract $2\pi$ for each full clockwise rotation, allowing the value of $\theta$ to take values in all of $\mathbb{R}$. Truly two-dimensional rotational diffusion corresponds to $\theta(t)$ being standard Brownian motion. We define a planar rotational mean square displacement from increments of the angle $\theta$,

$$D_\theta\left(\tau\right) = \left\langle\left(\theta(t+\tau) - \theta(t)\right)^2\right\rangle. \tag{5.39}$$

In Fig. 5.8 we show numerical results for $D_\theta\left(\tau\right)$. We see that for $g = 20$, when the boomerang is most flat, the

quantity $D_\theta$ is linear in time for all times to within statistical error bars, while for lower gravities we see some deviations from linearity, as expected since the definition of $\theta$ assumes the diffusion is essentially two-dimensional. We estimate the short-time planar rotation coefficient from our discrete trajectories using

$$\chi_\theta = D_\theta(\Delta t)/\Delta t, \tag{5.40}$$

and tabulate the computed values in Table 5.1. We see that $\chi_\theta$ is much larger for lower gravities, both because the boomerang diffuses more rapidly far from the wall, and also because in low gravity, the boomerang is not confined to the $x - y$ plane, and hence small changes in orientation can lead to large changes in our calculated two-dimensional angular displacement. The rotational diffusion coefficient measured experimentally in Ref. [154] for a boomerang confined between two microscope glass slips is $D_\theta = 0.044\,\mathrm{rad}^2/s$, which is much smaller than our result for $g = 20$, in large part to the absence of drag from the top wall. Additionally, without this second boundary, our simulated boomerang is able to rotate out of the $x - y$ plane more easily, reaching configurations where a small change in orientation can lead to a large change in $\theta(t)$.

## 5.4 Conclusion

In this chapter, we introduced methods for simulating the diffusive motion of rigid bodies immersed in a viscous fluid. We parameterized the orientation of the bodies using normalized quaternions, which are numerically robust, space efficient, and easy to accumulate. As far as we know, a quaternion representation has not been used to simulate the overdamped dynamics of rigid particles before. We wrote down a system of overdamped Langevin equations for the time evolution of this representation, verifying that the motion preserves the constraint on the quaternion and is time reversible with the correct Gibbs-Boltzmann distribution. We then introduced two schemes for integrating these equations, one based on the Fixman midpoint method and the other based on a random finite difference approach, paying special attention to handling the stochastic drift term in a computationally efficient way.

Several examples of rigid colloids diffusing near a no-slip boundary were studied using these schemes, and in particular we investigated the effect of the choice of tracking point on the translational mean square displacement Specifically, we examined the short-time as well as the long-time average quasi-two-dimensional diffusion coefficient of a rigid particle sedimented near a bottom wall due to gravity. For several particle shapes we explained how to choose the tracking point in a way that allows us to estimate the long-time diffusion coefficient parallel to the boundary using a Monte Carlo method to high accuracy. However, in general such a point does not always exist, and numerical techniques, such as the ones we introduced here, are necessary to study diffusion on longer timescales.

## 5.5 Addendum: Rotating a body

In this section, we derive eq. (5.7). We proceed by first writing the Rotate procedure using its definition, and then expand the trigonometric functions to second order. Letting $\boldsymbol{\theta} = \{s, \boldsymbol{p}\}$, and $\|\boldsymbol{\omega}\| = \omega$, we have

$$
\begin{aligned}
\mathrm{Rotate}(\boldsymbol{\theta}, \boldsymbol{\omega}\Delta t) &= \begin{bmatrix} s\cos\left(\frac{\omega\Delta t}{2}\right) - \boldsymbol{p}\cdot\sin\left(\frac{\omega\Delta t}{2}\right)\boldsymbol{\omega}/\omega \\ s\sin\left(\frac{\omega\Delta t}{2}\right)\boldsymbol{\omega}/\omega + \cos\left(\frac{\omega\Delta t}{2}\right)\boldsymbol{p} + \sin\left(\frac{\omega\Delta t}{2}\right)\boldsymbol{\omega}\times\boldsymbol{p}/\omega \end{bmatrix} \\
&= \begin{bmatrix} s(1 - \frac{\omega^2\Delta t^2}{8}) - \boldsymbol{p}\cdot\boldsymbol{\omega}\frac{\Delta t}{2} \\ s\boldsymbol{\omega}\frac{\Delta t}{2} + \left(1 - \frac{\omega^2\Delta t^2}{8}\right)\boldsymbol{p} + \boldsymbol{\omega}\times\boldsymbol{p}\frac{\Delta t}{2} \end{bmatrix} + O\left(\Delta t^3\right) \\
&= \begin{bmatrix} s - \boldsymbol{p}\cdot\boldsymbol{\omega}\frac{\Delta t}{2} \\ \boldsymbol{p} + s\boldsymbol{\omega}\frac{\Delta t}{2} - \boldsymbol{P}\boldsymbol{\omega}\frac{\Delta t}{2} \end{bmatrix} - \frac{\omega^2\Delta t^2}{8}\begin{bmatrix} s \\ \boldsymbol{p} \end{bmatrix} + O\left(\Delta t^3\right) \\
&= \boldsymbol{\theta} + \boldsymbol{\Psi}\boldsymbol{\omega}\Delta t - \frac{(\boldsymbol{\omega}\cdot\boldsymbol{\omega})\Delta t^2}{8}\boldsymbol{\theta} + O\left(\Delta t^3\right).
\end{aligned}
$$

## 5.6 Addendum: Torques

In simulating systems of rigid bodies with orientation, we will naturally want to consider potential energies that depend on this orientation. In this section, we consider the case when the torque is generated by a conservative potential $U_\varphi(\boldsymbol{\varphi})$, so that $\boldsymbol{\tau} = -\partial U_\varphi/\partial\boldsymbol{\varphi}$. Here $\boldsymbol{\varphi}$ represents the oriented angle associated with orientation. For the purposes of this discussion, we neglect the dependence of potential on location, since this will have no bearing

on the torque. Consider extending the energy to depend on a quaternion $U(\boldsymbol{\theta})$ such that when $\|\boldsymbol{\theta}\| = 1$, we have $U_{\boldsymbol{\varphi}}(\boldsymbol{\varphi}) = U(\boldsymbol{\theta_\varphi})$. We want to be able to write the torque, $\boldsymbol{\tau}$ in terms of $U(\boldsymbol{\theta})$ without needing to convert first to $\boldsymbol{\varphi}$.

Only quaternions with unit norm represent a viable orientation, and therefore the value of the potential off of this constraint has no physical meaning and should not affect the torque in any way. The projected gradient of $U(\boldsymbol{\theta})$ on the unit 4-sphere is

$$\frac{\tilde{\partial} U}{\partial \boldsymbol{\theta}} = \frac{\partial U}{\partial \boldsymbol{\theta}} - \left(\boldsymbol{\theta} \cdot \frac{\partial U}{\partial \boldsymbol{\theta}}\right)\boldsymbol{\theta} = \boldsymbol{P}_\theta \frac{\partial U}{\partial \boldsymbol{\theta}},$$

where $\boldsymbol{P}_\theta = \boldsymbol{I} - \boldsymbol{\theta}\boldsymbol{\theta}^T$ . In section 5.1.1, we saw that

$$d\boldsymbol{\theta} = \frac{1}{2}\left[\begin{array}{c} -\boldsymbol{p}^T \\ s\boldsymbol{I} + \boldsymbol{P} \end{array}\right] d\boldsymbol{\varphi} = \frac{1}{2}\left[\begin{array}{c} -\boldsymbol{p} \cdot d\boldsymbol{\varphi} \\ s\, d\boldsymbol{\varphi} + \boldsymbol{p} \times d\boldsymbol{\varphi} \end{array}\right],$$

so that the change in potential energy due to any small rotation $d\boldsymbol{\varphi}$ is

$$dU = -\boldsymbol{\tau} \cdot d\boldsymbol{\varphi} = \frac{\tilde{\partial} U}{\partial \boldsymbol{\theta}} \cdot d\boldsymbol{\theta} = -\frac{1}{2}\left[\frac{\tilde{\partial} U}{\partial s}\boldsymbol{p} \cdot d\boldsymbol{\varphi} - \frac{\tilde{\partial} U}{\partial \boldsymbol{p}} \cdot (s\, d\boldsymbol{\varphi} + \boldsymbol{p} \times d\boldsymbol{\varphi})\right].$$

Using the known formula

$$\boldsymbol{a} \cdot (\boldsymbol{b} \times \boldsymbol{c}) = \boldsymbol{c} \cdot (\boldsymbol{a} \times \boldsymbol{b}),$$

we can rewrite this as

$$\boldsymbol{\tau} \cdot d\boldsymbol{\varphi} = \frac{1}{2}\left[\frac{\tilde{\partial} U}{\partial s}\boldsymbol{p} - (s\boldsymbol{I} - \boldsymbol{P})\frac{\tilde{\partial} U}{\partial \boldsymbol{p}}\right] \cdot d\boldsymbol{\varphi},$$

leading to the identification of torque as

$$\boldsymbol{\tau} = \frac{1}{2}\left[\frac{\tilde{\partial} U}{\partial s}\boldsymbol{p} - (s\boldsymbol{I} - \boldsymbol{P})\frac{\tilde{\partial} U}{\partial \boldsymbol{p}}\right] = -\boldsymbol{\Psi}^T \frac{\tilde{\partial} U}{\partial \boldsymbol{\theta}} = -\boldsymbol{\Psi}^T \boldsymbol{P}_\theta \frac{\partial U}{\partial \boldsymbol{\theta}} = -\boldsymbol{\Psi}^T \frac{\partial U}{\partial \boldsymbol{\theta}}. \tag{5.41}$$

## 5.7 Addendum:Stochastic Drift for Rigid Bodies

Here we show that the temporal integrators introduced in Section 5.2 generate the correct stochastic drift terms, more precisely, they are first-order weakly accurate integrators. We will find it convenient in the following calculations to consider the drift term separated into multiple pieces as done in eq. (??). We first derive eq. (5.10), which we use in the following subsections. We start with the form of the drift written in eq. (5.9), letting $\boldsymbol{M} = \boldsymbol{M}_{\boldsymbol{\omega}\boldsymbol{\tau}}$ and using indicial notation with Einstein's implied summation convention for clarity,

$$\begin{aligned}
\left[\partial_{\boldsymbol{\theta}} \cdot \widetilde{\boldsymbol{M}}\right]_i = \partial_j \left(\widetilde{M}_{ij}\right) &= \partial_j \left(\Psi_{ik} M_{kl} \Psi_{jl}\right) \\
&= (\partial_j \Psi_{ik}) M_{kl} \Psi_{jl} + \Psi_{ik} (\partial_j M_{kl}) \Psi_{jl} + \Psi_{ik} M_{kl} (\partial_j \Psi_{jl}) = \\
&= (\partial_j \Psi_{ik}) M_{kl} \Psi_{jl} + \Psi_{ik} (\partial_j M_{kl}) \Psi_{jl} \\
&= -\frac{1}{4} M_{kk} \theta_i + \Psi_{ik} (\partial_j M_{kl}) \Psi_{jl}
\end{aligned}$$

where we used (5.6) to go from the second to the third line. To go from the third to the fourth line we used the relationship $(\partial_j \Psi_{ik})\Psi_{jl} = -\delta_{kl}\theta_i/4$, which can be shown by a straightforward calculation. In matrix notation, we can write

$$\partial_{\boldsymbol{\theta}} \cdot \widetilde{\boldsymbol{M}} = \boldsymbol{\Psi} \boldsymbol{M} \boldsymbol{\Psi}^T - \frac{1}{4}\text{Tr}(\boldsymbol{M})\boldsymbol{\theta}, \tag{5.42}$$

which we use in proving first-order weak accuracy of our numerical schemes next.

We also derive a similar relation for the drift including translational degrees of freedom, and given in eq. (5.24). We use Einstein's implicit summation notation, where $i, n, m$, and $p$ represent any component of $\boldsymbol{x}$, $j, k$, and $l$ represent indices that range over components of location $\boldsymbol{q}$, and $s, t$, and $u$ range over components of orientation $\boldsymbol{\theta}$. For simplicity of notation, we use superscripts to denote which block of the grand mobility matrix an entry comes from, for example the i,jth entry of $\boldsymbol{M}_{\boldsymbol{\omega}\boldsymbol{\tau}}$ is denoted $M_{ij}^{\boldsymbol{\omega}\boldsymbol{\tau}}$ . We now consider the drift, deriving eq. (5.24) as follows,

$$\left\{\partial_{\boldsymbol{x}} \cdot \left(\boldsymbol{\Xi N \Xi}^T\right)\right\}_i = \left\{\partial_{\boldsymbol{x}} \cdot \left[\begin{array}{cc} \boldsymbol{M_{vF}} & \boldsymbol{M_{v\tau}\Psi}^T \\ \boldsymbol{\Psi M_{\omega F}} & \boldsymbol{\Psi M_{\omega\tau}\Psi}^T \end{array}\right]\right\}_i = \left[\begin{array}{c} \left(\partial_j M_{ij}^{\boldsymbol{vF}}\right) + \partial_u \left(M_{it}^{\boldsymbol{v\tau}}\Psi_{tu}\right) \\ \partial_j \left(\Psi_{is} M_{sj}^{\boldsymbol{\omega F}}\right) + \partial_s \left(\Psi_{it} M_{tu}^{\boldsymbol{\omega\tau}}\Psi_{su}\right) \end{array}\right]$$

$$= \left[\begin{array}{c} \left(\partial_j M_{ij}^{\boldsymbol{vF}}\right) + \left(\partial_u M_{it}^{\boldsymbol{v\tau}}\right)\Psi_{tu} \\ \Psi_{is}\left(\partial_j M_{sj}^{\boldsymbol{\omega F}}\right) + \left(\partial_s \Psi_{it}\right)M_{tu}^{\boldsymbol{\omega\tau}}\Psi_{su} + \Psi_{it}\left(\partial_s M_{tu}^{\boldsymbol{\omega\tau}}\right)\Psi_{su} \end{array}\right] \tag{5.43}$$

$$= \Xi_{im}\left(\partial_n N_{mp}\right)\Xi_{np} + \left[\begin{array}{c} 0 \\ \left(\partial_s \Psi_{it}\right)\left(M_{tu}^{\boldsymbol{\omega\tau}}\right)\Psi_{su} \end{array}\right],$$

where we used the power rule and eq. (5.6) to go from the first to the second line.

## 5.7.1  Fixman's Method

To show that scheme (5.23) produces the correct drift terms, we consider the drift for $\boldsymbol{q}$ and $\boldsymbol{\theta}$ separately. In the following expression, Greek indices range only over components corresponding to $\boldsymbol{q}$ and not those corresponding to $\boldsymbol{\theta}$, and indices $s$, $t$, $u$, and $v$ correspond to only components of $\boldsymbol{\theta}$. All other indices range over every variable. The stochastic drift generated for $\boldsymbol{q}$ is equal to

$$\Delta_{\mathrm{th}}q_\alpha^n = \sqrt{k_B T \Delta t}\left(\partial_k N_{\alpha j}\right)\Delta x_k^{p,n+\frac{1}{2}}N_{jl}^{-\frac{1}{2}}\left(W_l^{n,1} + W_l^{n,2}\right)$$

$$= \sqrt{k_B T \Delta t}\left(\left(\partial_\beta N_{\alpha j}\right)\sqrt{k_B T \Delta t}N_{\beta m}^{\frac{1}{2}}W_m^{n,1} + \left(\partial_s N_{\alpha j}\right)\sqrt{k_B T \Delta t}\Psi_{st}N_{tp}^{\frac{1}{2}}W_p^{n,1}\right) \times$$

$$N_{jl}^{-\frac{1}{2}}\left(W_l^{n,1} + W_l^{n,2}\right).$$

The $\Psi_{st}$ term comes from expanding the rotation procedure. After taking expectation we obtain the deterministic drift

$$\langle\Delta_{\mathrm{th}}q_\alpha^n\rangle = k_B T \Delta t\left(\left(\partial_\beta N_{\alpha\beta}\right) + \left(\partial_s N_{\alpha t}\right)\Psi_{st}\right)$$

Note that $N_{\alpha\beta} = (M_{\boldsymbol{vF}})_{\alpha\beta}$, and $N_{\alpha t} = (M_{\boldsymbol{v\tau}})_{\alpha t}$, and hence the drift for $\boldsymbol{q}$ generated by the Fixman method matches the first row of eq. (??), which is what we want.

For the drift in the $\boldsymbol{\theta}$ direction, we expand the Rotate procedure to first order in $\Delta t$ to obtain

$$\Delta_{\mathrm{th}}\theta_s^n = \Psi_{st}\left(\sqrt{k_B T \Delta t}\left(\partial_k N_{ti}\right)\Delta x_k^{p,n+\frac{1}{2}}N_{ij}^{-\frac{1}{2}}\left(W_j^{n,1} + W_j^{n,2}\right)\right)$$

$$- \frac{k_B T \Delta t}{8}\left(\left(W_i^{n,1} + W_i^{n,2}\right)N_{ti}^{\frac{1}{2}}N_{tj}^{\frac{1}{2}}\left(W_j^{n,1} + W_j^{n,2}\right)\right)\theta_s^n$$

$$= \Psi_{st}\sqrt{k_B T \Delta t}\left(\left(\partial_\alpha N_{ti}\right)\sqrt{K_B T \Delta t}N_{\alpha k}^{\frac{1}{2}}W_k^{n,1}\right.$$

$$\left. + \left(\partial_u N_{ti}\right)\sqrt{k_B T \Delta t}\Psi_{uv}N_{vk}^{\frac{1}{2}}W_k^{n,1}\right)N_{ij}^{-\frac{1}{2}}\left(W_j^{n,1} + W_j^{n,2}\right)$$

$$- \frac{k_B T \Delta t}{8}\left(\left(W_i^{n,1} + W_i^{n,2}\right)N_{ti}^{\frac{1}{2}}N_{tj}^{\frac{1}{2}}\left(W_j^{n,1} + W_j^{n,2}\right)\right)\theta_s^n. \tag{5.44}$$

After taking expectation we obtain the deterministic drift

$$\langle\Delta_{\mathrm{th}}\theta_s^n\rangle = k_B T \Delta t\left[\Psi_{st}\left(\left(\partial_\alpha N_{t\alpha}\right) + \left(\partial_u N_{tv}\right)\Psi_{uv}\right) - \frac{1}{4}N_{tt}\theta_s^n\right]$$

Note that $N_{t\alpha} = (M_{\omega F})_{t\alpha}$ and $N_{tv} = (M_{\omega\tau})_{tv}$. The terms on the second line of (5.44) give the first and last terms in the bottom row of eq. (5.24), while we can see from eq. (5.10) that the last line of (5.44) gives the remaining drift term.

## 5.7.2  Random Finite Difference Scheme

To show that the random finite difference term generates the correct drift, all that is required is showing that $\frac{k_B T}{\delta}\left(\widetilde{\boldsymbol{N}} - \boldsymbol{N}^n\right)\widetilde{\boldsymbol{W}}$ is a good approximation to $\partial_{\boldsymbol{x}}\left(\boldsymbol{N}\right) : \boldsymbol{\Xi}^T$ in expectation. To do this, we expand the RFD term here using indicial notation for clarity.

$$\frac{k_B T}{\delta}\left(\widetilde{N}_{ij} - N_{ij}^n\right)\widetilde{W}_j = \frac{k_B T}{\delta}\partial_k\left(N_{ij}\right)\Delta\tilde{x}_k\widetilde{W}_j + O(\delta),$$

where $\Delta \widetilde{x}_k$ is the increment $\widetilde{x}_j - x_j^n$. We use the convention above where Greek indices correspond to translational degrees of freedom, $s$ and $t$ correspond to angular degrees of freedom, and the remaining indices are summed over all variables. Expanding the increment $\Delta \widetilde{x}_k$ gives

$$\frac{k_B T}{\delta} \partial_k \left( N_{ij} \right) \Delta \widetilde{x}_k \widetilde{W}_j = k_B T \partial_\alpha \left( N_{ij} \right) \widetilde{W}_\alpha \widetilde{W}_j + k_B T \partial_s \left( N_{ij} \right) \Psi_{st} \widetilde{W}_t \widetilde{W}_j.$$

Taking expectation then gives

$$\left\langle \frac{k_B T}{\delta} \partial_k \left( N_{ij} \right) \Delta \widetilde{x}_k \widetilde{W}_j \right\rangle = k_B T \partial_k \left( N_{ij} \right) \Xi_{kj},$$

which is what we needed to obtain the correct drift term.

## 5.8    Addendum: Rotational Diffusion Coefficient

In this addendum, we show that eq. (5.9) gives the correct rotational diffusion coefficient, defined by eq. (5.15). Without loss of generality, we will let $\boldsymbol{u}_i \left( \Delta t \right) = \boldsymbol{R}(\boldsymbol{\theta}_{\Delta t}) \boldsymbol{e}_i$ where $\boldsymbol{e}_i$ are the standard Cartesian basis vectors in the fixed Eulerian frame, and $\boldsymbol{R}_{\Delta t} = \boldsymbol{R}(\boldsymbol{\theta}_{\Delta t})$ is the rotation matrix associated with the quaternion at time $\Delta t$, $\boldsymbol{\theta}_{\Delta t} = \boldsymbol{\theta} \left( \Delta t \right)$. If the initial orientation is $\boldsymbol{\theta}_0 = \boldsymbol{\theta}(0)$, then the expression for the orientational displacement is given by eq. (5.13), which can be written as

$$\Delta \hat{\boldsymbol{u}} \left( \Delta t \right) = \frac{1}{2} \sum_{i=0}^{3} \left( \boldsymbol{R}_0 \boldsymbol{e}_i \right) \times \left( \boldsymbol{R}_{\Delta t} \boldsymbol{e}_i \right)$$

$$= \frac{1}{2} \sum_{i=0}^{3} \left( \boldsymbol{u}_i(0) \right) \times \left( \left( \Delta \boldsymbol{R} \right) \boldsymbol{u}_i(0) \right),$$

where $\Delta \boldsymbol{R}$ denotes a rotation matrix over the time interval $\Delta t$, i.e., the rotation matrix that satisfies $\boldsymbol{R}_{\Delta t} = \Delta \boldsymbol{R} \, \boldsymbol{R}_0$ and corresponds to the quaternion $\Delta \boldsymbol{\theta}$ which satisfies $\Delta \boldsymbol{\theta} \, \boldsymbol{\theta}_0 = \boldsymbol{\theta}_{\Delta t}$, i.e., $\Delta \boldsymbol{\theta} = \boldsymbol{\theta}_{\Delta t} \, \boldsymbol{\theta}_0^{-1}$.

Since we are taking the limit of small $\Delta t$, we only need to compute $\boldsymbol{\theta}_{\Delta t}$ from eq. (5.9) to order $1/2$,

$$\boldsymbol{\theta}_{\Delta t} = \boldsymbol{\theta} \left( 0 \right) + \sqrt{2 k_B T \Delta t} \boldsymbol{\Psi} \left( 0 \right) \boldsymbol{M}_{\omega\tau}^{\frac{1}{2}} \boldsymbol{W} + O \left( \Delta t \right)$$

$$\Rightarrow \Delta \boldsymbol{\theta} = \boldsymbol{I}_{\boldsymbol{\theta}} + \sqrt{2 k_B T \Delta t} \left( \boldsymbol{\Psi} \left( 0 \right) \boldsymbol{M}_{\omega\tau}^{\frac{1}{2}} \boldsymbol{W} \right) \cdot \boldsymbol{\theta}_0^{-1} + O \left( \Delta t \right), \tag{5.45}$$

where $\boldsymbol{W}$ are i.i.d. Gaussian variates. Evaluating the expression in the second line of (5.45) gives

$$\Delta \boldsymbol{\theta} = \left[ \begin{array}{c} 1 \\ \sqrt{\frac{k_B T \Delta t}{2}} \boldsymbol{M}_{\omega\tau}^{\frac{1}{2}} \boldsymbol{W} \end{array} \right] + O \left( \Delta t \right).$$

Computing the rotation matrix corresponding to $\Delta \boldsymbol{\theta}$, calculating $\boldsymbol{u}_i(\Delta t) = \left( \Delta \boldsymbol{R} \right) \boldsymbol{u}_i(0)$, and truncating at order $1/2$ gives

$$\Delta \boldsymbol{R} = \boldsymbol{I} - 2 \boldsymbol{P},$$

with $\boldsymbol{p} = \sqrt{\frac{k_B T \Delta t}{2}} \boldsymbol{M}_{\omega\tau}^{\frac{1}{2}} \boldsymbol{W}$.

This gives us the value of the orientational displacement as

$$\Delta \hat{\boldsymbol{u}} \left( \Delta t \right) = \frac{1}{2} \sum_{i=0}^{3} \boldsymbol{u}_i(0) \times \left( \boldsymbol{u}_i(0) - 2 \left( \boldsymbol{p} \times \boldsymbol{u}_i(0) \right) \right)$$

$$= - \sum_{i=0}^{3} \boldsymbol{u}_i(0) \times \left( \boldsymbol{p} \times \boldsymbol{u}_i(0) \right).$$

We then use the cross product property $\boldsymbol{a} \times \left( \boldsymbol{b} \times \boldsymbol{c} \right) = \boldsymbol{b} \left( \boldsymbol{a} \cdot \boldsymbol{c} \right) - \boldsymbol{c} \left( \boldsymbol{a} \cdot \boldsymbol{b} \right)$ to obtain

$$\Delta \hat{\boldsymbol{u}} \left( \Delta t \right) = - \sum_{i=0}^{3} \left( \boldsymbol{p} \left( \boldsymbol{u}_i(0) \cdot \boldsymbol{u}_i(0) \right) - \boldsymbol{u}_i(0) \left( \boldsymbol{p} \cdot \boldsymbol{u}_i(0) \right) \right)$$

$$= - 3 \boldsymbol{p} + \boldsymbol{p} = -2 \boldsymbol{p} = - \sqrt{2 k_B T \Delta t} \boldsymbol{M}_{\omega\tau}^{\frac{1}{2}} \boldsymbol{W},$$

where we used the properties $\boldsymbol{u}_i(0) \cdot \boldsymbol{u}_i(0) = 1$ and $\sum_{i=1}^{3} \boldsymbol{u}_i(0)(\boldsymbol{p} \cdot \boldsymbol{u}_i(0)) = \boldsymbol{p}$ since the $\boldsymbol{u}_i(0)$ are orthonormal. It is clear that this orientational displacement gives the correct rotational diffusion coefficient,

$$\langle (\Delta\hat{\boldsymbol{u}}\,(\Delta t))\,(\Delta\hat{\boldsymbol{u}}\,(\Delta t))^T \rangle = 2k_B T \Delta t\, \boldsymbol{M_{\omega\tau}} + o\,(\Delta t)\,,$$

demonstrating that our choice of the noise is consistent with (5.15).

# Chapter 6

# Conclusion

In this thesis, we developed several temporal integrators for a wide class of generic Langevin equations that arise when considering problems in fluctuating hydrodynamics and Brownian dynamics. The integration of these equations presents different challenges depending on the problem being studied and the regime of interest, and we constructed several schemes with goals that differ based on what is desirable and achievable in each setting. Systems with weak noise are well approximated by a linearization around their deterministic dynamics, which may be given a rigorous meaning in the space of Gaussian distributions. In Chapter 2, we introduced semi implicit methods that numerically linearize Langevin systems, allowing one to achieve second order weak accuracy for the linearized equations while avoiding the sometimes messy calculations involved in analytically linearizing the equations. We used these techniques to study giant fluctuations appearing in nonequilibrium steady states in binary liquid mixtures in Chapter 3.

Another feature common to fluctuating hydrodynamics problems is the presence of a large separation of timescales between a slowly evolving variable of interest and a rapidly evolving variable to which it is coupled. We described schemes which use an implicit approach to numerically perform adiabatic elimination, allowing for a larger time step size and thus greater computational efficiency. A first example to which we applied this techniques in Chapter 3 was the modeling of diffusive mixing in binary liquid mixtures in microgravity.

A second example of a fast-slow system was studied in Chapter 4, wherein we developed the Fluctuating Immersed Boundary method for simulating Brownian motion of spherical colloidal particles. In this context, we proposed a novel random finite difference scheme for obtaining the correct stochastic drift term that arises due to the presence of multiplicative noise in the effective equation for the slow variable. Furthermore, we were able to make additional specific optimizations of the temporal integrators by splitting the RFD term into pieces, allowing us to construct schemes that involve only a single Stokes solve per time step.

Many interesting systems involve Brownian particles of complex shapes [154, 157], and simulating their dynamics requires choosing a way to represent orientation in three dimensional space and formulating the appropriate stochastic equations for this representation. In Chapter 5 we proposed an overdamped Langevin system for the evolution using a quaternion representation of orientations, which offers several advantages. We went on to describe a temporal integration scheme for these equations in which we handled the stochastic drift term using a Random Finite Difference. We applied the developed techniques to study the quasi two-dimensional diffusion of dense nonspherical particles sedimented near a boundary.

## 6.1   Temporal integrators for linearized and multiscale systems

Chapter 2 focused on temporal integrators for Langevin equations. We constructed a general family of semi-implicit predictor-corrector schemes which are relatively easy to implement in existing computational fluid codes, and recommend two specific examples. The first is is a fully explicit midpoint rule, and the second is a semi-implicit trapezoidal scheme in which stiff terms are treated implicitly and the rest are treated explicitly. Stochastic forcing is added in a way that give the following desirable properties: second order weak accuracy for the linearized Langevin equations and first order weak accuracy for multiplicative kinetic noise. In particular, these schemes use a random finite difference approach to obtain the stochastic drift terms without requiring evaluation of derivatives.

The key idea in our approach was to discretize the original nonlinear Langevin equations with sufficiently weak noise, and let the algorithm do the linearization for us, without us having to even write the linearized equations explicitly. This has numerous advantages over the alternative approach of splitting the variables into a deterministic

mean plus fluctuations and then linearizing the equations manually. Firstly, the linearization needs to be done around an unknown time-dependent solution of the deterministic equations, which must itself be computed numerically in general. Secondly, the linearized equations typically have many more terms than the nonlinear equations, and do not obey conservation laws, leading to violation of conservation for the overall solution (mean+fluctuations). Lastly, our algorithms can, with care, also be used to integrate genuinely nonlinear Langevin equations, and thus numerically access the importance of terms neglected by linearization [66, 23]. Integrating the linearized equations to second-order weak accuracy proved to be relatively simple. Essentially, all that is required is to evaluate the noise amplitude in the corrector step at the correct value for the time-dependent deterministic solution, e.g., at the midpoint or end-point of the time step. In the general nonlinear setting, by contrast, obtaining second-order weak accuracy with derivative-free schemes is rather nontrivial [32].

We also proposed predictor-corrector schemes for integrating systems of Langevin equations containing a fast and a slow variable, in the limit of infinite separation of time scales. We limited our attention here to the simple but common case of the fast variable entering only linearly; the general case is much more subtle [45]. Our predictor-corrector schemes discretize the original equations but without the time derivative term in the equation for the fast variable, giving an effective integrator for the overdamped equations without ever explicitly even writing the limiting dynamics. One way to think about our integrators is as applying a backward Euler method to the fast variable, since this method finds a steady state solution of the fast variable in the limit when the time step size is much larger than the internal time scale of the fast variable. An essential difficulty in the construction of integrators for the nonlinear overdamped equations is capturing the stochastic drift terms that arise due to the kinetic interpretation of the noise. We accomplished this goal by using a combination of implicit and explicit random finite differences.

## 6.2 Fluctuating Hydrodynamics

In Chapter 3, we applied our methods to the equations of fluctuating hydrodynamics. We considered the one dimensional fluctuating Burger's equation to illustrate our approach, and then examined the two dimensional Navier-Stokes equations and a model for diffusive mixing in three dimensional binary liquid mixtures.

Spatio-temporal discretizations do not necessarily preserve the properties of the continuum equations, notably, they may not obey a discrete fluctuation-dissipation principle. This means that their equilibrium distribution is not a discrete form of the Gibbs-Boltzmann distribution. This sort of unphysical behavior can be avoided by carefully constructing the spatial discretization to obey a discrete-fluctuation principle with respect to a target discrete Gibbs-Boltzmann distribution. In this way, a coarse-grained semi-discrete model is obtained that obeys the principles of statistical mechanics, namely, obeys detailed balance at thermodynamic equilibrium. We showed explicitly how one can construct such spatial discretizations by first understanding the properties of the continuum model (even if only at a formal level) and then maintaining those properties in the spatial discretization. For fluctuating hydrodynamics, this means that certain relations between the discrete divergence, gradient and Laplacian operators must be preserved, such as the fact that the divergence and gradient operators are negative adjoints of each other. We showed how to construct spatial discretizations that obey a discrete fluctuation-dissipation principle for both the fluctuating Burgers and the fluctuating Navier-Stokes with the addition of a passively-advected scalar. These results were mostly a summary of discretizations previously constructed in somewhat disjoint bodies of literature, and are a stochastic equivalent of a method-of-lines approach for deterministic fluid dynamics [79].

The integrators proposed in Chapter 2 handle fast-slow systems by taking the limit of infinite separation of variables to eliminate the fast variable. Such an asymptotic limit is often a good approximation, as illustrated in Ref. [23], and also in Chapter 3 by modeling the development of giant fluctuations in microgravity during the GRADFLEX experiment [53]. However, we also studied here the dynamics of giant fluctuations in Earth gravity and found that the assumption of *uniform* separation of time scales between the fast velocity and slow concentration fails in practice for sufficiently small wavenumbers. In Section 3.5.3, we resorted to integrating the original (inertial) equations using a sufficiently small time step. It remains an important challenge for the future to develop *uniformly accurate* temporal integrators that remain weakly first-order accurate even when there is incomplete separation of time scales, while still allowing the use of large time step sizes, on the time scale of the slow variable. Such integrators must likely rely on the linearity of the equation and exponential integrators [187, 188, 124] for the fast variable. The key difficulty is to correctly capture the effects of the fast velocity on the slow concentration that arise due to the nonlinear advective term $\boldsymbol{v} \cdot \boldsymbol{\nabla} c$ [23].

## 6.3   Brownian Dynamics without Green's Functions

In Chapter 4, we developed a method for performing Brownian Dynamics (BD) with hydrodynamic interactions in confined geometries such as slit or square channels or chambers. Unlike traditional methods for BD, our FIB method does not rely on analytical Green's functions, and only requires the numerical solution of a single steady Stokes system per time step to capture both the deterministic, stochastic, and stochastic drift contributions to the overdamped dynamics of the hydrodynamically-coupled particles. The FIB method is particularly appealing when dealing with more complex boundary conditions such as confined flows in non-trivial channel geometries, since analytical solutions are quite involved and ensuring a positive semi-definite mobility is nontrivial, even in the presence of only a single no-slip planar wall [11, 98]. Computing analytical solutions in cases where there are osmophoretic flows at the boundaries, as in active suspensions of particles [123], is essentially impossible because the boundary condition itself comes from the solution of another nontrivial reaction-diffusion problem. The only alternative would be to use relatively-expensive and complex boundary integral methods [189, 190, 191], none of which, to our knowledge, include the effects of thermal fluctuations.

Following the completion of this work we learned about a related recent extension of the SELM approach to use a (P1-MINI) finite-element Stokes solver to generate the hydrodynamic response [129], very similar to the approach we independently took in this work. Note, however, that our temporal integrators are different from the Euler-Maruyama scheme used in Ref. [129], which requires calculating the divergence of the mobility by other means (We remark that the issue of computing the divergence of the mobility does not appear to be addressed directly in Ref. [129].). In terms of spatial discretizations, the key relation $-\mathcal{L}^{-1}L\mathcal{L}^{-1} = \mathcal{L}^{-1}$ is used in both works to generate the correct stochastic increments by simply solving the saddle-point steady Stokes problem. A key difference, however, is that on the structured MAC grid used in this work the generation of a stochastic stress tensor with covariance $\sim -L$ is straightforward [39], where as accomplishing the same for unstructured FEM grids appears to require an iterative stochastic multigrid method [129]. Furthermore, the P1-MINI discretization is only first-order spatially accurate and requires more degrees of freedom (DOF) per cell, where as the structured staggered (MAC) grid (which can be thought of as a particular FEM discretization) achieves second-order spatial accuracy with only a single velocity DOF per grid face and a single pressure DOF per cell center. This makes the methods developed here particularly attractive, due to their simplicity and efficiency, in simple confined geometries such as channels or chambers. At the same time, unstructured FEM discretizations have a notable advantage for complex geometries. Additionally, achieving variable spatial resolution is natural on unstructured grids [129] but requires (block structured) adaptive mesh refinement (AMR) techniques [86] on structured grids. Adaptive resolution is very important at low densities of suspended particles to avoid using a fine spatial grid to resolve long-ranged hydrodynamics; this is in fact a key advantage of using Green's functions instead of numerical solvers. In future work we will consider solving the fluctuating Stokes equations on block-structured refined staggered grids.

The FIB method presented here and related methods [103, 129] are only a first step toward the ultimate goal of performing Brownian (i.e., overdamped) dynamics for a collection of rigid and flexible bodies in flow in the presence of complex boundaries. We take further steps towards this goal in Chapter 5, where we write a Langevin system for arbitrary rigid bodies and develop temporal integrators for this system. However, achieving this goal may ultimately require a combination of techniques, such as multipole series, immersed boundary [192] and immersed finite-element [101], or boundary integral representations for the suspended structures, together with cut cell (embedded boundary) or finite-element methods [129] for representing the complex geometry. What our work makes evident is that thermal fluctuations are most easily and consistently included by using fluctuating hydrodynamics combined with appropriate multiscale temporal integrators. This illustrates the power of a bottom-up approach in which one starts with the fundamental formulation of the fluid dynamics of suspensions [116, 117, 118] and then coarse-grains in space and time to reach larger length scales and longer time scales, instead of starting at the top from a formulation of the equations of motion that contains difficult-to-calculate objects such as multi-body mobility or resistance tensors that hide all of the coarse-grained information inside them.

## 6.4   Brownian Dynamics for Suspensions of Rigid Bodies

In chapter 5, we studied the Brownian motion of rigid bodies of arbitrary shape immersed in a viscous fluid in the overdamped regime, in the presence of confinement and gravity. We parameterized the orientation of the rigid bodies with normalized quaternions, which offer several advantages over other previously-used representations. Furthermore, unlike the majority of prior works, we do not assume any particular symmetry for the rigid bodies, and we account carefully for the fact that the hydrodynamic mobility $N$ depends on the configuration due to confinement or hydrodynamic interactions with other particles. We derived the appropriate form of the overdamped

Langevin equations of motion, including all of the stochastic drift terms required to give the correct Gibbs-Boltzmann distribution in equilibrium, and to preserve the unit norm constraint of the quaternions.

In section 5.2 we developed temporal integrators for the rigid-body overdamped Langevin system and presented two ways to handle the stochastic drift term. The first approach is the well known midpoint Fixman scheme [12, 13], which generates the drift terms using a midpoint predictor step but requires a costly application or factorizatio of $N^{-1}$. The second approach employs a Random Finite Difference approach to generate the drift terms using only applications of $N$ and $N^{\frac{1}{2}}$, making it an appealing choice. The RFD approach is especially promising in situations where the action of the mobility and the stochastic terms are generated by using a fluctuating hydrodynamics fluid solver, as in the fluctuating force coupling method (FCM) [103], or extensions of our fluctuating immersed boundary (FIB) method [3] to include rotlet (and possible also stresslet) terms in the minimally-resolved blob model.

In Section 5.3 we performed several numerical simulations of the Brownian motion of rigid particles diffusing near a wall in the presence of gravity, motivated by a number of recent experiments studying the diffusion of asymmetric spheres [156], clusters of spheres [155, 157], and boomerang colloids [154, 159]. First, we studied the rotational and translational diffusion of a colloidal sphere with nonuniform density, modeling recently-manufactured "colloidal surfers" [123] in which a dense hematite cube is embedded in a polymeric spherical particle. Second, we examined the behavior of a tetramer formed by rigidly connecting four colloidal spheres together, modeling colloidal clusters that have been manufactured in the lab [155, 157]. Finally, we investigated the quasi two-dimensional diffusive motion of a dense boomerang colloid sedimented near a no-slip boundary, inspired by recent experimental studies of lithographed boomerang-shaped particles [154, 159]. We demonstrated that the choice of tracking point is crucial when computing the translational diffusion coefficient. In particular, we demonstrate that in some cases there exists a suitable choice of the origin (around which torques are expressed) which can be used to obtain an approximate but relatively accurate formula for the effective diffusion coefficient in the directions parallel to the boundary. At the same time, however, we find that there is no exact closed-form expression for the long-time quasi-two-dimensional coefficient; it appears necessary to perform numerical simulations in order to study the long-time diffusive dynamics of even a single rigid body in the presence of confinement. Our temporal integrators can easily be extended to study quasi-two-dimensional suspensions of passive or active particles sedimented near a boundary, which is quite relevant in practice since active particles often have metallic components and are therefore much denser than water [161, 123].

In our simulations, the time step size was strongly restricted in order to keep the rigid body from passing through the wall. To this end, we rejected steps that encountered an unphysical state (e.g., a configuration where the computed mobility matrix is not positive semi-definite). This naive approach modifies the dynamics in a way that violates ergodicity and detailed balance, and we reduced our time step size to avoid performing a significant number of rejections. Several more sophisticated approaches exist that may solve this problem, including Metropolization [153], adaptive time-stepping [178], or continious-time discretizations [193]. Employing these techniques in our integrators remains an area of future exploration.

In this work we relied on a simple rigid multi-blob or multi-bead [181] approach for computing the hydrodynamic mobilities, using direct dense linear algebra to compute inverses and Cholesky factorizations. This was useful for validating our methods, but it does not scale well with increasing numbers of rigid bodies or blobs per rigid body. Furthermore, the analytical approximation we used for the blob mobility is valid only for the case of a single no slip boundary [11], and even in that case it is not guaranteed to lead to a symmetric positive-definite grand mobility for all configurations. The RDF scheme developed in this work can be coupled with a computational fluid solver, similarly to the approach taken in the FIB method, in a way that will allow us to do simulations in more complex geometries such as slit channels, and scale to large numbers of blobs. The required rigid-body immersed boundary method has recently been developed [184] and implemented in the IBAMR software infrastructure [86], and in the future the temporal integrators developed in this work will be employed to include Brownian motion of the rigid particles.

# Bibliography

[1] S. Delong, B. E. Griffith, E. Vanden-Eijnden, and A. Donev. Temporal Integrators for Fluctuating Hydrodynamics. *Phys. Rev. E*, 87(3):033302, 2013.

[2] S. Delong, Y. Sun, B. E. Griffith, E. Vanden-Eijnden, and A. Donev. Multiscale temporal integrators for fluctuating hydrodynamics. *Phys. Rev. E*, 90:063312, 2014.

[3] S. Delong, F. Balboa Usabiaga, R. Delgado-Buscalioni, B. E. Griffith, and A. Donev. Brownian Dynamics without Green's Functions. *J. Chem. Phys.*, 140(13):134110, 2014.

[4] S. Delong, F. Balboa Usabiaga, and A. Donev. Brownian Dynamics of Confined Rigid Bodies. In preparation, to be submitted to J. Chem. Phys., 2015.

[5] M. Hütter and H.C. Öttinger. Fluctuation-dissipation theorem, kinetic stochastic integral and efficient simulations. *J. Chem. Soc., Faraday Trans.*, 94(10):1403–1405, 1998.

[6] L.D. Landau and E.M. Lifshitz. *Fluid Mechanics*, volume 6 of *Course of Theoretical Physics*. Pergamon Press, Oxford, England, 1959.

[7] P. Español and I. Zúñiga. On the definition of discrete hydrodynamic variables. *J. Chem. Phys*, 131:164106, 2009.

[8] P. Español, J.G. Anero, and I. Zúñiga. Microscopic derivation of discrete hydrodynamics. *J. Chem. Phys.*, 131:244117, 2009.

[9] G. Da Prato. *Kolmogorov equations for stochastic PDEs*. Birkhauser, 2004.

[10] James W Swan and John F Brady. Particle motion between parallel walls: Hydrodynamics and simulation. *Physics of Fluids*, 22:103301, 2010.

[11] James W. Swan and John F. Brady. Simulation of hydrodynamically interacting particles near a no-slip boundary. *Physics of Fluids*, 19(11):113306, 2007.

[12] M. Fixman. Simulation of polymer dynamics. I. General theory. *J. Chem. Phys.*, 69:1527, 1978.

[13] P.S. Grassia, E.J. Hinch, and L.C. Nitsche. Computer simulations of brownian motion of complex systems. *Journal of Fluid Mechanics*, 282:373–403, 1995.

[14] Brendan D Hoffman and Eric SG Shaqfeh. The effect of brownian motion on the stability of sedimenting suspensions of polarizable rods in an electric field. *Journal of Fluid Mechanics*, 624:361–388, 2009.

[15] K Hinsen. HYDROLIB: a library for the evaluation of hydrodynamic interactions in colloidal suspensions. *Computer physics communications*, 88(2):327–340, 1995.

[16] B Cichocki and K Hinsen. Stokes drag on conglomerates of spheres. *Physics of Fluids*, 7:285, 1995.

[17] A Ortega, D Amorós, and J García de La Torre. Prediction of hydrodynamic and other solution properties of rigid proteins from atomic-and residue-level models. *Biophysical journal*, 101(4):892–898, 2011. Code available at `http://leonardo.inf.um.es/macromol/programs/hydropro/hydropro.htm`.

[18] José García de la Torre, María L Huertas, and Beatriz Carrasco. Calculation of hydrodynamic properties of globular proteins from their atomic-level structure. *Biophysical Journal*, 78(2):719–730, 2000.

[19] Vladimir Lobaskin and Burkhard Dünweg. A new model for simulating colloidal dynamics. *New Journal of Physics*, 6(1):54, 2004.

[20] Simón Poblete, Adam Wysocki, Gerhard Gompper, and Roland G. Winkler. Hydrodynamics of discrete-particle models of spherical colloids: A multiparticle collision dynamics simulation study. *Phys. Rev. E*, 90:033314, 2014.

[21] A. P. S. Bhalla, R. Bale, B. E. Griffith, and N. A. Patankar. A unified mathematical framework and an adaptive numerical method for fluid-structure interaction with rigid, deforming, and elastic bodies. *Journal of Computational Physics*, 250:446–476, 2013.

[22] G.N. Milstein and M.V. Tretyakov. *Stochastic numerics for mathematical physics*. Springer, 2004.

[23] A. Donev, T. G. Fai, and E. Vanden-Eijnden. A reversible mesoscopic model of diffusion in liquids: from giant fluctuations to Fick's law. *Journal of Statistical Mechanics: Theory and Experiment*, 2014(4):P04004, 2014.

[24] A. Donev and E. Vanden-Eijnden. Dynamic Density Functional Theory with hydrodynamic interactions and fluctuations. *J. Chem. Phys.*, 140(23), 2014.

[25] Martin Hairer. Introduction to regularity structures. *arXiv preprint arXiv:1401.3014*, 2014.

[26] J. M. O. De Zarate and J. V. Sengers. *Hydrodynamic fluctuations in fluids and fluid mixtures*. Elsevier Science Ltd, 2006.

[27] J. L. Lebowitz, E. Presutti, and H. Spohn. Microscopic models of hydrodynamic behavior. *J. Stat. Phys.*, 51(5):841–862, 1988.

[28] Giambattista Giacomin, Joel L Lebowitz, and Errico Presutti. Deterministic and stochastic hydrodynamic equations arising from simple microscopic model systems. In *Stochastic Partial Differential Equations: Six Perspectives*, number 64 in Mathematical Surveys and Monographs, page 107. American Mathematical Soc., 1999.

[29] S. R. S. Varadhan. The complex story of simple exclusion. In *Ito's stochastic calculus and probability theory*, pages 385–400. Springer, 1996.

[30] C Kipnis, S Olla, and SRS Varadhan. Hydrodynamics and large deviation for simple exclusion processes. *Communications on Pure and Applied Mathematics*, 42(2):115–137, 1989.

[31] S.R.S. Varadhan. Scaling limits for interacting diffusions. *Communications in mathematical physics*, 135(2):313–353, 1991.

[32] A Abdulle, G Vilmart, and K Zygalakis. Weak second order explicit stabilized methods for stiff stochastic differential equations. *SIAM J. Sci. Comput.*, 35(4):A1792–A1814, 2013.

[33] A. J. Nonaka, Y. Sun, J. B. Bell, and A. Donev. Low Mach Number Fluctuating Hydrodynamics of Binary Liquid Mixtures. Submitted to CAMCOS, ArXiv preprint 1410.2300, 2015.

[34] H. Grabert. *Projection operator techniques in nonequilibrium statistical mechanics*. Springer-Verlag, 1982.

[35] J.D. Ramshaw and K. Lindenberg. Augmented Langevin description of multiplicative noise and nonlinear dissipation in Hamiltonian systems. *J. Stat. Phys*, 45(1):295–307, 1986.

[36] G. C. Papanicolaou. Some probabilistic problems and methods in singular perturbations. *Rocky Mountain J. Math*, 6(4):653–674, 1976.

[37] Grigorios A Pavliotis and Andrew M Stuart. *Multiscale methods: averaging and homogenization*, volume 53. Springer, 2008.

[38] Thomas Schaffter. Numerical integration of sdes: a short tutorial. *Swiss Federal Institute of Technology in Lausanne (EPFL), Switzerland, Unpublished manuscript*, 2010.

[39] F. Balboa Usabiaga, J. B. Bell, R. Delgado-Buscalioni, A. Donev, T. G. Fai, B. E. Griffith, and C. S. Peskin. Staggered Schemes for Fluctuating Hydrodynamics. *SIAM J. Multiscale Modeling and Simulation*, 10(4):1369–1408, 2012.

[40] N. Bou-Rabee and E. Vanden-Eijnden. Pathwise accuracy and ergodicity of metropolized integrators for SDEs. *Communications on Pure and Applied Mathematics*, 63(5):655–696, 2010.

[41] J.C. Mattingly, A.M. Stuart, and M.V. Tretyakov. Convergence of Numerical Time-Averaging and Stationary Measures via Poisson Equations. *SIAM Journal on Numerical Analysis*, 48:552, 2010.

[42] A. Donev, E. Vanden-Eijnden, A. L. Garcia, and J. B. Bell. On the Accuracy of Explicit Finite-Volume Schemes for Fluctuating Hydrodynamics. *Communications in Applied Mathematics and Computational Science*, 5(2):149–197, 2010.

[43] C. W. Gardiner. *Handbook of stochastic methods: for physics, chemistry & the natural sciences*, volume Vol. 13 of *Series in synergetics*. Springer, third edition, 2003.

[44] P. J. Atzberger. Spatially Adaptive Stochastic Numerical Methods for Intrinsic Fluctuations in Reaction-Diffusion Systems. *J. Comp. Phys.*, 229(9):3474 – 3501, 2010.

[45] C. W. Gardiner and M. L. Steyn-Ross. Adiabatic elimination in stochastic systems. I-III. *Phys. Rev. A*, 29:2814–2844, 1984.

[46] RZ Khasminskii. Principle of averaging for parabolic and elliptic differential equations and for markov processes with small diffusion. *Theory of Probability & Its Applications*, 8(1):1–21, 1963.

[47] Thomas G Kurtz. A limit theorem for perturbed operator semigroups with applications to random evolutions. *Journal of Functional Analysis*, 12(1):55–67, 1973.

[48] E.H. Twizell, A.B. Gumel, and M.A. Arigu. Second-order, $L_0$-stable methods for the heat equation with time-dependent boundary conditions. *Advances in Computational Mathematics*, 6(1):333–352, 1996.

[49] U.M. Ascher, S.J. Ruuth, and B.T.R. Wetton. Implicit-explicit methods for time-dependent partial differential equations. *SIAM Journal on Numerical Analysis*, pages 797–823, 1995.

[50] R.F. Fox and G.E. Uhlenbeck. Contributions to Non-Equilibrium Thermodynamics. I. Theory of Hydrodynamical Fluctuations. *Physics of Fluids*, 13:1893, 1970.

[51] A. Vailati and M. Giglio. Giant fluctuations in a free diffusion process. *Nature*, 390(6657):262–265, 1997.

[52] B. Davidovitch, E. Moro, and H.A. Stone. Spreading of viscous fluid drops on a solid substrate assisted by thermal fluctuations. *Phys. Rev. letters*, 95(24):244505, 2005.

[53] A. Vailati, R. Cerbino, S. Mazzoni, C. J. Takacs, D. S. Cannell, and M. Giglio. Fractal fronts of diffusion in microgravity. *Nature Communications*, 2:290, 2011.

[54] A. Donev, A. J. Nonaka, Y. Sun, T. G. Fai, A. L. Garcia, and J. B. Bell. Low Mach Number Fluctuating Hydrodynamics of Diffusively Mixing Fluids. *Communications in Applied Mathematics and Computational Science*, 9(1):47–105, 2014.

[55] A. Donev, A. J. Nonaka, A. K. Bhattacharjee, A. L. Garcia, and J. B. Bell. Low Mach Number Fluctuating Hydrodynamics of Multispecies Liquid Mixtures. *Physics of Fluids*, 27(3), 2015.

[56] D. Bedeaux, I. Pagonabarraga, J.M.O. de Zárate, J.V Sengers, and S. Kjelstrup. Mesoscopic non-equilibrium thermodynamics of non-isothermal reaction-diffusion. *Phys. Chem. Chem. Phys.*, 12(39):12780–12793, 2010.

[57] A. K. Bhattacharjee, K. Balakrishnan, A. L. Garcia, J. B. Bell, and A. Donev. Fluctuating hydrodynamics of multispecies reactive mixtures. Submitted to J. Chem. Phys., ArXiv preprint 1503.07478, 2015.

[58] K. Balakrishnan, A. L. Garcia, A. Donev, and J. B. Bell. Fluctuating hydrodynamics of multispecies nonreactive mixtures. *Phys. Rev. E*, 89:013017, 2014.

[59] R.V. Kohn, M.G. Reznikoff, and E. Vanden-Eijnden. Magnetic elements at finite temperature and large deviation theory. *Journal of nonlinear science*, 15(4):223–253, 2005.

[60] P. Español. Stochastic differential equations for non-linear hydrodynamics. *Physica A*, 248(1-2):77–96, 1998.

[61] H. C. Öttinger. *Beyond equilibrium thermodynamics*. Wiley Online Library, 2005.

[62] P.J. Morrison. Hamiltonian description of the ideal fluid. *Rev. Mod. Phys.*, 70(2):467, 1998.

[63] T.J. Bridges and S. Reich. Numerical methods for hamiltonian PDEs. *Journal of Physics A: Mathematical and General*, 39:5287, 2006.

[64] J. A. de la Torre and P. Español. Coarse-graining Brownian motion: From particles to a discrete diffusion equation. *J. Chem. Phys*, 135:114103, 2011.

[65] A. Donev, A. L. Garcia, Anton de la Fuente, and J. B. Bell. Diffusive Transport by Thermal Velocity Fluctuations. *Phys. Rev. Lett.*, 106(20):204501, 2011.

[66] A. Donev, A. L. Garcia, Anton de la Fuente, and J. B. Bell. Enhancement of Diffusive Transport by Nonequilibrium Thermal Fluctuations. *J. of Statistical Mechanics: Theory and Experiment*, 2011:P06014, 2011.

[67] A. Rocco, J. Casademunt, U. Ebert, and W. Van Saarloos. Diffusion coefficient of propagating fronts with multiplicative noise. *Physical Review E*, 65(1):012102, 2001.

[68] David S Dean. Langevin equation for the density of a system of interacting langevin processes. *Journal of Physics A: Mathematical and General*, 29(24):L613, 1996.

[69] A. Donev R. Cerbino, Y. Sun and A. Vailati. Dynamic scaling for the growth of non-equilibrium fluctuations during thermophoretic diffusion in microgravity. Submitted to Sci. Reps., ArXiv preprint 1502.03693, 2015.

[70] A. Oprisan and A. Leilani Payne. Dynamic shadowgraph experiments and image processing techniques for investigating non-equilibrium fluctuations during free diffusion in nanocolloids. *Optics Communications*, 290:100–106, 2012.

[71] F. Croccolo, H. Bataller, and F. Scheffold. A light scattering study of non equilibrium fluctuations in liquid mixtures to measure the Soret and mass diffusion coefficient. *J. Chem. Phys.*, 137:234202, 2012.

[72] C. Giraudet, H. Bataller, Y. Sun, A. Donev, J. M. Ortiz de Zárate, and F. Croccolo. Slowing-down of non-equilibrium concentration fluctuations in confinement. ArXiv preprint 1410.6524, 2015.

[73] F. Croccolo, D. Brogioli, A. Vailati, M. Giglio, and D. S. Cannell. Nondiffusive decay of gradient-driven fluctuations in a free-diffusion process. *Phys. Rev. E*, 76(4):041112, 2007.

[74] J. B. Bell, J. Foo, and A. L. Garcia. Algorithm refinement for the stochastic Burgers equation. *J. Comput. Phys.*, 223(1):451–468, 2007.

[75] M. Hairer and J. Voss. Approximations to the Stochastic Burgers equation. *Journal of NonLinear Science*, pages 1–24, 2010.

[76] H.C. Öttinger. Constraints in nonequilibrium thermodynamics: General framework and application to multicomponent diffusion. *J. Chem. Phys.*, 130:114904, 2009.

[77] A. Majda and I. Tomofeyev. Statistical mechanics for truncations of the Burgers-Hopf equation: a model for intrinsic stochastic behavior with scaling. *Milan Journal of Mathematics*, 70(1):39–96, 2002.

[78] Y. Morinishi, T.S. Lund, O.V. Vasilyev, and P. Moin. Fully conservative higher order finite difference schemes for incompressible flow. *J. Comp. Phys.*, 143(1):90–124, 1998.

[79] A. K. Bhattacharjee, G. I. Menon, and R. Adhikari. Fluctuating dynamics of nematic liquid crystals using the stochastic method of lines. *J. Chem. Phys.*, 133:044112, 2010.

[80] E. Vanden-Eijnden and G. Ciccotti. Second-order integrators for Langevin equations with holonomic constraints. *Chemical physics letters*, 429(1-3):310–316, 2006.

[81] G. Ciccotti, T. Lelièvre, and E. Vanden-Eijnden. Projection of diffusions on submanifolds: Application to mean force computation. *Communications on Pure and Applied Mathematics*, 61(3):371–408, 2008.

[82] F.H. Harlow and J.E. Welch. Numerical calculation of time-dependent viscous incompressible flow of fluids with free surfaces. *Physics of Fluids*, 8:2182–2189, 1965.

[83] A. S. Almgren, J. B. Bell, and W. G. Szymczak. A numerical method for the incompressible Navier-Stokes equations based on an approximate projection. *SIAM J. Sci. Comput.*, 17(2):358–369, March 1996.

[84] A.S. Almgren, J.B. Bell, and W.Y. Crutchfield. Approximate projection methods: Part I. Inviscid analysis. *SIAM Journal on Scientific Computing*, 22:1139, 2000.

[85] B.E. Griffith. An accurate and efficient method for the incompressible Navier-Stokes equations using the projection method as a preconditioner. *J. Comp. Phys.*, 228(20):7565–7595, 2009.

[86] B.E. Griffith, R.D. Hornung, D.M. McQueen, and C.S. Peskin. An adaptive, formally second order accurate version of the immersed boundary method. *J. Comput. Phys.*, 223(1):10–49, 2007. Software available at http://ibamr.googlecode.com.

[87] M. Cai, A. J. Nonaka, J. B. Bell, B. E. Griffith, and A. Donev. Efficient Variable-Coefficient Finite-Volume Stokes Solvers. *Comm. in Comp. Phys. (CiCP)*, 16(5):1263–1297, 2014.

[88] Jose Maria Ortiz de Zarate, Jose Antonio Fornes, and Jan V. Sengers. Long-wavelength nonequilibrium concentration fluctuations induced by the Soret effect. *Phys. Rev. E*, 74:046305, Oct 2006.

[89] W. E, W. Ren, and E. Vanden-Eijnden. A general strategy for designing seamless multiscale methods. *J. Comp. Phys.*, 228(15):5437–5453, 2009.

[90] A. Vailati and M. Giglio. Nonequilibrium fluctuations in time-dependent diffusion processes. *Phys. Rev. E*, 58(4):4361–4371, 1998.

[91] C. J. Takacs, G. Nikolaenko, and D. S. Cannell. Dynamics of long-wavelength fluctuations in a fluid layer heated from above. *Phys. Rev. Lett.*, 100(23):234502, 2008.

[92] W. E and J.G. Liu. Projection method III: Spatial discretization on the staggered grid. *Mathematics of Computation*, 71(237):27–48, 2002.

[93] W. E and J.G. Liu. Gauge method for viscous incompressible flows. *Commun. Math. Sci.*, 1(2):317–332, 2003.

[94] J. B. Bell, P. Colella, and H. M. Glaz. A second order projection method for the incompressible Navier-Stokes equations. *J. Comp. Phys.*, 85(2):257–283, 1989.

[95] N. Sharma and N. A. Patankar. Direct numerical simulation of the Brownian motion of particles by using fluctuating hydrodynamic equations. *J. Comput. Phys.*, 201:466–486, 2004.

[96] O. B. Usta, A. J. C. Ladd, and J. E. Butler. Lattice-Boltzmann simulations of the dynamics of polymer solutions in periodic and confined geometries. *J. Chem. Phys.*, 122(9):094902, 2005.

[97] Anthony JC Ladd, Rahul Kekre, and Jason E Butler. Comparison of the static and dynamic properties of a semiflexible polymer using lattice Boltzmann and Brownian-dynamics simulations. *Physical Review E*, 80(3):036704, 2009.

[98] Rahul Kekre, Jason E. Butler, and Anthony J. C. Ladd. Comparison of lattice-Boltzmann and Brownian-dynamics simulations of polymer migration in confined flows. *Phys. Rev. E*, 82:011802, 2010.

[99] B. Dünweg and A.J.C. Ladd. Lattice Boltzmann simulations of soft matter systems. *Adv. Comp. Sim. for Soft Matter Sciences III*, pages 89–166, 2009.

[100] P. J. Atzberger. Stochastic Eulerian-Lagrangian Methods for Fluid-Structure Interactions with Thermal Fluctuations. *J. Comp. Phys.*, 230:2821–2837, 2011.

[101] Adrian M Kopacz, Neelesh A Patankar, and Wing K Liu. The immersed molecular finite element method. *Computer Methods in Applied Mechanics and Engineering*, 233:28–39, 2012.

[102] F. Balboa Usabiaga, R. Delgado-Buscalioni, B. E. Griffith, and A. Donev. Inertial Coupling Method for particles in an incompressible fluctuating fluid. *Comput. Methods Appl. Mech. Engrg.*, 269:139–172, 2014. Code available at https://code.google.com/p/fluam.

[103] Eric E. Keaveny. Fluctuating force-coupling method for simulations of colloidal suspensions. *J. Comp. Phys.*, 269(0):61 – 79, 2014.

[104] F. Balboa Usabiaga and R. Delgado-Buscalioni. A minimal model for acoustic forces on Brownian particles. *Phys. Rev. E*, 88:063304, 2013.

[105] T. Iwashita, Y. Nakayama, and R. Yamamoto. A Numerical Model for Brownian Particles Fluctuating in Incompressible Fluids. *Journal of the Physical Society of Japan*, 77(7):074007, 2008.

[106] Y. Chen, N. Sharma, and N. Patankar. Fluctuating Immersed Material (FIMAT) dynamics for the direct simulation of the Brownian motion of particles. In *IUTAM Symposium on Computational Approaches to Multiphase Flow*, pages 119–129. Springer, 2006.

[107] R. M. Jendrejack, J. J. de Pablo, and M. D. Graham. Stochastic simulations of DNA in flow: Dynamics and the effects of hydrodynamic interactions. *J. Chem. Phys.*, 116(17):7752–7759, 2002.

[108] Richard M Jendrejack, David C Schwartz, Michael D Graham, and Juan J de Pablo. Effect of confinement on DNA dynamics in microfluidic devices. *J. Chem. Phys.*, 119:1165, 2003.

[109] J. P. Hernandez-Ortiz, J. J. de Pablo, and M. D. Graham. Fast Computation of Many-Particle Hydrodynamic and Electrostatic Interactions in a Confined Geometry. *Phys. Rev. Lett.*, 98(14):140602, 2007.

[110] Yu Zhang, Juan J de Pablo, and Michael D Graham. An immersed boundary method for brownian dynamics simulation of polymers in complex geometries: Application to dna flowing through a nanoslit with embedded nanopits. *The Journal of Chemical Physics*, 136:014901, 2012.

[111] Shidong Jiang, Zhi Liang, and Jingfang Huang. A fast algorithm for brownian dynamics simulation with hydrodynamic interactions. *Mathematics of Computation*, 82(283):1631–1645, 2013.

[112] A. Sierou and J. F. Brady. Accelerated Stokesian Dynamics simulations. *J. Fluid Mech.*, 448:115–146, 2001.

[113] James W Swan and John F Brady. The hydrodynamics of confined dispersions. *Journal of Fluid Mechanics*, 687:254, 2011.

[114] Raphaël Pesché and Gerhard Nägele. Stokesian dynamics study of quasi-two-dimensional suspensions confined between two parallel walls. *Physical Review E*, 62(4):5432, 2000.

[115] Adolfo J Banchio and John F Brady. Accelerated stokesian dynamics: Brownian motion. *The Journal of chemical physics*, 118:10323, 2003.

[116] E. H. Hauge and A. Martin-Lof. Fluctuating hydrodynamics and Brownian motion. *J. Stat. Phys.*, 7(3):259–281, 1973.

[117] D. Bedeaux and P. Mazur. Brownian motion and fluctuating hydrodynamics. *Physica*, 76(2):247–258, 1974.

[118] E. J. Hinch. Application of the Langevin equation to fluid suspensions. *J. Fluid Mech.*, 72(03):499–511, 1975.

[119] J. N. Roux. Brownian particles at different times scales: a new derivation of the Smoluchowski equation. *Phys. A*, 188:526–552, 1992.

[120] F. Balboa Usabiaga, X. Xie, R. Delgado-Buscalioni, and A. Donev. The Stokes-Einstein Relation at Moderate Schmidt Number. *J. Chem. Phys.*, 139(21):214113, 2013.

[121] Tri T Pham, Ulf D Schiller, J Ravi Prakash, and Burkhard Dünweg. Implicit and explicit solvent models for the simulation of a single polymer chain in solution: Lattice boltzmann versus brownian dynamics. *J. Chem. Phys.*, 131:164114, 2009.

[122] I. Theurkauff, C. Cottin-Bizonne, J. Palacci, C. Ybert, and L. Bocquet. Dynamic clustering in active colloidal suspensions with chemical signaling. *Phys. Rev. Lett.*, 108:268303, 2012.

[123] Jeremie Palacci, Stefano Sacanna, Asher Preska Steinberg, David J Pine, and Paul M Chaikin. Living crystals of light-activated colloidal surfers. *Science*, 339(6122):936–940, 2013.

[124] P. J. Atzberger, P. R. Kramer, and C. S. Peskin. A stochastic immersed boundary method for fluid-structure dynamics at microscopic length scales. *J. Comp. Phys.*, 224:1255–1292, 2007.

[125] S. Lomholt and M.R. Maxey. Force-coupling method for particulate two-phase flow: Stokes flow. *J. Comp. Phys.*, 184(2):381–405, 2003.

[126] M. R. Maxey and B. K. Patel. Localized force representations for particles sedimenting in Stokes flow. *International journal of multiphase flow*, 27(9):1603–1626, 2001.

[127] D Liu, EE Keaveny, Martin R Maxey, and George E Karniadakis. Force-coupling method for flows with ellipsoidal particles. *Journal of Computational Physics*, 228(10):3559–3581, 2009.

[128] C.S. Peskin. The immersed boundary method. *Acta Numerica*, 11:479–517, 2002.

[129] Pat Plunkett, Jonathan Hu, Christopher Siefert, and Paul J Atzberger. Spatially adaptive stochastic methods for fluid–structure interactions subject to thermal fluctuations in domains with complex geometries. *Journal of Computational Physics*, 277:121–137, 2014.

[130] Marshall Fixman. Construction of langevin forces in the simulation of hydrodynamic interaction. *Macromolecules*, 19(4):1204–1207, 1986.

[131] Jens Rotne and Stephen Prager. Variational treatment of hydrodynamic interaction in polymers. *The Journal of Chemical Physics*, 50:4831, 1969.

[132] JR Blake. A note on the image system for a stokeslet in a no-slip boundary. In *Proc. Camb. Phil. Soc*, volume 70, pages 303–310. Cambridge Univ Press, 1971.

[133] P. J. Atzberger. A note on the correspondence of an immersed boundary method incorporating thermal fluctuations with Stokesian-Brownian dynamics. *Physica D: Nonlinear Phenomena*, 226(2):144–150, 2007.

[134] Kyongmin Yeo and Martin R Maxey. Dynamics of concentrated suspensions of non-colloidal particles in couette flow. *Journal of Fluid Mechanics*, 649(1):205–231, 2010.

[135] R. W. Nash, R. Adhikari, and M. E. Cates. Singular forces and pointlike colloids in lattice boltzmann hydrodynamics. *Physical Review E*, 77(2):026709, 2008.

[136] F. Balboa Usabiaga, I. Pagonabarraga, and R. Delgado-Buscalioni. Inertial coupling for point particle fluctuating hydrodynamics. *J. Comp. Phys.*, 235:701–722, 2013.

[137] A. Pal Singh Bhalla, B. E. Griffith, N. A. Patankar, and A. Donev. A Minimally-Resolved Immersed Boundary Model for Reaction-Diffusion Problems. *J. Chem. Phys.*, 139(21):214112, 2013.

[138] B.E. Griffith, X. Luo, D.M. McQueen, and C.S. Peskin. Simulating the fluid dynamics of natural and prosthetic heart valves using the immersed boundary method. *International Journal of Applied Mechanics*, 1(01):137–177, 2009.

[139] G. Tabak and P.J. Atzberger. Systematic stochastic reduction of inertial fluid-structure interactions subject to thermal fluctuations. *arXiv preprint arXiv:1211.3798*, 2013.

[140] A. Donev, T. G. Fai, and E. Vanden-Eijnden. Reversible Diffusion by Thermal Fluctuations. Arxiv preprint 1306.3158, 2013.

[141] H Hasimoto. On the periodic fundamental solutions of the stokes equations and their application to viscous flow past a cubic array of spheres. *J. Fluid Mech*, 5(02):317–328, 1959.

[142] Alexandre M Roma, Charles S Peskin, and Marsha J Berger. An adaptive version of the immersed boundary method. *J. Comput. Phys.*, 153(2):509–534, 1999.

[143] L. Greengard and J. Lee. Accelerating the nonuniform fast fourier transform. *SIAM Review*, 46(3):443–454, 2004.

[144] Eric R Dufresne, David Altman, and David G Grier. Brownian dynamics of a sphere between parallel walls. *EPL (Europhysics Letters)*, 53(2):264, 2001.

[145] Thorben Benesch, Sotira Yiacoumi, and Costas Tsouris. Brownian motion in confinement. *Phys. Rev. E*, 68:021401, 2003.

[146] Carl Wilhelm Oseen. *Neuere methoden und ergebnisse in der hydrodynamik*. Akademische Verlagsgesellschaft, 1927.

[147] John C Crocker. Measurement of the hydrodynamic corrections to the brownian motion of two colloidal spheres. *J. Chem. Phys.*, 106:2837, 1997.

[148] Lukas Holzer, Jochen Bammert, Roland Rzehak, and Walter Zimmermann. Dynamics of a trapped brownian particle in shear flows. *Physical Review E*, 81(4):041124, 2010.

[149] Jochen Bammert, Lukas Holzer, and Walter Zimmermann. Dynamics of two trapped brownian particles: Shear-induced cross-correlations. *The European Physical Journal E*, 33(4):313–325, 2010.

[150] C. W. J. Beenakker. Ewald sum of the Rotne-Prager tensor. *J. Chem. Phys.*, 85:1581, 1986.

[151] Paul J. Atzberger. Incorporating shear into stochastic eulerian-lagrangian methods for rheological studies of complex fluids and soft materials. *Physica D: Nonlinear Phenomena*, 265(0):57 – 70, 2013.

[152] A. Furukawa and H. Tanaka. Key role of hydrodynamic interactions in colloidal gelation. *Phys. Rev. Lett.*, 104(24):245702, 2010.

[153] N. Bou-Rabee, A. Donev, and E. Vanden-Eijnden. Metropolis Integration Schemes for Self-Adjoint Diffusions. *SIAM J. Multiscale Modeling and Simulation*, 12(2):781–831, 2014.

[154] Ayan Chakrabarty, Andrew Konya, Feng Wang, Jonathan V Selinger, Kai Sun, and Qi-Huo Wei. Brownian motion of boomerang colloidal particles. *Physical review letters*, 111(16):160603, 2013.

[155] Stephen M. Anthony, Minsu Kim, and Steve Granick. Translation-rotation decoupling of colloidal clusters of various symmetries. *The Journal of Chemical Physics*, 129(24):–, 2008.

[156] Stephen M Anthony, Liang Hong, Minsu Kim, and Steve Granick. Single-particle colloid tracking in four dimensions. *Langmuir*, 22(24):9812–9815, 2006.

[157] Daniela J. Kraft, Raphael Wittkowski, Borge ten Hagen, Kazem V. Edmond, David J. Pine, and Hartmut Löwen. Brownian motion and the hydrodynamic friction tensor for colloidal particles of complex shape. *Phys. Rev. E*, 88:050301, 2013.

[158] Jan KG Dhont. *An introduction to dynamics of colloids*. Elsevier, 1996.

[159] Ayan Chakrabarty, Feng Wang, Chun-Zhen Fan, Kai Sun, and Qi-Huo Wei. High-precision tracking of brownian boomerang colloidal particles confined in quasi two dimensions. *Langmuir*, 29(47):14396–14402, 2013.

[160] Donald L Koch and Ganesh Subramanian. Collective hydrodynamics of swimming microorganisms: Living fluids. *Annual Review of Fluid Mechanics*, 43:637–659, 2011.

[161] Daisuke Takagi, Adam B Braunschweig, Jun Zhang, and Michael J Shelley. Dispersion of self-propelled rods undergoing fluctuation-driven flips. *Phys. Rev. Lett.*, 110(3):038301, 2013.

[162] Raphael Wittkowski and Hartmut Löwen. Self-propelled brownian spinning top: Dynamics of a biaxial swimmer at low reynolds numbers. *Phys. Rev. E*, 85:021406, 2012.

[163] Miguel X Fernandes and José García de la Torre. Brownian dynamics simulation of rigid particles of arbitrary shape in external fields. *Biophysical journal*, 83(6):3039–3048, 2002.

[164] B. R. Acharya, A. Primak, and S. Kumar. Biaxial Nematic Phase in Bent-core Thermotropic Mesogens. *Phys. Rev. Lett.*, 92:145506, 2004.

[165] Tom Richard Evensen, Stine Nalum Naess, and Arnljot Elgsaeter. Free rotational diffusion of rigid particles with arbitrary surface topography: a brownian dynamics study using eulerian angles. *Macromolecular Theory and Simulations*, 17(2-3):121–129, 2008.

[166] Tom Richard Evensen, Stine Nalum Naess, and Arnljot Elgsaeter. Brownian dynamics simulations of rotational diffusion using the cartesian components of the rotation vector as generalized coordinates. *Macromolecular Theory and Simulations*, 17(7-8):403–409, 2008.

[167] Masato Makino and Masao Doi. Brownian motion of a particle of general shape in newtonian fluid. *Journal of the Physical Society of Japan*, 73(10):2739–2745, 2004.

[168] Eric Dickinson, Stuart A Allison, and J Andrew McCammon. Brownian dynamics with rotation–translation coupling. *Journal of the Chemical Society, Faraday Transactions 2: Molecular and Chemical Physics*, 81(4):591–601, 1985.

[169] RB Jones and FN Alavi. Rotational diffusion of a tracer colloid particle: IV. Brownian dynamics with wall effects. *Physica A: Statistical Mechanics and its Applications*, 187(3):436–455, 1992.

[170] Xiuquan Sun, Teng Lin, and J Daniel Gezelter. Langevin dynamics for rigid bodies of arbitrary shape. *The Journal of chemical physics*, 128(23):234107, 2008.

[171] Ruslan L Davidchack, Richard Handel, and MV Tretyakov. Langevin thermostat for rigid body dynamics. *The Journal of chemical physics*, 130(23):234101, 2009.

[172] W. H. Furry. Isotropic rotational brownian motion. *Phys. Rev.*, 107:7–13, 1957.

[173] Hansklaus Rummler. On the distribution of rotation angles how great is the mean rotation angle of a random rotation? *The Mathematical Intelligencer*, 24(4):6–11, 2002.

[174] Roger E Miles. On random rotations in rˆ3. *Biometrika*, pages 636–639, 1965.

[175] MJ Prentice. On invariant tests of uniformity for directions and orientations. *The Annals of Statistics*, pages 169–176, 1978.

[176] David C Morse. Theory of constrained brownian motion. *Advances in Chemical Physics*, 128(65-189):110, 2004.

[177] José M García Bernal, De La Torre, and José García. Transport properties and hydrodynamic centers of rigid macromolecules with arbitrary shapes. *Biopolymers*, 19(4):751–766, 1980.

[178] H Lamba, Jonathan C Mattingly, and Andrew M Stuart. An adaptive euler–maruyama scheme for sdes: convergence and stability. *IMA journal of numerical analysis*, 27(3):479–506, 2007.

[179] Adolfo Vazquez-Quesada, Florencio Balboa Usabiaga, and Rafael Delgado-Buscalioni. A multiblob approach to colloidal hydrodynamics with inherent lubrication. *The Journal of Chemical Physics*, 141(20), 2014.

[180] John J Molina and Ryoichi Yamamoto. Direct numerical simulations of rigid body dispersions. i. mobility/friction tensors of assemblies of spheres. *The Journal of chemical physics*, 139(23):234105, 2013.

[181] James W Swan, John F Brady, Rachel S Moore, et al. Modeling hydrodynamic self-propulsion with stokesian dynamics. or teaching stokesian dynamics to swim. *Physics of Fluids*, 23:071901, 2011.

[182] Ramzi Kutteh. Rigid body dynamics approach to stokesian dynamics simulations of nonspherical particles. *J. Chem. Phys.*, 132(17):–, 2010.

[183] T.T. Bringley and C.S. Peskin. Validation of a simple method for representing spheres and slender bodies in an immersed boundary method for Stokes flow on an unbounded domain. *J. Comp. Phys.*, 227(11):5397–5425, 2008.

[184] B. Kallemov, A. Pal Singh Bhalla, B. E. Griffith, and A. Donev. An immersed boundary method for rigid bodies. Submitted to Comput. Methods Appl. Mech. Engrg., 2015.

[185] Eligiusz Wajnryb, Krzysztof A Mizerski, Pawel J Zuk, and Piotr Szymczak. Generalization of the rotne–prager–yamakawa mobility and shear disturbance tensors. *Journal of Fluid Mechanics*, 731:R3, 2013.

[186] John Happel and Howard Brenner. *Low Reynolds number hydrodynamics: with special applications to particulate media*, volume 1. Springer Science & Business Media, 1983.

[187] C.M. Mora. Weak exponential schemes for stochastic differential equations with additive noise. *IMA journal of numerical analysis*, 25(3):486–506, 2005.

[188] Gabriel J Lord and Antoine Tambue. Stochastic exponential integrators for the finite element discretization of spdes for multiplicative and additive noise. *IMA J Numer Anal*, 33(2):515–543, 2013.

[189] Leslie Greengard and Mary Catherine Kropinski. An integral equation approach to the incompressible navier–stokes equations in two dimensions. *SIAM Journal on Scientific Computing*, 20(1):318–336, 1998.

[190] Anna-Karin Tornberg and Leslie Greengard. A fast multipole method for the three-dimensional stokes equations. *Journal of Computational Physics*, 227(3):1613–1619, 2008.

[191] Eric E Keaveny and Michael J Shelley. Applying a second-kind boundary integral equation for surface tractions in stokes flow. *Journal of Computational Physics*, 230(5):2141–2159, 2011.

[192] D. Devendran and C. S. Peskin. An immersed boundary energy-based method for incompressible viscoelasticity. *J. Comp. Phys.*, 231(14):4613–4642, 2012.

[193] Nawaf Bou-Rabee and Eric Vanden-Eijnden. Continuous-time random walks for the numerical solution of stochastic differential equations. *arXiv preprint arXiv:1502.05034*, 2015.